Inaugural Dissertation

for obtaining the doctoral degree of the

Combined Faculty of Mathematics, Engineering and Natural Sciences

of the Ruprecht - Karls – University Heidelberg

Presented by

Anne Jenseit, M.Sc.

born in: Darmstadt, Germany

Oral examination: June 17th, 2024

Developing targeted therapies for pediatric PFA ependymoma

Referees:

Prof. Dr. Rob Russell

Prof. Dr. Stefan M. Pfister

Declaration

The work and results of the following dissertation were performed and obtained from May 2020 until March 2024 under the supervision of Prof. Dr. Marcel Kool and Prof. Dr. Stefan M. Pfister in the Division of Pediatric Neurooncology at the German Cancer Research Center (DKFZ), Heidelberg, Germany and the Hopp Children’s Cancer Center (KiTZ), Heidelberg, Germany.

Parts of the introduction (chapters 1.3.2 and 1.4) are taken from the review paper “EZHIP: a new piece of the puzzle towards understanding pediatric posterior fossa ependymoma” published in Acta Neuropathologica in 2022, which I wrote and illustrated with curations from Aylin Camgöz (Hopp Children’s Cancer Center (KiTZ), Heidelberg, Germany). Figures 4, 5, and 6 are taken from this publication [4]. Data included in this dissertation is partially included in the manuscript “USP7 de-ubiquitinates and stabilizes EZHIP making it a therapeutic target in PFA ependymoma”, written by me, which has not yet been submitted for publication. Contributions from collaborators are indicated. Data in Figure 19 is based on work by, but not generated by, Jaqueline Mohr. She performed the experiments under my supervision and with my input as part of her thesis internship for her degree as Bachelor of Science in the lab of Prof. Dr. Marcel Kool.

I hereby declare that I have written and submitted this dissertation myself and have not used any other sources than those indicated. Furthermore, I declare that I have not applied to be examined at any other institution, nor have I used the dissertation in this or any other form at any other institution as an examination paper, nor submitted it to any other faculty as a dissertation.

Anne Jenseit

Abstract

PFA ependymomas are highly aggressive brain tumors typically arising in young children (median age 3 years) and characterized by a poor outcome (10-year OS < 60%). Standard of care therapy for PFA ependymoma consists of surgery and radiotherapy, while chemotherapy has been largely ineffective and proposed targeted therapies have not yet translated to the clinics. This is also routed in the fact that for a long time, no genetic driver mutations could be identified for PFA ependymoma. Recently, aberrant EZHIP overexpression has been identified as likely driver of PFA ependymoma. By inhibiting EZH2, the catalytic subunit of the polycomb repressive complex 2 (PRC2), EZHIP prevents the distribution of the epigenetic repressor mark H3K27me3, resulting in de-repression of PRC2 target genes and corresponding expression changes. However, without any known enzymatic function, EZHIP cannot serve as the drug target, which is so urgently needed. Therefore, in my thesis I focused on the identification, mechanistic characterization and validation of potential alternative treatments for PFA ependymoma.

Firstly, published IP-MS data from non-PFA ependymoma cells was analyzed to identify druggable interaction partners of EZHIP. After the identification of the deubiquitinase USP7, the interaction of USP7 and EZHIP in the nucleus was confirmed in PFA ependymoma cells by co-IP and immunofluorescence, and was found to be independent of EZH2, a separate interaction partner of both proteins. Functionally, USP7 interacts with EZHIP via the USP7 TRAF-like domain, resulting in deubiquitination of EZHIP, which prevents it from being degraded. This stabilization of EZHIP is mediated by the six lysine residues of EZHIP. Previously described somatic EZHIP mutations in patients were not found to interfere with the EZHIP-USP7 interaction. Genetic and pharmacological interventions were used to illustrate the vulnerability of PFA ependymoma cells to a loss of USP7 *in vitro*. PFA ependymoma cells were sensitive to USP7 inhibitors, while normal healthy human astrocytes were not affected, thereby presenting a potential therapeutic window. However, *in vivo* validation treatments in the PFA ependymoma PDOX model BT232 using a maximally tolerated dosing of the USP7 inhibitors P22077 and P005091 did not result in tumor growth inhibition or improved survival of the animals. The reason for this is unclear but could be due to limited brain penetrance or too low exposure of the USP7 inhibitors. Therefore, mid-throughput drug library screening of PFA ependymoma cells was applied to identify drugs that improve their performance in combination with USP7 inhibitors. Based on the appearance of multiple BET inhibitors as top hits of the screen, the drug class of BET inhibitors was identified and their synergy with USP7 inhibitors in PFA ependymoma was validated *in vitro*. Treatments of subcutaneous PFA ependymoma PDX models with the BET inhibitor OTX015, alone and in combination with P005091, are ongoing.

Secondly, epigenetic drug library screening was performed in the PFA ependymoma cell line EPD210FH and two ST-ZFTA ependymoma cell lines (EP1NS, BT165) to identify drugs that would target ependymoma. Overall, BET and HDAC inhibitors showed high potencies. The 10 drugs showing sensitivity in the PFA ependymoma cells included four BET inhibitors, and three drugs were selective for the PFA subtype of ependymoma: Curcumin, the histone methyltransferase inhibitor Chaetocin and the EZH2 inhibitor UNC199.

Thirdly, three publication-informed targets were tested in *in vitro* drug treatments of different PFA ependymoma cell lines. EZH2 inhibitors were evaluated for their ability to further unbalance the PRC2 complex. While UNC199 affected EPD210FH viability at micromolar potency, DZNep significantly reduced PFA ependymoma viability at nanomolar levels *in vitro*. In contrast, although PPARγ was found to be specifically overexpressed in PFA ependymoma in a cohort of pediatric brain tumors and in PFA ependymoma cell lines, PPARγ agonists failed to reduce PFA ependymoma survival *in vitro*. Moreover, As EZHIP might play a role in DNA damage repair, EZHIP-expressing cells were tested for their acclaimed sensitivity to PARP inhibition. Of the four tested PARP inhibitors, Talazoparib affected PFA ependymoma cells at nanomolar potencies, but also affected human astrocytes or ST-ZFTA cells. Furthermore, USP7 and PARP inhibitors were tested in combination for potential synergism, but this did not appear to be the case for PFA ependymoma.

Taken together, my work presents USP7 as a potential target for PFA ependymoma. I identified the stabilization of the oncogenic driver EZHIP through deubiquitination by USP7. Targeting USP7 genetically or pharmacologically reduced EZHIP levels and affected PFA ependymoma survival, rendering USP7 inhibitors a mechanistically sound option to further validate for PFA ependymoma therapy. Additionally, further experiments should be performed to explore EZH2 and PARP inhibitors as therapeutic options for PFA ependymoma.

Zusammenfassung

PFA Ependymome sind höchst aggressive kindliche Gehirntumore, die hauptsächlich in jungen Kindern vorkommen (Medianalter 3 Jahre) und deren Patienten eine schlechte Prognose haben (10-Jahres Überleben < 60%). Der Therapiestandard für PFA Ependymome ist die Kombination aus Resektion und Strahlentherapie, da Chemotherapie weitestgehend keinen Effekt hat und sich zielgerichtete Therapien noch nicht in der Klinik befinden. Dies liegt auch daran, dass lange Zeit keine genetischen Grundlagen der Entstehung von PFA Ependymomen bekannt waren. Vor Kurzem wurde die abnormal hohe Expression von EZHIP als Treiber von PFA Ependymomen ausgemacht. Durch die Inhibierung von EZH2, der katalytischen Untereinheit des PRC2 Komplexes, verhindert EZHIP die Verteilung des epigenetischen Unterdrückungssignals H3K27me3. Dies verhindert die Herunterregulierung von PRC2 Zielgenen und hat dementsprechende Änderungen der Genexpression zur Folge. Jedoch kommt EZHIP als Ziel von dringend benötigten Therapien noch nicht in Frage, da es keine enzymatische Funktion besitzt. Deswegen habe ich mich in meiner Arbeit mit der Identifizierung, mechanistischen Charakterisierung und Validierung von möglichen alternativen Therapiestrategien für PFA Ependymome beschäftigt.

Als Erstes habe ich veröffentlichte IP-MS Daten analysiert, um Interaktionspartner von EZHIP zu bestimmen. Nach der Identifizierung des Deubiquitinierungsenzyms USP7 habe ich dessen Interaktion mit EZHIP in den Zellkernen von PFA Ependymomen mit Hilfe von co-IP and Immunfluoreszenz bestätigt, sowie eine Abhängigkeit der Interaktion von EZH2 ausgeschlossen. Auf funktioneller Ebene wechselwirken EZHIP and USP7 über die TRAF-ähnliche Domäne von USP7, was die Deubiquitinierung von EZHIP zur Folge hat und EZHIP vor Abbau schützt. An dieser Stabilisierung sind alle sechs Lysine von EZHIP beteiligt, in der Literatur beschriebene Mutationen in EZHIP jedoch nicht. Durch genetische und pharmazeutische Manipulationen von USP7 konnte ich zeigen, dass PFA Ependymome verletzlich auf den Verlust von USP7 *in vitro* reagieren. Im Gegensatz zu gesunden humanen Astrozyten reagierten PFA Ependymom Zellen sensitiv auf eine Behandlung mit USP7 Inhibitoren, was eine therapeutische Option aufzeigt. Die *in vivo* Validierung dieser Behandlung mit den maximal tolerierten Dosen der USP7 Inhibitoren P22077 und P005091 in einem orthotrop injiziertem PFA Ependymom Mausmodell zeigte keinen Effekt. Die Gründe hierfür sind noch unklar, aber fehlende Gehirngängigkeit oder zu geringe Dosen der Inhibitoren könnten eine Rolle spielen. Deswegen wurde ein mittel-Durchsatz Screening mit epigenetischen Wirkstoffen durchgeführt, um Inhibitoren zu finden, die mit USP7 Inhibitoren kombiniert werden könne, um deren Wirkung zu verstärken. Da mehrere BET Inhibitoren in dem Screening als wirkungsverstärkt identifiziert wurden, wurde im nächsten Schritt deren Synergismus mit USP7 Inhibitoren *in vitro* validiert. Eine Behandlungsstudie mit der Kombination aus dem USP7 Inhibitor P005091 und dem BET Inhibitor OTX015 in einem subkutanen PFA Ependymom Mausmodell läuft.

Des Weiteren wurde eine epigenetische Wirkstoffbibliothek auf ihre Wirksamkeit in der PFA Ependymom Zelllinie EPD210FH und zwei ST-ZFTA Ependymom Zelllinien (EP1NS, BT165) getestet. BET und HDAC Inhibitoren zeigten übergreifende hohe Wirkung. Es wurden 10 Wirkstoffe identifiziert, auf die PFA Ependymom Zellen sensitiv reagiert haben, darunter vier BET Inhibitoren. Drei der 10

Substanzen waren selektiv wirksam in den PFA Ependymom Zellen: Kurkumin, der Histon Methyltransferase Inhibitor Chaetocin und der EZH2 Inhibitor UNC199.

Zusätzlich habe ich drei Therapieansätze aus Veröffentlichungen auf ihre Wirksamkeit PFA Ependymome *in vitro* anzugreifen getestet. EZH2 Inhibitoren wurden getestet, da sie den PRC2 Komplex weitergehend angreifen könnten. UNC199 reduzierte das Überleben der EPD210FH Zellen in micromolaren Konzentrationen, wohingegen DZNep schon in nanomolaren Konzentrationen PFA Ependymome *in vitro* in ihrer Vitalität eingeschränkt hat. Dementgegen steht das Ergebnis, dass PPARγ Agonsiten nicht in der Lage waren, die Vitalität von PFA Ependymom Zellen *in vitro* zu reduzieren, obwohl PPARγ im Vergleich zu anderen kindlichen Gehirntumoren in PFA Ependymomen besonders hoch exprimiert wird. Des Weiteren wurde die Sensibilität von PFA Ependymomen auf eine Behandlung mit PARP Inhibitoren getestet, da EZHIP durch seine Rolle in der DNA Reparatur Zellen angeblich sensibilisiert. Vier PARP Inhibitoren wurden getestet, von denen Talazoparib am vielversprechendsten war, da bereits nanomolare Konzentrationen PFA Ependymom Zellen stark beeinträchtigt haben. Jedoch war ein vergleichbarer Effekt auf humane Astrocyten und ST-ZFTA Zellen zu beobachten. Weiterhin wurde ein potentieller Synergismus zwischen PARP und USP7 Inhibitoren getestet, konnte jedoch in den PFA Ependymom Zellen nicht bestätigt werden.

Insgesamt geht aus meiner Arbeit USP7 als potentielles Ziel von PFA Ependymom Therapien hervor. Ich konnte zeigen, dass EZHIP als Tumortreiber durch USP7 deubiquitiniert und stabilisiert wird. Durch genetische oder pharmazeutische Manipulation von USP7 wird EZHIP reduziert und die Vitalität von PFA Ependymomen beeinträchtigt. Deswegen scheinen USP7 Inhibitoren ein guter Ansatzpunkt für neue PFA Ependymom Therapien zu sein, jedoch sollten EZH2 and PARP Inhibitoren auch weiterhin als therapeutische Optionen für PFA Ependymome untersucht werden.

List of Abbreviations

PD-L1	PD-1 ligand
PD-1	programmed cell death protein 1
CAR	chimeric antigen receptors
STR	sub-total resection
ABC transporter	ATP-binding cassette transporter
ACVR1	activin receptor type 1A
ALL	acute lymphoblastic leukemia
AMP	adenosine monophosphate
AP-1	activator protein 1
Approx..	approximately
ATP	adenosine triphosphate
ATRT	atypical teratoid rhabdoid tumor
BAX	Bcl-2-associated X protein
BBB	blood brain barrier
C	cysteine
CHX	cycloheximide
CIN	chromosomal instability
CML	chronic myeloid leukemia
CNS	central nervous system
CNV	copy number variations
d.p.i.	days after infection
$dcDSS_{asym}$	differential combo DSS
DIPG	diffuse intrinsic pontine glioma
DMG	diffuse midline glioma
DMSO	dimethyl sulfoxide
DNA	deoxyribonucleic acid
DSS_{asym}	drug sensitivity score
DUB	deubiquitinase
ECM	extracellular matrix
EPOP	Elongin BC and Polycomb repressive complex 2-associated protein
ER	endoplasmic reticulum
ESC	embryonic stem cell
ESS	endometrial stromal sarcoma
EZHIP	EZH inhibitory protein
FDA	food and drug agency
FOS	Finkel–Biskis–Jinkins murine osteogenic sarcoma virus
GEMM	genetically engineered mouse models
GFP	green fluorescent protein

GO	gene ontology
GTR	gross-total resection
h	hour(s)
H3K27ac	histone 3 lysine 27 acetylation
H3K27me1/2	histone 3 lysine 27 mono/di-methylation
H3K27me3	histone 3 lysine 27 trimethylation
HAUSP	herpesvirus-associated ubiquitin-specific protease
HDAC	histone de-acetylase
HEK293	human embryonic kidney cells 293
HGG	high-grade glioma
HIF1a	hypoxia-inducible factor-1a
HMT	histone methyltransferase
HR	homologous recombination
HSV-1	herpes simplex virus 1
i.p.	intraperitoneal
IC50	Inhibiting Concentration 50%
ICD-O	International Statistical Classification of Diseases and Related Health Problems – Oncology
ICR	Institute of cancer research
IDH1	isocitrate dehydrogenase 1
IDR	intrinsically disordered repeats
IFN	interferon
IP	immunoprecipitation
IP-MS	immunoprecipitation followed by mass spectrometry
iPSC	induced pluripotent stem cell
ITCC-P4	Innovative Therapies for Children with Cancer Pediatric Preclinical Proof-of-Concept Platform
IUE	in-utero electroporation
IVC	individually ventilated cages
K	lysine
KD	knock-down
KiTZ	Kindertumorzentrum
KLP	K27M-like peptide
KO	knock-out
LGG	low-grade glioma
LOF	loss-of-function
MAGE	melanoma-associated antigen
MAMLD1	mastermind like domain containing 1
MAPK	mitogen-activated protein kinase
Mb	megabase
MBTD1	malignant brain tumor domain containing 1

MDM2	mouse double minute 2 homolog
MELK	maternal embryonic leucine zipper kinase
MMR	mismatch repair
MS	mass spectrometry
NA	not applicable
NMR	nuclear magnetic resonance spectroscopy
NPC	neuronal progenitor cell
NSCLC	non-small cell lung cancer
nt	non-targeting/ not treated
NTR	near-total resection
NVU	neurovascular unit
OS	overall survival
p.i.	post infection
p.o.	per os / per oral
P53	tumor protein 53
PARP	poly (ADP-ribose) polymerase
PcG proteins	polycomb-group proteins
PDGFRA	platelet-derived growth factor receptor alpha
PDOX	patient-derived orthotopic xenograft
PDX	patient-derived xenograft
PEG	poly (ethylene glycol)
PFA ependymoma	posterior fossa ependymoma, group A
PFB ependymoma	posterior fossa ependymoma, group B
PF-EPN	posterior fossa ependymoma
PF-EPN	posterior fossa ependymoma
PF-SE	subependymoma of the posterior fossa
PNS	peripheral nervous system
PPARγ	peroxisome proliferator-activated receptor gamma
PRC1	polycomb repressive complex 1
PRC2	polycomb repressive complex 2
PROTAC	proteolysis targeting chimera
PTEN	tumor suppressor phosphatase and tensin homolog
PTL	sesquiterpene lactone parthenolide
PTM	post-translational modification
RNA	ribonucleid acid
RS	relative survival
RTK	receptor tyrosine kinase
SAM	S- adenosylhomocysteine
scRNAseq	single cell RNA-sequencing
$sDSS_{asym}$	selective drug sensitivity score
SE	subependymoma

SEM	standard error of mean
sgNT	non-targeting sgRNA
sgRNA	single guide RNA
SHH	sonic hedgehog
shRNA	short hairpin RNA
siRNA	short interfering RNA
SNV	single nucleotide variant
SP-EPN	spinal ependymoma
ST-(EPN-)ZFTA	supratentorial ependymoma, *ZFTA*-fusion positive
ST-EPN	supratentorial ependymoma
ST-EPN-YAP1	suprotentorial ependymoma, *YAP1* fusion-positive
TDSU	targeted drug screening unit
TNFa	tumor necrosis factor alpha
TRAF	tumor necrosis factor receptor–associated factor
TRIM27	tripartite motif-containing 27
TSM	tumor stem medium
TSS	transcription start site
UBL	ubiquitin-like
USA	United States of America
USP7	ubiquitin-specific protease 7
WNT	wingless-type
WT	wildtype
YAP1	yes-associated protein 1
ZFTA	zinc finger translocation associated

List of Figures

List of Tables

Table of Contents

I Introduction

1.1 Pediatric Cancer

Cancer in children is different from adult malignancies. Even though both adult and pediatric cancers are the leading cause of death by disease in their respective age groups, the two deviate in a plethora of characteristics [10, 11]. Adult cancer types arise mainly in tissues of epithelial origin, represented by the manifold of carcinomas that account for over 80% of all adult cancers [12]. In contrast, pediatric cancer types more commonly arise in tissues of the mesoderm or ectoderm, including the neuroectoderm. For cancers that arise in the same tissue in children and adults, mortality rates can differ in both directions, but therapy-induced morbidities occur more often in children [13].

The current believe is that pediatric cancer is a disease of development. Morphologically, many cancers in children overlap with embryonal tissues and arise during circumcised developmental windows. Additionally, some cancer types in children do not arise in adults, which could be routed in the fact that the cell of origin of the pediatric cancer is not present in adults anymore [13]. Comparisons with embryonal tissues showed large overlaps with specific developmental lineages and substantiated that pediatric cancer cells arrest during healthy development. This developmental block keeps the cells proliferating and prevents differentiation or cell cycle exits [14-16]. Additionally, the presence of tumor-predisposing germline mutations in the DNA of ~10% of pediatric patients allow for an early onset of disease [17]. Somatic DNA mutations, on the other hand, are main drivers of adult and childhood cancer. While these mutations in adults are high in frequency (1.8 mutations per Mb DNA) and are mainly caused by environmental exposure that accumulates over time, in children they are observed at low frequencies (0.13 mutations per Mb) and pediatric tumors are often driven by the occurrence of one somatic mutation [18].

The main pediatric cancer types are the systemic cancers: leukemias and lymphomas. Leukemias account for ~ 30% of all childhood cancers. Dominant are the acute versions acute lymphocytic leukemia (ALL) and acute myeloid leukemia (AML), which both originate from dysregulated hematopoietic stem and progenitor cells from the bone marrow. Lymphoma at ~ 15% also arise from leukocyte precursors, but in the lymphatic system [19]. The second most common pediatric cancer are tumors of the central nervous system (CNS) at ~ 24%, followed by soft tissue sarcomas (5.7%), tumors of the peripheral nervous system (5.5%), bone (5.1%), or kidney (4.5%), as well as germ cell tumors (3.9%), carcinomas (3.2%) and others (4.5%). Boys are affected by slightly higher incidence rates than girls at all ages and incidence rates peak in infants below the age of one year (**Figure 1**).

In Germany, approx. 2250 new cases of pediatric cancers are diagnosed each year. Although this might seem like a low number, these cases scale up to an estimated yearly 150,000 – 250,000 cancer diagnoses worldwide in children aged 0-19 years [6, 20]. While pediatric cancer incidence rates in the United States of America (USA) increased by 0.8 per year between 1975 and 2022, death rates per 100,000 declined by 71% in children under 14 years and by 61% in adolescents between 15 and 19 years of age. This decrease reflects the dramatic progress in leukemia treatments reducing death rates by 84% in children under 14 and by 75% in adolescents achieving remission rates of 90-100% in childhood ALL [12].

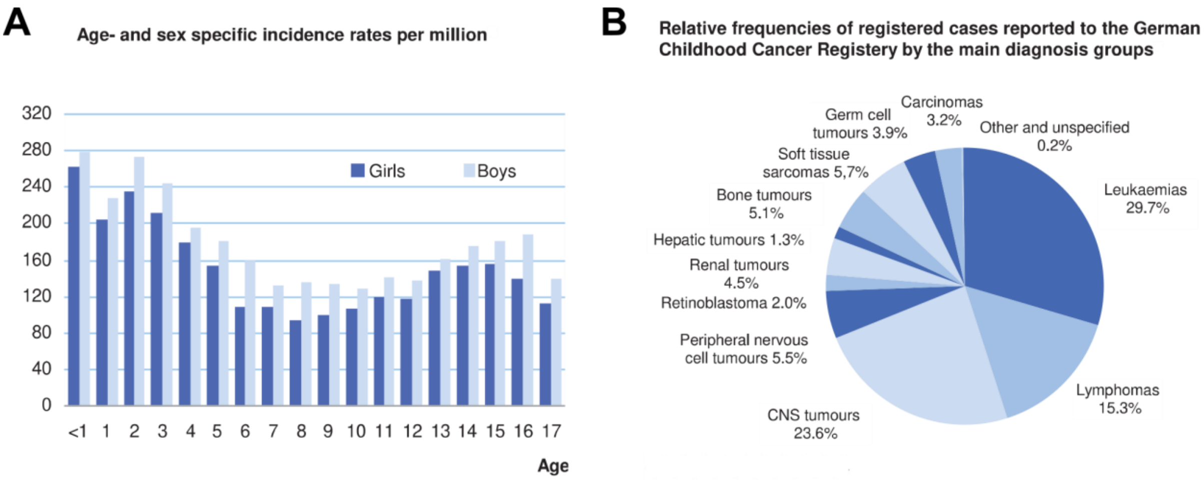

Figure 1 | Age and diagnosis distribution of pediatric cancers in Germany

*(**A**) Age- and sex specific incidence rates per million. (**B**) Relative frequencies of main diagnosis groups. CNS: Central nervous system. Data from 2009-2018, based on 21831 patients under 18 years. Figure adapted from Spix et al., 2023 [6].*

1.2 Pediatric CNS Tumors

Tumors of the CNS are the most common pediatric solid tumors (**Figure 1B**). Throughout the brain and the spinal cord, different entities of tumors characterized by different histologies, incidences or outcomes can arise. Therefore, understanding the similarities and differences is of great importance to ensure optimal patient care. After first attempts by Baily and Cushing to discriminate different types of brain tumors started in 1925 [21], the world health organization (WHO) united efforts and aims to help understand these tumors better to stratify patients and improve their treatment.

1.2.1 WHO classification of CNS tumors

The classification of brain tumors has evolved over the past decades [22]. While the first official WHO classification of CNS tumors in 1979 already discriminated 90 tumor types, the newest 5th edition in 2021 now includes 130 ICD-O coded diseases [23, 24]. For decades, the classification of CNS tumors was based on histology and clinical features, resting on the location of the tumor in the brain, the morphology of cells and their similarity to presumed tissues of origin as assessed by neuropathologists. Aggressiveness of tumors was categorized into four stages from grade I (benign) to grade IV (highly malignant), based on the prognosis after removal [23, 25, 26]. However, inter- and intra-observer variance in classification and grading is high and can have significant impact on clinical treatment recommendations [27-30].

Therefore, modern genetic and molecular biology methods have been increasingly incorporated into the classification of CNS tumors. One milestone has been the establishment of DNA methylation analysis as basis for CNS tumor classification [15]. DNA methylation refers to the modification of the DNA nucleotide cysteine with a methyl-group at position carbon five. This modification is often found at cysteines located next to a glycine creating a CpG nucleotide, the smallest unit of so-called CpG islands

[31]. As these islands are often concentrated in transcription start sites or enhancer regions, changes in their methylation status can regulate gene transcription. DNA methylation is tightly epigenetically regulated during healthy development and patterns are passed on to daughter cells, making DNA methylation patterns a footprint of cell status [32, 33]. Differences in CpG island methylation are most commonly observed in promotor regions of cancer cells, which mainly reflects their cell-of-origin [34]. In 2018, Capper et al. published the first DNA methylation-based CNS tumor classifier, an online application based on DNA methylation data of a reference cohort of over 2800 histologically well-described brain tumors [15]. This tool helps to identify tumor type identities and was shown to lead to a change of diagnosis for 12% of cases when applied to a prospective histologically diagnosed cohort, underscoring the importance of molecular tools for tumor classification. Therefore, the 5th WHO CNS tumor classification in 2021 has now integrated DNA methylation profiling for an improved diagnosis of CNS tumors. Additionally, many new tumor types and subtypes identified by DNA methylation were included in the latest WHO classification [24]. Moreover, adding DNA or RNA sequencing methods can be used to further characterize tumor types and identify (sub)type specific mutations or gene fusions. Specifically, gene panel sequencing can be used to identify genetic alterations in pre-defined gene sets easily from little input material [35, 36]. A recent study combined DNA methylation profiling and targeted panel sequencing in a prospective cohort of 1200 newly diagnosed pediatric CNS cancer patients, which improved diagnostic accuracy compared to a histologically based diagnosis and allowed for the detection of diagnostically or therapeutically relevant genetic alterations, like mutations in isocitrate dehydrogenase 1 (IDH1), BRAF or histone 3, or underlying cancer predisposition syndromes [37].

Further profiling methods, such as transcriptome analysis, are continuously improving and can be used to stratify tumor identities [38]. A new development is the implementation of DNA sequencing and DNA methylation-based tumor classification during surgery. Compared to the evaluation of tumor sections by a pathologist, methods such as nanopore sequencing give the surgeon a more reliable and faster option to tailor the extent of tumor resection to disease type or disease risk [39, 40]. Additionally, single cell RNA-sequencing (scRNAseq) techniques are used increasingly and many studies have been performed matching tumor cells to specific cellular hierarchies during development [41-45]. At the moment, these studies focus on gaining knowledge about the developmental origins and intra-tumoral structures of cancer, but could be used for further subtyping or other applications such as identification of therapy resistant subclones. However, these more elaborate methods are analysis-intense, less accessible and less affordable, which needs to be considered when implementing structures globally. Additionally, tumor entity sub-classification should be seen as a clinical tool and is only meaningful if separations provide information on differences in outcome or treatment regimens.

1.2.2 An overview of pediatric CNS tumors

Tumors of the CNS are the most common pediatric solid tumors accounting for ~ 24 - 30% of childhood tumors, while contributing to ~ 14% of cancers young adults (15-39 years). In adults aged 40 years or older, only 4% of all diagnosed cancers are located within the CNS [6, 46]. Pediatric CNS tumors are highly divers and can occur in all locations throughout the brain and spinal cord. Originally, they were mainly diagnosed and classified based on histology, but in recent years more and more molecular data has been integrated into the diagnosis. However, updated data adhering to the most recent classification is rare, which is why histology-based data is included here to provide an overview. Most pediatric CNS tumors are located in forebrain, which includes the cerebrum and the four lobes (21.6%) as well as the pituitary and craniopharyngeal duct (18%), followed by the hindbrain, including the cerebellum (13.9%), and the brain stem (10.1%). Less frequent locations include the cranial nerves (7.5%), the ventricles (5.2%), the spine (5.1%) and others (18.5%) (**Figure 2A**).

Based on their histopathological features, ~ 43% of CNS tumors are classified as gliomas (**Figure 2B**) [47]. This umbrella term describes a multitude of tumor entities with different biology and clinical characteristics, which are divided into five pediatric groups in the 2021 WHO CNS tumor classification: Pediatric diffuse low grade glioma (LGG), pediatric diffuse high-grade glioma (HGG), circumscribed astrocytic gliomas, glioneuronal and neuronal tumors, and ependymal tumors. Ependymal tumors, which account for ~ 5% of all pediatric CNS tumors, will be covered in more detail in the next chapter [47]. Both circumscribed astrocytic gliomas and the group of glioneural and neuronal tumors are largely considered LGG due to their generally good prognosis and their WHO grade I or II grading. Together, pediatric LGG account for ~ 25-30% of all childhood CNS tumors and include the most frequent single entity pilocytic astrocytoma, accounting for ~ 15% of all pediatric CNS tumors, diffuse and anaplastic astrocytoma (~ 5% of all pediatric CNS tumors) and oligodendrogliomas and oligoastrocytic tumors (together ~ 1 %) [48]. Molecular data including DNA methylation did not yield oligoastrocytoma as separate entity, which is why they are not included in the current 2021 CNS tumor classification [49]. In contrast, HGG are WHO grade III or IV and considered highly aggressive. They are less common than LGG and include diffuse gliomas of the hemispheres and the midline (other gliomas, ~ 13%) and glioblastoma (~ 2.7%) (**Figure 2B**) [2]. Tumors histopathologically classified as tumors of the pituitary are the second-largest group of pediatric CNS tumors (14.7%) followed by embryonal tumors (9.2%), which include medulloblastoma, atypical teratoid rhabdoid tumor (ATRT), embryonal tumors with multilayered rosettes (ETMR) and others (**Figure 2B**). Meningioma and tumors of the pituitary show a clearly higher incidence in females, whereas germ cell tumors, embryonal tumors and gliomas are more likely to occur in males [2]. However, gender distributions can be highly subtype specific, as can be illustrated in medulloblastoma. Tumor of the Wingless-type (WNT) subgroup have a gender ratio of 45% male to 55% female, while 78% of subtype III of the group3/4 medulloblastoma arise in males [50].

Although pediatric CNS tumors are the most frequent cause of cancer-related mortalities and morbidities in children aged 0-14 years, the survival probabilities for children with CNS tumors improved steadily over the past decades [6, 51]. In Germany, children diagnosed between 1981 and 1990 had a 10-year survival probability of only 58% [6]. In 2019, the 10-year survival probability of children diagnosed with CNS, intracranial or intraspinal tumors had increased to 77%. Yet, the 10-year probability of event-free survival is only 48% [6, 10]. The same trend is observed in the USA [47, 52], where the 10-year relative survival of pediatric brain tumor patients diagnosed between 2015 and 2019 was at 81.1% [2]. However, outcomes vary drastically between the different types and subtypes of brain tumors. Although they can both be called glioma, the 5-year survival rate of pilocytic astrocytoma, a LGG, is 97.2%, whereas the rate for HGG is 25.3% [46, 51], which can drop to less than 5% for Diffuse Midline Glioma, H3K37M mutated (DMG) that account for about 50% of HGG [37, 53, 54]. Another example can be found in medulloblastoma. While patients with a medulloblastoma WNT have a 5-year OS of ~ 95%, patients

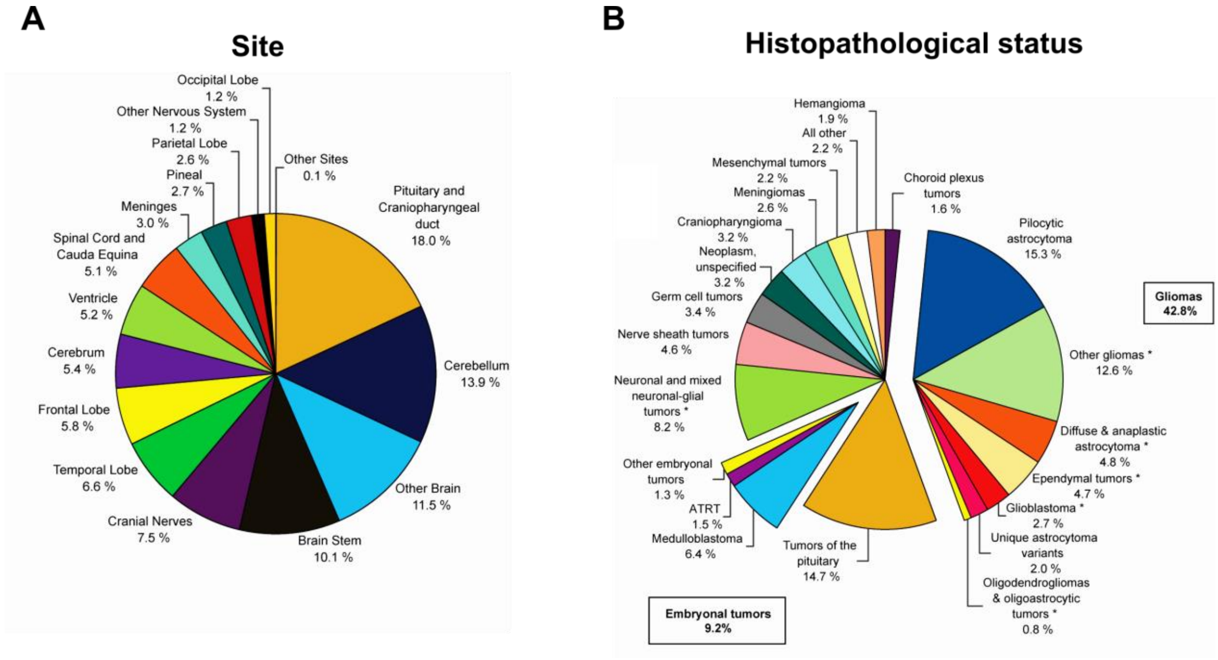

Figure 2 | Distribution of pediatric brain tumors by location and histopathological diagnosis

*Primary Brain and CNS tumor distribution of 25340 cases in children (0-19 years) in the USA between 2015 and 2019 by location (**A**) or histopathology (**B**).Figure adapted from Ostrom et al., 2022 [2].*

with a Group3 medulloblastoma face a 5-year OS of only ~50% [55]. The difference in survival of the subtypes of medulloblastoma underlines this further, as the 5-year OS of the medulloblastoma Group 3/4 type III is 43%, whereas type IV has a 5-year OS of 80% [50]. This highlights the importance of exact tumor type and subtype determination for clinicians and patients.

Driving events in pediatric brain tumors are different between tumor entities and from adult tumors. Whilst adult tumors show high numbers of somatic mutations, they are 14-times lower in pediatric tumors [18, 56]. Exceptions are so-called “hypermutator” tumors (>10 mutations/Mb), which often are deficient in DNA mismatch repair (MMR) [57], and are only found among pediatric HGG [18]. More abundant than in adult patients are germline mutations in cancer predisposition genes in 7-8% of all pediatric CNS patients [18]. The main associated pathways affected by cancer predisposition genes are DNA repair, transcription, the mitogen-activated protein kinase (MAPK) pathway and epigenetic pathways, while the most frequent germline mutations were found in the *tumor protein P53* gene and in *BRCA2*, two of the most famous cancer-predisposition genes, as well as *RB1*, *NF1* or *ALK* [18]. Which mutations occur is highly context dependent. In medulloblastoma, for example, mutations in *SUFU*, *PTCH1* or *ELP1* are most common [58, 59]. Children with underlying germline mutations of *P53* (Li-Fraumeni syndrome) are very likely to develop multiple tumors during their life time and have a cumulative risk of 50% to develop a tumor by the age of 30 [60]. Some tumor types are enriched for patients with Li-Fraumeni syndrome. Children with a sonic hedgehog (SHH)- driven medulloblastoma were reported to have an underlying *P53* mutation in 8%, and in 20% in the age group of five to 16 years of age [58]. Additionally, a recent study reported germline *P53* mutations in four out of seven pediatric HGG-MYCN [61]

Most pediatric CNS cancers are propelled by a single driver event [62, 63]. Often, this main driver event is a gene fusion. Gene fusions can occur inter-chromosomally or intra-chromosomally and the results are either an altered expression of one of the fusion partners or a combined transcript with parts of both genes [64]. In pediatric brain tumors, fusions often involve kinases, such as the *KIAA1549-BRAF* fusion in LGG leading to constitutive activation of the MAPK pathway [65], or transcriptional regulators as in the *ZFTA-RELA* fusions of *zinc finger translocation associated* (*ZFTA*; formerly *C11orf95*) with the transcriptional activator *RELA* found in 70% of supratentorial ependymoma (ST-EPN) [1, 66, 67]. Another example for driver mutations are the mutations found in HGG in histone 3: position lysine 27 (H3K27) can be exchanged for a methionine (K27M), or position glycine 34 (H3G34), which can be mutated either into a valine (G34V) or arginine (G34R) [68]. The two glioma subtypes are different in their clinical and histopathological parameters. While G34 mutated glioma arise mainly in the hemispheres of the brain, K27M-driven glioma are located in the midline locations (including the pons and thalamus) [68, 69]. Additional to mutations, pediatric CNS tumors are often characterized by copy number variations (CNV) and fusion genes [70]. Common are amplifications of *MYC* or *MYCN*, which are found in several CNS tumor types like medulloblastoma, ependymoma, or HGG, and are often associated with worse prognosis [71, 72]. A subset of ~ 30 CNS embryonal tumors has recently been reported to be characterized by amplifications of the *PLAGL1* or *PLAGL2* gene [73].

1.3 Ependymoma

In children, ependymoma account for 5-6% of all malignant brain tumors (**Figure 2B**) [49, 74]. They can occur across all ages but are about 2.5 times more common in children than in adults, which is why they are largely considered a pediatric tumor [75]. WHO subgrouping of ependymoma is based on both their anatomical location and molecular characteristics including DNA methylation clustering [49]. Anatomically, ependymoma can arise anywhere within the neuroaxis: in the supratentorial brain (ST-EPN), which covers the cerebral hemispheres, in the hindbrain or posterior fossa (PF-EPN), which includes the cerebellum and brainstem, or anywhere in the spinal cord (SP-EPN) [1, 76]. ST-EPN and PF-EPN comprise three molecular subgroups each, while four distinct molecular groups have been identified in the spine (**Figure 3A**).

In each location, subependymoma (SE) are a benign molecular group identified by a distinct histological appearance, an adult patient population and a highly favorable outcome (five-year OS 100%) [1]. Molecularly, SP-SE can have deletions of the chromosome arm 6q, but SE at other locations are characterized by an overall stable genome [77].

Besides the SE, the two other molecular groups of ST-EPN are ST-EPN-YAP1 and ST-EPN-ZFTA (ST-ZFTA). Both groups are characterized by oncogenic translocations and the consecutive expression of group specific fusion genes, which have been shown to be tumor-inducing in mice [66, 78]. ST-EPN-YAP1 tumors have gene fusions involving the transcriptional coregulator *yes-associated protein 1* (*YAP1*) and multiple fusion partners, most frequently (86%) *mastermind like domain containing 1* (*MAMLD1*) [1, 78, 79]. They occur predominantly in younger children (median age 1.4 years) and show great 5-year OS at 100%. In contrast, ST-EPN-ZFTA, which constitute over 70% of ST-EPN and ~ 11-18% of all ependymoma (adults and children), arise in young patients at a median age of eight years and show a 10-year OS of only 49% (**Figure 3**) [1, 80]. This group is driven by the expression of fusions involving *zinc finger translocation associated* (*ZFTA*), a poorly characterized gene on chromosome 11 (previously known as *C11orf95*). The main *ZFTA* fusion partner is the transcription factor of the canonical NFkB pathway, *RELA* (p65) [67, 81, 82]. *ZFTA* and *RELA* can be fused at different breakpoints whilst always including the zinc finger domain of *ZFTA* and the transactivation domain of *RELA*. Other fusion partners of *ZFTA* include *MAML2*, *MAML3*, *NCOA1* and *NCOA2* [66, 83]. The proximity of the genomic location of *ZFTA* and its fusions on chromosome 11 is characterized by chromothripsis, but the rest of the genome seems stable despite recurrent focal *CDKN2A/B* deletions in ~15 % of ST-EPN-ZFTA patients [1, 67]. In a recent study, 12/200 molecularly defined ST-EPN-ZFTA were reported as located in the PF and were characterized by early progression or relapse [3].

Like the SP-SE, the other three spinal ependymoma groups mainly arise in adults and combined only make up for about 15% of all ependymoma. Myxopapillary ependymoma (SP-MPE), named after their histological structures, are usually benign and show some chromosomal instability (CIN) [80]. SP-EPN tumors, on the other hand, often develop in patients with germline or somatic mutations in the *neurofibromatosis type 2* (*NF2*) gene and are found in 18-53% of patients with the cancer predisposition syndrome NF2 [84-87]. The most recently identified ependymoma subgroup, SP-MYCN, is driven by amplifications and high expression of the proto-oncogene *MYCN*. Even though only limited data is available so far, it seems that this subgroup is characterized by a broad age at diagnosis (median 32 years, range 12-56 years), high rate of metastasis and bad outcome (10-year OS 32%) [3, 71].

The majority of ependymoma (90%) occur intracranially, with two-thirds of these cases located in the posterior fossa [76]. PF-EPN are divided into three main molecular groups: subependymoma (PF-SE), PF-EPN, group A (PFA) and PF-EPN, group B (PFB). PFB ependymoma comprise ~15% of all ependymoma, occur mainly in adolescents and adults and show a 10-year OS of 88%, but only a 10-year progression-free survival (PFS) of 56%. Even though five subgroups of PFB ependymoma have been described based on DNA methylation, no oncogenic driver has yet been identified, but tumors can show CIN and loss of chromosome 13q was suggested as risk marker of reduced survival [88]. In contrast, PFA ependymoma are a disease of young children (58% younger than four years, 41% 4-18 year, 1% adults). This subgroup accounts for almost 50% of all molecular ependymoma groups (**Figure 3B**) and is a driver of the bad outcome of ependymoma in young children (10-year OS 56%) [1]. Molecularly and histopathologically, PFA ependymoma are highly distinct. Immunohistochemically, they show a loss of the epigenetic mark histone 3 lysine 27 trimethylation (H3K27me3). Additionally, the

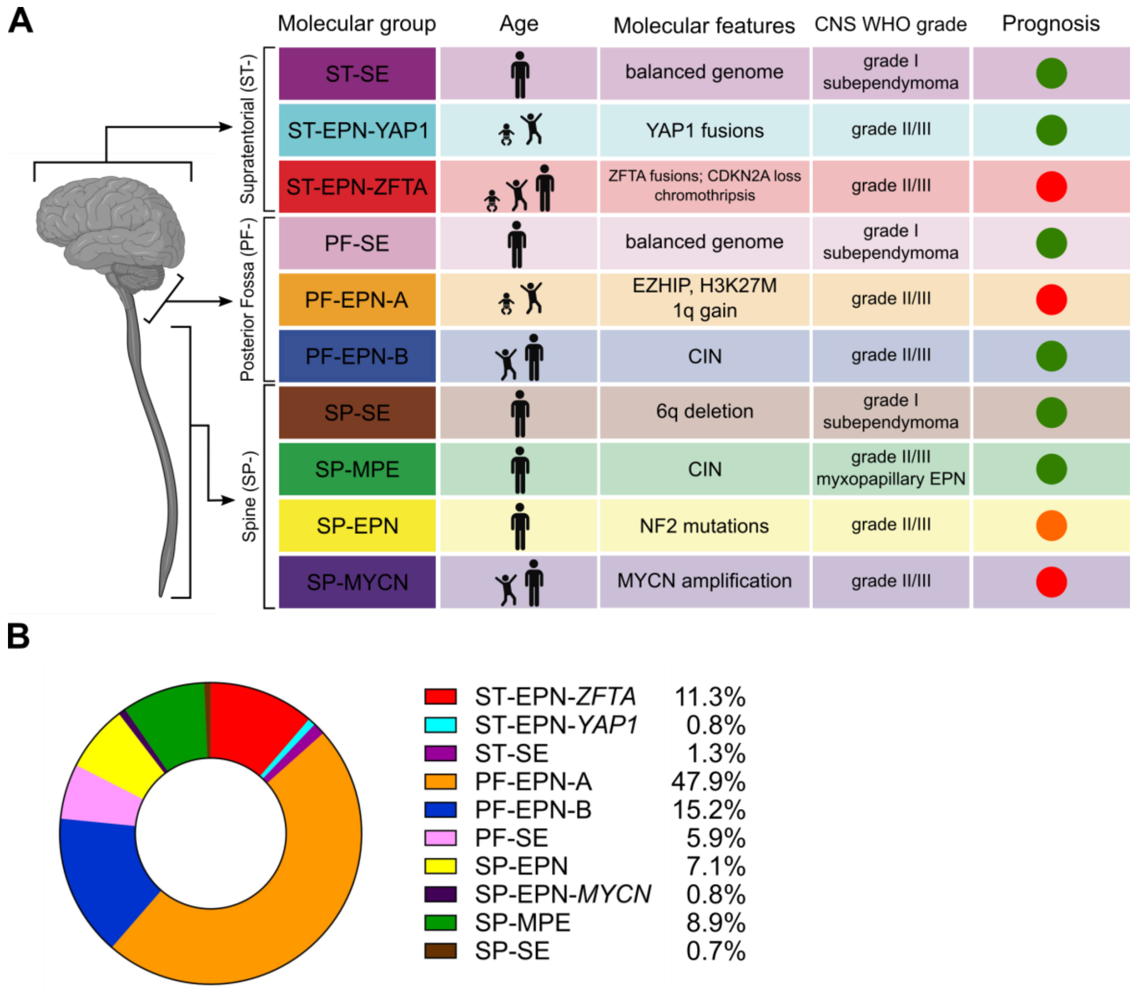

Molecular group	Age	Molecular features	CNS WHO grade	Prognosis
ST-SE	🧍	balanced genome	grade I subependymoma	🟢
ST-EPN-YAP1	👶 🧒	YAP1 fusions	grade II/III	🟢
ST-EPN-ZFTA	👶 🧒 🧍	ZFTA fusions; CDKN2A loss chromothripsis	grade II/III	🔴
PF-SE	🧍	balanced genome	grade I subependymoma	🟢
PF-EPN-A	👶 🧒	EZHIP, H3K27M 1q gain	grade II/III	🔴
PF-EPN-B	🧒 🧍	CIN	grade II/III	🟢
SP-SE	🧍	6q deletion	grade I subependymoma	🟢
SP-MPE	🧍	CIN	grade II/III myxopapillary EPN	🟢
SP-EPN	🧍	NF2 mutations	grade II/III	🟠
SP-MYCN	🧒 🧍	MYCN amplification	grade II/III	🔴

🟥	ST-EPN-*ZFTA*	11.3%
🟦	ST-EPN-*YAP1*	0.8%
🟪	ST-SE	1.3%
🟧	PF-EPN-A	47.9%
🟦	PF-EPN-B	15.2%
🟪	PF-SE	5.9%
🟨	SP-EPN	7.1%
⬛	SP-EPN-*MYCN*	0.8%
🟩	SP-MPE	8.9%
🟫	SP-SE	0.7%

Figure 3 | Characteristics of ependymoma

*(**A**) The 10 molecular subgroups of ependymoma located supratentorially (ST), in the posterior fossa (PF) or spine (SP). Figure was adapted and updated from Pajtler et al., 2015 [1]. Figure was generated with the help of biorender.com. (**B**) Relative occurrence of the different subgroups. Based on rounded data (n=2023) from Pohl et al. [3]*

tumors can show specific chromosomal gains or losses, whilst presenting with an otherwise rather stable genome. Present in 25% of cases, chromosome 1q gain occurs frequently in PFA ependymoma, but also seen in PFB ependymoma (18%) and ST-EPN-ZFTA (24 %) [1]. In PFA ependymoma, 1q gain is associated with significant difference in OS, but not in PFB ependymoma or ST-EPN-ZFTA [1, 88-90]. In PFA, loss of 6q is an additional high-risk prognostic factor, and their combination defines a very high-risk group of ependymoma, but the pathogenic mechanism of both has not been clearly identified yet [91-94]. A recent study showed that 12/32 PFA ependymoma relapses presented new 1q gains and 6q losses compared to the primary tumors. Additionally, chromosomal aberrations were intratumorally located in areas of high cell density, whose presence was associated with poor outcome [95].

The unfavorable clinical outcome of mostly pediatric ependymoma is at least partially routed in the limited treatment options. The current standard of care therapy is a combination of surgery and radiotherapy [96, 97]. A 2021 study on 53 patients (age group 1-25 years) including 27 patients with PFA ependymoma could show that patients benefit from gross-total or near-total resection (GTR/NTR), which improved five-year OS to 48.7% compared to 5.3% in patients that did not receive GTR or NTR [98]. A more recent analysis compared the effect of extent of resection (GTR vs sub-total resection (STR)) between the molecular groups of ependymoma. When looking at all 946 ependymomas in this study, STR was confirmed to negatively impact PFS and OS. ST-EPN-ZFTA patients, however, did not significantly benefit from GTR, while PFA ependymoma patients showed better PFS and OS upon GTR and PFB ependymoma patients showed a reduced relapse rate at comparable OS [3]. Success of surgery should be monitored by magnetic resonance imaging (MRI) and second-look surgery can be utilized [99]. Post-operative conformal radiation therapy is recommended for most ependymomas, as it can increase local tumor control rates and thus prolong patient survival and prevent tumor recurrence [100]. However, interventions are associated with long-term decline in neurocognitive functions. This is especially critical in younger patients, which is why monitoring of cognitive functions after radiotherapy is recommended [96, 101]. Chemotherapy could not show patient survival improvement in previous studies, but sometimes may be considered for patients with recurrent disease that do not qualify for re-surgery [96, 102-104]. Ependymomas recur frequently at the same site or within the CNS in up to 50% of pediatric patients, while extraneural metastasis are rare [96, 105].

1.3.1 Preclinical Models of ependymoma

Disease models are needed at every step of preclinical research to characterize tumor-driving mechanisms, identify functional relationships and test and develop therapies, e.g. via drug testing. Thus, the continuous development of preclinical tumor disease models is crucial to further improve patient outcomes. An ideal model should mimic the tumor in terms of genetic events, anatomic location, histopathological characteristics and latency of tumor development. The model should recapitulate the inter- and intratumoral heterogeneity and be predictive of patient´s responses to treatment [106]. To maximize success, it is important to understand strengths and weaknesses of different model types and the availabilities of existing ependymoma models.

1.3.1.1 In vitro ependymoma models

In vitro models are the most common model system of ependymoma. Ideally, they are easy to handle in culture, also in large-scale high-throughput experiments, robust, fast-growing, well-characterized, easy to engineer genetically and comparably low in cost [107]. However, their biggest disadvantage is that they can be too oversimplified and estranged from the disease they model. The advantage of having a robust reproducible model system often comes at the expense of a lack of heterogeneity. Cells in culture lack the impact and connection with the (tumor)microenvironment and the related pathways, which is an integer hallmark of cancers [108, 109]. Additionally, culture conditions influence cell growth, can change gene signatures or induce cell differentiation in different lineage-directions and put selection pressure on cells to adapt to culture. For brain (tumor) models especially, the lack of a blood-brain barrier (BBB) is a real limitation, especially for drug testing [110-112]. In consequence, a limited predictive value of cell lines for drug effectiveness in patients has been reported [113].

At the moment, patient-derived cell lines are the main *in vitro* model system for ependymoma, even though the number of well-established and easy to handle cell lines is still low [114]. One main hurdle is the lack of proliferation capacity when cells are taken into culture. Often, cells will not multiply, but arrest and potentially differentiate. Therefore, change of character is a second obstacle in ependymoma culturing. Regular testing for cell identity, e.g. via DNA methylation or DNA sequencing analysis, can help prevent cultures to change their identity (CNV changes, mutations, cell line swaps) and should be carried out regularly as quality control [115].

When creating a new cell line, tumor chunks are harvested from patients during surgery or at biopsy and can be taken into culture as small chunks or as single-cell suspension, still resembling the clonality of tumor cells and mixture of different cell populations, including non-tumor cells [116, 117]. Over time, the culture conditions will affect the composition of the culture and established cell lines will often be a genetically and phenotypically homogenous population [118, 119]. The choice of media and culture conditions is essential to cellular growth and identity, as highlighted by recent studies about the role of hypoxia on PFA ependymoma culturing that suggested to start and keep fresh PFA ependymoma cultures under hypoxia [120]. Applicability of this discovery to new and existing cultures is limited. According to the publication, exposure to normoxia nullifies the benefits of hypoxia culturing, questioning the benefit of transferring established cells to hypoxia. Secondly, access to hypoxia incubators and hoods is not the standard, nor is the availability of fresh PFA ependymoma tissue for new cell line establishment.

One approach to improve cellular heterogeneity in culture is the culturing of cells as tumor neurospheres. One general observation, which was confirmed for neurospheres, is that more aggressive tumors are easier to establish as *in vitro* culture, which is why there are many cell lines established from metastases and the limited number of available ependymoma cell lines are from the most aggressive ependymoma subtypes ST-EPN-ZFTA and PFA ependymoma [121-123]. A more elaborate and relatively new approach to ependymoma modeling is the use of brain organoids. Organoids are three-dimensional structures derived from embryonic stem cells (ESCs) or induced pluripotent stem cells (iPSCs) that at least partially mimic the structure of a designated organ. Over the past decade, a variety of protocols has been established to create brain organoids that are specific to anatomic sites and developmental time points of the brain [124]. Genetic engineering to induce tumor formation can be performed before organoid formation or at the organoid level and different strategies to target specific cell populations can be employed [124, 125]. A recent protocol even described the generation of vascularized brain organoids to mimic the BBB [126, 127]. Research is ongoing, but no genetically engineered ependymoma organoid model has been published yet [128].

1.3.1.2 In vivo ependymoma models

Almost all *in vivo* models of ependymoma are mouse models. The mouse genome overlaps at 90% with the human genome, is well characterized and annotated. Mice and humans are physiologically similar and the CNS is highly conserved between the species [129, 130]. Their additional natural properties render them the gold standard model for disease modeling and drug testing: mice have a short lifespan of one-to-two years, have a fast reproduction cycle (19-21 days) and are of small body sizes (20-60 g) [131, 132]. There are two main types of ependymoma mouse models: genetically engineered mouse models (GEMM) and patient-derived xenografts (PDX).

GEMM model tumors by creating simplified tumor-specific genetic backgrounds in either the complete animal (germline) or in specific target cells. Classical examples are the overexpression of oncogenes or the deletion of tumor suppressors, alone or in combination. Tissue-targeting can be achieved by using tissue-specific promotors, and time-sensitive induction can be applied using doxycycline-inducible systems. A clear advantage of GEMM is the presence of an intact immune system and BBB in the mice [133]. GEMMs can be established by germline genome editing and specific crossing of animal or by using somatic gene transfer technique. One technique applied for ependymoma GEMMs is *in-utero* electroporation (IUE), which is especially feasible to create pediatric brain tumor models through introduction of genetic perturbances into specific locations of the developing mouse brain [134, 135]. After retroviral gene transfer of *ZFTA-RELA* into NSCs in mice induced tumor formation [136], an ependymoma IUE model of ST-EPN-YAP1 was established overexpressing the YAP1-MAMLD1 fusion gene in the cerebral cortex [78]. Further groups build on this and reported multiple ST-EPN-ZFTA IUE models introducing different ZFTA-fusions to create tumors, which histologically and molecularly resembled patient tumors [66, 137]. No GEMM for PFA ependymoma, potentially driven by the expression of *EZHIP*, could be generated yet (see Chapter 1.3.4) [123].

In contrast to GEMM, PDX models are created by injecting fresh or early-passage human tumor cells into immunocompromised mice (or other animals [138]), either into the flanks of the mice or orthotopically at the exact location of the tumor in the patient. A variant of the classic PDX is the injection of (genetically engineered) cell lines, patient- or iPSC-derived [139]. Orthotopically (PDOX), the microenvironment reflects the original tumor site better, but the main inherent disadvantage is the lack of the immune compartment in this model [140]. Additionally, as PDX cells are passaged through mice, the tumor cell composition and identity may drift, resulting in more aggressive tumors with shorter lag times, while maintaining genetic and histological characteristics of the patient tumor [140-142]. However, PDX models in general are reported to show high correlation to patients upon treatment [143, 144].

As PDX models are based on patient material, they reflect the inter-tumoral heterogeneity between patients. This can be an advantage, e.g. to identify biomarkers or test treatment responses in different subgroups, but unbiased results depend on sufficiently large cohort sizes implying high efforts and costs [145]. Thus, many groups have been putting large efforts into establishing PDX biobanks [141, 146, 147]. The international Innovative Therapies for Children with Cancer Pediatric Preclinical Proof-of-Concept Platform (ITCC-P4) aimed to establish and characterize over 400 pediatric PDX models between 2017 and 2022 across different high-risk pediatric tumor types [148, 149]. Again, only the most aggressive molecular ependymoma groups ST-EPN-ZFTA and PFA ependymoma were represented in this collection with five models each. Also, only ST-EPN-ZFTA and PFA ependymoma and no other subgroups are available from published established PDX cohorts [150-152].

1.3.2 PFA ependymoma

This chapter 1.3.2 is part of the review paper "EZHIP: a new piece of the puzzle towards understanding pediatric posterior fossa ependymoma", published in Acta Neuropathologica in 2022, written by me (Anne Jenseit), together with Aylin Camgöz, Stefan Pfister and Marcel Kool [4]. Text and Figures taken from the review have originally been conceptualized, researched and written or created by me. Where needed, I minimally curated the text to fit the focus of this chapter.

DNA methylation analysis of larger series of posterior fossa ependymomas revealed further heterogeneity within the PFA group, identifying two major subgroups (PFA-1 and PFA-2) and nine distinct subtypes (PFA-1a-e and PFA-2a-c) within PFA (**Figure 4**) [153], all with distinct demographics, copy number alterations and transcriptional profiles. While no significant differences in outcome were observed between the two major PFA subgroups, the outcome between the nine PFA subtypes differed significantly. PFA subtypes associated with a very poor outcome included PFA-1c, which is highly enriched for cases with 1q gain, PFA-1d, and PFA-1e (10 years OS 42%, 40% and 44%, respectively). In contrast, PFA-2c tumors, characterized by high levels of OTX2 expression, which is not seen in any of the other PFA ependymomas, are associated with a very good outcome (10 years OS 95%) [153].

RNA sequencing has not identified any recurrent fusion transcripts in posterior fossa ependymomas. Also, initial whole-genome and whole-exome sequencing approaches revealed an extremely low overall mutation rate and found no relevant recurring somatic single nucleotide variants (SNV) [67], suggesting that these tumors are most likely driven by alternative and possibly epigenetic mechanisms. This initial hypothesis was further supported by later more in-depth sequencing efforts on larger series of PFA ependymomas in which rare but recurrent mutations were identified in epigenetic proteins like EZHIP and Histone H3 (H3) [153].

Moreover, whole genome DNA methylation analyses showed that PFA and PFB have very distinct DNA methylomes [154]. For instance, promoter CpG islands were found to be hypermethylated in PFA compared to PFB ependymomas. As this seemed to come with a downregulation of epigenetically regulated genetic programs in PFA, epigenetic control aberrations were suspected to play a role especially in PFA tumorigenesis. This was supported in the same study showing that the global distribution of repressive histone mark H3K27me3 across the genome differs between PFA and PFB ependymomas, and that differential H3K27me3 marks could be used to distinguish them [154]. The initial conclusion, however, that the CpG hypermethylation and the differential H3K27me3 levels were caused by an overly active Polycomb Repressive Complex 2 (PRC2), responsible for setting the H3K27me3 marks, now seems to be overturned by more recent studies. As DNA methylation and histone methylation are closely linked in epigenetic regulations, Bayliss *et al*. investigated H3K27 and CpG island methylation in ependymomas and demonstrated the inverse relationship between CpG island and H3K27 methylation. In other words, PFA with high CpG island methylation reveals global reduction in H3K27me3 levels compared to PFB [155]. Altogether, these findings strengthened the impression that PFA ependymomas are driven by epigenetic changes in DNA and histone methylation.

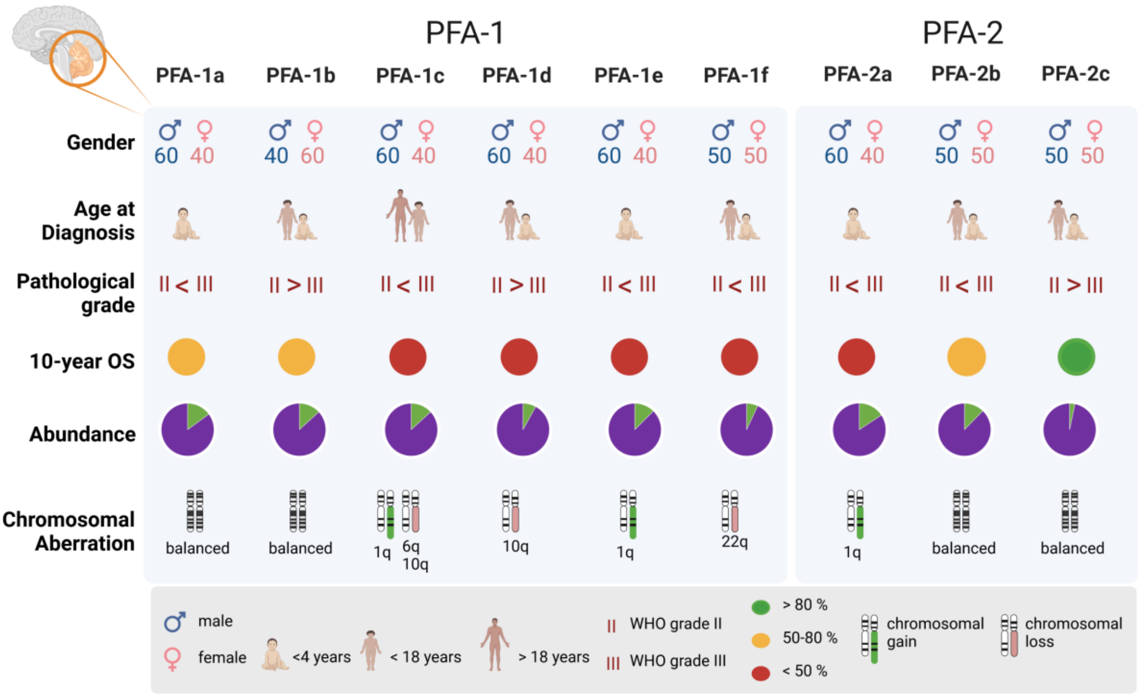

Figure 4 | Clinical characteristics of PFA ependymoma subtypes

PFA ependymomas are divided into six PFA-1 and 3 PFA-2 subtypes. Characteristics shown are the gender distribution of patients, their average age at diagnosis, the occurrence of WHO grades II and III, the 10-year overall survival (OS), the abundance of the subtype within PFA ependymomas and the most occurring chromosomal aberrations. Figure created by me using biorender.com, taken from Jenseit et al., 2022 [4].

1.4 EZHIP

The complete chapter 1.4 is part of the review paper "EZHIP: a new piece of the puzzle towards understanding pediatric posterior fossa ependymoma", published in Acta Neuropathologica in 2022, written by me (Anne Jenseit), together with Aylin Camgöz, Stefan Pfister and Marcel Kool [4]. Text and Figures taken from the review have originally been conceptualized, researched and written or created by me.

The global loss of H3K27me3 in PFA ependymomas strongly suggested epigenetic mechanisms as tumorigenic drivers of this disease. However, H3K27M mutations that cause low H3K27me3 levels in diffuse midline gliomas (DMG), are rare in PFA ependymomas and have been identified in only 4.2% of the cases [153, 156, 157]. In our series [153], H3K27M mutations were limited to 13/310 PFA cases (4.2%), which all belong to the PFA-1 subgroup, and were highly enriched in the PFA-1f subtype (69%; 9/13). Instead, we and others identified EZHIP (previously known as CXorf67) as the main responsible protein for the diminished H3K27me3 levels in PFA ependymomas [5, 153, 158]. EZHIP is expressed in almost every PFA ependymoma, but not in cases that harbor the H3K27M mutation or in any of the other EPN groups.

In other CNS tumors, *EZHIP* is not expressed except for a small group of CNS germ cell tumors [153]. Recent reports also described DMG with elevated *EZHIP* expression in cases that lack H3 mutations, which is in line with the mutual exclusivity between *EZHIP* expression and H3 mutations seen in PFA (**Figure 5**) [159, 160]. Due to this high specificity, EZHIP expression is discussed as a simple but reliable prognostic IHC biomarker for PFA ependymomas and EZHIP expressing DMGs [156, 161]. Outside the

CNS, EZHIP expression is found in endometrial stromal sarcoma (ESS) [162] and squamous non-small cell lung cancer (NSCLC) [163].

The fact that *EZHIP* is expressed only in this small subset of tumors is considered the reason for its late recognition, even though we already described it in 2015 as part of a PFA signature [1]. Only few experiments have been performed in the limited number of available PFA cell lines, as they are generally slow growing and difficult to culture [153]. A recent study on the metabolism of PFA ependymomas suggested that lower oxygen levels improves *in vitro* growth [120]. Moreover, in this study it was shown that hypoxia drives the expression of *EZHIP* and the PRC2 modulators *Elongin BC and Polycomb repressive complex 2-associated protein* (*EPOP*) in primary PFA cultures. Together with an increase in catabolic processes like glycolysis and glutaminolysis and reductive carboxylation of glutamine, inhibited PRC2 activity contributes to a modulated epigenetic state of the cells, resulting in a growth benefit in cell culture [120]. Independent of the oxygen status, EZHIP expression, like many others, is regulated via its promotor CpG island methylation. As such, hypomethylated *EZHIP* promoters are found in PFA tumors but not in other posterior fossa ependymomas [164]. PFAs with H3K27M mutations showed an almost two-fold higher methylation of the *EZHIP* promoter than tumors with wild type H3*,* in accordance with the mutually exclusivity of H3K27M mutations and EZHIP expression in PFA and DMG [153, 159, 160]. Non PFA cancer cell lines with EZHIP expression include the Daoy cell line, for a longtime presumed to be a medulloblastoma cell line, and the osteosarcoma U2OS cell line [158, 164]. If expressed, EZHIP protein localizes mainly to the nucleus, but can be detected in cytoplasmic fractions as well [5].

Until today, it is not clear whether EZHIP is naturally expressed during PFA tumor initiation in the cell of origin or becomes activated in the process of tumorigenesis. The latter seems to be the case in squamous non-small-cell lung cancer (NSCLC) [163] and might seem likely for PFA, too, as the only healthy tissues to express EZHIP are oocytes, testis and ovaries, but not the adult brain [165]. We can only speculate about the expression of EZHIP during brain development, as the cartography of expression in the developing fetal brain is far from complete.

A retrospective analysis of sequencing data of 30 PF ependymomas identified somatic mutations in *EZHIP* in five PFA tumors. Targeted sequencing of another 234 PFA tumors revealed single-nucleotide variants (SNVs) in 22 tumors (9.4%), with mutations detected in seven out of the nine PFA subtypes; not in PFA1-f and PFA2-c. Only three SNVs were present in more than one tumor and the majority of all mutations identified (68%) was located in a hot-spot region between codons 71 and 122 [67, 153]. *EZHIP* mutations do not correlate with clinical or pathological parameters, nor do they seem to influence *EZHIP* expression levels. Across other tumor entities, *EZHIP* mutations are rare. The highest frequency (5.8%; n=599) is found in endometrial stromal sarcomas (ESS), a tumor entity frequently comprising fusion genes involving PRC2 components [153, 162]. Interestingly, one case-based study of ESS reported two tumors where EZHIP acted as 3`-fusion partner for Malignant Brain Tumor Domain

Containing 1 gene (MBTD1). Both fusions included the functional serine-rich region of EZHIP [162], which further highlights the universal function of EZHIP, and of the serine-rich region in particular.

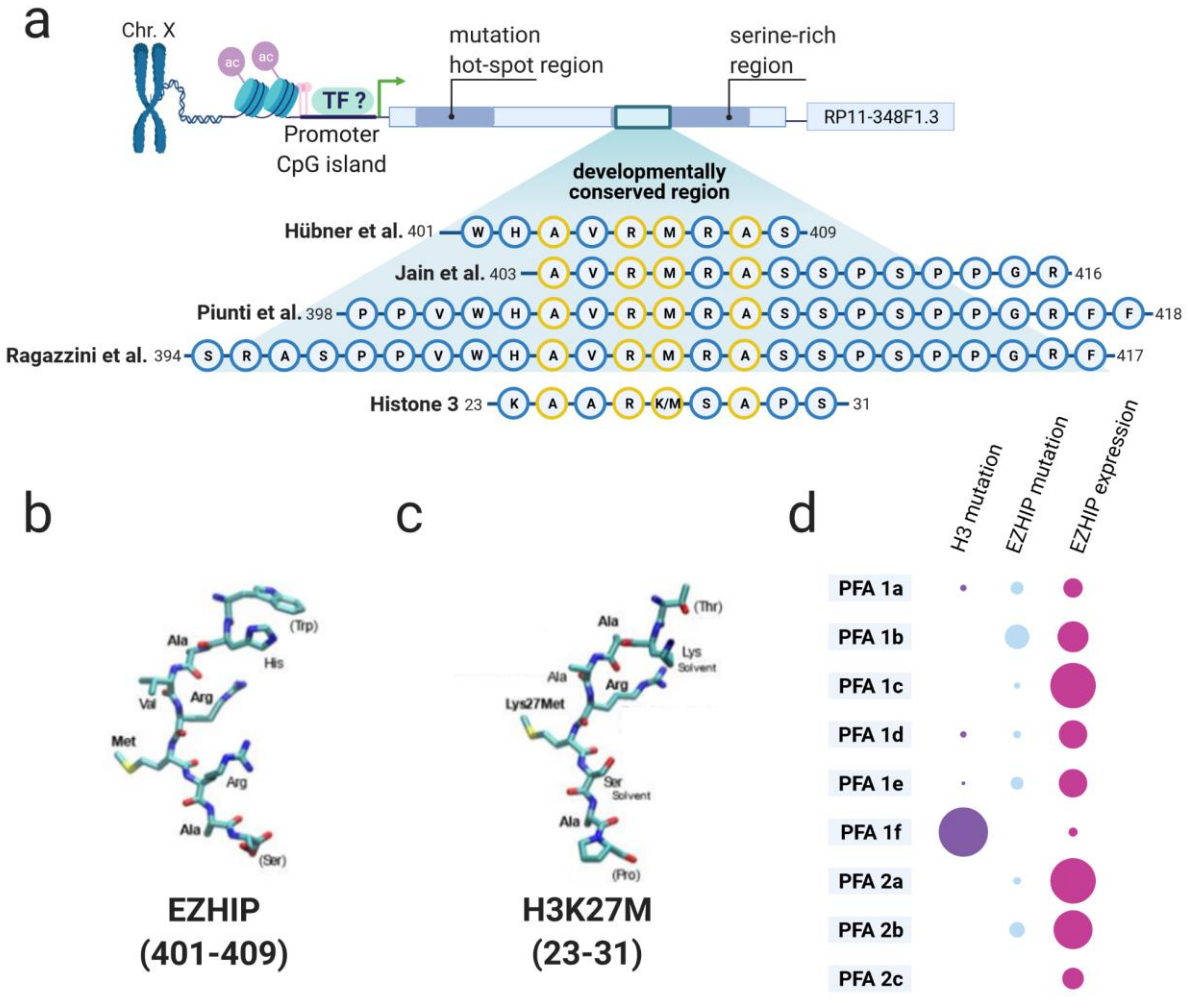

Figure 5 | The relationship of EZHIP and H3K27M

*(**a**) Schematic gene structure of EZHIP on chromosome X. Zoom in to the developmentally conserved region and the consensus region as it was used in different publications. Alignment with the tail region of histone 3 shows the high similarity to the H3K27M motif, with perfectly matched amino acids in yellow. (**b,c**) Amino acid structure of the EZHIP consensus region (b) and the H3K27M oncohistone region (c) when folded into the EZH2 binding pocket, adapted from Hübner et al.[5] (**d**) Comparison of histone 3 mutations, EZHIP mutations and EZHIP expression levels between the PFA subtypes showing the mutual exclusivity of histone 3 mutations with EZHIP expression. Figure created by me using biorender.com, taken from Jenseit et al., 2022 [4].*

1.4.1 The structure of EZHIP

The human *EZHIP* gene is nested into the introns 1-2 of the RP11-348F1.3 non-coding gene at Xp11.22 [162]. In a single exon, *EZHIP* comprises an open reading frame of 1512 bases, coding for a 51 kDa protein of 503 amino acids. It does not contain any common domains, but instead is predicted to be intrinsically disordered. The SNV hot-spot region at the N-terminus, however, might be of order and may contain a potential protein-protein interaction domain, implicating functional consequences of the mutations [153]. However, until today it is still unclear how the mutations in EZHIP affect the function of the protein or what their role is in ependymoma tumorigenesis.

The *EZHIP* gene is present only in placental mammals and conservation between species is low. The exception is a highly-conserved short consensus motif within the serine-rich region towards the C-terminus. Depending on the study and how stringent the consensus motif was defined, it stretches somewhere between amino acids 398 to 418 [5, 158, 164, 166]. Interestingly, this region always includes a shorter motif of highly conserved amino acids that match (even though not perfectly) the amino acids 23-31 of H3. This H3 sequence includes the often post-translationally modified or mutated K27 matching the methionine M406 of EZHIP [5, 158, 164]. As the H3K27M mutations increase the sequence homology to EZHIP, the consensus motif has also been called K27M-like peptide (KLP) [158].

H3K27M (but not H3 wt) interferes with the function of EZH2 [167]. Intriguingly, the conserved region of EZHIP binds the catalytic site of EZH2 in a highly comparable way. The consensus motif of EZHIP even is remarkably close to a previously calculated "optimal" EZH2 target sequence, which would perfectly fit the catalytic preferences of EZH2. In EZHIP, this similarity is reinforced by the amino acid at the -1 position to the crucial lysine (M406 in EZHIP) that is an arginine as preferred by EZH2. This R405 of EZHIP directly interacts with the EZH2 residues D652 and Q648 via salt bridges. Further interactions with EZH2 residues are most likely performed by non-identical, but similar enough, amino acids in the consensus motif [5, 158, 168].

1.4.2 The function of EZHIP

After the first report of its mutation and overexpression in PFA ependymomas, increased attention sparked the start of the ongoing functional characterization of EZHIP not only in PFA [5, 158], but also in ESS [164] and germ cells [166].

The natural role of EZHIP during development, as suggested by its expression pattern, might be a rather small one, as *Ezhip* knockout (KO) mice showed no developmental defects or abnormalities and adults were not distinguishable from wild-type (wt) mice [166]. Males (-/Y) were fertile with only little effect of the *Ezhip* KO on spermatozoa mobility. Female fertility, on the other hand, was impaired age-dependently. Interestingly, homozygous KO females had smaller ovaries than heterozygous (+/-) mutants and wt mice. The stronger effect of *Ezhip* KO on females might be rooted in the almost 4-times higher expression of *Ezhip* in ovaries compares to testis, but may also be influenced by the localization of *Ezhip* on chromosome X, as it will be silenced in spermatocytes during meiotic sex chromosome inactivation [166]. However, this does not seem to translate to human cancer. So far, no sex bias on clinical prevalence, severity or EZHIP expression was detected in PFA or DMG patients [153, 169].

In cultured cells, depletion of EZHIP reduces growth and increases elimination but shows only little effect on the growth of engrafted Daoy cells [153, 170]. Effects in culture were smaller than of the elimination of EZH2 [164], which goes in line with the results of a CRISPR-screen in primary PFA cells that did not identify *EZHIP*, but *EZH2* and other PRC2 components, as essential genes for growth in PFA [120]. It thus seems that EZHIP keeps the activity of the PRC2 complex at the crucial level, which is needed for PFA tumorigenesis while at the same time inhibiting EZH2 enough to change gene expression. This proposed "Goldilocks-Model" of balance between inhibition and activity again highlights the importance of PRC2 in PFA and might be indicative for future therapeutic approaches targeting the epigenetic nature of these tumors.

Indeed, EZHIP is not the primal single player keeping this delicate balance of PRC2 as global gene expression changes conferred by EZHIP were smaller than initially expected. Single-oocyte RNA-sequencing revealed de-regulation of only 100 genes upon KO. *EZHIP* KO in human U2OS cells leads to changes in genes described by the gene ontology (GO) terms nucleosomes, DNA packaging and extracellular space [166]. In contrast, the overexpression of EZHIP in HEK293 led to the deregulation of genes associated with neurogenesis, enzyme linked receptors, CNS development or regulation of cell differentiation. The serine-rich region, including the consensus region, is sufficient and essential to convey these expressional changes [5]. The main mode of action of EZHIP to convey these changes still seems to be via the PRC2 complex, as deregulated genes are often PRC2 target genes and overlap with genes sensitive to H3K27M expression or PRC2 component deletion [5, 158]. However, EZHIP does not interfere with the expression of PRC2 components themselves or their association with each other [164, 166].

In addition, recent data suggested a potential role of EZHIP independent of the PRC2 complex. EZHIP was found to interact with participants of the homologous recombination (HR)-mediated DNA repair pathway, preventing the smooth function of the PALB2-BRCA2 axis. Upon DNA-damage, EZHIP localizes to the damage sites and ultimately prevents the resolution of DNA double strand breaks. Having a motif (aa 420-432) similar to the part of BRCA2 that interacts with the WD40 domain of PALB2, EZHIP competes with BRCA2 and prevents it from being recruited to the damage sites, thereby interrupting the HR process [170]. From many other cancers, impaired HR capacity (most famously due to mutations in the *BRCA* genes) is a known sensitizing factor for the use of PARP inhibitors due to synthetic lethality [171]. In their study, Han *et al*. thus continued to also test the effect of PARP inhibition on EZHIP expressing cells and (non-PFA) PDX models. Even though their results seem promising, more experiments need to be done in PFA cells and tumor models, as their biology is crucially different from cancer cell lines like Daoy or U2OS. The limited penetration of the blood brain barrier (BBB) by PARP inhibitors is an additional concern that needs to be tackled by future research including PFA-specific pharmacokinetic and pharmacodynamic characterizations [172-176].

1.4.3 EZHIP reduces H3K27me3 via EZH2

As EZHIP itself probably does not possess an enzymatic function, the identification of functional interaction partners was the focus of early research. EZHIP was shown to interact with PRC2 components in different compositions in multiple publications (**Figure 6**). Immunoprecipitation followed by mass-spectrometry (IP-MS) not only identified all PRC2 enzymatic core components (EZH2, SUZ12, EED, RBBP4) as EZHIP interaction partners, but also PRC2 associated proteins (e.g. JARID2, MTF2) [153, 158, 166]. Antibody-based detection confirmed the direct interaction of EZHIP with EZH2 and SUZ12. EED might not directly interact with EZHIP, but it seems that its presence increases the association of EZHIP with EZH2 [5, 164, 177]. The interaction with EZH2 and SUZ12 is conveyed by the C-terminal region of EZHIP. In contrast, the interaction with RBBP4 is mediated by the N-terminal region of EZHIP and its interaction with JARID2 or AEBP2 depends on the SET domain of EZH2 [158, 164]. Also, one study connected the interaction of EZHIP with PRC2 core members to the presence of the EZH2 co-factor S-Adenosyl methionine (SAM) [158].

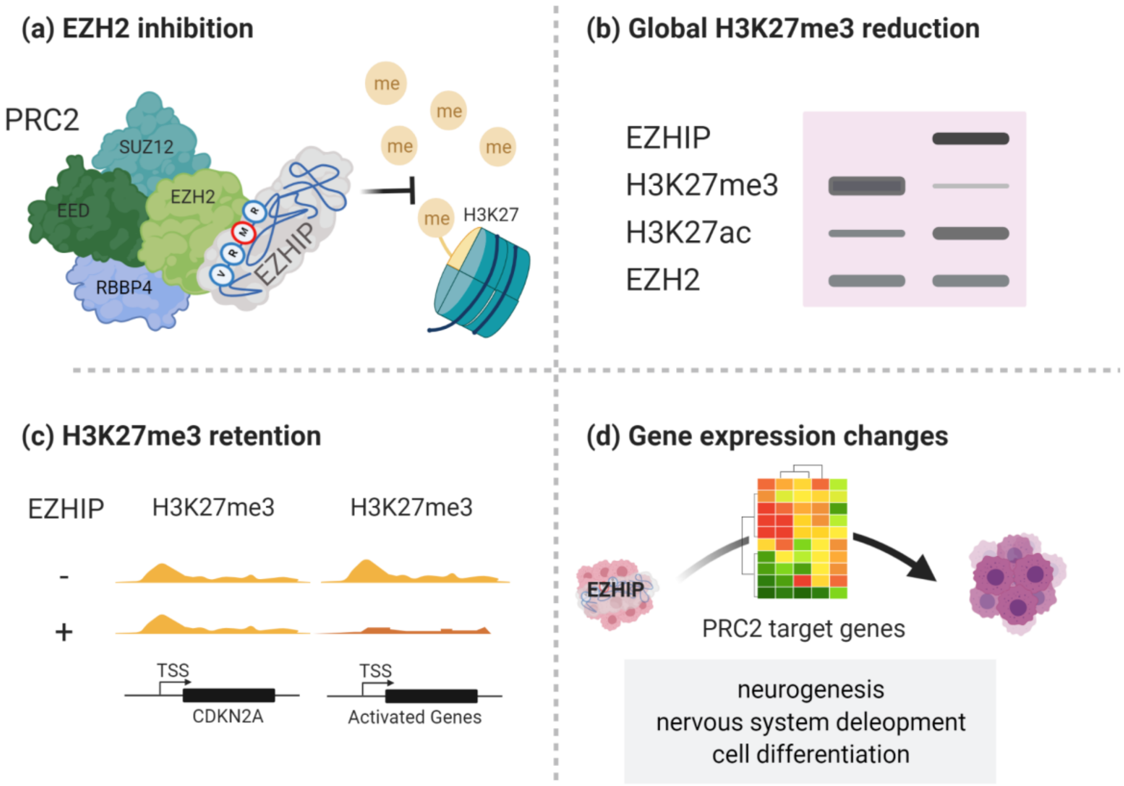

Figure 6 | Downstream effects of EZHIP expression

EZHIP inhibits EZH2 in the PRC2 complex and thereby reducing the repressive H3K27me3 mark. The loss of H3K27me3 activates gene expression, but specific genes (e.g. CDKN2A) retain the H3K27me3 upon EZHIP expression. Global gene expression changes conveyed by EZHIP expression resemble PRC2 target gene repression. Figure created by me using biorender.com, adapted from Jenseit et al., 2022 [4].

EZHIP also inhibits EZH1, the paralog of EZH2, via interaction with the protein but with a lower affinity for EZH1 than for EZH2 [158]. In a competitive mode of inhibition, EZHIP prevents the methylation of H3K27 dose-dependently. While the allosteric activation of EZH2 via H3K27me3 binding to EED is not disturbed, it seems that EZHIP prevents the PRC2 complex from spreading the H3K27me3 mark after the initial recruitment to chromatin [158, 177, 178]. Two studies revealed a stronger inhibitory potential (lower 50% inhibitory concentration (IC50)) for EZH2 of EZHIP than of H3K27M peptides [5, 158]. Interestingly, the minimum consensus sequence around M406 seems insufficient to inhibit EZH2 alone. The degree of extension of this sequence needed to enable full inhibition, just as the definition of the consensus sequence itself, is dissimilar between reports even though all confer the same basic message. Hübner *et al*. report a slight increase of four amino acids N-and C-terminally each (V400-P420) to be necessary and sufficient for an EZHIP peptide to reach the inhibitory potential of the commercial EZH2 inhibitor GSK126 [5]. On the other hand, Jain *et al*. find that their KLP (A403-R423) is a strong PRC2 inhibitor in cell-free assays, but fails to inhibit PRC2 in HEK293T cells, even if extended to stretch amino acids 317-423 or 395-423. The additions of serine rich intrinsically disordered repeats (IDRs) either C- or N-terminally of the consensus sequence, predicted to mediate protein-protein interactions, seem to overcome this shortcoming successfully. Even though not potent alone, the central role of M406 as a H3K27 mimic becomes clear upon mutation. The inhibitory effect of EZHIP diminishes upon mutation of M406 into a basic (M406K or M406R) or not-acidic amino acid (M406E) [158]. Mutation into isoleucine (M406I), on the other hand, does not affect the inhibitory potential, and M406K even converts EZHIP into an EZH2 target. Additional mutations in the EZHIP hotspot region never interfere with the inhibitory function of EZHIP [158].

Globally, the inhibition of EZH2 by EZHIP translates into altered post-translational modifications (PTMs) on H3K27. PFA tumor tissue is characterized by low H3K27me3 and H3K27me2 levels. In contrast, H3K27me1 levels are higher in PFA than in ST-EPN, as is H3K27 acetylation (H3K27ac), an activating mark in competition with H3K27me3 [120]. The reduction of H3K27me3 (up to 80%) in PFA tissue is especially strong in intergenic regions and retained marks are characterized by smaller, sharper peaks in Chromatin-Immunoprecipitation followed by sequencing (ChIP-seq) experiments [158]. This is independent of the PFA identity, as cell lines of any background expressing EZHIP (endogenously or exogenously) show the same phenotype of low H3K27me2/3 levels and increased H3K27ac. H3K27me3 marks are gained as sharp peaks around transcriptional start sites (TSS), correlating with chromatin occupation by SUZ12 and PRC2 target gene repression [166]. *EZHIP* KO in U2OS or Daoy cell lines reverses this effect without affecting related marks set by PRC1, like H3K27me1 or H2Aub [153, 164, 166]. It can be assumed that a removal of EZHIP in PFA would show the same effects, but experimental proof is still pending.

Some loci, however, retain the repressive H3K27me3 mark in PFA, even upon EZHIP overexpression. At these loci, ChIP-Seq peaks are of smaller width as it can be observed for instance at the *CDKN2A* locus. The tumor suppressor gene is kept under repression in PFA, H3K27M positive gliomas, as well as in EZHIP expressing cell lines [158, 166]. The criteria for a locus to remain repressed by H3K27me3 upon EZH2 inhibition are still under investigation. Identifying a pattern would be of great power, as releasing tumor suppressors by therapy presents a potential treatment option against these tumors.

1.4.4 A comparison to DMGs

Diffuse intrinsic pontine gliomas (DIPG), more recently now included in the category known as DMG, are deadly pediatric malignancies found in the brain stem. Like PFA ependymomas, they are characterized by a midline location, young patients, bad outcome and global loss of H3K27me3, in their case mostly caused by the oncohistone H3K27M. As mentioned earlier and similar as in PFA, H3K27M mutations in DMG are 100% mutually exclusive with EZHIP expression [153, 159]. Understanding the mechanisms of how H3K27M mutations and EZHIP drive tumorigenesis in PFA and DMGs may form a base to create better therapeutic options for the patients.

However, in contrast to PFA, DMGs harbor a variety of genetic aberrations in different combinations [179]. Additional to mutations in H3, DMGs are characterized by P53 loss-of-function (LOF) mutations in 40-50% of tumors. Receptor tyrosine kinase (RTK) pathways are commonly affected, with amplifications or activating mutations of *platelet-derived growth factor receptor alpha* (*PDGFRA*) in 30% or 5% of cases, respectively [180-182]. Other common findings are six different somatic mutations of *activin receptor type 1A* (*ACVR1*) detected in 21-32% of DMG patients [183, 184]. The genetic background of DMGs is thus clearly different than in PFA.

Just like EZHIP in PFA, H3K27M is the defining driver of DMGs and significantly worsens patient overall survival. However, H3K27M is also not the sole driver of DMG tumorigenesis and acts tumorigenic only when supported by the aforementioned mutational background [69, 179, 185]. This fact is mirrored in how genetic mouse models for DMGs are created. For mice to develop DMG tumors, additional genetic events as well as the correct location and time point of gene delivery or induction are crucial, showing the necessity for a correct biological background [186-189]. Histone methylation is especially variable during development and might be an essential confounding factor in the cell of origin [190]. So far, neither the precise cell of origin nor additional hits to EZHIP are known for PFA tumorigenesis. Thus, identification of the correct target cell for genetic manipulations will be a crucial step forward in modeling PFA ependymomas [41, 44].

1.4.4.1 H3K27M and EZHIP act background-independent

Independent of the affected H3 variant (heterozygous mutations can occur at different variants of H3: *HIST1H3B*, *HIST1H3c*, *H3F3A*), expression of H3K27M directly results in a global reduction of H3K27 methylation in the tumor tissue. H3K27me3 is lost especially in intergenic regions, but specific sites, such as for instance the *CDKN2A* locus, retain their marks, and activating H3K27ac marks are unaffected or unchanged [167, 191-195]. This re-distribution of PTMs on H3 is highly reminiscent of the effect of EZHIP in PFA and indicates that the effects of H3K27M and EZHIP are independent of tumor cell context [167, 192].

With the shared mechanism of EZH2 inhibition, the effects of EZHIP and H3K27M on gene expression are much alike: both PFA and DMGs show an overall de-repression of PRC2 target genes [5, 164, 166, 192]. Their general moderate effect on gene expression is highest on H3K27me3-silenced or lowly expressed genes [158, 192]. Experiments with DMG further characterized many of them as genes with bivalent promoters (H3K4me and H3K27me3 positive), which are often involved in developmental processes [196, 197]. If this is caused by the nature of PRC2 targets and not a characteristic of the cell of origin of DMGs, one should expect similar results for PFA. Regardless of all the mechanistic similarities between DMG and PFA and independent of the expression of H3K27M or EZHIP, their overall expression profiles and DNA methylation characteristics are still very distinct [159], though, most likely due to a different cellular origin and the presence of additional tumorigenic events and mutations in DMG tumors.

1.4.4.2 Common targets in DMG and PFA ependymoma

Despite their inhibition, PFA and DMG tumors both heavily rely on PRC2 core components to sustain proliferation. Independent experiments showed that tumor cells of both entities are sensitive to inhibition of EZH2 and EED *in vitro*. In addition to the identification of PRC2 components as essential genes in PFA, they also react to a lack of the EZH2 co-factor SAM. *EZH2* KO prolongs the survival of DMG tumor bearing mice and proliferation can be impaired by a SUZ12 knock-down. The effects seem to rely on the presence of H3K27M in DMG, independent of the affected H3 variant [120, 188, 189]. Taken together, it seems that the residual PRC2 activity after inhibition is a necessity in PFA and DMG for tumor maintenance. This further highlights the importance of genes that retain their H3K27me3 marks and might be a possible starting point for therapy.

The two-faced role of EZH2 in PFA and DMG – repressed but also essential in its residual activity - fits the overall highly ambiguous role of EZH2 in cancer [198]. In some entities, like T-cell Acute

Lymphoblastic Leukemia (T-ALL) or lung adenocarcinoma, EZH2 fits the role of a tumor suppressor and is found deleted or inactivated by mutations [199, 200]. In contrast, EZH2 overexpression and activating mutations are reported for prostate, breast, gastric cancer and others [201-203]. So far, a clear understanding of what determines whether EZH2 acts oncogenic or tumor suppressive is missing. PFA and DMG research should benefit from increased knowledge in other entities and might act as a two-in-one model system at the same time. As different EZH2 inhibitors are already being tested for a variety of epigenetically driven tumors, their use might prove useful in PFA and DMG in the future [198].

Besides focusing on specific targets, general epigenetic therapy is an often discussed option for DMG and PFA. Among others, histone deacetylase (HDAC) inhibitors have been tested in several clinical trials for DMG [204]. Ideally, increasing the activating H3K27ac mark releases downregulated tumor suppressing genes. The same goal is driving the idea to use DNA demethylating agents. Even though PFA and DMG are characterized by global DNA hypomethylation and loss of DNA methylation seems to increase HGG tumorigenesis, CpG island hypermethylation can be observed frequently [155, 194, 205]. Treatment of posterior fossa ependymoma xenograft models with DNA demethylating agents was found to decrease tumor burden and increase survival and positive effects of DNA demethylation have been described for *IDH1* mutant glioma [154, 206].

1.5 USP7

The ubiquitin-specific protease 7 (USP7, also known as HAUSP) is a de-ubiquitinating enzyme with a wide variety of targets. USP7 is involved in several cancers and a multitude of inhibitors have been developed over the past years.

1.5.1 Ubiquitin Signaling

Post-translational modifications (PTMs) are covalent attachments to proteins that can expand and finetune their functionality and add a crucial layer of protein regulation. A variety of alterations can be attached during translation or after folding: functional groups like hydroxyl-, methyl-, acetyl- or phosphor groups, sugar (glycosylation) or fatty acid (lipidation) chains, as well as the small molecules SUMO and ubiquitin. As the modifications can target different but almost all amino acids throughout the protein, the combinations of modifications and their results are manifold [207]. Many PTMs are important for correct cellular signaling, control the location of proteins within the cells or regulate protein stability or three-dimensional structures. Their dynamic is comparably quick and they therefore allow for flexible control of protein functions without the need to degrade and synthesize new proteins [207, 208].

One of the most common PTMs is the covalent addition of the small 8.5 kDa protein ubiquitin. Ubiquitin, identified in 1975 as “ubiquitous immunopoietic peptide”, is ubiquitously expressed in all eukaryotic cells and its sequence of 76 amino acids is strongly conserved between species [209-211]. The coupling of ubiquitin to a target protein follows a specific pathway which involves three major enzyme types: E1 activating enzymes, E2 conjugating enzymes and E3 ligases (**Figure 7A**) [212]. So far, two E1 enzymes, 40 E2 enzymes and over 600 putative E3 enzymes have been described in humans [213, 214]. The process of ubiquitination (also called ubiquitylation) starts with free ubiquitin proteins that are “loaded” to an E1 enzyme. Under adenosine triphosphate (ATP) hydrolysis, the E1 enzyme adenylates the C-terminal glycine of ubiquitin. Releasing adenosine monophosphate (AMP), the ubiquitin is then attached to the active cysteine of E1 [215]. Next, the activated ubiquitin is transferred to the active site cysteine of an E2 enzyme. Catalyzed by an E3 ligase, the ubiquitin protein is then transferred into an amide isopeptide bond with its target site, an ε-amino group of the amino acid lysine. The transfer can either be directly from the E2 enzyme or via a covalent intermediate with the E3 ligase, depending on the E3 ligase class [212, 216-218]. Target specificity and selectivity of the ubiquitination is conferred by the E3 ligase, explaining the need for the large number of ligases.

The “ubiquitin code” refers to the different combinations of ubiquitination that confer the functions of ubiquitin-mediated signaling. There are two main categories of ubiquitination: monoubiquitination and polyubiquitination. Monoubiquitination is the addition of single ubiquitin proteins to one or multiple lysine residues of a target protein (**Figure 7B**). A prominent example of monoubiquitination is the addition of a single ubiquitin to histone H2A by the Ring1B E3 ligase of the polycomb repressive complex 1 (PRC1), which results in transcriptional repression of the region of H2Aub deposition in the genome [219]. However, the results of monoubiquitination are versatile and distinct, as the same monoubiquitination on histone H2B confers transcriptional initiation and elongation [220, 221]. In other contexts such as DNA damage response, monoubiquitination is known to regulate substrate activity, intracellular localization as well as protein-protein interactions [222], and mediates degradation of some small (< 150 amino acids) proteins [223-225]. Polyubiquitination, on the other hand, is the addition of multiple ubiquitin molecules to a single target lysine. This is achieved by the connection of ubiquitin molecules to each other in chains. Ubiquitin itself can be ubiquitinated at its seven lysines (K6, K11, K27, K29, K33, K48 and K63) or at the first methionine M1, allowing for differently linked ubiquitin chains [210]. Homotypic chains are all connected via the same location in ubiquitin, whereas heterotypic chains are of mixed linkage [226]. Additionally, ubiquitin can be modified by other PTMs itself, including SUMOylation or acetylation (**Figure 7B**) [227]. Even though this set-up allows for numerous amounts of ubiquitin-chain combinations, certain chain types are highly abundant and well-studied. K63-linked ubiquitin chains are involved in mediating DNA damage responses, signaling and endocytosis [228], whereas chains on M1-linked ubiquitins were shown to be involved in NF-kB pathway activation [229-231]. K48-linked ubiquitin chains are the most abundant type (~ 50%) and, together with K11-linkages, responsible for the phenotype ubiquitin signaling is known for most: marking target proteins for proteasomal degradation in the multi-subunit complex 26S proteasome [226, 228]. The other chain types are less well studied, but as the above mentioned ones as well, can have implications in a variety of processes [232].

Proteins marked for degradation are recognized by the ubiquitin receptors of the proteasome, RPN1, RPN10 and RPN13 or by the transiently bound ubiquitin receptors RAD23 and DSK2 [233]. Another prerequisite is the presence of an unstructured region within the protein, either terminally or internally, as it is present e.g. in EZHIP [153, 234, 235]. Together with a multitude of other functionally diverse proteins, the ubiquitin receptors are located in the 19S cap of the 26S proteasome. The second main subcomplex of the 26S proteasome is the 20S proteasome, which harbors the ATP-dependent proteolytic core [236]. These complex structures are located mainly in the cytosol, but also found in other organelles such as the endoplasmic reticulum (ER) or mitochondria [233].

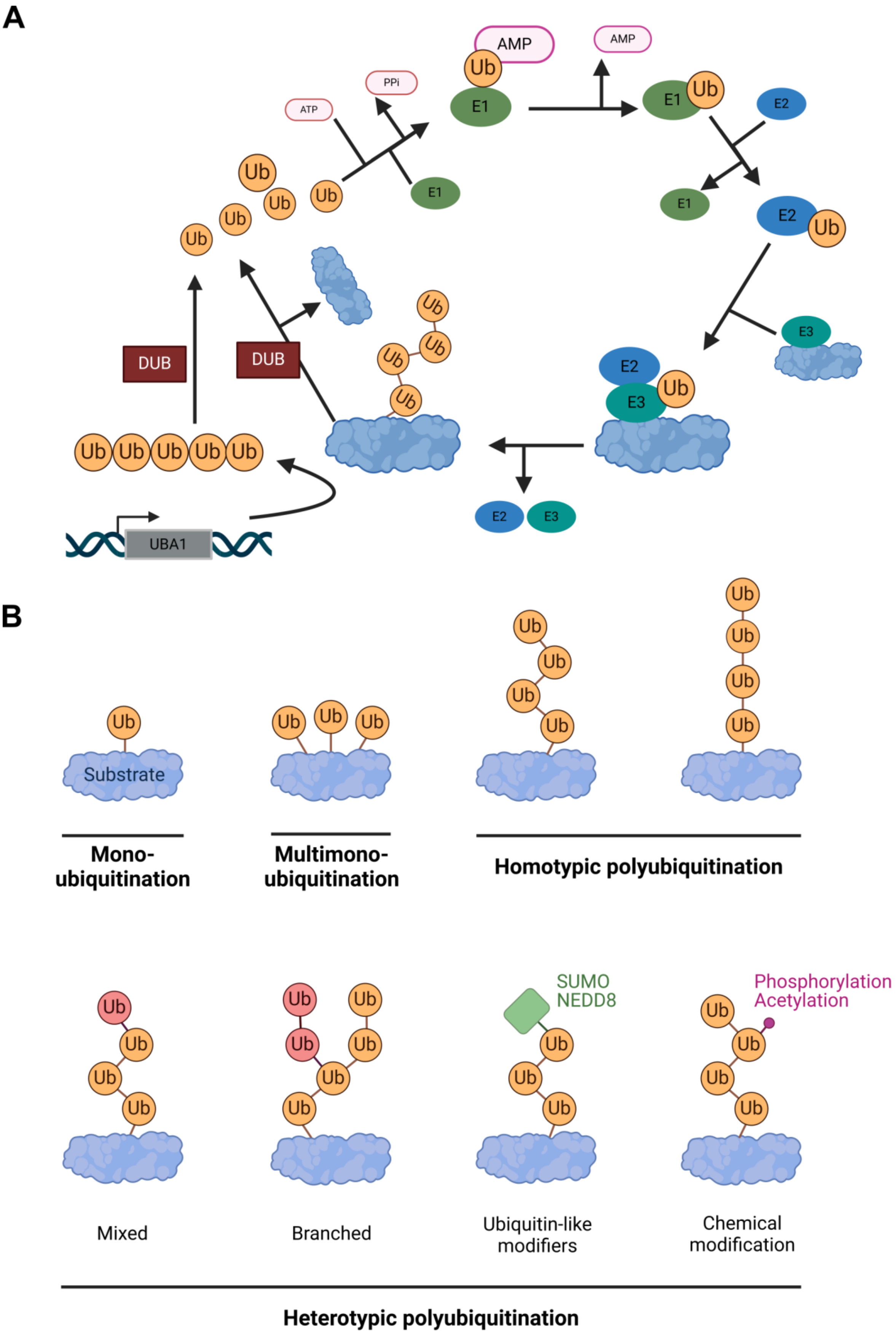

Figure 7 | The ubiquitination pathway

*(**A**) Ubiquitination is a multi-step process involving the three main enzmyes E1 activating enzyme, E2 conjugating enzymes and E3 ligase. Deubiquitinatinases (DUBs) remove ubiquitin from substrates and create the free ubiquitin pool after translation of ubiquitin chains from the UBA1 gene. (**B**) Different forms of subtrate ubiquitination. The figure was created using biorender.com..*

1.5.2 Deubiquitination

Contrasting the ubiquitination machinery, the enzyme family of deubiquitinases (DUBs) are proteases specialized in the cleavage of ubiquitin chains. DUBs are responsible for maintaining the free ubiquitin pool inside the cell as they cleave off ubiquitin from target proteins and reduce chains to single ubiquitins. Additionally, DUBs also cleave precursor chains of ubiquitin that are translated from the ubiquitin-coding *UBA1* gene (**Figure 7A**) [237]. On their target proteins, DUBs can act either as on/off-switches, removing ubiquitin entirely from them, or as fine tuners that regulate the amount and type of ubiquitin chains [9]. Challenged by the high complexity of the “ubiquitin code” and putative targets, ~ 100 human DUBs have been described so far [238]. The processes they regulate range from signaling over epigenetic regulation to protein stability. Many DUBs have been shown to interfere with pathways in a pathogenic fashion. They can be mutated or overly active themselves, or are regulators of oncogenes and tumor suppressors contributing to every hallmark of cancer [239]. DUB specificity can either mean target specificity or ubiquitin chain specificity and DUBs will often only be specific in one way. When cleaving the ubiquitin, DUBs can show either endo-, exo- or en bloc- activity, cleaving chains from the end, from within or only as complete chain [9].

DUBs can be separated into seven structurally distinct superfamilies, of which six are cysteine-based and one consists of zinc-binding metalloproteases. The largest and cysteine-based family is the ubiquitin-specific proteases (USP) group with ~60 identified members. They are agnostic to the ubiquitin chain type, but their specificity is provided by additional domains that recognize specific targets and usually remove all ubiquitin chains from them [239, 240]. However, the overall mechanism of ubiquitin cleavage is shared between DUBs. The catalytic cycle of DUBs has them shuttling between target-free, (ubiquitinated) target-bound and product/ubiquitin-bound states. After target recognition, the DUB binds to both the target and the added ubiquitin while positioning the scissile isopeptide bond across their catalytic center. After cleavage, the target is released first and the DUB stays shortly in the ubiquitin-bound state before releasing the ubiquitin (chain) [9]. For USPs, the catalytic cleavage is mediated by the thiol group of the cysteine in the catalytic triad. The second amino acid of the triad is a basic histidine, which lowers the pKa of the cysteine and improves its nucleophilic attack on the isopeptide bond of the ubiquitin. The third amino acid is usually either an asparagine, aspartate or glutamate, which can help further polarize the basic histidine. The three residues of the catalytic triad are often not located next to each other by sequence, but come close in the three-dimensional structure of the enzyme [9, 241].

1.5.3 USP7 – structure and function

One of the most researched DUBs is the ubiquitously expressed USP7 [165]. It was first described by Meredith et al. in 1994 as 135 kDa binding partner of the ICP0 protein of herpes simplex virus 1 (HSV-1), which lead to its first naming as herpesvirus-associated ubiquitin-specific protease (HAUSP) [242-244]. The 1120 amino acid protein mainly localizes to the nucleus of cells, but can also be detected in the cytoplasm and in mitochondria [242, 245, 246]. Like most other USPs, USP7 is almost agnostic to the ubiquitin chain of its targets and cleaves both mono- and K-linked polyubiquitin chains, whereas it fails to cleave M1-linked chains [247, 248].

As a modular DUB, USP7 has several clearly defined domains that serve different functions (**Figure 8A**). The N-terminal region includes 50 amino acids with stretches of several glutamine residues that is conserved across human, mouse and rat, but whose function is not specified yet [249]. The amino acids 54-204 form the tumor necrosis factor receptor associated factors (TRAF)-like domain, which is the main target interaction domain and contributes to USP7 target specificity [250]. Three of USP7`s most established targets, the tumor suppressor P53, mouse double minute 2 homolog (MDM2) and the viral Epstein-Barr nuclear antigen 1 (EBNA1) all bind the so-called TRAF-pocket [251-253]. This pocket binds targets containing a P/A/ExxS consensus motif through contact with the USP7 amino acids D164 and W165 [250, 252, 254]. The catalytic domain of USP7 (amino acids 207-538) shows high similarity to other USPs, but has the specific feature that its three-dimensional structure of the subdomains resembles the fingers, palm and thumb of an extended right hand (**Figure 8B**) [251, 255]. The thumb and palm form the active catalytic cleft, which contains the catalytic triad of USP7: cysteine C223, histidine H464 and aspartic acid D481 [8]. The C-terminal domain of USP7 (amino acids 562-1081) consists of the five ubiquitin-like (UBL) modules UBL1-5, which are found in several USPs and are of high similarity with ubiquitin but can´t be conjugated to lysines [247]. Additionally to the TRAF-like domain, the UBL modules are involved in ubiquitin binding and target recognition and a second binding pocket is located in UBL2 [256]. The C-terminal tail of USP7 is highly conserved and serves an important regulatory function. As described above for USPs in general, USP7 shuttles between states of target binding (**Figure 8C**). In an inactive sate, USP7 additionally shifts between an open or closed conformation, which does not allow for target binding [9]. In this unbound state, the catalytic domain is in an unproductive confirmation, as the C223 is too far away from the other partners of the catalytic triad to allow hydrogen bonding. Binding of ubiquitin initiates conformational changes that realign the catalytic residues. This active USP7-target complex is further stabilized by the C-terminal tail, which is flexible and binds in the catalytic cleft where it interacts with the fingertips and the cleft between the palm and thumb [247, 251, 257].

In addition to this intramolecular activation via its C-terminal domain, USP7 is modulated via external PTMs. The phosphorylation at serine 18 acts as an activity regulator, which shift the affinity of USP7 between MDM2 (phosphorylated) and P53 (un-phosphorylated) [258]. While the role of phosphorylated serine 963 is unclear, the ubiquitination of lysine K869 by tripartite motif-containing 27 (TRIM27) promotes tumor necrosis factor alpha (TNFa)-induced apoptosis [8, 259]. In chronic myeloid leukemia (CML), USP7 is aberrantly phosphorylated by the fusion BCR-ABL at tyrosine Y243, which leads to an increased deubiquitination and nuclear exclusion of the tumor suppressor phosphatase and tensin homolog (PTEN) [260].

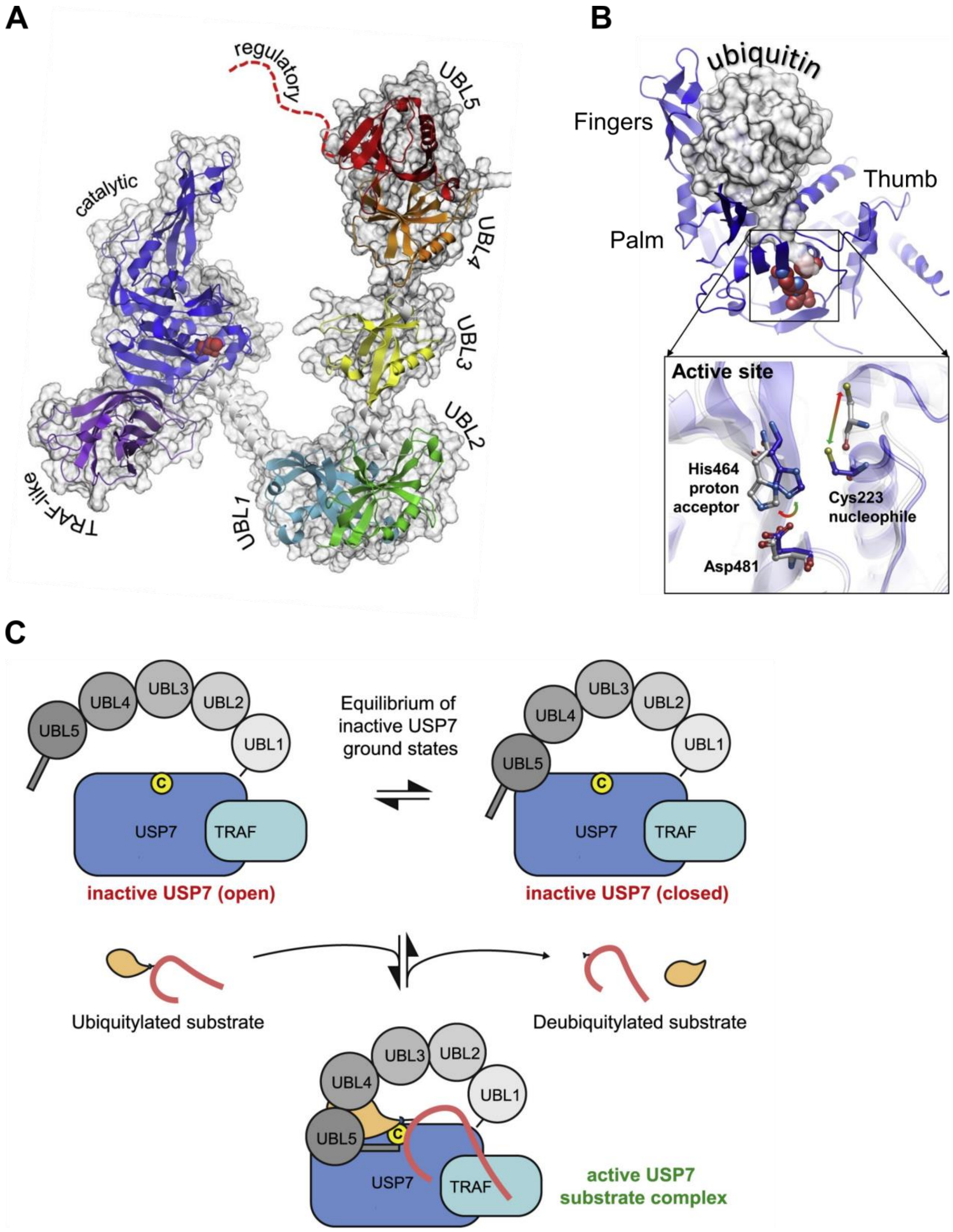

Figure 8 | Structure and intramolecular regulation of USP7

*(**A**) Structural model of full length USP7: TRAF-like (purple), catalytic (blue), UBL1 (cyan), UBL2 (green), UBL3 (yellow), UBL4 (orange), UBL5 (red), the C-terminus is shown as red dotted line. Figure adapted from Pozhidaeva et al. [8] (**B**) Structure of the catalytic core of USP7 (blue) in the shape of a right hand forming fingers, palm and thumb. The C-terminal part of ubiquitin (grey) extends into the catalytic cleft and interact with the catalytic triad (red spheres). Zoom-in to the active site shows the conformational rearrangements upon ubiquitin binding from inactive (grey) to active (blue). Figure adapted from Pozhidaeva et al. [8] (**C**) Schematic of the equilibrium of USP7 in its inactive unbound states and the conformational change in the active target bound complex. Figure adapted from Lange et al. [9]*

1.5.4 USP7 in health and disease

Like most DUBs, USP7 deubiquitinates and interacts with many different targets. Its ubiquitous expression and the early embryonic lethality of USP7 KO mice underline the importance of USP7 in healthy cells [165, 261]. This is further confirmed by recent studies showing a crucial role of USP7 in early embryonal development and lineage differentiation [262, 263]. Moreover, dominant heterozygous variants of USP7, frameshift or missense mutations on chromosome 16p13.2, underly the rare Hao-fountain syndrome (HAFOUS), a neurodevelopmental syndrome characterized by impaired global and intellectual development [264-266]. In these patients, dysfunctional USP7 impairs endosomal protein recycling [266]. In neural progenitor cells (NPCs), USP7 stabilizes the transcription factor REST, which helps maintain NPC self-renewal and cellular identity [267]. In SHH medulloblastoma, a brain tumor of the cerebellum arising in children and adults, the expression of USP7 correlates with the expression of REST in patients with poorer survival [268]. Recent efforts aimed to profile the ubiquitome of USP7 by mass spectrometry (MS) or multi-omics approaches [269, 270], but most studies focus on the characterization of single targets.

Overall, the role of USP7 in diseases like cancer is highly context-dependent [239]. This is also reflected in the most prominent targets of USP7: the tumor suppressor P53 and the P53-ubiquitinating E3 ligase MDM2, which both are bound via TRAF-like domain consensus motif recognition [252, 271, 272]. Thus, USP7 can regulate P53 stability in two ways: directly via P53- deubiquitination, which will stabilize P53, or indirectly via MDM2 deubiquitination, which leads to a more stable MDM2 and increased ubiquitination and degradation of P53. Under stress-free conditions, USP7 preferentially deubiquitinates MDM2 and therefore prevents transcription of P53 target genes and apoptosis induction. Therefore, inhibition of USP7 presents a therapeutic opportunity as it can lead to activated P53 signaling [249]. However, there are also plenty of USP7 mediated functions that are P53-independent [273].

USP7 deubiquitinates multiple epigenetically involved proteins including members of the PRC1 and PRC2 complexes. At the PRC2 complex, USP7 was shown to stabilize the catalytic subunit EZH2 in multiple cancers [274], including cervical [275] and prostate cancer [276]. In mESCs, EZH2 recruits USP7 to regulate neuronal gene expression [277], a role which also has been assigned to the PRC2 associated protein EPOP before [278]. By regulation of multiple PRC1 members like the ubiquitin ligase RING1B, USP7 helps increase histone H2B monoubiquitination and repression of downstream targets such as the tumor suppressor *INK4A* [279-281]. During meiosis in male mice, recruitment of USP7 to sex chromosomes is associated with reduced histone H2A ubiquitination [282]. However, this effect seems to be indirect, as USP7 was not able to deubiquitinate H2A *in vitro [283, 284]*. The regulation of PRC1.1 assembly is mediated by the DUB-E3 ligase combination USP7 and TRIM27; both are reciprocally needed for PRC1.1 integration and prevention of PRC1.1 disassembly in AML cells [285]. USP7 and TRIM27 often associate and regulate protein stability together, also in complexes with melanoma-associated antigen (MAGE) proteins, as pair while regulating each other at the same time [259, 285-287]. In hepatocellular carcinoma, the TRIM27-USP7 complex promotes progression via STAT3 activation [288], whilst also being describes as regulators of TNFa-induced apoptosis and type I interferon (IFN) signaling [259, 289].

Additional pathways regulated by USP7 include cell cycle progression and DNA damage. The inhibition of USP7 promotes uncontrolled CDK1-cyclin B activity and leads to premature mitosis and cellular toxicity [290, 291], whereas the stabilization of CHK1 induces cell cycle arrest [292]. P21-dependent G1/S-arrest was reported as indirect downstream effect of the RING E3 ligase stabilization by USP7, which promotes P21 downregulation via HDAC1 [293-295]. Due to its involvement in DNA damage response, USP7 has been called a guardian of genome integrity [249, 296]. In the NCI-60 cancer cell line panel, low USP7 mRNA expression correlated with genomic instability [297]. Despite its role in P53 regulation, USP7 has also been shown to be involved in multiple P53-independent DNA damage repair pathways, e.g. via RNF168 [296, 298-300]

Further, USP7 has been reported to control both oncogene and tumor suppressor functions. The deubiquitination of the oncogene MYCN by USP7 contributes to neuroblastoma and SCLC growth [301, 302]. In healthy NSC cells, the pairing of USP7 and the E3 ligase TRIM32 balances CMYC levels [303], but hypoxia-induced tumor progression is fostered by the stabilization of the hypoxia-inducible factor-1a (HIF1-a) [304]. Other oncogenic pathways with proposed regulation by USP7 are WNT in colorectal cancer, NOTCH in ALL and the hippo pathway in hepatocellular carcinoma [305-307]. Yet, USP7 is also involved in tumor suppressor regulation. Removal of monoubiquitination from PTEN increases nuclear exclusion and limits PTEN in its tumor suppressing functions [308]. Taken together, USP7 is involved in the regulation of a plethora of pathways, in healthy cells as well as cancer. Even though this clearly highlights the importance of USP7 research, it also increases the complexity thereof.

1.5.5 Targeting USP7

Designing and synthesizing inhibitors for USP7 has proven to be difficult. Challenges include the selectivity for USP7 in comparison to other DUBs. With the highly conserved structure of their catalytic domain, it is difficult to discriminate binding to USP7 from other DUBs, and screening libraries never cover all ~ 100 DUBs [309, 310]. Also, many of the available USP7 inhibitors only show low micromolar potency and only few are in the nanomolar range. Options to overcome this problem would be the identification of new inhibitor binding sites in USP7 and better screening methods for compounds [311]. Reported screening options are often either costly or of low efficacy and accuracy [309]. Thus, many newer developments are based on structural insights and USP7- compound crystal structures [248, 312-314]. Since the role of USP7 as cancer regulator was established, many efforts were put towards developing USP7 inhibitors for therapy. Although no USP7 inhibitors entered clinical trials yet, a multitude of compounds for targeting USP7 has been created [310]. Often, they are classified by their mechanisms of DUB inhibition or according to the chemical structures these small molecules are based on [9].

The first reported USP7 inhibitor was developed by Hybrigenics in 2009. HBX41108 was discovered by fluorometric high-throughput screening and was shown to inhibit USP7 non-covalently in cell-free assays with an IC50 of 424 nM. The resulting P53-stabilization, apoptosis and reduced proliferation at micromolar concentrations were shown in HCT116 colorectal cancer cells [315]. However, subsequent studies reported a poor selectivity towards USP7 and inhibition of further DUBs including USP5, USP78 and USP10, as well as improved features with the newer amidotetrahydroacridine derivatives

HBX19818 and HBX28258. However, the reported IC50 values of these irreversibly-binding inhibitors were in the low micromolar range and their specificity was only tested against a panel of six DUBs [316].

Two of the best-characterized and commercially available USP7 inhibitors are the nitrothiophene derivatives P005091 and P22077, initially identified by Progenra [317-319]. Both target the catalytic cleft of USP7 and bind covalently and irreversible to C223 of USP7, but both also inhibit USP47 at similar rates. Additionally, reports noted poor solubility but high general toxicity for these compounds [320, 321]. Nevertheless, P005091 and P22077 are the USP7 inhibitors with the most published *in vivo* experiments and follow-up studies after initial report [322]. P005091 has been shown to reduce tumor growth and prolong mouse survival at 5 -25 mg/kg in PDX models of multiple myeloma [318], hepatocellular carcinoma [323] and esophageal squamous cell carcinoma [324]. In an orthotopic glioblastoma PDOX, P005091 reduced tumor size to less than 50% and extended mouse survival, allowing the assumption of P005091 to be BBB-penetrant [325]. *In vivo* studies of P22077 involved treatments of orthotopic neuroblastoma [326], melanoma [327], pancreatic [328] and hepatocellular carcinoma [329] at comparable drug concentrations of 5-30 mg/kg daily. P22077 was not only tested in solid tumors, but also showed the ability to reduce tumor burden and prolong mouse survival in AML [285] and CML, even though the effect in the later is thought to be conveyed by USP47 inhibition [330].

In cooperation with Genentech, di Lello et al. reported the nuclear magnetic resonance spectroscopy (NMR)-aided identification of the 2-amino-4-ethylpyridin derivatives GNE 6640 and GNE6776. Both are allosteric inhibitors that penetrate the catalytic cleft at the ubiquitin-binding site between the thumb and the fingers, preventing the binding of ubiquitin. Since these inhibitors do not target the highly conserved catalytic C223, it is not surprising that they show high selectivity when screened in a panel of 36 DUBs [248, 331]. Additional USP7 inhibitors from Genentech are compound 11, GNE3086 and GNE3093, which have a cyanopyrrolidine warhead that upon binding convert C223 of USP7 into a dehydroalanine irreversibly destructing this site for nucleophilic attacks [332].

A bigger group of USP7 inhibitors are based on 4-hydroxypiperidine derivatives. Turnbull et al. published a series of derivatives identified from screening of ~500,000 compounds using a ubiquitin-rhodamine assay. The two lead compounds with high USP7 selectivity were FT671 and FT827. FT827 forms a covalent bond C223 of USP7, while FT671 non-covalently binds the catalytic cleft at a reported IC50 of 52 nM. In a multiple myeloma PDX model, FT671 was able to reduce tumor volume by up to 50% at 200 mg/kg [312]. Structure-based analyses identified the non-covalent active site inhibitor, binding interaction pockets in the thumb-palm cleft of USP7 selectively at 90 nM IC50 [311]. Disclosed to have similar sites, the irreversibly binding XL177A inhibitor was reported to work with sub-nanomolar concentrations in a P53-dependant fashion [333]. Further, the allosteric 4-hydroxypiperidine-based inhibitor ALM34 was reported to act at 1.5 nM IC50 and at high selectivity [313, 334]. However, as for XL188 and XL177A, follow-up publications confirming these actions are missing. Binding to a similar pocket as XL188, compound 41 (or USP7-797) is one of the most potent sub-nM USP7 inhibitors created by RAPT Therapeutics [335]. In PDX models of multiple myeloma, the orally available thienopyridine-derived compound 41 is able to reduce tumor volume to less than 25% and rescue mouse survival [301, 335, 336]. However, as of now, compound 41 is not commercially available for research.

Additional publications reported USP7 inhibitors designed based on the structure of P005091 and P22077. The thiazole-derivatives C7 and C19 were the most potent with IC50 potencies in the low micromolar range [337, 338]. While these compounds were identified by looking into their structure-function relations, another group synthesized 55 piperidinol derivatives and screened them for USP7 inhibition and against a panel of six DUBs. The lead compound L55 binds between the palm and thumb of USP7 at low nanomolar potency and was briefly shown to exhibit anti-tumor activity *in vitro* [339]. In contrast, sesquiterpene lactone parthenolide (PTL) was characterized for its *in vitro* effects. PTL does not seem to modify C223 and shows partial capacity against other DUBs. However, the compound seems to have low solubility and bioavailability [310, 340]. Furthermore, some additional naturally-sourced USP7 inhibitors have been reported, but literature visibility and relevance, possibly due to micromolar potencies and impracticality, seem low [341-346].

A rising method to target proteins are Proteolysis Targeting Chimeras (PROTACs), which bring E3 ubiquitin ligases in proximity with new targets and induced their ubiquitination and thus degradation [347]. PROTACS are heterobifunctional three-parted molecules: (1) a part binding the target protein, often based-off small molecule inhibitors, (2) a linker connecting part (1) to structure (3), which will recruit a E3 ubiquitin ligase. Commonly used E3 ligases are the Von-Hippel-Lindau protein (VHL) and cereblon (CRBN), whose use in PROTACs improved development significantly [348]. After the first clinical trial of a protein degrader in 2020, 26 PROTACs are in clinical trials in 2023, showing the safety, drug-like usage and immense potential of these molecules [348, 349]. Three USP7-targeting degraders have been published so far. U7D-1 is based on the USP7 inhibitor compound 4, linked to a CRBN recruiter. This first described USP7 PROTAC showed clear USP7 reduction and P53-independent anti-proliferative effects at low micromolar potencies [350]. In contrast, PU7-1 uses the structure of XL177A to bind USP7, which is linked to lenalidomide as recruiter for CRBN. PU7-1 strongly reduces USP7 protein levels within 72 h and is able to reduce proliferation in triple-negative breast cancer cells *in vitro* [299]. The third published USP7 PROTAC also recruits CRBN, but is based on the XL177A predecessor XL188 [351]. PROTAC 17, or Gü3866, was shown to reduce viability of MM1.S myeloma cells by up to 50% at 10 µM treatment concentration and specificity was validated using mass spectrometry. Through a collaboration, Gü3866 was available for this study together with an unpublished improved version, Gü4095.

Taken together, USP7 inhibitors have been developed with many efforts, but further improvements in terms of potency, specificity and BBB penetrance, which has barely been addressed so far, are necessary for clinical implementations.

II Objective of the study

Pediatric PFA ependymoma are highly aggressive pediatric brain tumors. They mainly arise in young children (median age 3 years) and are characterized by a poor outcome (10-year OS < 60%) [1]. Currently, therapy is limited to surgical resection and radiotherapy. Despite recent advances in the understanding of PFA ependymoma biology, including the identification of EZHIP overexpression as oncogenic driver, no proposed druggable targets have been translated to the clinics so far [5, 153]. The expression of EZHIP results in a de-repression of PRC2 target genes and corresponding expression changes, which are thought to drive PFA ependymoma formation. Targeting EZHIP pharmacologically is not yet possible, as the structure of the protein is not deciphered and EZHIP possesses almost no conserved domains and targetable regions. Thus, this work applied several strategies to find alternative targeted treatment options for PFA ependymomas.

One approach focused on the identification of interaction partners of EZHIP, as targeting them may interfere with EZHIP, its stability or PRC2 complex interaction. Thus, published IP-MS data from non-ependymoma cancer cells was collected and overlapping EZHIP binding partners from three experiments were identified. Potential candidates were then further characterized in PFA ependymoma cells and their interaction with EZHIP as well as their role in PFA ependymoma biology was analyzed. Additionally, *in vitro* and *in vivo* small molecule treatments were used to test the targeting of EZHIP interaction partners in PFA ependymoma.

Second, mid-throughput drug library screening was employed. As ependymoma are epigenetically de-regulated tumors, a library composed of over 100 drugs targeting epigenetic readers, writers or regulators was tested for their ability to affect the survival of two ST-ZFTA cell lines and one PFA ependymoma cell line.

Thirdly, literature was screened for hypothesis-based druggable targets of PFA ependymoma. Targets were chosen based on the mechanism-of-action and potential connections to the role of EZHIP, as well as target expression in PFA ependymoma.

IV Materials & Methods

4.1 Material

4.1.1 Cell Material

Table 1 | Cell lines and patient-derived xenografts (PDX)

Cell line/PDX	Entity	Supplier
HEK293	Human embryonic kidney cells	ATCC, CRL-1573
(HEK)293T	Human embryonic kidney cells, SV40 T antigen containing	ATCC, CRL-3216
EPD210FH	PFA ependymoma	Brain Tumor Resource Lab (www.btrl.org/)
BT214	PFA ependymoma	Till Milde, DKFZ, Heidelberg (established originally as PDX)
BT232	PFA ependymoma	Till Milde, DKFZ, Heidelberg (established originally as PDX)
VBT420	PFA ependymoma	Daniela Lötsch-Gojo, Vienna
Human Astrocytes	Human fetal astrocytes	Sciencell Research Laboratories, Carlsbad, USA , 1800
U2OS	Osteosarcoma	Lab of Prof. Dr. Jeroen Krijgsveld, DKFZ, Heidelberg
Daoy	Medulloblastoma	In-house
EP1NS	ST-ZFTA ependymoma	Till Milde, DKFZ, Heidelberg[122]
BT165	ST-ZFTA ependymoma	Till Milde, DKFZ, Heidelberg (established originally as PDX)
B193	DMG, EZHIP expressing	Chris Jones, ICR, London
R059	DMG, K27M	Laura van Soosten, DKFZ, Heidelberg

Table 2 | Genetically engineered cell lines

Cell line	Genetic Manipulation	Selection
HEK 293 EZHIP-FLAG-HA	pLVX-puro-EZHIP-FLAG-HA	Puromycine
HEK293 EZHIP-3K-FLAG-HA	pLVX-puro-EZHIP-3K-FLAG-HA	Puromycine
HEK293 EZHIP-6K-FLAG-HA	pLVX-puro-EZHIP-6K-FLAG-HA	Puromycine
U2OS EZH2-WT	no	Single cell clone
U2OS EZH2-NT-04	pL.CRIPSR.v2-puro-sgNT	Puromycine, single cell clone 4
U2OS EZH2-03	pL.CRIPSR.v2-puro-sgEZH2	Puromycine, single cell clone 3
U2OS EZH2-13	pL.CRIPSR.v2-puro-sgEZH2	Puromycine, single cell clone 13
U2OS USP7-WT	no	Single cell clone
U2OS USP7 NT-01	pL.CRIPSR.v2-puro-sgNT	Puromycine, single cell clone 1

U2OS USP7-6-11	pL.CRIPSR.v2-puro-sgUSP7-6	Puromycine, single cell clone 11
U2OS USP7-1-03	pL.CRIPSR.v2-puro-sgUSP7-1	Puromycine, single cell clone 3
U2OS USP7-1-46	pL.CRIPSR.v2-puro-sgUSP7-1	Puromycine, single cell clone 46

4.1.2 Recombinant DNAs

Table 3 | Commercial or gifted plasmids

Plasmid	Catalog number	Supplier
pCMV-VSV-G	#12259	Addgene, Cambridge, USA
psPAX2	#12260	Addgene, Cambridge, USA
pcDNA3.1-NMyc-USP7	#131242	Addgene, Cambridge, USA
pcDNA3.1-NMyc-USP7-C223S	#131243	Addgene, Cambridge, USA
pFN31K-MDM2	N1641	Promega, Madison, WI, USA
HaloTag Ubiquitin	N272A	Promega, Madison, WI, USA
pcDNA3.1-empty	NA	Patricia Benites, DKFZ, Heidelberg
pL.CRIPSR.v2-puro	NA	Pavle Boskovic, DKFZ, Heidelberg
pL.CRIPSR-GFP	NA	Patricia Benites, DKFZ, Heidelberg
pLKO.1-puro	NA	In-house
pGreenFire-Luciferase	#TR011-PA1 (on-demand order)	Systemic Biosciences, Palo Alto, USA

Table 4 | Cloned Plasmids in this thesis

Cloned Plasmid	Resistance/Selection	Plasmid Type
pLKO.1-puro-sh-EZH2-3	Puromycine	Lentiviral
pLKO.1-puro-sh-Scrambled	Puromycine	Lentiviral
pLKO.1-puro-sh-USP7-8	Puromycine	Lentiviral
pL.CRIPSR.v2-puro-sgNT	Puromycine	Lentiviral
pL.CRIPSR.v2-puro-sgEZH2	Puromycine	Lentiviral
pL.CRIPSR.v2-puro-sgUSP7-1	Puromycine	Lentiviral
pL.CRIPSR.v2-puro-sgUSP7-6	Puromycine	Lentiviral
pL.CRIPSR-GFP-sgNT	GFP	Lentiviral
pL.CRIPSR-GFP-sgUSP7-1	GFP	Lentiviral
pL.CRIPSR-GFP-sgUSP7-6	GFP	Lentiviral
pL.CRIPSR-GFP-sgUSP7-7	GFP	Lentiviral
pL.CRIPSR-GFP-sgUSP7-10	GFP	Lentiviral
pLVX-IRES-puro-EZHIP-FLAG-HA	Puromycine	Lentiviral
pLVX-IRES-puro-EZHIP-FLAG	Puromycine	Lentiviral
pLVX-IRES-hygro-EZHIP-FLAG	Puromycine	Lentiviral

pcDNA3.1-NMyc-USP7-dTRAF	NA	Eukaryotic
pLVX-IRES-puro-EZHIP-FLAG-HA-3K	Puromycine	Lentiviral
pLVX-IRES-puro-EZHIP-FLAG-HA-6K	Puromycine	Lentiviral
pLVX-IRES-puro-EZHIP-FLAG-HA-K9R	Puromycine	Lentiviral
pLVX-IRES-puro-EZHIP-FLAG-HA-K12R	Puromycine	Lentiviral
pLVX-IRES-puro-EZHIP-FLAG-HA-K127R	Puromycine	Lentiviral
pLVX-IRES-puro-EZHIP-FLAG-HA-K140R	Puromycine	Lentiviral
pLVX-IRES-puro-EZHIP-FLAG-HA-K149R	Puromycine	Lentiviral
pLVX-IRES-puro-EZHIP-FLAG-HA-K161R	Puromycine	Lentiviral
pLVX-IRES-puro-EZHIP-FLAG-HA-K9R-K127R	Puromycine	Lentiviral
pLVX-IRES-puro-EZHIP-FLAG-HA-K9R-K149R	Puromycine	Lentiviral
pLVX-IRES-puro-EZHIP-FLAG-HA-K127R-K149R	Puromycine	Lentiviral
pLVX-IRES-puro-EZHIP-FLAG-A366T	Puromycine	Lentiviral
pLVX-IRES-puro-EZHIP-FLAG-F110C	Puromycine	Lentiviral
pLVX-IRES-puro-EZHIP-FLAG-I88F	Puromycine	Lentiviral
pLVX-IRES-puro-EZHIP-FLAG-R214G	Puromycine	Lentiviral
pLVX-IRES-puro-EZHIP-FLAG-S30P	Puromycine	Lentiviral
pFN21A-EZHIP	NA	Eukaryotic
pFN21A-EZHIP-3K	NA	Eukaryotic
pFN21A-EZHIP-6K	NA	Eukaryotic
pFN31K-USP7	NA	eukaryotic
pFN31K-USP7-C223S	NA	Eukaryotic
pFN31K-USP7-dTRAF	NA	Eukaryotic

4.1.3 Oligonucleotides

Table 5 | Mutagenesis primers

Name	Sequence
EZHIP_K9_F	GACATGGAGAgGGAGCAGAAG
EZHIP_K9_R	TGACTGAGTGGCCATGGT
EZHIP_K12_F	AAGGAGCAGAgGCACCAGCAG
EZHIP_K12_R	CTCCATGTCTGACTGAGTGG
EZHIP_K127_F	GGGCCCCAGAgGGCCACTGGC
EZHIP_K127_R	CACAGCGGCCTGGCTGCC
EZHIP_K140_F	GCCCAGACCAgGAGCCCCGGG
EZHIP_K140_R	CAGGTGCTCGTCGGCGTG
EZHIP_K149_F	CGTCGTAGGAgGCAGCCCTGC
EZHIP_K149_R	GCTGTTCCCGGGGCTCTTG
EZHIP_K161_F	CCGGCTCAGAgGCCTCCAGGG
EZHIP_K161_R	GGCAGCCTGGTTGCGGCA
EZHIP_K9_3K_F	AGTCAGACATGGAGAGGGAGCAGAAGCACCA
EZHIP_K9_3K_R	TGGTGCTTCTGCTCCCTCTCCATGTCTGACT

EZHIP_K12_6K_F	TGGAGAGGGAGCAGAGGCACCAGCAGGACGA
EZHIP_K12_6K_R	TCGTCCTGCTGGTGCCTCTGCTCCCTCTCCA
EZHIP_K127_3K_F	CTGTGGGGCCCCAGAGGGCCACTGGCCACGC
EZHIP_K127_3K_R	GCGTGGCCAGTGGCCCTCTGGGGCCCCACAG
EZHIP_K140_6K_F	ACCTGGCCCAGACCAGGAGCCCCGGGAACAG
EZHIP_K140_6K_R	CTGTTCCCGGGGCTCCTGGTCTGGGCCAGGT
EZHIP_K149_3K_F	ACAGCCGTCGTAGGAGGCAGCCCTGCCGCAA
EZHIP_K149_3K_R	TTGCGGCAGGGCTGCCTCCTACGACGGCTGT
EZHIP_K161_6K_F	CTGCCCCGGCTCAGAGGCCTCCAGGGCGGCG
EZHIP_K161_6K_R	CGCCGCCCTGGAGGCCTCTGAGCCGGGGCAG
EZHIP_A366T_F	GTCTGGGTCAaCTGATGAGAATCCTTC
EZHIP_A366T_R	AGAGAGCGGCGGCTGAGA
EZHIP_F110C_F	CACGAAGTTTgTGGGTGTGTGGTG
EZHIP_F110C_R	AGGACTGCGGCAGTCCTG
EZHIP_I88F_F	GGGGCTGCCAtTCATAGCTGC
EZHIP_I88F_R	GAGGCCTCATCGGTGATG
EZHIP_R214G_F	GCCTGCTACCgGAAGCCGCAT
EZHIP_R214G_R	CTTGCCTCAGATGCGTGG
EZHIP_S30P_F	CGCCCTTGCCcCCGGGGATGC
EZHIP_S30P_R	GTTTCGTTGTTCAGCCCTCCCTGC

Table 6 | Cloning primers

Name	**Sequence**
EZHIP_EcoRI_F	CCGGAATTCGCCACCATGGCCACTCAGTCA
EZHIP_NotI_R	TTGCGGCCGCAGCATAATCTGGAACATCA
FLAG_NotI_R	GCGGCCGCAATCACTTATCGTCGTCATCC
EZHIP_XhoI_F	CTCGAGGCCACCATGGCCACTCAGTCA
FLAG_SmaI_R	GGCCCTCACTTATCGTCGTCATCCTTA
dTRAF_InFusion_F	GACACAACTGGGATTCAAAGAAGCACACCG
dTRAF_InFusion_R	AATCCCAGTTGTGTCCATCACTCAGGGC
EZHIP_SgfI_f	ATAGGCGATCGCCATGGCCACTCAGTCAGACATGGAGA
EZHIP_PmeI_r	ATAGGTTTAAACCGGCTCAGGCGGTGTTGCGGGGTGA
USP7_SgfI_f	TAATGCGATCGCCATGAACCACCAGCAGCAGCA
USP7_PmeI_r	CCGGGTTTAAACTCAGTTATGGATTTTAATGGCCTTTTCAAGG

Table 7 | PCR primers

Name	Sequence
EZH2_sg_amp_3F	TGGCAATCGTTTCCTGTTCT
EZH2_sg_amp_3R	AGCAGTCATTAACAGTTGCACA
USP7_sg_amp_1F	AGTGTGGTATAGCATGTTTTCAAAT
USP7_sg_amp_1R	GGTGTAGGCAATCTTGAAACTCAAA
USP7_sg_amp_6F	AGGTCTCTCCACTCACTTGGT
USP7_sg_amp_6R	AGGCTATGTAGAGGCAGCAAA

Table 8 | shRNA and sgRNA oligonucleotides

Name	Sequence
sh-Scrambled_F	CCGGCCTAAGGTTAAGTCGCCCTCGCTCGAGCGAGGGCGACTTAACCTTAGGTTTTTG
sh-Scrambled_R	AATTCAAAAACCTAAGGTTAAGTCGCCCTCGCTCGAGCGAGGGCGACTTAACCTTAGG
sh-EZH2-3_F	CCGG TATGATGGTTAACGGTGATCA CTCGAG TGATCACCGTTAACCATCATATTTTTG
sh-EZH2-3_R	AATTCAAAAATATGATGGTTAACGGTGATCACTCGAGTGATCACCGTTAACCATCATA
sh-USP7-8_F [306]	CCGGCTCAGAACCCTGTGATCAACTCGAGTTGATCACAGGGTTCTGAGTTTTTG
sh-USP7-8_R [306]	AATTCAAAAACTCAGAACCCTGTGATCAACTCGAGTTGATCACAGGGTTCTGAG
sg-NonTargeting(NT)_F	CACCGTCGGCGCTTCGCTAATTGA
sg-NonTargeting(NT)_R	AAACTCAATTAGCGAAGCGCCGAC
sg-EZH2_F	CACCGACCAAGAATGGAAACAGCGA
sg-EZH2_R	AAACTCGCTGTTTCCATTCTTGGTC
sg-USP7-1_F	CACCGGGTTCTGAGTAATTCTTGGT
sg-USP7-1_R	AAACACCAAGAATTACTCAGAACCC
sg-USP7-6_F [352]	CACCGGATTTCGCACAAAACACGGA
sg-USP7-6_R [352]	AAACTCCGTGTTTTGTGCGAAATCC
sg-USP7-7_F [305]	CACCGATCATTTAAACTGTCTTACG
sg-USP7-7_R [305]	AAACCGTAAGACAGTTTAAATGATC
sg-USP7-10_F [305]	CACCGGGCATCACCATAATCTTCCA
sg-USP7-10_R [305]	AAACTGGAAGATTATGGTGATGCCC

4.1.4 Antibodies

Table 9 | Primary and secondary antibodies

Antibody	Supplier	Catalog Number / RRID
Anti-beta Actin antibody [AC-15] (HRP)	Abcam	ab49900; RRID:AB_867494
Anti-CXorf67 antibody produced in rabbit	Sigma Aldrich	HPA004003; RRID:AB_2667113
Anti-Histone H3 (tri methyl K27) antibody [mAbcam 6002] - ChIP Grade	Abcam	ab6002; RRID:AB_305237
Anti-Mouse HRP	Cell Signaling	7076, RRID:AB_330924
Anti-Rabbit HRP	Cell Signaling	7074, RRID:AB_2099233
Bax antibody	Cell Signaling	2772; RRID:AB_10695870
Donkey anti-Mouse IgG (H+L) Highly Cross-Adsorbed Secondary Antibody, Alexa Fluor™ 488	Invitrogen	A21202; RRID:AB_141607
Donkey anti-Rabbit IgG (H+L) Highly Cross-Adsorbed Secondary Antibody, Alexa Fluor™ 568	Invitrogen	A10042; RRID:AB_2534017
DYKDDDDK Tag Antibody	Cell Signaling	CS2368; RRID:AB_2217020
Ezh2 (D2C9) XP® Rabbit mAb	Cell Signaling	5246S; RRID:AB_10694683
GFP	Abcam	Ab13970; RRID:AB_300798
goat anti-chicken IgY-HRP	Santa Cruz	sc-2428; RRID:AB_650514
MDM2 Monoclonal Antibody (IF2)	Thermo Fisher	33-7100; RRID:AB_2533136
Mouse IgG2a Isotype Control from murine myeloma	Sigma Aldrich	M5409; RRID:AB_1163691
Myc-Tag (71D10)	Cell Signaling	2278; RRID:AB_490778
Purified Mouse Anti-Human P53	BD Biosciences	554293; RRID:AB_395348
Rabbit IgG	Millipore	PP64; RRID:AB_97852
Recombinant Anti-P21 antibody [EPR3993]	Abcam	ab109199; RRID:AB_10861551
Ubiquitin Monoclonal Antibody (Ubi-1)	Thermo Fisher	13-1600; RRID:AB_2533002
USP7 Polyclonal Antibody (GT481)	Thermo Fisher	MA5-31515; RRID:AB_2787146

4.1.5 Small Molecules

Table 10 | Inhibitors and degraders

Name	Target	Company	ID
CPI-1205	EZH2	Enzo Life Sciences	BV-B2509-1
Tazemetostat	EZH2	Hölzel Diagnostika	HY-13803-5
DS-3201 (Valemetostat)	EZH2	Hölzel Diagnostika	HY-109108AS-1mg
UNC199	EZH2	Biomol	CAY14621-1
P22077	USP7	Biotrend/Aobious	AOB0547
GNE6776	USP7	Hölzel Diagnostika	HY-107986-5mg
FT671	USP7	Hölzel Diagnostika	HY-107985-1mg

USP7-IN-1	USP7	Hölzel Diagnostika	HY-16709-5mg
P005091	USP7/USP47	Hölzel Diagnostika	HY-15667-5mg
HBX41108	USP7	Biomol	Cay23759-1
Rosiglitazone	PPARΓ agonist	Sigma Aldrich	R2408
PPAR Agonist IX, GQ-16	PPARΓ agonist	Sigma Aldrich	516571-25MG
DZNep	EZH2/SAM	Hölzel Diagnostika	A11377-1
MAK683	EED	Enzo Life Sciences	B1972-5
MG-132	proteasome	Biomol	AG-CP3-0011
Talazoparib	PARP	Hölzel Diagnostika	TargetMol T6253
Veliparib	PARP	Santa Cruz	sc-394457A
Olaparib	PARP	Hölzel Diagnostika	TMO-T3015-100mg
Pamiparib	PARP	Hölzel Diagnostika	HY-104044-5mg
Cycloheximid	Translation	Merck Millipore	239763
OTX015 (Birabresib)	bromodomain	Hölzel Diagnostika	A13890-25
Mivebresib (ABBV-075)	bromodomain	Hölzel Diagnostika	MOLN-M11890-10mg
I-BET151	bromodomain	Hölzel Diagnostika	MOLN-M11204-10mg
P22077 (in vivo)	USP7	Selleckchem	S7133
P005091 (in vivo)	USP7	Selleckchem	S7132
Gü3866	USP7	Christian Steinebach, Uni Bonn	
Gü4095	USP7	Sophie Wittenberg, Uni Bonn	

4.1.6 Databases and Software

Table 11 | Databases and software tools

Software	Weblink/Supplier
Biorender	https://www.biorender.com/
Blood-Brain-Barrier-Drug-Penetration-Predictions (BDPP) [7]	https://unite-bdpp.dkfz.de/
EndNote 20	Thomson, ResearchSoft, Carlsbad, USA
FlowJo v10.8.1	https://www.flowjo.com/
GraphPad Prism 9	https://www.graphpad.com/
ImageJ 1.52h	https://imagej.nih.gov/ij/
iTREX [353]	https://itrex.kitz-heidelberg.de/iTReX/
Mechnetor Mechanistic Networks Explorer [354]	http://mechnetor.russelllab.org/
NEBaseChanger	https://nebasechanger.neb.com/
Perseus v2.0.7.0 [355]	NA
R 4.2.2.	//www.R-project.org/
R2 Microarray Analysis and Visualization Platform	https://hgserver1.amc.nl/cgi-bin/r2/main.cgi?open_page=login
ShinyGO 0.80 [356]	http://bioinformatics.sdstate.edu/go/
Studylog 4.2.1.3	Studylog Systems Inc., San Francisco, USA
SynergyFinderPlus [357]	https://tangsoftwarelab.shinyapps.io/synergyfinder/_w_89407382/#!/
Synthego ICE analysis	https://ice.synthego.com/

4.2 Methods

4.2.1 Cell lines

HEK293, HEK293T, U2OS and Daoy cells were cultured in DMEM (Gibco, D6046), supplemented with 10% FBS (Gibco, 10082147) and 1% Penicillin/Streptomycin (Gibco,015140122), at 37 °C and 5% CO2. Cells were passaged or harvested using trypsin (Sigma, T3924). EPD210FH, VBT420 and BT214 were cultured in NeuroCult NS-A Basal media (Stem Cell Technologies, 5750), supplemented with NeuroCult NS-A Proliferation Supplements (Stem Cell Technologies, 5753), 75 ng/ml BSA (Thermo Scientific, B14), 1% Penicillin/Streptomycin (Gibco,015140122), 2 mM L-Glutamine (Thermo Fisher Scientific, 25030024), 20 ng/ml human EGF (Peprotech, AF-100-15-100) and 20 ng/ml human FGF basic (Peprotech, AF-100-18B-50), at 37 °C and 5% CO2. BT232 cells were cultured in 50% DMEM/F12 (Sigma, D8062) and 50% Neurobasal media (Thermo Fisher, 21103049), supplemented with 1x B27 (Gibco, 17504044), 1x N2 (Gibco, 17502048), 1% Penicillin/Streptomycin (Gibco, 015140122), 10 mM Hepes (Gibco, 15630056), 2.5 µg/ml Heparin (Sigma, H3149), 20 ng/ml human EGF (Peprotech, AF-100-15-100) and 20 ng/ml human FGF.basic (Peprotech, AF-100-18B-50), at 37 °C and 5% CO2. Human Astrocytes were cultures in DMEM (Gibco, D6046), supplemented with 10% FBS (Gibco, 10082147), 1% Penicillin/Streptomycin (Gibco,015140122), 1 mM Sodium Pyruvate (Thermo Fisher, 11360070), 1x N2(Gibco, 17502048) and 1% GlutaMAX™ (Thermo Fisher, 13462629). BT165 and EP1NS cells were cultured in in Neurobasal-A medium (Thermo Fisher Scientific, 10888022) supplemented with 1µg/mL Heparin (Sigma, H3149), 2mM L-Glutamine (Thermo Fisher Scientific, 25030024), 1% Penicillin/Streptomycin (Gibco, 015140122), 1x B27 (Gibco, 1750404420 ng/ml human EGF (Peprotech, AF-100-15-100) and 20 ng/ml human FGF.basic (Peprotech, AF-100-18B-50) at 37 °C and 5% CO2. R059 and B193 were cultured in tumor stem medium (TSM) (**Table M1**) supplemented as shown in **Table M2** at 37 °C and 5% CO2. EPD210FH, B193 and BT214 were cultured on surfaces coated with 10 µg/ml laminin (Sigma, L2020) in PBS for 30 min at 37 °C. BT232, BT165, EP1NS and VBT420 were cultured on surfaces coated with Geltrex (Gibco, A1569601) in PBS for 30 min at 37 °C. All ependymoma or DMG cell lines were passaged and harvested using accutase (Gibco, A6964) when grown adherent and using accumax™ (Invitrogen, 00-4666-56) when grown as spheres. All cell lines were regularly tested for mycoplasma and identities were confirmed by regular DNA methylation analysis.

Table 12 | TSM base recipe

Reagent	Vendor	Catalog number	Volume
Neurobasal-A Medium (1X)	Invitrogen	10888-022	250 ml
D-MEM/F-12 (1X)	Invitrogen	11330-032	250 ml
HEPES Buffer Solution (1M)	Invitrogen	15630-080	5 ml
MEM Sodium Pyruvate Solution (100x)	Invitrogen	11360-070	5 ml
MEM Non-Essential Amino Acids Solution (100x)	Invitrogen	11140-050	5 ml
GlutaMAX	Invitrogen	35050-061	5 ml
Antibiotic-Antimycotic (100x)	Invitrogen	15240-096	5 ml

Table 13 | Supplemented TSM recipe

Reagent	Vendor	Catalog number	Working concentration	Stock concentration	Volume
TSM Base					50 ml
B-27 Supplement	Gibco	1750404420	1x	50x	1 ml
hEGF	Peprotech	AF-100-15-100	20 ng/ml	20 µg/ml	50 µl
hFGF	Peprotech	AF-100-18B-50	20 ng/ml	20 µg/ml	50 µl
hPDGF	Peprotech	100-13A-50	10 ng/ml	10 µg/ml	25 µl
Heparin	Sigma	H3149	2 µg/ml	2 mg/ml	50 µl

4.2.2 sgRNA and shRNA cloning

For sgRNA cloning, two complementary oligos with the required overhangs were annealed and phosphorylated using 1 µl per oligo (100 µM), 1 µl T4 ligation buffer (Thermo Fisher Scientific, B69), and 0.5 µl polynucleotide kinase (Thermo Fisher Scientific, EK0032) in a 10 µl reaction, which incubated at 37 °C for 30 min., followed by 95 °C for 5 min. and slow cooling (0.1 °C/s) to 25 °C. Afterwards, 100 ng lentiviral vector (pL.CRIPSR.v2-puro or pL.CRIPSR-GFP-) was mixed with 1x Tango buffer (Thermo Fisher Scientific, BY5), 50 nM DTT (New England Biolabs, Bl034A), 0.5 µl T4 Ligase (NEB, M0202), 1 µl Esp3I (Thermo Fisher Scientific, ER0451) and 2 µl annealed oligos (250x-diluted in H2O) in a 20 µl reaction, which was subjected to 6 cycles of 37 °C for 5 min. and 20 min. for 5 min. The product was used to transform Stbl3 chemically competent E.coli cells spread on a LB-Agar Ampicilin (1 µg/ml) selection plate. Individual colonies were selection and purified plasmids were confirmed using Sanger Sequencing (eurofinsgenomics) with a U6 promotor primer.

pLKO.1-puro was a kind gift from Pavle Boskovic, pLKO.1-GFP was a kind gift from Patricia Benites. For shRNA cloning, the backbones were digested with AgeI (Thermo Fisher Scientific, FD1464) and EcoRI (Thermo Fisher Scientific, FD0274). Linearized product was purified from a 1% TAE-agarose gel using the QIAGEN Gel Extraction Kit (QIAGEN, 28704). shRNA oligos with respective overhangs annealing was performed as described above. 1:200 diluted oligos were ligated into 50 ng digested backbone using the T4 DNA Ligase (NEB, M0202). Transformation and Selection was performed as above. Purified plasmids were confirmed using Sanger Sequencing (eurofinsgenomics) with a TetO-pLKO-puro sequencing primer.

4.2.3 EZHIP overexpression constructs

pLVX-IRES-puro and pLVX-IRES-hygro were a kind gift from Pavle Boskovic. pLVX-puro-EZHIP-FLAG-HA was created by transferring the EZHIP-FLAG-HA from a previously published construct [5]. The sequence was PCR amplified using the Q5 Hotstart Polymerase (NEB, M0493) introducing EcoRI and NotI cutting sites. pLVX-IRES-puro was linearized using these two enzymes, and the purified insert was ligated using a T4 DNA Ligase (NEB, M0202). The product was used to transform Stbl3 chemically competent E.coli cells spread on a LB-Agar Ampicilin (100 ng/ml) selection plate. Individual colonies were selected and purified plasmids were confirmed using Sanger Sequencing (eurofinsgenomics) with an EF1a promotor and IRES primer. EZHIP-FLAG (with and without mutations) was transferred into pLVX-IRES-puro as described above using a reverse PCR primer binding the FLAG-tag sequence. EZHIP-FLAG (with and without mutations) was transferred into pLVX-IRES-hygro as described above using a forward primer introducing a XhoI cutting site and reverse PCR primer binding the FLAG-tag sequence introducing a SmaI cutting site. pLVX-IRES-hygro was linearized using these two enzymes. Ligation, transformation and clonal selection were performed as above. Sanger sequencing (eurofinsgenomics) was performed using a CMV and IRES reverse primer.

4.2.4 USP7 overexpression constructs

pcDNA3.1-NMyc-USP7 (#131242) and pcDNA3.1-NMyc-USP7-C223S (#131242) were bought from addgene. The pcDNA3.1-NMyc-USP7-dTRAF construct was created with the In-Fusion® HD Cloning Kit (Clontech, PT5162). PCR primers were designed to amplify the complete plasmid without the USP7 TRAF domain (Thr54-Ala204) using the Q5 Hotstart Polymerase (NEB, M0493). PCR products was purified using the QIAquick PCR purification kit (QIAGEN, 28106) and submitted to the In-Fusion reaction. Product was used to transform Stbl3 chemically competent E.coli cells spread on a LB-Agar Ampicilin (1 µg/ml) selection plate. Individual colonies were selection and purified plasmids were confirmed using Sanger sequencing (eurofinsgenomics) with a CMV and BGH_reverse primer.

4.2.5 Site-directed mutagenesis

pLVX-IRES-puro-EZHIP-FLAG-HA-3K and pLVX-IRES-puro-EZHIP-FLAG-HA-6K were created from the pLVX-IRES-puro-EZHIP-FLAG-HA plasmid using the GeneArt® Site-Directed Mutagenesis PLUS Kit (Thermo Fisher Scientific, A14604) and the AccuPrime™ Pfx DNA Polymerase (Thermo Fisher Scientific, 12344-024). First, the three mutations K9R, K127R and K149R were introduced simultaneously to create the 3K plasmid. Afterwards, the K12R, K140R and K161R mutations were added simultaneously to generate the 6K plasmid. Plasmid identities were confirmed by Sanger sequencing with a CMV and IRES reverse primer. All single point mutations were introduced into pLVX-IRES-puro-EZHIP-FLAG-HA or pLVX-IRES-puro-EZHIP-FLAG via PCR using the Q5 Hotstart Polymerase (NEB, M0493) with primers designed using the NEBaseChanger (https://nebasechanger.neb.com/) online tool. PCR reactions were submitted to a KLD reaction (NEB, M0554S) and afterwards used to transform Stbl3 chemically competent E.coli cells spread on a LB-Agar Ampicilin (100 ng/ml) selection plate. Individual colonies were selected and purified plasmids were confirmed using Sanger sequencing (eurofinsgenomics) with a EF1a and IRES reverse primer. The same procedure was used to introduce the K127R mutation into the pLVX-IRES-puro-EZHIP-FLAG-HA-K9R and pLVX-IRES-puro-EZHIP-FLAG-HA-K149R plasmid, as well as the K9R mutation into the pLVX-IRES-puro-EZHIP-FLAG-HA-K149R plasmid.

4.2.6 Lentivirus production

psPAX2, pMD2.G and the lentiviral plasmid were co-transfected into 80-90% confluent low-passage HEK293T cells with a DNA ratio of 1 µg:0.33 µg:1.6 µg respectively using PolyFect Transfection reagent (QIAGEN, 301105). Media was refreshed after 18-24h. Supernatant was collected at 72 h.p.t., cleared for 5 min. at 300 xg and filtered using a Millex HA 0.45 µm filter (Merck, SLHA033SS). If not used directly, virus was stored at -80 °C.

4.2.7 Lentivirus production for PDX-labeling

Low passage (< passage 10) HEK293T cells were seeded at 4x10^6 into 10 cm dishes. After 24 h, psPAX2, pMD2.G and the lentiviral Greenfire-Luciferase plasmid were co-transfected into 80-90% confluent cells using PolyFect Transfection reagent (QIAGEN, 301105). After 72 h, supernatant was cleared for 5 min. at 300 xg and filtered using a Millex HA 0.45 µm filter (Merck, SLHA033SS) into a SW41 centrifuge tube (Beckman Coulter, 331362) and ultracentrifuged at 15000 rpm at 4 °C for 90 min (L8-M ultracentrifuge, Beckmann Coulter). Afterwards, the supernatant was discarded carefully and the pellet was resuspended in 15 µl PBS (Thermo Fisher Scientific, 21600010). The solution was stored at -80 °C until use.

4.2.8 CRIPSR/Cas9 or shRNA mediated knock-out/down

EPD210FH or BT214 cells were seeded at 1.5x10^6 cells and Daoy at 1x10^6 cells into 6-wells with 1 ml appropriate growth media and infected with 500 µl virus. After 18-24h, media was exchanged for 1 ml appropriate growth media. If applicable, puromycin selection (Bioaustralis, BIA-P1230; 1 µg/ml) was started 72h p.i. and performed until all uninfected cells were dead. For Western blot, cells were harvested 7 days p.i. or used for further experiments.

4.2.9 CRISPR/Cas9 knock-out cell lines

U2OS cells were seeded at 1x10^5 cells into 6-wells with 1 ml media and infected with 500 µl virus supernatant. After 18-24h, media was exchanged for 1 ml appropriate growth media. Puromycin selection (Bioaustralis, BIA-P1230; 2 µg/ml) was started 48h p.i. and continued until all uninfected cells were dead. 9 day p.i., cells were harvested with trypsin (Sigma, T3924) into PBS (Thermo Fisher Scientific, 21600010)+ 20% FBS (Gibco, 10082147)+ 1% Penicilin/Streptomycin (Gibco,015140122) and adjusted to 1x10^6 cells in 200 µl. Cells were sorted as single cells based on forward and side scatter into 96-well cell cultures plates with DMEM (Gibco, D6046)+ 20% FBS (Gibco, 10082147)+ 1% Penicilin/Streptomycin (Gibco,015140122) using a BD FACSAria™ III sorter. Plates were checked for colony outgrowth regularly and media was maintained. Full 96-wells were transferred to 6-wells using trypsin (Sigma, T3924) and media was switched to standard to expand the cells. Colonies were screened in a two-step process: on protein level using Western blot (see below) and on DNA level using Sanger Sequencing after PCR. For both, cell pellets were generated by detaching cells with typsin (Sigma, T3924) and centrifugation at 300 xg for 5 min. Genomic DNA was extracted using the Maxwell® RSC Genomic DNA Kit (Promega, AS1610). Q5 Hotstart Polymerase (NEB, M0493) was used to amplify the region of sgRNA targeting from 100 ng input DNA. Products were purified from a 1% agarose TAE gel using the QIAquick gel extraction kit (QIAGEN, 28704) and submitted for Sanger Sequencing (eurofinsgenomics) with the corresponding PCR forward primer. ABI files were submitted to Synthego ICE analysis (https://ice.synthego.com/) and compared to the WT DNA PCR products. FACS sorting was performed at the DKFZ FACS core facility.

4.2.10 EZHIP overexpression

HEK293 cells were seeded into 6-wells at 5x10^5 cells/well/1ml and infected with 500 µl viral supernatant. After 28-24h, media was changed. Selection with puromycin (Bioaustralis, BIA-P1230; 1

µg/ml) was started 72 h p.i. and continued until all uninfected cells were dead. For Western blot, cells were harvested at 10 days p.i. or used for further experiments.

4.2.11 USP7 overexpression

HEK293 EZHIP-FLAG-HA expressing cells were seeded into 6-wells at 5x10^5 cells/well/1ml. After 24 h, cells were transfected or not with the indicated USP7 plasmids using PolyFect Transfection reagent (QIAGEN, 301105). 48 h p.t. cells were harvested using trypsin (Sigma, T3924) and pelleted at 300 xg for 5 min.

4.2.12 Immunoprecipication

Cells were grown to 90% confluency on 15cm dishes, detached with either accutase (Gibco, A6964; EPD210FH) or trypsin (Sigma, T3924; Daoy, U2OS, HEK293), and pelleted at 300 xg for 5 min. Cells were lysed with LB200 buffer (20 mM Tris-HCl pH 8, 200 mM NaCl, 1 mM EGTA, 1 mM EDTA, 1% Triton-X100), supplemented with complete protease inhibitor (Roche, 11873580001) and phosphatase inhibitor (Roche, 4906845001) for 30 min. on ice. Lysates were cleared from debris at 10000 xg at 4 °C for 20 min and transferred to fresh tubes. Protein concentrations were determined using the Pierce™ BCA Protein Assay Kit (Thermo Fisher Scientific, 23225). Lysates were adjusted to equal concentrations in 1200 µl between conditions as input. 25 µl Protein G Dynabeads ™ (Thermo Fisher Scientific, 10003D) were washed with LB200 twice, then incubated with 1 ml lysate for 1 h at 4 °C while rotating to pre-clear. Beads and liquids were separated using a magnetic stand. Pre-cleared lysate was split between 30 µl washed beads with either 2 mg/ml antibody or 2 mg/ml species-matched IgG control and incubated rotating overnight at 4 °C. Supernatant was removed, beads were washed twice with LB200 and twice with LB200. For Western blot analysis, samples were eluted in 40 µl elution buffer (LB200, 10x NuPAGE™ reducing agent (Thermo Fisher Scientific, NP0009), 4x NuPAGE™ sample buffer (Thermo Fisher Scientific, NP0007)) for 5 min. at 95 °C.

4.2.13 Western blot

Cell pellets were washed once with PBS (Thermo Fisher Scientific, 21600010), resuspended in 30-50 µl RIPA (Thermo Fisher Scientific, 89900)+ protease inhibitor (Roche, 11873580001) according to their size and lysed on ice for 20 min. Lysates were cleared at 14200 xg for 20 min. at 4 °C and transferred to fresh tubes. Protein concentrations were determined using the Pierce™ BCA Protein Assay Kit (Thermo Fisher Scientific, 23225). Samples were prepared for equal protein between conditions using the 10x Novex Sample Reducing Agent (Thermo Fisher Scientific, NP0004) and 4x LDS Loading Dye (Thermo Fisher Scientific, NP0007) and boiled for 5 min. at 95 °C. Proteins were separated by size on NuPAGE, 4-12% Bis-Tris, 1.0 mm, 10-15 well gels (Thermo Fisher Scientific, NP0323BOX, NP0322BOX, NP0335PK2) for 1.15 h at 130 V in Novex NuPAGE MES Buffer (Thermo Fisher Scientific, NP0002). Proteins were blotted to PVDF membranes (Thermo Fisher Scientific, 88520) in blotting buffer (25 mM Tris, 200 mM glycine, 20% methanol) for 1.15 h at 20 V. Membranes were blocked with milk (5% milk powder (Roth, T145.3) in TBST at room temperature for 1 h. Primary antibodies were incubated overnight at 4 °C. All antibodies were diluted 1:1000 in 5% Milk/TBST except for EZHIP (1:250). After washing with TBST, secondary HRP-coupled antibodies incubated on the membranes for 1 h at room temperature. Membranes were developed using the Chemostar ECL Imager (Intas Science Imaging) with ECL (Merck, GERPN2109) or ECL Prime (Merck, GERPN2232). For quantifications, images were exported from the Imager as .tif format. ImageJ was used to quantify signal intensities from Western blot bands using equal field sizes. Intensity values were used relative to each other with Actin as loading control.

4.2.14 Immunofluorescence microscopy

Removable 12-well chambers (Ibidi, 81201) were coated with 100 µl laminin (Sigma, L2020) per well for 1 h at 37 °C. Cells were seeded at 5x10^4 cells/well/200 µl media and let attach overnight. Media was removed and cells were washed with 150 µl/well PBS (Thermo Fisher Scientific, 21600010). Cells were fixed for 10 min. at room temperature with 4% PFA (Sigma, 158127), then washed twice with TBS + 0.1% Triton X-100 (Sigma, X100). Cell were permeabilized with blocking buffer (TBS + 3% BSA (Roth, T844.4) and 0.1% Triton X-100 (Sigma, X100)) for 1h at room temperature and incubated with 60 µl primary antibody 1:100 in blocking buffer overnight in a humidified chamber at 4 °C. Wells were washed twice with TBS + 0.05% TritonX-100 (Sigma, X100) before the incubation with 60 µl secondary antibody 1:400 in TBS for 1 h in a humidified chamber at room temperature. After two washed, the chambers were removed, the slide was washed once with ddH2O and a cover slip was mounted on to it using ProLong Glass Antifade Mountant with NucBlue (P36985, Sigma). Images were taken at a Leica SP8 as Z-Stacks at 20x magnification, which were stacked and merged using ImageJ. All imaging was performed at the DKFZ Light Microscopy core facility.

4.2.15 USP7 inhibitor treatment

For Western blots, 1x10^6 cells were seeded into 6-wells in 1 ml media. Cells were allowed to attach overnight. Cell were treated with the indicated concentrations of P22077 (Biotrend, AOB0547) and MG132 (Biomol, AG-CP3-0011) for 20 h (EPD210FH, BT232, BT214). Afterwards, cells were harvested using accutase (Gibco, A6964) and pelleted at 300 xg or 5 min. For microscopy images, 0.8 x10^6 EDP210FH or BT214 cells were seeded into coated 6-wells in 1ml media. Cells were allowed to attach overnight. Cell were treated with the indicated concentrations of P22077 (Biotrend, AOB0547) or P005091 (Hölzel Diagnostika, HY-15667). After 72 h, media and drugs were refreshed. Brightfield images were taken at 10x magnification at random locations of the wells using a Zeiss Axiovert 5 microscope. Exposure times were kept steady within time points and images were processed all in the same way increasing the brightness using ImageJ.

4.2.16 USP7 PRTOAC treatment

0.8x10^6 EPD210FH cells were seeded into 6-wells in 1 ml media. Cells were allowed to attach overnight. Treatments with 100 µM USP7 Protac Gü3866 and eventually 4 µM MG132 (Biomol, AG-CP3-0011) were started at the indicated time points. DMSO control levels were adjusted to the highest DMSO concentration for 72 h. After 72 h, cells were harvested using accutase (Gibco, A6964) and pelleted at 300 xg or 5 min.

0.5 x 10^6 HEK293 cells were seeded into 6-wells in 1 ml media. Cells were allowed to attach overnight and then treated with equal DMSO, 0.391 µM, 3.125 µM or 25 µM Gü3866 or Gü4095. After 24 h, cells were harvested using trypsin (Sigma, T3924) and pelleted at 300 xg or 5 min.

4.2.17 Mass Spectrometry

EPD210FH cells were treated with P22077 or Gü3866 for 6 h or 24 h as described above. Cell pellets from biological triplicates were collected at -80 °C and further processed in parallel after no longer than 4 weeks. Pellets were lysed with 30 µl RIPA (Thermo Fisher Scientific, 89900) + protease inhibitor (Roche, 11873580001) + 25 U/ml benzonase (Millipore, 70746) and lysed on ice for 30 min. Lysates were cleared at 14200 xg for 30 min. at 4 °C and transferred to fresh tubes. Protein concentrations were determined using the Pierce™ BCA Protein Assay Kit (Thermo Fisher Scientific, 23225). Samples were diluted in lysis buffer at 1 µg/µl in 25 µl. Samples were submitted for Mass Spectrometry Analysis to the DKFZ Proteomics core facility. Proteins (10 ug) were digested with Trypsin (Sigma, T3924) using a AssayMAP Bravo liquid handling system (Agilent technologies) running the autoSP3 protocol according to Müller et al. (Muller et al., 2020). LC-MS/MS analysis was carried out on an Ultimate 3000 UPLC system (Thermo Fisher Scientific) directly connected to an Orbitrap Exploris 480 mass spectrometer for a total of 120 min. Peptides were online desalted on a trapping cartridge (Acclaim PepMap300 C18, 5µm, 300Å wide pore; Thermo Fisher Scientific) for 3 min using 30 ul/min flow of 0.05% TFA in water. The analytical multistep gradient (300 nl/min) was performed using a nanoEase MZ Peptide analytical column (300Å, 1.7 µm, 75 µm x 200 mm, Waters) using solvent A (0.1% formic acid in water) and solvent B (0.1% formic acid in acetonitrile). For 102 min the concentration of B was linearly ramped from 4% to 30%, followed by a quick ramp to 78%, after two minutes the concentration of B was lowered to 2% and a 10 min equilibration step appended. Eluting peptides were analyzed in the mass spectrometer using data independ acquisition (DIA) mode. A full scan at 120k resolution (380-1400 m/z, 300% AGC target, 45 ms maxIT) was followed by 47 DIA windows with optimized window placement (Zhang et al., 2015) and 1 Da overlap to cover the mass range from 400-1000 m/z for MS2 spectra acquisition. Fragment spectra were recorded with 30k resolution, using 28% NCE, 1000% AGC target and a maxIT of 54 ms.

Data analysis was performed with the Biognosys software Spectronaut (Biognosys, version 17.1.221229.55965) in directDIA+ (deep) library-free mode. Default settings were applied with the following adaptions. GlyGly (K) was added to variable modifications, PTM localization filter was set to a minimum of 0.75, the fragment ion range was set to 300-1800 m/z, the minimum fragment ion intensity was set to 5%, PTM localization was enabled with the default parameters. The data was searched against the human proteome from Uniprot (HUMAN, containing 81,837 unique entries from 26.10.2022) and the contaminants FASTA from MaxQuant (246 unique entries from 22.12.2022).”PG.Quantity” values were further processed using Perseus. Values were log2 transformed and signal had to be present in at least 2 samples. Fold-change between conditions was calculated and two-sided t-testing was performed. LC-MS/MS and raw data analysis were perfored together with the DKFZ MS-Based Protein Analysis core facility.

4.2.18 Gene Ontology term analysis

Gene Ontology (GO) term analysis was performed using ShinyGO 0.80 online application (http://bioinformatics.sdstate.edu/go/)[356]. Significantly enriched (>1.5 Difference (log2 fold change); >1.5 -log10 (p-value)) or deriched (<-1.5 Difference (log2 fold change); >1.5 -log10(p-value)) proteins after 24 h treatments were compared to all detected proteins. FDR cutoff was set to 0.05, redundancies were removed. GO terms for cellular compartments were extracted.

4.2.19 Cycloheximide assay

0.5x10^6 HEK293 cells stably overexpressing EZHIP-FLAG-HA, EZHIP-3K-FLAG-HA or EZHIP-6K-FLAG-HA were seeded into 6-wells in 1 ml media. Cells were allowed to attach overnight and were then treated with 1 mg/ml cycloheximide solved in water (Millipore, 239763) for the indicated time points. Cells were harvested using trypsin (Sigma, T3924) and pelleted at 300 xg for 5 min.

4.2.20 NanoBret Assay EZHIP-USP7

cDNAs of the different EZHIP and USP7 constructs were amplified to introduce SgfI and PmeI restriction enzyme sites using the Q5 Hotstart Polymerase (NEB, M0493). PCR products were purified from 1% TAE-agarose gel using the QIAGEN Gel Extraction Kit (QIAGEN, 28704). Ligated into the Promega Flexi® Vector System (Promega, N1821) and following cloning was performed according to protocol (Promega, C9320). Plasmid purification was performed using the QIAGEN Maxiprep Kit (QIAGEN, 12163) and plasmid identities were confirmed by sanger sequencing (eurofinsgenomics). NanoBret experiments were conducted according to protocol using HEK293 cells and a NanoLuc-USP7 to EZHIP-HaloTag ratio of 1:100 with always 24 h between seeding, transfection, reseeding and readout at a GloMax plate reader (Promega). All conditions were measured in technical triplicates and NanoBRET ratios were calculated according to protocol.

4.2.21 NanoBRET Assay EZHIP-Ubiquitin

Detection of interactions between EZHIP and Ubiquitin were performed according to the instructions of the NanoBRET™ Ubiquitination Assay (Promega, ND2690), which included the HaloTag®-Ubiquitin Fusion Vector. EZHIP cDNA was cloned from the above mentioned HaloTag-EZHIP vector into the NanoLuc-EZHIP vector according to protocol (Promega, C9320). The NanoLuc-MDM2 (Promega, N160A) was included in the Promega Flexi® Vector System (Promega, N1821). NanoBret experiments were conducted according to protocol using HEK293 cells and a NanoLuc-EZHIP or NanoLuc-MDM2 to HaloTag®- Ubiquitin ratio of 1:100 with always 24 h between seeding, transfection, reseeding and readout at a GloMax plate reader (Promega). All conditions were measured in technical triplicates and NanoBRET ratios were calculated according to protocol. For the USP7 degrader treatment, Gü4095 or equal DMSO was added at a concentration of 3.125 µM during re-seeding 24 h before readout. For the overexpression of USP7, 0 µg (nt), 0.5 µg, 1 µg or 2 µg of plasmid (pcDNA3.1-USP7, pcDNA3.1-USP7-C223S, pcDNA3.1-empty) were added to the transfection mix.

4.2.22 Competitive drop-out assay

Cells were seeded into coated 24-wells at 1.5x10^5 cells in 1 ml media and infected (or not) with 25-50 µl virus. The next day, media was exchanged for fresh 1 ml. At 96 h.p.i., cells were detached using accutase (Gibco, A6964), pelleted at 300 xg for 5 min. and resuspended in 900 µl fresh media. 8 coated 96-wells were seeded with 100 µl each and 2 with 50 µl. Starting at 7 d.p.i., 1-2 wells were harvested at 6 time points using accutase (Gibco, A6964) and collected into U-bottom 96-well plates. After pelleting at 300 xg for 5 min., cells were resuspended in 150 µl media and cells were analyzed for GFP-positivity with a BD Fortessa. 7 d.p.i. was used as reference for the further analysis and thus set as day 0 (followed by day 3, day 7, day 11, day 14 and day 21). Data was processed using the FlowJo v10.8.1 software. A minimum of 5000 cells was analyzed. Live cell populations were determined using the forward versus side scatter area (FSC-A/SSC-A). From them, doublets were excluded in the FSC height versus FSC area plot (FSC-H/FSC-A). From the single cells, the GFP positive population was calculated and values at day 0 were set to 100%. Flow cytometry was performed using analyzers from the DKFZ Flow Cytometry core facility.

4.2.23 Apoptosis Assay

EPD210FH cells were seeded into coated 96-well plates at 5000 cells per well in 90 µl media. After 24 h, cells were treated in triplicates with P005091 (DMSO, 0.75 µM, 1.5 µM, 3 µM), OTX015 (DMSO, 0.75 µM, 1.5 µM, 3 µM) or both using a cross-scheme approach (to also get DMSO+DMSO) using equal DMSO in all wells. Three wells were untreated as background. Apoptosis was determined using the Caspase 3/7 Glo Assay System (Promega, G8090) at 8 h, 24 h and 48 h after treatment using the Glomax plate reader (Promega). Mean background was subtracted from all values. Relative luminescence was calculated against the double DMSO control.

4.2.24 Ependymoma Growth Curves

EP1NS and EPD210Fh cells were seeded into 11 coated 96-well plates (costar, 3610) at densities of 20000, 15000, 10000, 7500, 5000, 4000, 3000, 2000, 1000 or 500 cells/well in 100 µl media in triplicates. The outer wells were filled with 200 µl PBS. Over the course of the experiment, 50% media was refreshed every two or three days. At 24 h, 48 h, 72 h, 96 h, 120 h, 144 h, 168 h, 192 h, 240 h, 288 h and 366 h after seeding, cell viability was assessed using the CellTiter-Glo® Luminescent Cell Viability Assay (Promega, G7571) and the Mithras plate reader (Berthold). Triplicates were averaged for analysis in GraphPad Prism.

4.2.25 Cell Viability Assessments

Cells were seeded into coated 96-well clear bottom plates (costar, 3610) at 5000 cells/well in 80 µl media. 24 h after seeding, drugs were prepared from stocks (in DMSO according to manufacturer´s instructions) as a serial dilution (1:2 or 1:5) in 20 µl with a corresponding DMSO control and added to the wells. If readout was not performed after 72 h, media and drugs were replenished. After 144 h, cell viability was assessed using the CellTiter-Glo® Luminescent Cell Viability Assay (Promega, G7571) and the Mithras plate reader (Berthold). Samples were always measured as technical triplicates and averaged over them before being normalized to the DMSO control of the same plate. Values from three biologically independent experiments were analyzed using GraphPad Prism. IC50 values were determined using the Asymmetric Sigmoidal five parameter standard curve interpolation.

4.2.26 PARPi+USP7i synergy determination

Cells were seeded into coated 96-well clear bottom plates (costar, 3610) at 5000 cells/well in 80 µl media. 24 h after seeding, drugs were prepared from stocks (in DMSO according to manufacturer´s instructions) as serial dilution in media at equal DMSO at 20 µl with a corresponding DMSO only control and added to the wells. USP7 inhibitors (P005091, P22077, FT671) were applied at 8 µM, 6 µM, 4 µM, 2 µM and 1 µM in a matrix-layout combined with Talazoparib at 6 µM, 2 µM, 666.67 nM, 222.22 nM, 74.07 nM, 24.69 nM, 8.23 nM, 2.74 nM or 0.91 nM. 72 h after treatment, media and drugs were replenished carefully. After 144 h, cell viability was assessed using the CellTiter-Glo® Luminescent Cell

Viability Assay (Promega, G7571) and the Mithras plate reader (Berthold). Viability was calculated in relation to the double DMSO control. Synergy was determined using synergyfinder.org [357].

4.2.27 Drug BBB Penetrance Estimation

The potential BBB penetrance of FT671, P22077 and P005091 was assessed using the Blood-Brain-Barrier-Drug-Penetration-Predictions (BDPP) online tool (https://unite-bdpp.dkfz.de/) [7] in collaboration with Julia Benzel. Chemical properties of the drugs were extracted from PubChem.

4.2.28 Animal Experiments

All animal experiments were done in accordance with legal and ethical regulations and approved by the regional council (Regierungspräsidium Karlsruhe, Germany). The experiments were part of the following protocols: G227/19 (toxicity test), G91/20 & G228/19 (treatment with USP7 inhibitors). All handling of mice was performed by in-house mouse technicians. Nonobese diabetic/severe combined immunodeficiency gamma, NOD-SCID gamma® mice (NOD.Cg-Prkdc^{scid} Il2rg^{tm1Wjl}/SzJ), called NSG mice from here on, were used and obtained from the in-house breeding facility (German Cancer Research Center, Heidelberg, Germany). Housing of mice was in individually ventilated cages (IVC) and all animals were monitored daily for health status and tumor-related symptoms. Tracking of mice was performed using the studylog software. Mice were euthanized as soon as they showed or any termination criteria listed in the animal protocol including symptoms of tumor growth or severe weight loss of 20%.

4.2.29 Luciferase-labeling of BT232 PDOX cells

To label the BT232 PDX cells, the cells were taken into short-term *in vitro* culture in NeuroCult NS-A Basal media (Stem Cell Technologies, 5750), supplemented with NeuroCult NS-A Proliferation Supplements (Stem Cell Technologies, 5753) as single cells. Cells were infected with Greenfire-Luciferase carrying virus at 10 µl for every 3 x10^6 cells. 24 h p.i., the cells were washed twice with PBS (Thermo Fisher Scientific, 21600010), collected by centrifugation at 300 xg for 5 min., suspended in their culture media and orthotopically injected into NSG mice as described below. As soon as the mice showed tumor-related symptoms, the mice were euthanized. Tumors were resected and brought into single-cell suspension in PBS (Thermo Fisher Scientific, 21600010), from which the GFP-positive population was sorted using a BD Fortessa. GFP-positive cells were re-injected orthotopically into NSG mice to expand the labelled BT232-Luc cells and be able to cryo-preserve aliquots for future experiments.

4.2.30 Orthotopic injection of PDOX cells

To create PDOX models, PDX cells were orthotopically injected intracranially. Analgesia was administered to NSG mice subcutaneously 20 min. before surgery with 200 mg/kg Metamizol (WDT, 793-333). Mice were anesthetized by inhaled 1.5-2.5 Vol% isoflurane (cp-pharma, 1214) and checked by monitoring respiratory rate and toe pinch reflex. When anesthetized, mice were transferred to a stereotactical frame (Stereotaxic Instrument Model 900, David Kopf Instruments) on a heating pad (AccuLux ThermoLux, Conrad) and Bepanthen® (Bayer Vital, 00829388) was applied to both eyes. An incision of ~0.5 cm was set along the mediolateral line using a scalpel (NeoLab, 2-7125). Afterwards, the skull was exposed with a cotton-tipped applicator and cleaned of minor connective tissue or blood.

With an 18G canula, a hole was burred at the cerebellum at -7 mm bregna, 1 mm lateral left and 2 mm depth. A Hamilton needle (10 µl Rainin Pipette-Lite fitted with a 2-10 µl ART tips barrier non-filtered pipette tip; World Precision Instruments) was filled with 4 µl of 0.25x10^6 cells/µl cell, inserted into the stereotactical frame and brought to the respective site in the brain. The suspension was injected with a slow and steady flow with a maximum injection speed of 2 µl/minute. Afterwards, the needle was maintained in this position for two additional minutes to prevent reflux of the cells. When the needle was retracted the incision was closed with veterinary-grade surgical glue (Vetbond, 3M). Then, the isoflurane inhalation was removed and mice were transferred back to their cages and monitored for the duration of recovery. For post-surgical analgesia, Metamizol (WDT, 793-333) was administered via drinking water at 800 mg/kg/day for 72 h.

4.2.31 *In vivo* treatment with USP7 inhibitors

4.2.31.1 Preparation of drugs for in vivo treatments

The two USP7 inhibitors P22077 (Selleckchem, S7133) and P005091 (Selleckchem, S7132) were used for *in vivo* preclinical studies. Both drugs were solved in DMSO and brought into vehicle at 10% DMSO (Sigma-Aldrich, 472301), 45% Saline (Braun, 10311), 40% PEG (Carl, Roth, 2632.1), 5% Tween®20 (Merck, 817072) at 10 mg/ml. This ready-to-use solution was stored at 4 °C and prepared freshly each week.

4.2.31.2 Toxicity test of P22077 and P005091

NSG mice were treated with P22077 at 10 mg/kg, 15 mg/kg or 20 mg/kg or with vehicle for five days/week (five days on, two days off) intraperitoneally (i.p.) once a day, with P005091 at 15 mg/kg or 20 mg/kg for for five days/week (five days on, two days off) intraperitoneally (i.p.) twice per day. Weight of the mice was monitored three times per week. Drugs were prepared from the ready-to-use solution according to the latest measured weight. Mice were euthanized as soon as they showed or any termination criteria listed in the animal protocol including weight loss of 20% of their starting weight or after 6-weeks of treatment.

4.2.31.3 Treatment study of BT232 DOX

NSG mice were orthotopically injected with 1x10^6 BT232-Luc cells as described above. Starting two weeks after injection, luciferase tumor signal was monitored weekly. For bioluminescence imaging animals were anesthetized using inhaled isoflurane (1.5-2.5 Vol%) and injected with VivoGlo™ Luciferin solution (Promega, P1041) i.p. at 10 ml/kg and 15 mg/ml. Imaging was performed using IVIS Lumina Series III (PerkinElmer) luminescence imager with an exposure time of 5 min. Once the signal reached 2x10^6 photons/second (p/s), mice were randomized into three treatment groups: 10 mg/kg P22077 (13 animals), 10 mg/kg P005091 (13 animals) or vehicle (12 animals). Mice were treated as described above. Mice were euthanized as soon as they showed or any termination criteria listed in the animal protocol including symptoms of tumor growth.

4.2.32 USP7 inhibitor combination screen

Mid-throughput drug screening was performed in collaboration with Heike Peterziel, Aileen Friedenauer and Ina Oehme at the Translational Drug Screening Unit (TDSU) at the KiTZ. To identify drugs which increase their effectivity on cell viability, a library of 104 drugs was tested in combination with P22077

(Biotrend, AOB0547) and P005091 (Hölzel Diagnostika, HY-15667). First in EPD210FH, specific absolute IC25 values for both USP7 inhibitors were determined using the above-described approach, but using uncoated U-bottom plates and a readout after 72 h. All drug screening experiments were performed in 384-well round bottom ultralow attachment spheroid microplates (referred to as assay plates; # 3830, Corning) to allow the formation of three-dimensional spheroids. Bulk ATP quantitation with CellTiter-Glo® 2.0 (CTG; #G9243, Promega) was performed 72 h after treatment according to the manufacturer´s protocol to determine the relative number of metabolically active cells per well as a read-out for cell viability.

The drug screening library comprised 104 drugs, covering standard chemotherapeutics, epigenetic modifiers, metabolic modifiers, kinase inhibitors, apoptotic modulators, and others (modified from [353, 358, 359]; **Supplementary Table 1**). Two replicates of each ready-to-use assay plates were generated by 1) printing 25 nL stamps from source plates (87 drugs and assay controls) using a Mosquito HTS liquid handler (sptlabtech), and 2) by adding seventeen substances (tenovin-6, GSK2879552, chaetocin, TIC10, pracinostat, TAC-901, mivebresib, pacritinib, MI-2, barasertib, CUDC-907, abexinostat, TG101209, quercetin, salermide, and the two USP7i P22077 and P005091) using a D300e digital dispenser (Tecan). Wells with 100 µM benzethoniumchloride (BztCl), 250 nM staurosporine (STS), and 0.1% DMSO were included as maximum, intermediate and minimum effect controls. All drugs were printed at five tenfold concentrations with every condition present in duplicate on one plate. An additional STS concentration range served as a technical control.

The absIC25 concentration of P22077 (3 µM) and P00591 (4.5 µM), respectively, was dispensed on one replicate of the drug concentration ranges of each assay plate with a D300e digital dispenser (Tecan). Until use, the ready-to-use assay plates were reposited in a San Francisco StoragePod system (Roylan Developments Ltd), providing an oxygen- and moisture-free environment at room temperature. EPD210FH cells were seeded at a density of 500/25 µL per well in the ready-to-use assay plates, followed by centrifugation of the plates at 500 g for 3 min. The plates were incubated at 37°C/5% CO2 and residual metabolic activity of the cells determined after 72h as described above.

Drug effects were calculated as drug sensitivity scores (DSSasym) using the web-based drug analysis pipeline iTReX (https://itrex.kitz-heidelberg.de/iTReX/) [353, 359] .Single drug DSS values (DSSmono) were calculated based on the mean DMSO control raw data. To assess the effect of the combination with USP7i, the mean of the fixed concentration of P22077 and P00519, respectively, was used as the minimum effect (negative) control to calculate DSScombo [353]. Combination partners with additional effects were identified by calculating the difference between the DSS of a single drug in the presence and in the absence of the fixed concentration of the USP7i (dcDSS = DSScombo-DSSmono (ElHarouni et al., 2022).

4.2.33 BETi/USP7i synergy analysis

A 9 × 5 matrix design was used to measure synergy metrics, covering nine half-logarithmic dilutions (10 µM – 1 nM) of the BETi Mivebresib, i-BET151 and OTX015 and five twofold dilutions of P22077 and P005091 (6 µM to 0.375 µM). Wells with 100 µM BztCl and 0.1% DMSO were included as maximum and minimum effect controls. All conditions were present in duplicate. Drugs were dispensed with a

D300e digital dispenser (Tecan); ready-to-use assay plates were stored in a San Francisco StoragePod system (Roylan Developments Ltd) until use.

EPD210FH and BT214 cells were seeded on the ready-to-use assay plates at a density of 500 cells/25 µL, followed by centrifugation of the plates at 500 xg for 3 min. The plates were incubated at 37°C/5% CO2 and ATP quantitation performed after 72h as described above. Synergy was determined using synergyfinder.org[357].

4.2.34 Targeted epigenetic library screen

Mid-throughput drug screening was performed in collaboration with Heike Peterziel, Aileen Friedenauer and Ina Oehme at the Translational Drug Screening Unit (TDSU) at the KiTZ. All drug screening experiments were performed in 384-well round bottom ultralow attachment spheroid microplates (referred to as assay plates; # 3830, Corning) to allow the formation of three-dimensional spheroids. Bulk ATP quantitation with CellTiter-Glo® 2.0 (CTG; #G9243, Promega) was performed 72 h after treatment according to the manufacturer´s protocol to determine the relative number of metabolically active cells per well as a read-out for cell viability.

The drug screening library comprised 104 drugs targeting epigenetic modifiers and other epigenetically involved enzymes [353, 358, 359] (**Supplement Table 2**). Two replicates of each ready-to-use assay plates were generated by 1) printing 25 nL stamps from source plates (87 drugs and assay controls) using a Mosquito HTS liquid handler (sptlabtech), and 2) by adding seventeen substances (tenovin-6, GSK2879552, chaetocin, TIC10, pracinostat, TAC-901, mivebresib, pacritinib, MI-2, barasertib, CUDC-907, abexinostat, TG101209, quercetin, salermide, and the two USP7i P22077 and P005091) using a D300e digital dispenser (Tecan). Wells with 100 µM benzethoniumchloride (BztCl), 250 nM staurosporine (STS), and 0.1% DMSO were included as maximum, intermediate and minimum effect controls. All drugs were printed at five tenfold concentrations with every condition present in duplicate on one plate. An additional STS concentration range served as a technical control.

EPD210FH, BT165 or EP1NS cells were seeded at a density of 500/25 µL per well in the ready-to-use assay plates in their respective media, followed by centrifugation of the plates at 500 g for 3 min. The plates were incubated at 37°C/5% CO2 and residual metabolic activity of the cells determined after 72h as described above. Drug effects were calculated as drug sensitivity scores (DSSasym) using the web-based drug analysis pipeline iTReX (https://itrex.kitz-heidelberg.de/iTReX/) [353, 359]

4.2.35 Expression analysis in R2

PPARγ expression was assessed using the R2: Genomics Analysis and Visualization Platform (http://r2.amc.nl). Expression in different pediatric brain tumors was extracted from the Tumor Brain (DKFZ-public) dataset, which includes 2482 affymetrix array (u133p2) based expression profiles collected by Marcel Kool, and filtered for the shown tumor subtypes. PPARγ expression in the ependymoma cell lines was extracted from the Cell line Brain Tumor (2023-01-24) dataset, which includes 123 affymetrix array (u133p2) based expression profiles collected by Marcel Kool including expression profiles I submitted from our PFA ependymoma and ST-ZFTA cell lines.

4.2.36 USP7 recognition site prediction

USP7 recognition site were predicted using the Mechnetor mechanistic network explorer (mechnetor.russellab.com). Motif detection was activated.

4.2.37 IP-MS analysis

Data for U2OS and Daoy EZHIP IP-MS data was obtained upon request from Pajtler et al., 2018 [153]. FLAG-IP data for EZHIP-FLAG in HEK293 was obtained from Hübner et al., 2019 [5]. Data was filtered for identified proteins with a p-value < 0.05 and overlap from all three experiments was calculated. For the heatmap, log2 LFQ values of the different FLAG-IPs in HEK293 normalized to the log2 LFQ values of the IgG control were calculated.

4.2.38 Statistical Analysis

Statistical analysis details can be found in corresponding figures and figure legends. If not reported otherwise, statistical analysis was conducted using GraphPad Prism. P-values <0.05 were considered significant and indicated with *, whereas p<0.01 are indicated with ** and p<0.001 with ***.

V Results

Pediatric PFA ependymoma, characterized by young patients and a dismal prognosis, lack mechanism-of-action based treatment options. Molecularly, these tumors are driven by the expression of EZHIP. However, since EZHIP cannot yet be pharmacologically targeted itself, this study aimed to leverage the molecular understanding of PFA ependymoma to identify alternative treatment options.

5.1 USP7 is an interaction partner of EZHIP

To find druggable targets for PFA ependymoma, I aimed to find potential interaction partners of EZHIP, as they might be regulators of EZHIP or other essential pathways in PFA ependymoma. Thus, I collected published Immunoprecipitation followed by Mass Spectrometry (IP-MS) data from Pajtler et al., 2018 [153] and Hübner et al., 2019 [5] (**Figure 9A**). Pajtler et al. performed IP-MS from endogenous EZHIP in the two non-ependymoma cancer cell lines Daoy and U2OS, whereas Hübner et al. used an overexpression system in HEK293 cells, which endogenously express EZHIP lowly below the Western blot detection limit, using FLAG-tagged full length EZHIP (EZHIP-Full) or truncates representing the N-terminal (EZHIP-N), middle (EZHIP-M) or C-terminal (EZHIP-C) part of EZHIP (**Figure 9B**). For the initial interaction partner identification, I compared the significantly identified proteins in Daoy, U2OS or EZHIP-Full expressing HEK293 cells. There were 13 overlapping proteins identified in the EZHIP IP-MS data from all three experiments: EZHIP, SUZ12, EED, EZH2, USP7, PLEC, RBBP4, TUBB2A, TJP1,

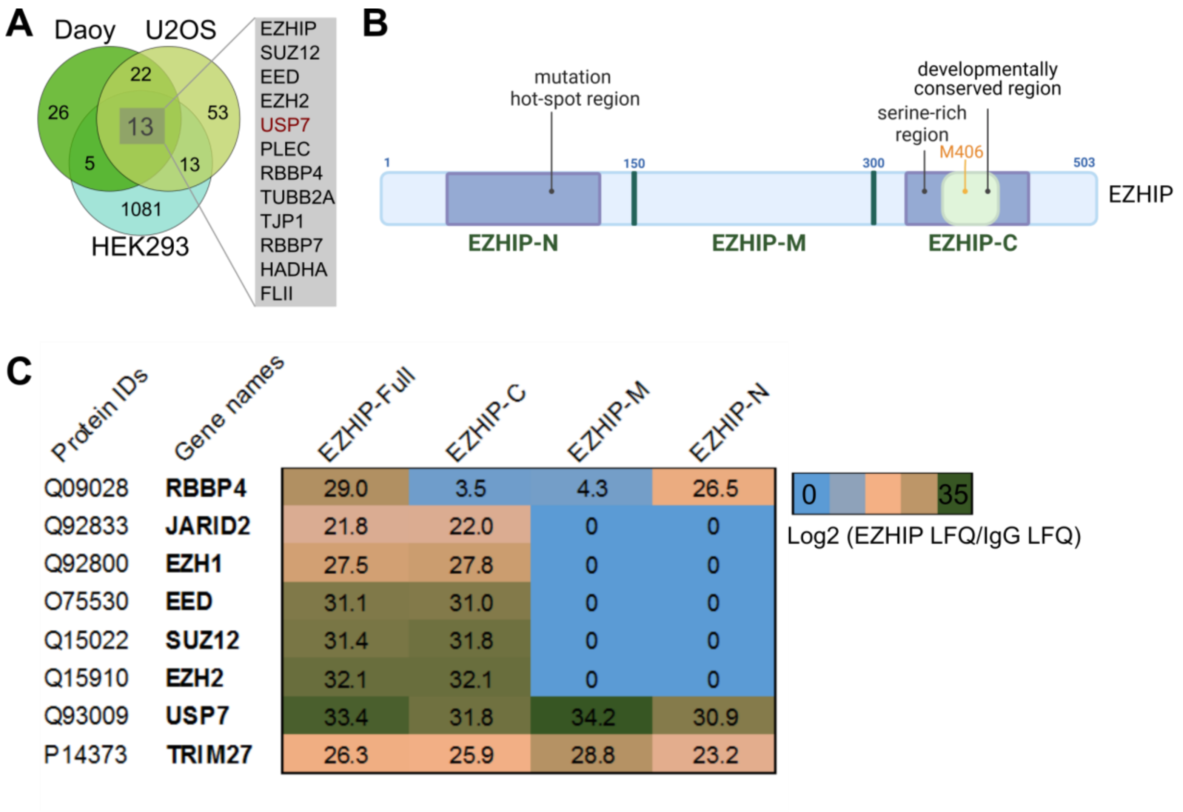

Protein IDs	Gene names	EZHIP-Full	EZHIP-C	EZHIP-M	EZHIP-N
Q09028	**RBBP4**	29.0	3.5	4.3	26.5
Q92833	**JARID2**	21.8	22.0	0	0
Q92800	**EZH1**	27.5	27.8	0	0
O75530	**EED**	31.1	31.0	0	0
Q15022	**SUZ12**	31.4	31.8	0	0
Q15910	**EZH2**	32.1	32.1	0	0
Q93009	**USP7**	33.4	31.8	34.2	30.9
P14373	**TRIM27**	26.3	25.9	28.8	23.2

Figure 9 | IP-MS identifies USP7 as interaction partner of EZHIP

*(**A**) Venn diagram of published EZHIP IP-MS data in Daoy, U2OS and HEK293 cells. Overlapping 13 identified proteins are shown. (**B**) Schematic of the EZHIP construct overexpressed in HEK293 cells from Hübner et al. EZHIP was either used as full length or as truncates EZHIP-C (aa 1-149), EZHIP-M (aa 150-299) or EZHIP-N (aa300-503).(**C**)Heatmap of IP-MS data from Hübner et al. showing the log2 transformed LFQ values for EZHIP over the IgG control for selected detected proteins.*

RBBP7, HADHA and FLII. In addition to EZHIP itself were the expected PRC2 members SUZ12, EED, EZH2, RBBP4 and RBBP7, as well as seven further interaction partners (**Figure 9A**). From these, I chose to focus on USP7 due to its documented association with various cancer-associated pathways and the variety of inhibitors available [312]. I used the full dataset from Hübner et al. to query the interaction of USP7 with the different parts of EZHIP, as most PRC2 proteins mainly interact via the C-terminal part of EZHIP. USP7, in contrast, was identified as interaction partner of all three truncates as well as EZHIP-Full with LFQ values in a similar range (**Figure 9C**).

Next, I sought to validate the interaction of USP7 and endogenous EZHIP and identify the intracellular localization of the interaction in PFA ependymoma. Using IP followed by Western blot, I showed the direct interaction of USP7 and endogenous EZHIP in the PFA ependymoma cell line EPD210FH (**Figure 10A**). I used the Daoy cancer cell line as positive control and included the known EZHIP interaction partner EZH2, which seemed to also interact with USP7 in Daoy (**Figure 10B**). Using Immunofluorescence, I showed that USP7 is primarily but not exclusively expressed in the nucleus, and co-localizes with EZHIP in the nucleus of the two PFA ependymoma cell lines EPD210FH and BT214 (**Figure 10C**).

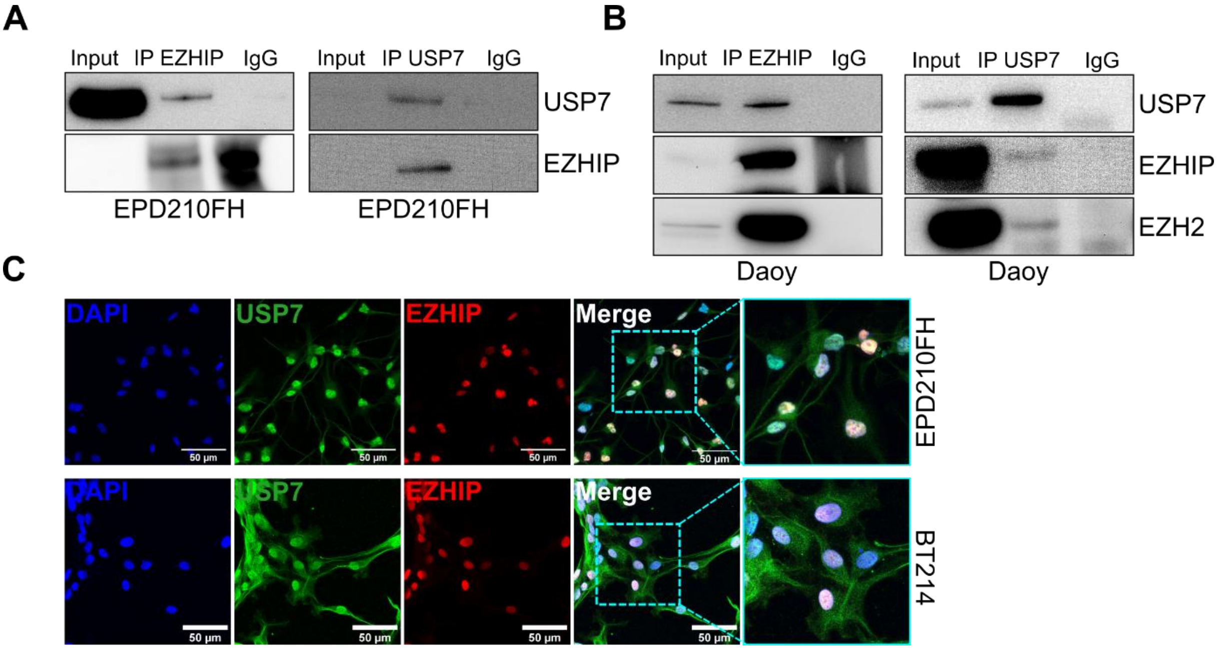

Figure 10 | EZHIP and USP7 interact in PFA ependymoma

*(**A**) Western blot for USP7 and EZHIP of EZHIP-IP or USP-IP in EPD210FH. (**B**) Western blot for USP7, EZHIP and EZH2 of EZHIP-IP or USP-IP in Daoy cells. (**C**) Co-IF staining for DAPI (blue), USP7 (green) and EZHIP (red) in EPD210FH and BT214 cells. Scale bars are 50 µM.*

5.2 The interaction of USP7 and EZHIP is independent of EZH2

As my data and several previous reports have shown EZH2 to interact with USP7, thereby recruiting USP7 to its own interaction partners [275-277], I wanted to determine whether EZH2 mediates the USP7-EZHIP interaction in PFA ependymoma. To show the independence from the presence of EZH2, I performed IP-Western blot experiments in different model systems lacking EZH2. First, I generated a Daoy cell line stably expressing an EZH2 targeting shRNA (shEZH2) as well as the corresponding control using a scrambled shRNA (shScr), which resulted in a considerable KD of EZH2 (**Figure 11A**). Western blots of co-IP experiments showed no difference in USP7-EZHIP interaction between the Daoy shEZH2 and Daoy shScr cells.

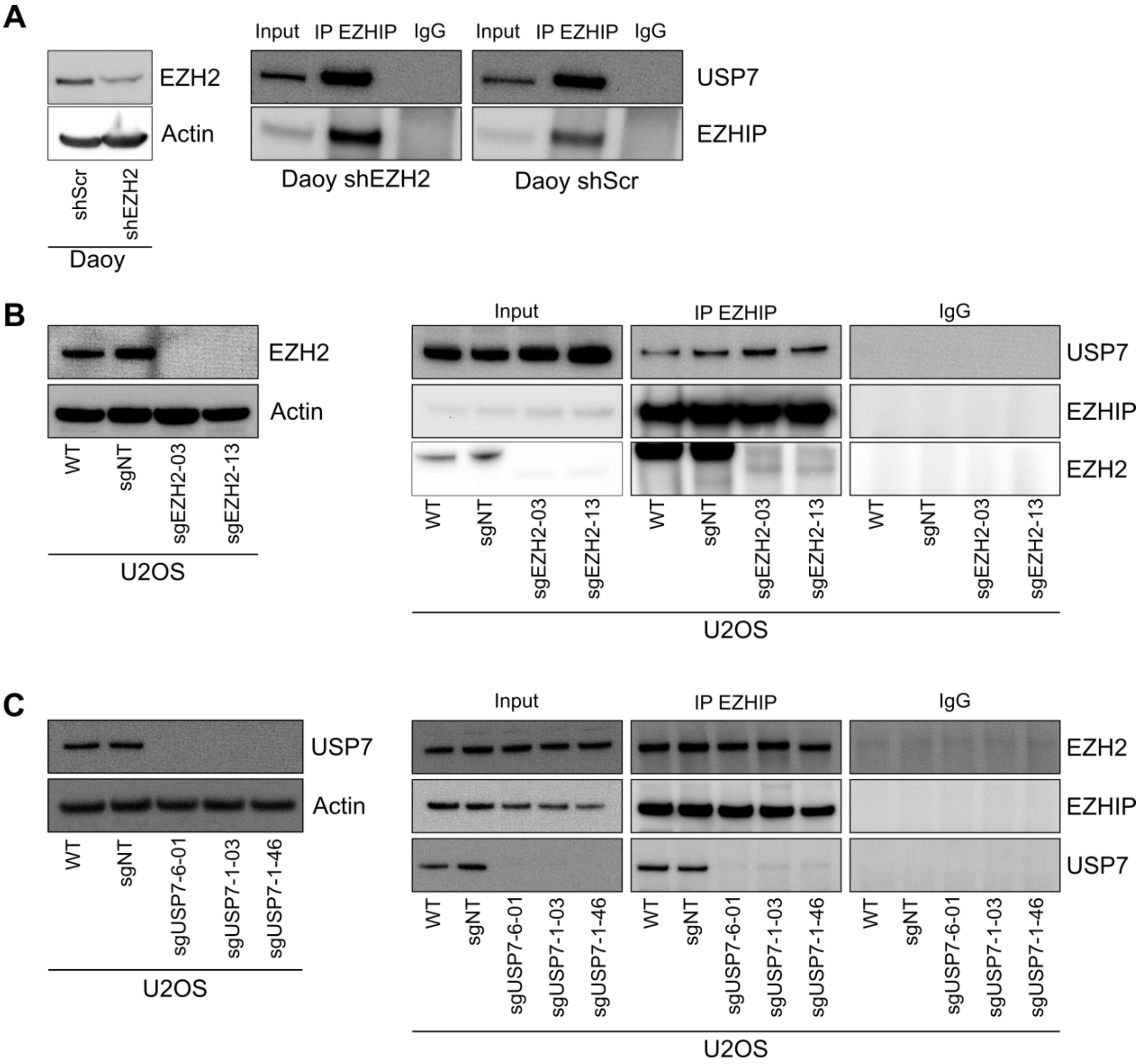

Figure 11 | The interaction of EZHIP and USP7 in independent of EZH2

*(**A**) Western blots showing the KD of EZH2 in the Daoy shEZH2 cells compared to shScr control. Actin was used as loading control (left panel). Western blot for USP7 and EZHIP of EZHIP-IP in Daoy shEZH2 and Daoy shScr cells. (**B**) Western blots of clonal U2OS EZH2 KO cells lines sgEZH2-03 and sgEZH2-13 together with clonal WT and control cells (sgNT) for EZH2. Actin was used as loading control (left panel). Western blot for USP7, EZHIP and EZH2 of EZHIP-IP in the different cell lines, including Input and IgG control. (**C**) Western blots of clonal U2OS USP7 KO cells lines sgUSP7-6-01, sgUSP7-1-03 and sgUSP7-1-46 together with clonal WT and control cells (sgNT) for USP7. Actin was used as loading control (left panel). Western blot for EZH2, EZHIP and USP7 of EZHIP-IP in the different cell lines, including Input and IgG control.*

To exclude the possibility of residual EZH2 in the shEZH2 cells facilitating the USP7-EZHIP interaction, I used the CRISPR/Cas9 genome editing system to generate EZH2 knock-out (KO) cells without residual EZH2 expression. Since PFA cells cannot be cultured as single cells – a necessary step for clonal outgrowth of KO clones - and the Daoy cell line has a gene amplification with multiple copies of EZH2, I used the other EZHIP-expressing cancer cell line U2OS. The complete KO of EZH2 was validated on the protein level using Western blot, whereas the underlying genetic perturbances were identified using sanger sequencing of the region targeted by the sgRNA (**Figure 11B and Supplementary Figure 1**). A non-targeting (nt) sgRNA or no sgRNA (WT) were used in parallel to generate clonal control cell lines. Western blots after co-IP again showed no difference in USP7-EZHIP interaction between the control and KO cells, implying that the interaction of USP7 and EZHIP is independent of the presence of EZH2. To characterize the interaction of USP7 with EZH2 and EZHIP further, I additionally wanted to exclude the option that the presence of USP7 could affect the interaction of EZH2 and EZHIP. Thus, as described for EZH2 above, I created clonal USP7 KO and control U2OS cell lines (**Figure 11C and Supplementary Figure 1**). co-IP experiments revealed that the EZH2-EZHIP interaction is not affected by the loss of USP7. Taken together, I could show that USP7 is an interaction partner of both EZHIP and EZH2 independently of each other.

5.3 The USP7 TRAF domain interacts with EZHIP

In contrast to EZHIP, the structure of USP7 has been researched and well described. Roughly, USP7 possesses seven domains: a TRAF–like domain, followed by a catalytic domain with the enzymatically active cysteine 223 and five UBL domains in the C-terminus (**Figure 12A**). Known interactions of USP7 are often mediated via the TRAF domain [250]. I consulted the protein-protein interaction explorer Mechnetor [354] for amino acid motifs within EZHIP that might be involved in the binding to USP7. Indeed, Mechnetor predicted multiple recognition sites of the USP7 TRAF-like domain to be present throughout the EZHIP protein (**Figure 12A**; dark red). Thus, I used the NanoBRET interaction assay to quantify the interaction strength between EZHIP and USP7, comparing it to a catalytically dead C223S mutant USP7 and a USP7 lacking the TRAF-like domain (dTRAF). Inactivating the catalytic center of USP7 did not significantly change the interaction with EZHIP, whereas the lack of the TRAF-like domain significantly reduced this interaction (**Figure 12B**). Since the interaction was not completely diminished, it can be assumed that the UBL domains are also involved in the interaction with EZHIP.

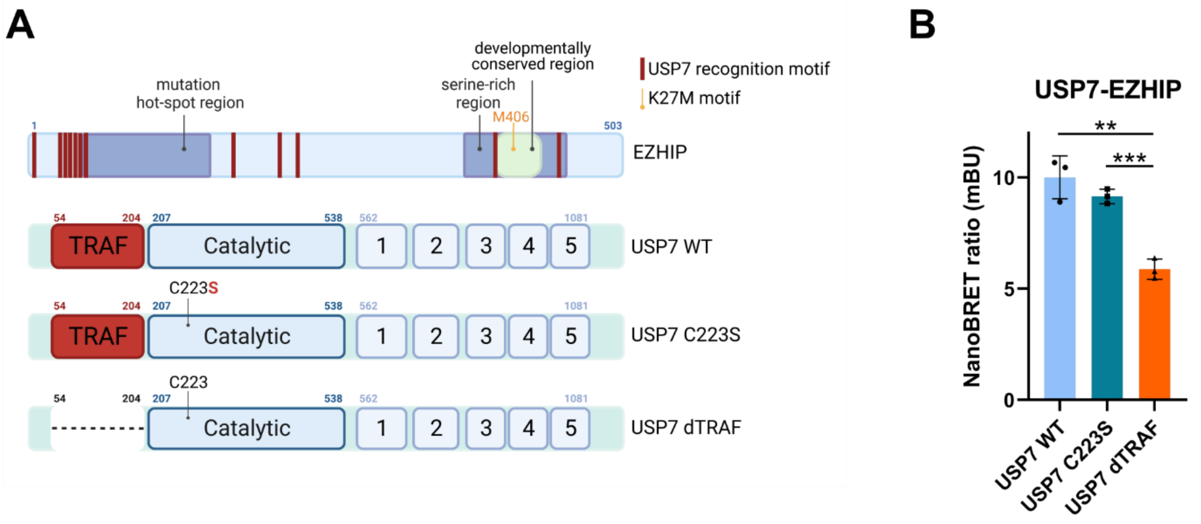

Figure 12 | USP7 interacts with EZHIP via its TRAF domain

*(**A**) Schematic of the overexpression constructs of EZHIP and USP7. Throughout EZHIP highlights show the predicted USP7 TRAF domain recognition motifs (dark red) and the K27M-motif centered around the M406 of EZHIP. USP7 with its five UBL domains, the catalytic domain around the active cystine 223, which is mutated in the C223S construct, and the TRAF interaction domain (light red), which is truncated in the USP7 dTRAF construct. (**B**) NanoBRET interaction assay quantified the interaction strength between EZHIP and USP7 WT, USP7 C223S and USP7 dTRAF. . Replicate values from three individual experiments, mean and SEM are shown. Two-tailed t-test was performed, ** indicates p<0.01 and *** p<0.001.*

5.4 USP7 regulates EZHIP protein levels

After validating the physical interaction of USP7 and EZHIP, I proceeded to characterize the functionality of this interaction. As USP7 is a de-ubiquitinating enzyme and proteasomal degradation is the most common result of ubiquitination [238], I examined the effect of a loss of USP7 on EZHIP protein levels. Using the USP7 degrading PROTAC Gü3866 [351], I was able to follow the effect of loss of USP7 in the PFA ependymoma cell line EPD210FH over time (**Figure 13A**). USP7 protein levels were already highly reduced after 12 h and continued to almost completely diminish until the 72 h time point. The reaction of EZHIP to the treatment followed a similar dynamic, indicating that a loss of USP7 leads to a loss of EZHIP protein. The known USP7 downstream targets P21, BAX and MDM2 reacted as expected with an increase in the indirect targets P21 and BAX and a decrease in the direct USP7 target MDM2. Interestingly, the protein levels of the proposed USP7 target EZH2 were only slightly affected in the 72 h time point and showed an increase instead of the expected decrease. To see whether the reduction in protein abundance is caused by proteasomal degradation, I used the proteasome inhibitor MG132 in addition to the USP7 degradation. USP7 levels were rescued to the DMSO control level, EZHIP protein levels were slightly reduced compared to control, but stronger than the corresponding degrader only treatment (**Figure 13A**). I validated the effect of a loss of USP7 on EZHIP protein levels using two USP7 KO or KD systems. **Figure 13B** shows the reduced EZHIP levels in the above mentioned U2OS USP7 KO cells in comparison to the controls. Again, EZH2 protein levels did not change upon the loss of USP7. Additionally, I infected EPD210FH cells with a USP7 targeting shRNA or a scrambled shRNA. As before, already the reduction of USP7 protein levels led to reduced EZHIP levels (**Figure 13C**).

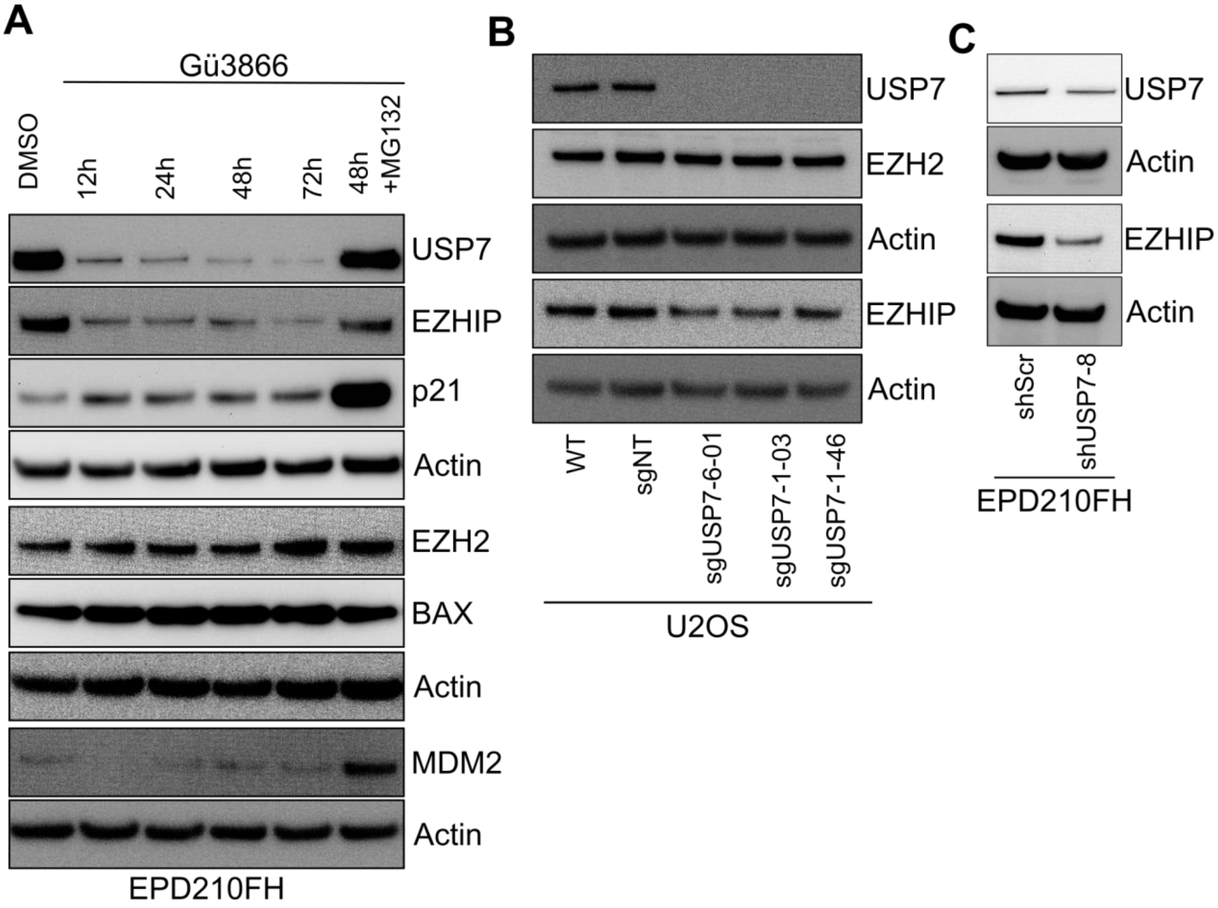

Figure 13 | Reduction of USP7 protein levels impacts EZHIP

(A) Western blot of EPD210FH cells treated with 100 µM Gü3866 and eventually 4 µM MG132 or equal DMSO (72 h) for the indicated times. For each membrane, Actin as loading control is shown. (B) Western blot of U2OS CRISPR clones: WT (no CRISPR), sgNT (control), sgUSP7-6-01, sgUSP7-1-03 and sgUSP7-1-46 for USP7, EZH2 and EZHIP. Actin as loading control. (C) Western blot for USP7 and EZHIP of EPD210FH shScr (control) or shUSP7-8 cells. Actin as loading control.

Next, I wanted to determine whether the catalytic activity of USP7 is involved in the regulation of EZHIP protein levels. Thus, I treated three different PFA ependymoma cell lines – BT214, EPD210FH, BT232 - with increasing concentrations of the USP7 inhibitor P22077 alone or in combination with the proteasome inhibitor MG132. USP7 levels were not affected by any of the treatments. Although the effect is milder compared to the degrader treatments, the treatment with 10 µM P22077 for 24 h reduced EZHIP protein levels in all three cell lines (**Figure 14**). In the BT214 cell line, 1 µM P22077 treatment increased EZHIP protein levels compared to the DMSO control at unchanged USP7 levels and a similar effect can be seen in the EPD210FH cells upon the 3 µM treatment (**Figure 14A**). In both the BT214 and the EPD210FH cells, the addition of MG132 increased the EZHIP protein levels compared to the P20077 only treated cells, but not to a level of MG132 treatment alone, which showed higher protein levels than the DMSO control. The P21 protein levels increased mainly upon the treatment with the lower P22077 concentrations, but increased strongly upon MG132 treatments, which is a known effect and can act as positive control for MG132 treatment together with the increased total ubiquitin staining. The BT232 cells showed the lowest effect on EZHIP protein levels upon P20077 treatment (**Figure 14B**). Additionally, in these cells, one can see that EZH2 protein levels did not change, neither upon USP7 inhibitor nor upon MG132 treatment. In contrast, the levels of P53, a known indirect USP7 target, increased strongly upon proteasomal inhibition and slightly upon treatment with 10 µM P22077. Overall, these drug treatments showed that the catalytic activity of USP7 is responsible for the regulation of EZHIP protein levels, even though the effects of a complete depletion of USP7 were stronger.

A more in-depth comparison of the effects of the USP7 degrader Gü3866 with the USP7 inhibitor P22077 was the goal of a MS-based proteome analysis after treatment of the PFA ependymoma cell line EPD210FH for 6 h (**Figure 15A+C**) or 24 h (**Figure 15B+D**). Both treatments were compared to a DMSO control. Between the treatments, the number of overall detected proteins was highly comparable with over 7000 proteins per sample and 6981 proteins identified in all samples, of which 6206 were quantified. After 6 h, the overall proteome changes observed were smaller than after 24 h, independent of the treatment. After 6 h treatment with P22077 or Gü3866, 12 or 23 proteins respectively showed significant change, whereas 57 (P22077) or 106 (Gü3866) proteins showed significant changes after 24 h (**Figure 15A+B**). For both P22077 and Gü3866, decreased protein abundance was more common than increased abundance, which was expected as USP7 mainly stabilizes proteins. After 24 h, only two proteins were significantly upregulated in the Gü3866 treated cells and 20 different proteins were significantly upregulated upon P22077 treatment (**Figure 15A).** Gü3866 treatment resulted in 104 downregulated proteins after 24h, while P22077 treatment led to a downregulation of 37 proteins. However, only two proteins were down regulated by both inhibitors: ATAD2 and CKAP2 (**Figure 15B**). USP7 itself shows a clear reduction upon the treatment with Gü3866, which is stronger after 24 h, but barely changed upon P22077 treatment. This compares well to the Western blots in **Figure 14**. The known direct USP7 target TRIM27 shows a decrease upon both treatments. Although it didn’t meet the significance threshold of 1.5-fold increase/reduction with a -log(p-value) of 1.5 or higher in the P22077 treated samples, the trend is clear and it served as positive control. This observation is also in line with

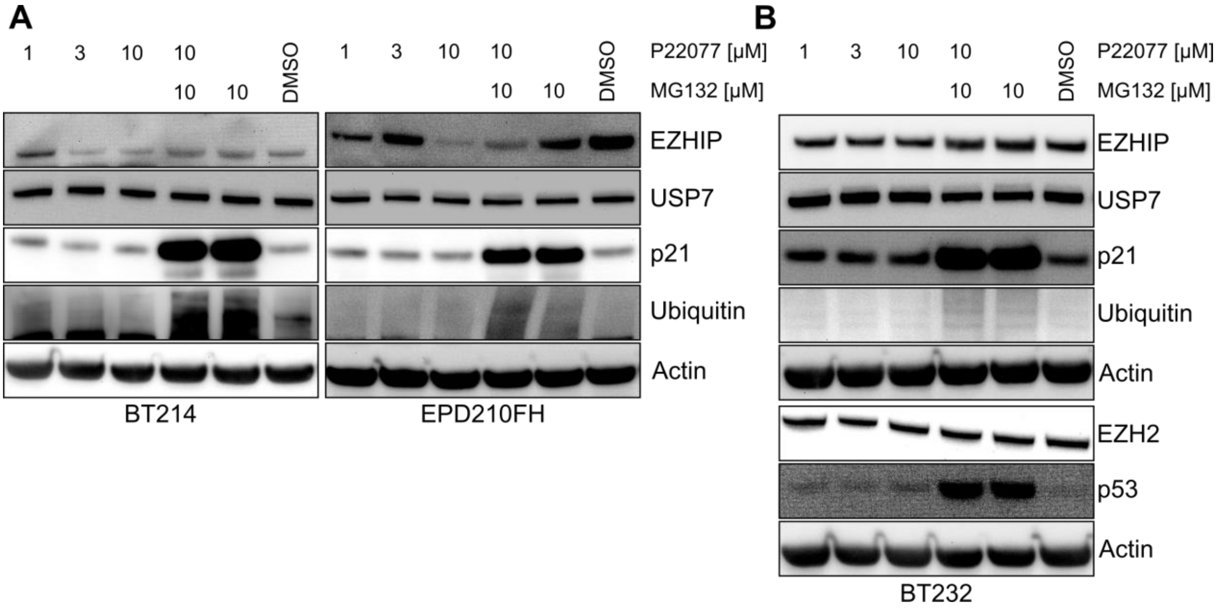

Figure 14 | Inhibition of USP7 affects EZHIP protein

*(**A**) Western blot of BT214 and EPD210FH cells treated with P22077 and eventually MG132 or equal DMSO for 20 h with the indicated concentrations. Actin as loading control. (**B**) Western blot of BT232 cells treated with P22077 and eventually MG132 oı equal DMSO for 20 h with the indicated concentrations. Actin as loading control for each membrane.*

the detected TRIM27-USP7 interaction in the published IP-MS data (**Figure 9C**). The MS data also validated the clear reduction of EZHIP upon Gü3866 treatment, while EZH2 levels barely changed or slightly increased. Also, P21 reacted to the USP7 PROTAC treatment and increased after 24 h (**Figure 15C+D**). Whilst the same can be observed after 24 h of P22077 treatment for P21, I did not detect a change in EZHIP protein levels (**Figure 15E+F**). Particularly noticeable was an increase in apoptotic proteins upon P22077 treatment, which did not occur upon Gü3866 treatment: FOSB (Finkel–Biskis–Jinkins murine osteogenic sarcoma virus B), JUN, JUNB and JUND. All four are transcription factor subunits and are part of the activator protein 1 (AP-1) transcription factor, which is involved in apoptotic regulation, cell growth and differentiation [360].

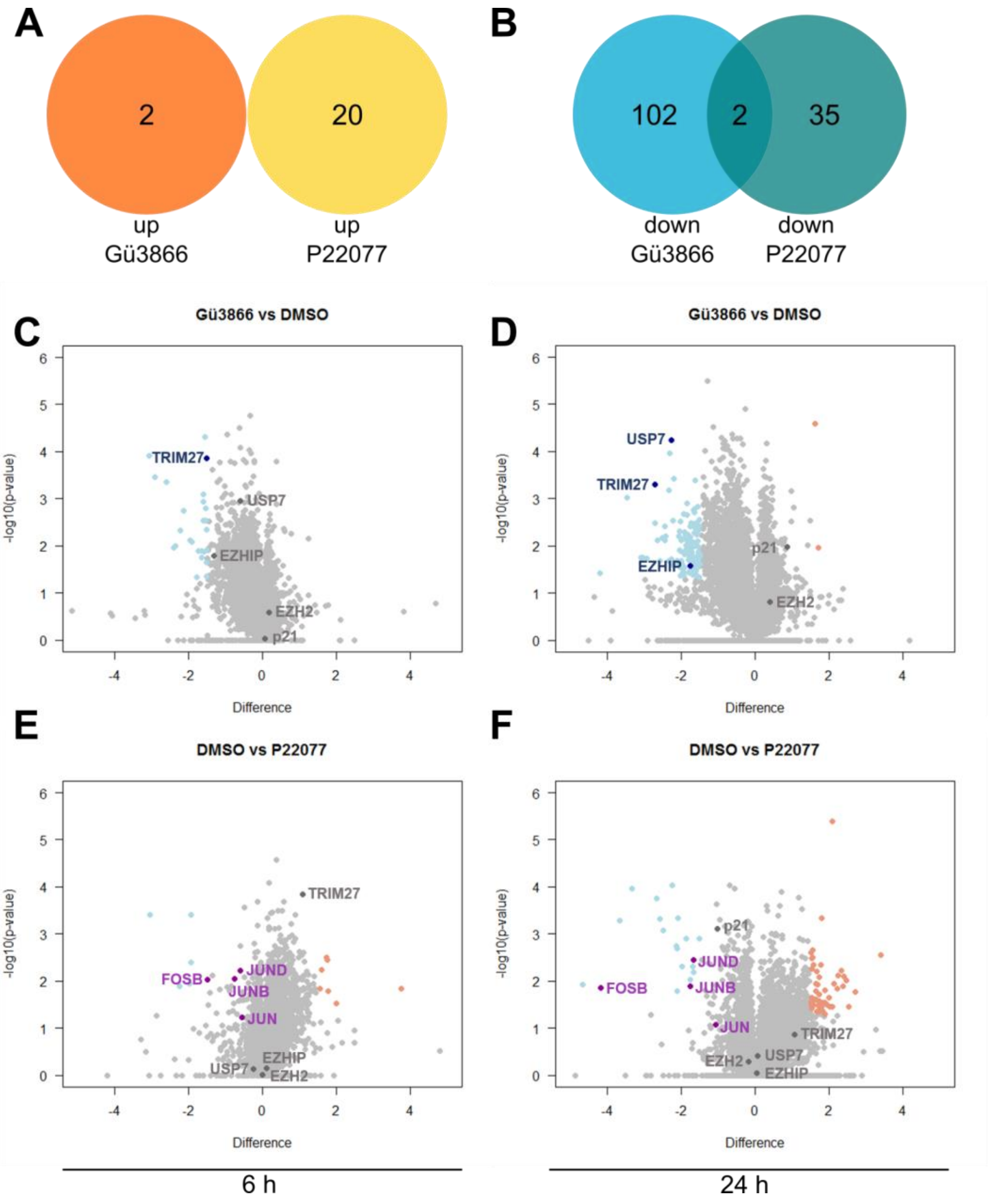

Figure 15 | Comparison of protein changes upon USP7 degradation and inhibition

*Venn diagrams of proteins significantly up (**A**) and down (**B**) in EPD210FH cells treated for 24 h with Gü3866 or P22077. Significance cut-off as described below. (**C-F**)Volcano plot of differentially expressed proteins in EPD210FH after 6 h (**C**) or 24 h (**D**) of Gü3866 treatment (100 µM) or 6 h (**E**) or 24 h (**F**) of P22077 treatment (10 µM). Orange indicates increased expression (>1.5 Difference (log2 fold change); >1.5 -log10 (p-value)), light blue marks decreased expression (<-1.5 Difference (log2 fold change); >1.5 -log10(p-value)). Selected proteins are labeled. Data from three individual experiments.*

To understand the difference in treatment response to P22077 and Gü3866 better, I performed a gene ontology (GO) term analysis for cell compartments with the 24 h data using the ShinyGO application (**Figure R16**). Indeed, the AP-1 transcription factor complex is the highest enriched term for the P20077 treatment, followed by several terms linked to the (mitotic) spindle and chromosomes (**Figure R16B**). In contrast, the Gü3866 is rather characterized by terms of movement (costamere, myosin complex), cell-cell communication (axon hillock, exon-exon junction) and stress. Interestingly, polycomb group proteins (PcG protein complex) was also an enriched term (**Figure 16A**). However, this analysis should be interpreted cautiously, as the number of differentially expressed proteins is low and the background of EPD210FH general expression might hinder more in-depth analysis.

Taken together, the data presented in this chapter showed that USP7 regulates EZHIP protein levels in PFA ependymoma cells. This EZH2-independent regulation can be visualized by genetic depletion, PROTAC degradation or small molecule inhibitor treatments of USP7.

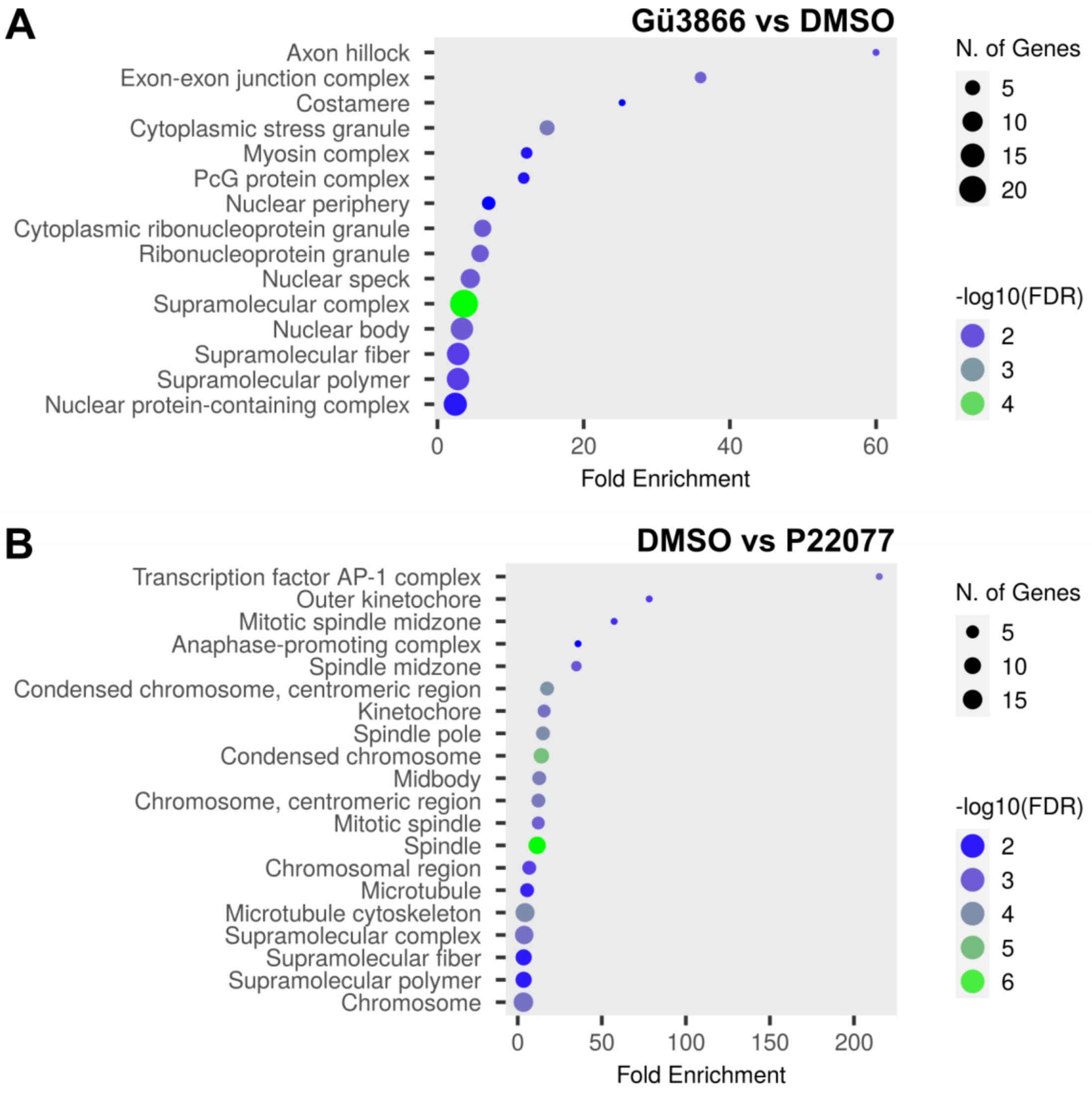

Figure 16 | GO assessment of USP7 degradation or inhibition in PFA ependymoma

*Cellular compartments GO terms of EPD210FH cells treated for 24 h with 100 µM Gü3866 (**A**) or 10 µM P22077 (**B**) based on the significantly differentially expressed proteins.*

5.5 USP7 changes the ubiquitination of EZHIP

After showing that USP7 regulates the abundance of EZHIP in PFA ependymoma, I wanted to confirm that USP7`s enzymatic activity and functionality as a de-ubiquitinase are necessary and responsible. First, I overexpressed myc-tagged USP7 WT, USP7 C223S or USP7 dTRAF (see **Figure 12A**) in HEK293 cells stably expressing EZHIP. In concurrence with the USP7 KD or inhibition experiments that reduced EZHIP levels, the increase of USP7 WT resulted in a detectable increase in EZHIP protein level (**Figure 17A**). In contrast, the catalytically dead C223S mutant of USP7 did not mediate increased EZHIP levels and the dTRAF truncate only increased EZHIP levels slightly. Next, I wanted to investigate how USP7 affects the ubiquitination of EZHIP. Thus, I used the NanoBRET assay to quantify the interaction strength of EZHIP and ubiquitin. As a positive control, I performed experiments in parallel looking at the interaction of ubiquitin and MDM2, which is known to be de-ubiquitinated by USP7. As expected, the addition of USP7 WT reduced the interaction of ubiquitin with both MDM2 and EZHIP (**Figure 17B**). The size of the effect was highly comparable and was relative to the amount of plasmid DNA used for the overexpression (corresponding to higher protein amounts). To rule out any effect mediated by the increased plasmid concentrations, I performed the experiments with an empty vector control. The addition of the empty vector did not affect the interaction of ubiquitin and EZHIP or MDM2. In contrast, the addition of the catalytically dead USP7 C223S led to a reduction of ubiquitin-EZHIP/MDM2 interaction, similar to the USP7 WT effect. This was unexpected, but could be explained by the catalytically dead USP7 binding to EZHIP and blocking the ubiquitination site, therefore preventing ubiquitination of EZHIP. To confirm the effect of increased USP7 on EZHIP-ubiquitin interaction, I wanted to investigate the effect of decreased USP7 levels. To get a good reduction in USP7 protein, I compared the previously used USP7 degrader Gü3866 to a new unpublished USP7 degrader Gü4095, with regards to their potential to reduce USP7 in HEK293 cells. Mechanistically, they recruit different E3 ligases to their target: Gü3866 recruits cereblon (CRBN), whereas Gü4095 recruits the von Hippel-Lindau (VHL) protein, which are both expressed in HEK293 cells (data not shown). After 24 h, Gü4095 had reduced USP7 completely at 25 µM and 3.125 µM, and almost completely at 0.391 µM, whereas Gü3866 was not able to completely abolish USP7 at any concentration (**Figure 17C**). Thus, I proceeded with Gü4095 and treated the cells during the NanoBRET assay for 24 h with 3.125 µM to achieve complete USP7 reduction. The treatment lead to increased EZHIP-ubiquitin and MDM2-ubiqutin interaction (**Figure R9D**). The increase in EZHIP-Ubiquitin interaction was slightly stronger with up to over 1.5-fold enrichment. Overall, this line of experiments confirmed that the enzymatic function of USP7 to deubiquitinate EZHIP is regulating EZHIPs stability.

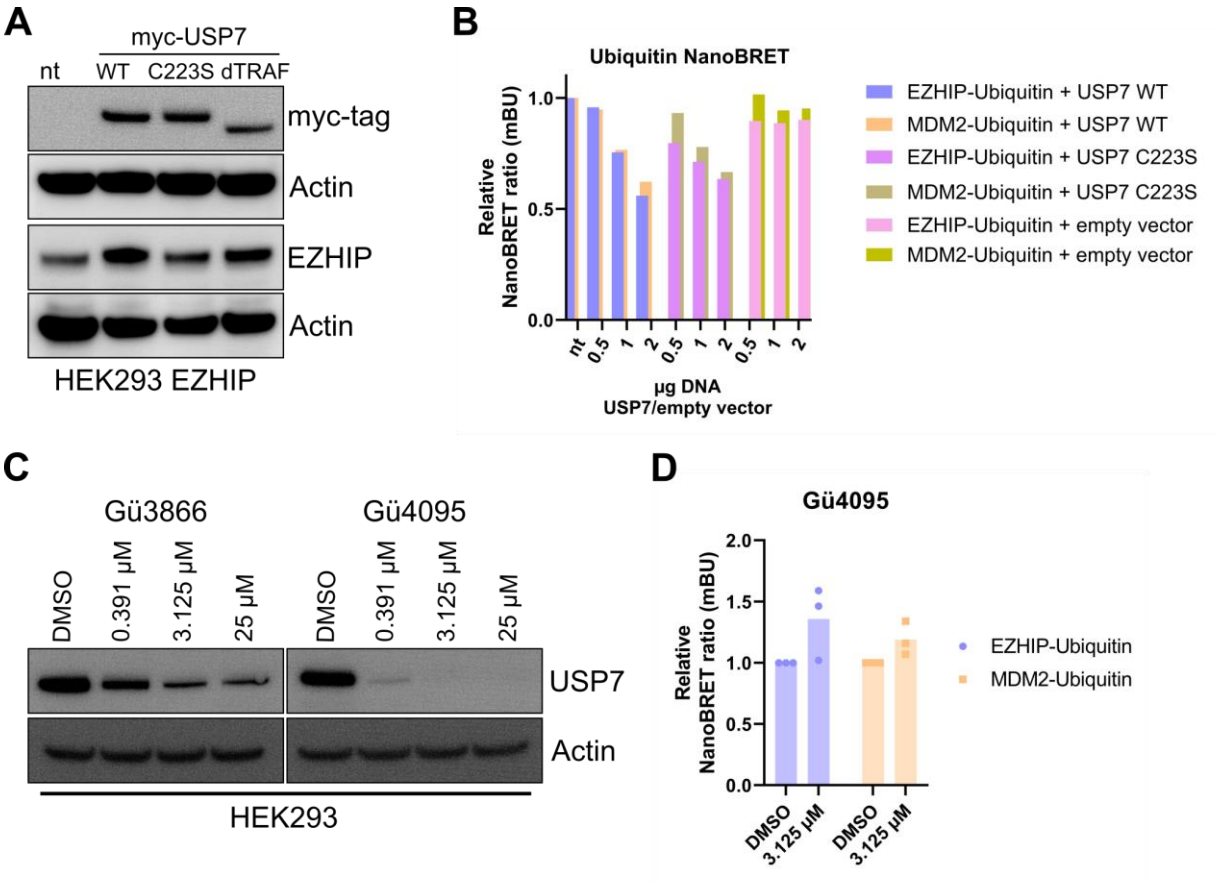

Figure 17 | The effect of USP7 on EZHIP ubiquitination

*(**A**) Western blot of HEK293 cells stably expressing EZHIP, transfected with or not (nt) myc-tagged USP7-WT, USP7-C223S or USP7-dTRAF for 24 h. Actin as loading control for every membrane. (**B**) NanoBRET interaction assay for EZHIP and Ubiquitin (purple, pink, light pink) or MDM2 and Ubiquitin (orange, mustard, yellow). Conditions with or without (nt) additional overexpression of 0.5, 1 or 2 µg of USP7- WT (purple, orange), USP7-C223S (pink, mustard) or empty vector (light pink; yellow). NanoBRET ratios are shown relative to the EZHIP-Ubiquitin or MDM2-Ubiquitin nt condition. Data is from technical replicates (n=3). (**C**) Western blot for USP7 of HEK293 cells treated with the USP7 degraders Gü3866 or Gü4095 at the indicated concentrations or with equal DMSO for 24 h. Actin as loading control. (**D**) NanoBRET interaction assay for EZHIP and ubiquitin or MDM2 and ubiquitin. Cell were treated for 24 h with 3.125 µM Gü4095 or equal DMSO before readout. Data is from three independent biological experiments.*

5.6 EZHIPs stability is mediated by its lysine residues

Subsequently, I focused on a deeper understanding of the protein-protein interaction between EZHIP and USP7. Apart from the highly conserved region around the H3K27M-mimicking M406 in the EZHIP protein, structure and function of most other parts of EZHIP are unknown and difficult to predict [5]. EZHIP contains six lysine residues (Lys; K) which are distributed across the entire protein: K9, K12, K127, K140, K149, K161 (**Figure 18A**). As lysine residues are the most likely points of ubiquitination, and the main point of USP7-mediated deubiquitination [247], I was wondering which and how many of the lysines were mediating the stability of EZHIP. To test each of these sites, I created six EZHIP constructs carrying single point lysine-to-arginine missense mutations, one construct harboring a mutation in every second lysine (EZHIP-3K: K9R, K127R, K149R) and one with all six (EZHIP-6K) lysine-to-arginine mutations. Upon overexpression in HEK293 cells, none of the single lysine mutations had an effect on EZHIP protein levels (**Figure 18B**). However, with both the EZHIP-3K and the EZHIP-6K mutants I could observe a substantial increase in EZHIP protein levels, suggesting that multiple lysines are responsible for the stability of EZHIP and are part of the EZHIP-3K construct. I thus created all possible combinations of lysine-to-arginine combinations with K9, K127 and K149. Upon overexpression in HEK293, none of the combinations resulted in increased protein levels, which led me to conclude that all three lysines of EZHIP-3K are involved in EZHIP stability (**Figure 18C**). To validate this, I treated HEK293 cells stably expressing either EZHIP-WT, EZHIP-3K or EZHIP-6K with cycloheximide (CHX), inhibiting the synthesis of new protein to follow the stability of existing protein over time. As can be seen in **Figure 18D**, EZHIP-WT was already diminished after 2 h of treatment. EZHIP-3K levels reduced after 2 h, but stayed stable over time, whereas EZHIP-6K stayed stable for 4 h, and was at the level of EZHIP-3K after 24 h. This showed that the mutation of the additional lysines in EZHIP-6K does make EZHIP more stable over time, so it is likely not solely the three lysines in EZHIP-3K that are conveying the stabilization. As localization changes can be caused by differential ubiquitination and could explain changed protein abundances on a Western blot, I investigated whether the introduction of the lysine-to-arginine mutations changed the intracellular location of EZHIP. I stained HEK293 cells stably expressing EZHIP-WT, EZHIP-3K or EZHIP-6K utilizing the proteins´ FLAG-tag. All three constructs localized to the nuclei of the cells. EZHIP-3K and EZHIP-6K showed a stronger signal intensity than EZHIP-WT, recapitulating the effect seen on Western blot (**Figure 18E**). Next, I wanted to see whether the lysine mutations changed the interaction of EZHIP and USP7. I utilized two different assays: the NanoBRET interaction assay (**Figure 18F**) and a co-IP followed by Western blot (**Figure 18G**). The EZHIP IP worked well for all three EZHIP constructs and reflected the amount of EZHIP present in the cells. Additionally, the lysine-to-arginine mutations did not influence the capability to bind to EZH2. All three EZHIP constructs showed a clear co-IP signal for USP7. EZHIP-3K and EZHIP-6K pulled down more total USP7, but less in comparison to the precipitated EZHIP. Additionally, even though the EZHIP levels are comparable between them, EZHIP-3K seemed to co-IP more USP7 than EZHIP-6K. Because co-IPs with a Western blot readout are semiquantitative, this trend could not be quantified. Thus, I additionally used the NanoBRET assay and could indeed detect a significant reduction of EZHIP-USP7 interaction strength for EZHIP-3K and even more for EZHIP-6K, validating the impression from the Western blot. Overall, I could thus show that the interaction between USP7 and EZHIP, physically and functionally, is mediated by EZHIP´s lysine residues.

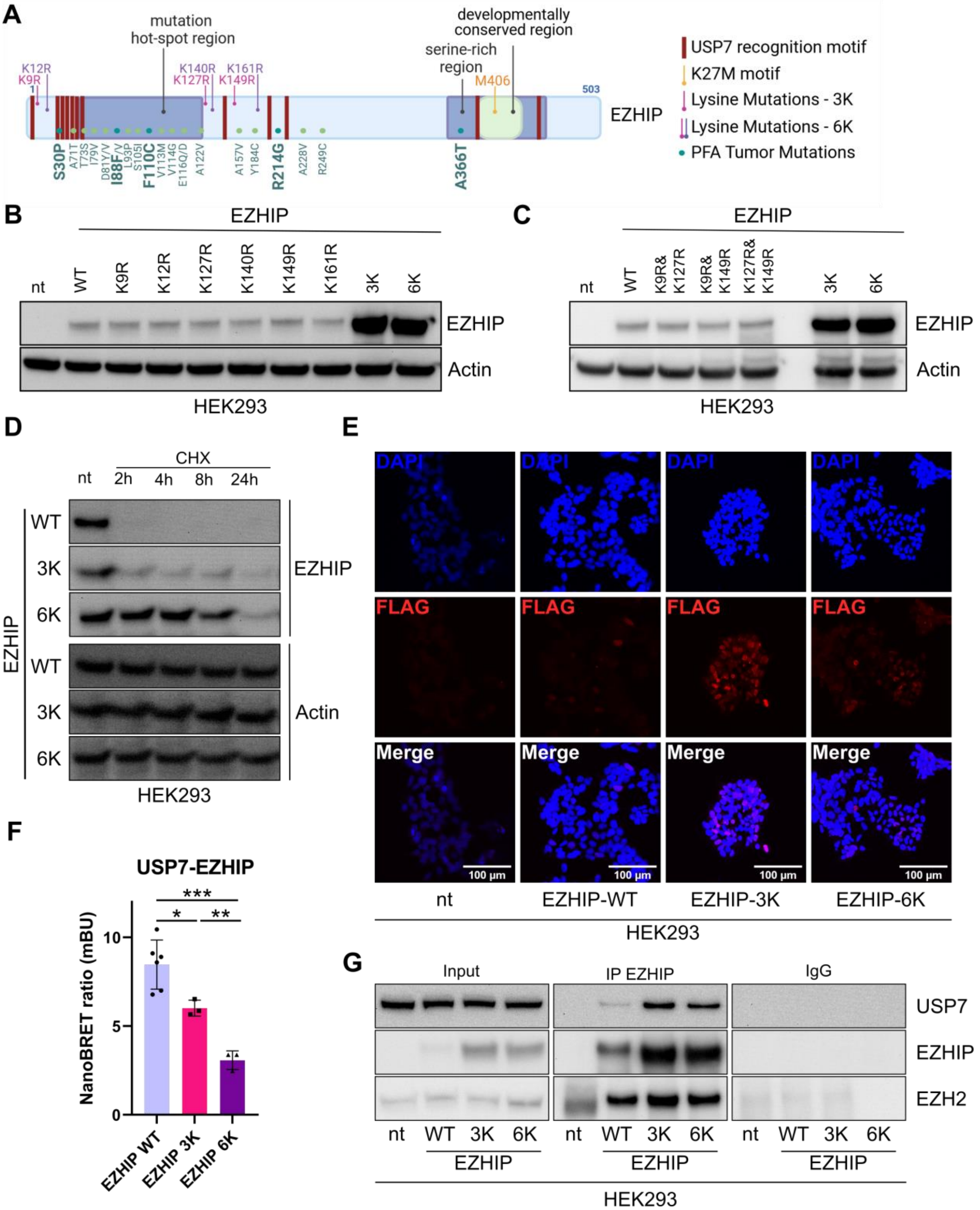

Figure 18 | Lysines mediate EZHIP stability

*(**A**) Schematic structure of EZHIP. Highlighted are the USP7 recognitions motifs predicted by Mechnetor (red) and the K27M mimicking M406 residue (yellow). PFA tumor mutations are in green with the 5 mutations used later in bold. The six lysines are marked, with the three mutated in the 3K construct in pink, and the additional three for the 6K construct in purple. (**B**) Western blot for EZHIP of the different K-R mutations, EZHIP wildtype (WT), EZHIP-3K and EZHIP-6K in HEK293. Actin as loading control. (**C**) Western blot for EZHIP of the different 2x K-R combinations within the EZHIP-3K construct, EZHIP WT, EZHIP-3K and EZHIP 6K. Actin as loading control. (**D**) Western blot of HEK293 expressing EZHIP WT, EZHIP-3K or EZHIP-6K treated or not with 1 mg/ml Cycloheximide (CHX) for the indicated times. Actin as loading control. (**E**) Immunofluorescence of HEK293 cells stably expressing EZHIP-WT, EZHIP-3K or EZHIP-6K. Staining for DAPI (blue) and FLAG-tag (red). Scale bars are 100 µm.(**F**) NanoBRET interaction assay of USP7 and EZHIP-WT, EZHIP-3K, or EZHIP-6K. Replicate values from minimum 3 individual experiments, mean and SEM are shown. Two-tailed t-test was performed. * shows P-value <0.05, ** indicates p<0.01 and *** p<0.001 (**G**) Western blot after co-IP of EZHIP with USP7 and EZH2 in HEK293 cells expressing (or not; nt) EZHIP-WT, EZHIP-3K or EZHIP-6K.*

5.7 EZHIP tumor mutations do not affect its interaction with USP7

Somatic EZHIP missense mutations have been described in 9.4% of PFA patients [153]. Tumors always carry only one mutation, and the majority of them is located towards the N-terminus of the protein (**Figure 18A**; green). However, the function or role of these EZHIP mutations has not been uncovered yet. As shown above, the TRAF-like domain of USP7, which has known patterns of recognizing its targets, is involved in the interaction with EZHIP (**Figure 12B + Figure 17A**). I observed that most of the predicted USP7 TRAF-like domain recognition sites on EZHIP (see Chapter 5.3) were close to a tumor mutation locus. This sparked the hypothesis that the mutations found in patients could influence the interaction of EZHIP with USP7, thereby potentially increasing EZHIP stability and fostering tumor growth. To test this, I created five EZHIP overexpression constructs harboring different mutations identified in patient samples. The five mutations (S30P, I88F, F110C, R214G, A366T) were selected to cover different regions of the protein, including two mutations from the hotspot region and different amino acids affected (**Figure 18A**; dark green). Upon overexpression in HEK293 cells, three mutated EZHIP constructs (S30P, F110C, and R214G) showed a slight increase in protein expression levels compared to EZHIP-WT (**Figure 19A**). However, a NanoBRET assay did not reveal any quantifiable difference in interaction strength with USP7 between EZHIP-WT and the different mutated EZHIP proteins (**Figure 19B**). Therefore, I concluded that the PFA tumor mutations do not influence the interaction of EZHIP and USP7.

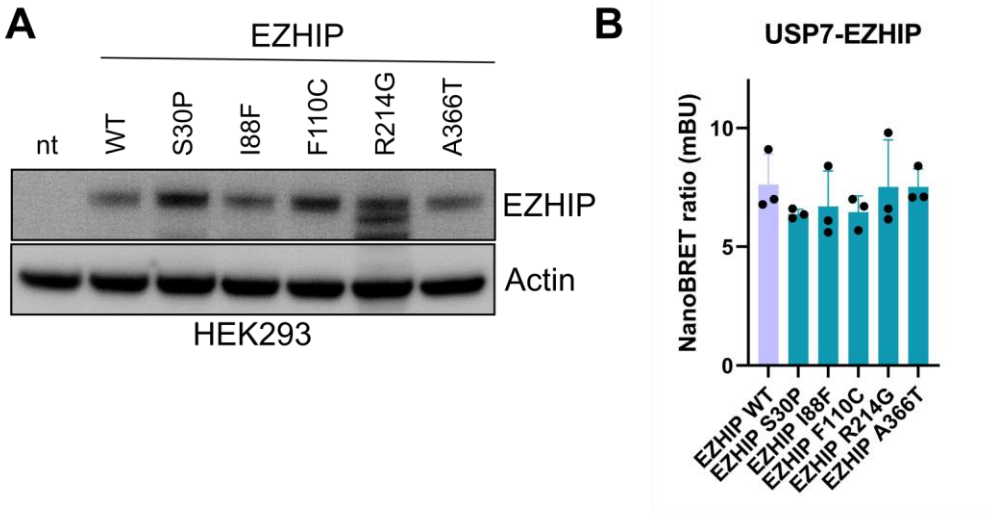

Figure 19 | EZHIP mutations do not affect its interaction with USP7

(A) Western blot for EZHIP of HEK293 overexpressing (or not; nt) EZHIP-WT or EZHIP with different tumor mutations as indicated. Actin as loading control. (B) NanoBRET interaction assay of USP7 and EZHIP-WT or EZHIP with indicated tumor mutations. Replicate values from 3 individual experiments, mean and SEM are shown.

5.8 PFA ependymoma are affected by a loss of USP7

As the aim of this project was to find new drug targets for PFA ependymoma, I wanted to query PFA ependymoma cells for a vulnerability for the loss of USP7 using a competitive drop-out assay. For this assay, I created lentiviral plasmids harboring GFP as fluorescent marker and either a shRNA or sgRNA in combination with Cas9. For both assay options, I prepared corresponding controls: a GFP empty vector as control for the shRNAs or a non-targeting sgRNA. PFA ependymoma cells were infected with these constructs aiming for about 50% infection rate. Using flow cytometry, I then monitored the abundance of GFP positive cells over time. If the targeting shRNAs or sgRNAs had an effect on cell viability or growth, I could observe the GFP positive population dilute out over time.

First, I used two shRNAs targeting USP7. I validated their ability to reduce USP7 protein levels in EPD210FH cells on Western blot, additionally quantifying the effect in relation to the expression of GFP to normalize for the infection rate in the tested population (**Figure 20A**). Both shRNAs reduced the abundance of the infected cells to under 50% within 15 days, whereas the empty GFP construct control stayed stable over time, indicating a susceptibility of PFA ependymoma cells to a loss of USP7 (**Figure 20B**).

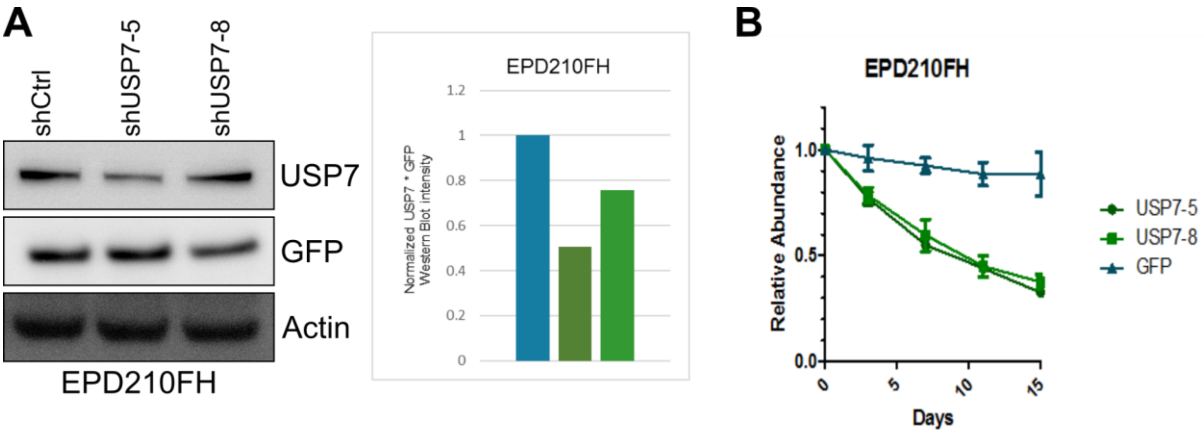

Figure 20 | USP7 KD affects survival of PFA ependymoma cells

*(**A**) Western blot for USP7. GFP and Actin (left panel) of EPD210FH cells expressing a control shRNA (shCtrl) or USP7-targeting shRNAs (shUSP7-5 and shUSP7-8). Quantification of the USP7 signal in relation to GFP normalized to Actin (right panel). (**B**) Competitive dropout assay in EPD210FH. Genetic (RNA interference) targeting of USP7 (green) with multiple shRNAs leads to a reduced growth over time. Normalized data represents mean and SEM of n=2 individual experiments.*

However, the assay was unstable in handling and shRNAs only interfere on the RNA level. Even though the hypothesis based on the discovered mechanisms of USP7 and EZHIP is focused on the protein level, I decided to switch to a CRISPR/Cas9-based system, interfering with genes on the DNA level.

Additionally, I included sgRNAs targeting EZHIP to be able to compare the effect on PFA ependymoma viability, which had never been published in such detail before. I designed multiple sgRNAs per target, tested them on for their ability to reduce target protein in PFA ependymoma cell population, and decided for the best three sgRNAs per target. A validation of them reducing protein levels on Western blot comparing them to the effect of a non-targeting sgRNA (sgNT) in EPD210FH cells is shown (**Figure 21A +B**). The sgNT infected EPD210FH and BT214 cells were stable in the population over time in the competitive drop-out assay. In EPD210FH, their relative abundance reduced to 81%, in BT214 their abundance increased over time. The effect in the EPD210FH could be justified by replicative stress that the activity of the CRISPR machinery and the overexpression in general puts on the cells. In my observation, EPD210FH are more sensitive to such stressors. The USP7-targeting sgRNAs reduced the abundance of infected EPD210FH and BT214 cells. In EPD210FH cells, the effect of all three sgRNAs was similar, reducing the relative abundance to 30-47%. In the BT214, the effects were less pronounced, with endpoint reduction as low as 70%, and the effect took longer to manifest. However, the change compared to the sgRNA is still clear (**Figure 21C**). Both EPD210FH and BT214 reacted similarly to the infection with EZHIP-targeting sgRNAs. Again, the three sgRNAs affected the EPD210FH cells in a highly comparable way, whereas the spread between the sgRNAs in the BT214 was more. sgEZHIP-6 showed a comparatively early effect, whereas sgEZHIP-3 took longer to act (**Figure 21D**). Overall though, the response of the PFA ependymoma cells to the infection with sgRNAs targeting USP7 or EZHIP followed a similar dynamic, hinting toward similar effector mechanisms and supporting the hypothesis that USP7 affects PFA ependymoma cells via EZHIP.

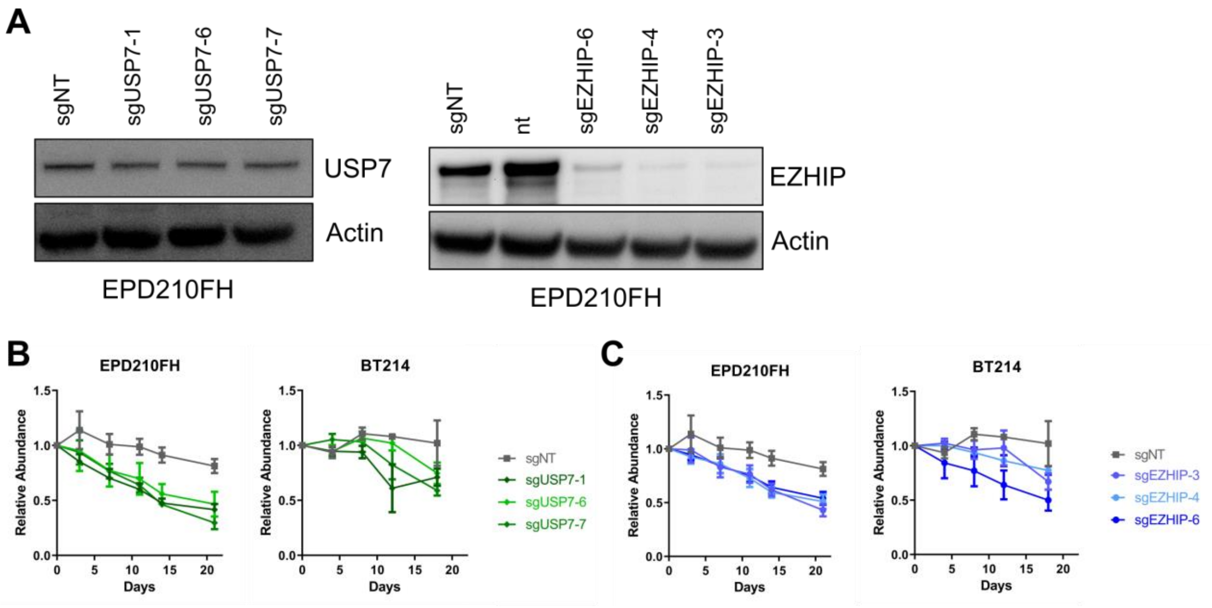

Figure 21 | Genetic targeting of USP7 or EZHIP affects PFA ependymoma

*(**A**) Western blots for USP7 (left panel) or EZHIP (right panel) in EPD210FH infected with sgRNAs targeting USP7, EZHIP or non-targeting (sgNT). (**B+C**) Competitive dropout assay in EPD210FH and BT214. Genetic (CRISPR/Cas9) targeting of USP7 (**B**; green) or EZHIP (**C**; blue) with multiple sgRNAs or non-targeting control (sgNT; grey) over time. Normalized data represents mean and SEM of n=3 individual experiments.*

5.9 USP7 as pharmacological target in PFA ependymoma

Since PFA ependymoma cells showed a susceptibility for targeting USP7 genetically in the previous experiments, I wanted to test whether PFA ependymomas are also vulnerable to pharmacological targeting of USP7.

5.9.1 Targeting USP7 pharmacologically– *in vitro*

In order to perform viability assessments *in vitro*, I had to optimize the seeding density for ependymoma cells in a 96-well format. The aim was to find a density that was high enough to allow the cells to grow, but not too dense so the untreated cells would not be confluent before or at the end of the time period, as this would lead to a plateau in growth and measured viability (metabolic readout via cell titer glo). I performed a growth curve analysis in two ependymoma cell lines: The ST-ZFTA cell line EP1NS and the PFA ependymoma cell line EPD210FH. I seeded the cells in ten different densities from 500 cells/well to 20 000 cells/well and measured the cell viability every 24 h for ten days, followed by three measurements after 48 h each with the last measurement after 14 days (336 hours) (**Figure 22A+B**). At the last time point, both cell lines were not confluent only when seeded at 500-2000 cells/well. However, according to the viability measurements, the cell growth did not plateau yet, which is likely due to the cells overgrowing. To find the best seeding density for the planned 72 h and 144 h treatments, I checked which densities were in a good growth phase until these time points. For EP1NS cells, a minimum of 3000 cells/well was needed for proper growth, whereas EPD210FH needed a minimum of 5000 cells/well. As ependymoma cells in general grow slowly, I decided to proceed with the lower density of 5000 cells/well to be able perform more experiments with fewer cells.

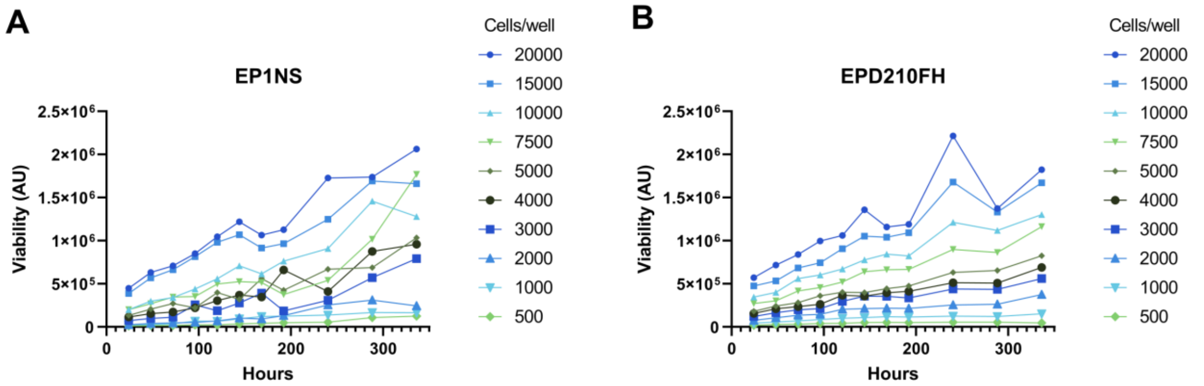

Figure 22 | Growth curves of ependymoma cells

*Growth curves determined by metabolic readout for EP1NS (**A**) and EPD210FH (**B**) cells in a 96-well format with the indicated seeding densities at start. Data represents technical triplicates.*

For targeting USP7, I used the variety of small molecular inhibitors. I compared all commercially available inhibitors based on reported IC50 values, specificity for USP7, mechanism of action (covalent binding, targeted pockets) and previously reported *in vivo* data (see chapter 1.5.5). Based on these parameters, I chose the following seven USP7 inhibitors as most promising and multi-mechanistic: P22077, P005091, GNE6776, FT671, USP7-Inhibitor 1 (USP7-IN-1), HBX41108 and XL177A. XL177A was not part of the initial selection, but was added at a later stage, which is why less experiments were performed with this inhibitor. Firstly, I treated the PFA ependymoma cell line EPD210FH and the ST-ZFTA cell line EP1NS with the six USP7 inhibitors for 144 h, including a change in media and drug after

72 h. I chose the range of concentrations based on previously reported IC50 values, either applying a 1:2 dilution or a 1:5 dilution range starting at 100 µM. Since my project was focused on PFA ependymoma, I performed the experiments for the EPD210FH in biological triplicate, whereas for the EP1NS, which I used as a comparison, only technical triplicates are shown (**Figure 23**). Interestingly, the response of the two cell lines to the different USP7 inhibitors was not completely uniform. The treatments with FT671 resonated slightly more strongly with the EP1NS cells, whilst HBX41108, USP7-IN-1, and GNE6776 affected either cell line to a comparable, but low, extend. On the other hand, P22077 and P005091 reduced the viability of EPD210FH to a much greater extend than in EP1NS (**Table 14**). Since FT671, P22077 and P005091 showed promising low micromolar IC50 values in EPD210FH nevertheless, I decided to continue testing them in more PFA ependymoma cell lines.

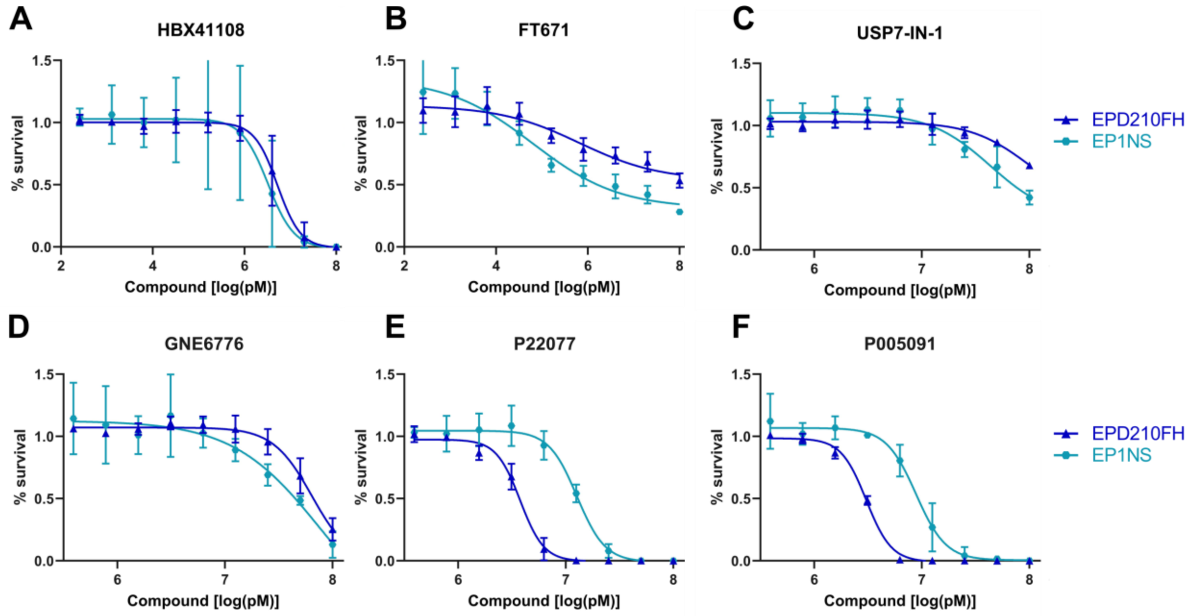

Figure 23 | Survival comparison of EPD210FH and EP1NS cells upon USP7 inhibition

*EPD210FH (blue) and EP1NS (turquoise) cells were treated for 144 h with the indicated concentrations of the USP7 inhibitors HBX41108 (**A**), FT671 (**B**), USP7-IN-1 (**C**), GNE6776 (**D**), P22077 (**E**) or P005091 (**F**). Survival rates are normalized to DMSO control. Data represents three biological replicates, mean and SEM are shown.*

In order to understand whether USP7 inhibitors are targeting PFA ependymoma cell proliferation, I proceeded to measure the effect of FT671, P22077 and P005091 on the viability of four different PFA ependymoma cell lines. As representation of healthy brain cells, I compared the effect to human astrocytes (**Figure 24A**). All four PFA ependymoma cell lines were more sensitive to the three USP7 inhibitors than the human astrocytes. The BT232 cell line, with an IC50 value of 110 nM, was the most sensitive to FT671 inhibition. It is noteworthy that FT671 did not reduce the viability of any PFA ependymoma cell line below 20%. In contrast, P005091 and P22077 abolished live cells of all tested cell lines with the higher applied concentrations. For both, the VBT420 PFA ependymoma cell line was clearly the most sensitive cell line with IC50 values of 1.6 µM (P005091) and 1.8 µM (P22077), which is over 6-times more sensitive than the human astrocytes (IC50 P005091 12µM, IC50 P22077 12.5 µM) creating a reasonable therapeutic window (**Table 14**). I additionally tested the USP7 inhibitor XL177A in EPD210FH and BT214 cells, which was less potent than the previously tested inhibitors (**Figure 24C**).

One reason could be the reported P53-mediated effect of XL177A, whilst I was never able to detect P53 signaling in these two PFA ependymoma models [333].

Since pediatric DMGs are also driven by epigenetic disruptions, they are often compared to PFA ependymoma. In DMGs, either the occurrence of the K27M oncohistone or an aberrant EZHIP expression lead to the inhibition of the PRC2 complex and the consecutive loss of H3K27me3 marks. Thus, I was curious to see whether DMG cells, driven by EZHIP expression especially, are also sensitive to USP7 inhibitors. I tested two DMG cell lines, the B193 line with high EZHIP expression and the R059 line which expresses the oncohistone K27M. Interestingly, both DMG cell lines were more sensitive to FT671 treatment than the ependymoma cell lines and only B193 reacted with a complete loss of viability to higher concentrations of FT671 (**Figure 24B**). Also, the EZHIP expressing B193 cell line was clearly more sensitive than the K27M-driven R059 line, which would align with the lack of a mechanistical link between K27M and USP7 so far. However, the R059 data only represents technical replicates. For the P005091 and P22077 treatments, the two DMG cell lines were less affected than PFA ependymoma cells, confirming the high sensitivity of PFA ependymoma cell lines for those inhibitors.

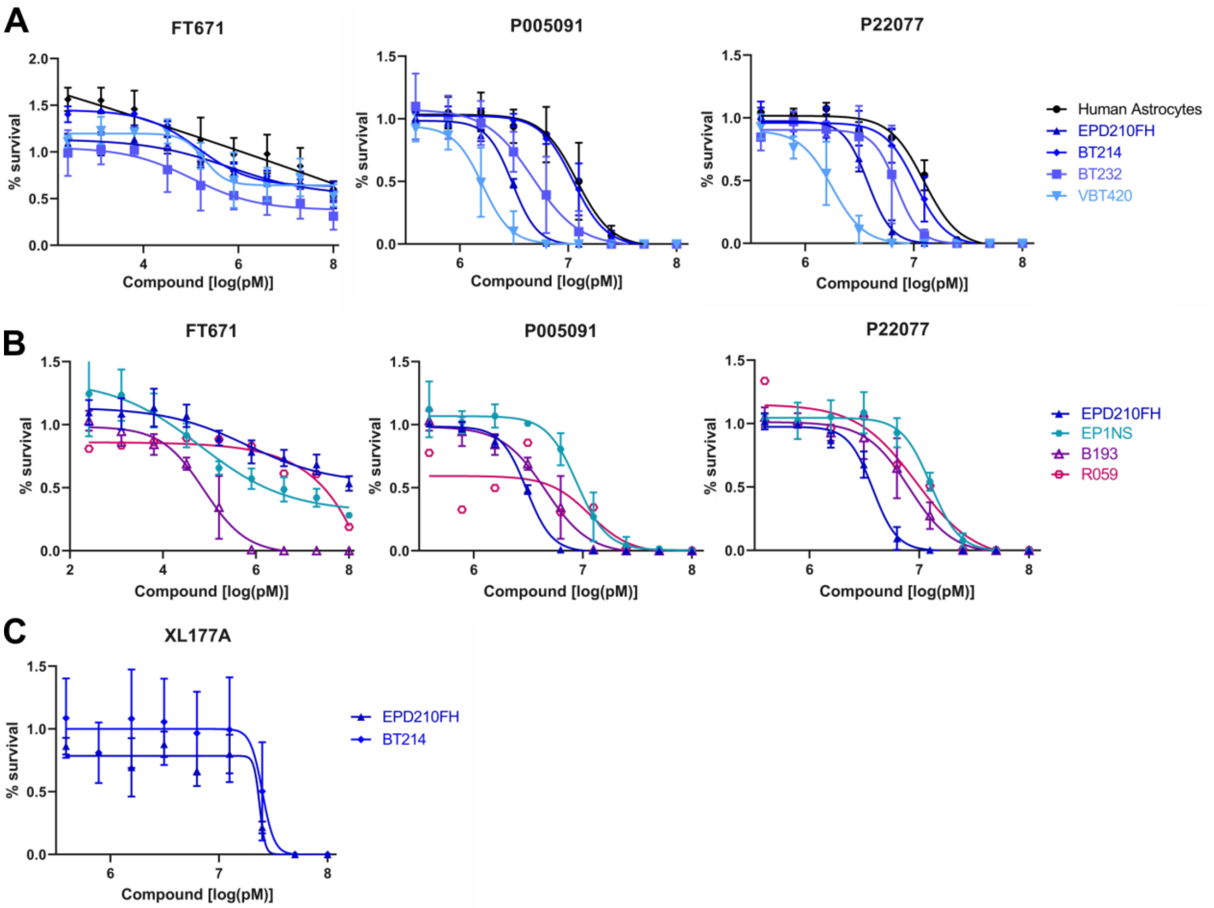

Figure 24 | The effect of USP7 inhibitors on ependymoma and DMG cells

*(**A**) Dose-responses of human astrocytes, EPD210FH, BT214, BT232 and VBT420 cells treated with the USP7 inhibitors FT671, P005091 or P22077 at the indicated concentrations for 144 h. Survival is relative to DMSO control. Data represents mean and SEM from three independent experiments. (**B**) Dose-responses of EPD210FH, EP1NS, B193 and R059 cells treated with the USP7 inhibitors FT671, P005091 or P22077 at the indicated concentrations for 144 h. Survival is relative to DMSO control. Data represents mean and SEM from three independent experiments (EPD210FH, EP1NS, B193) or three technical replicates (R059). (**C**) Dose-responses of EPD210FH and BT214 cells treated with the USP7 inhibitor XL177A at the indicated concentrations for 144 h. Survival is relative to DMSO control. Data represents mean and SEM from two independent experiments.*

This sensitivity can be underscored by the visual impression of the PFA ependymoma cells upon USP7 inhibitor treatment as presented in **Figure 25**. Brightfield images of P22077 (**Figure 25A**) or P005091 (**Figure 25B**) treated EPD210FH or BT214 cells showed that the effects of the inhibitors are already present after 24 h, but are much stronger at the end of the treatment after 144 h. Detaching of cells also showed that the cells died from the treatment and not just arrested in growth.

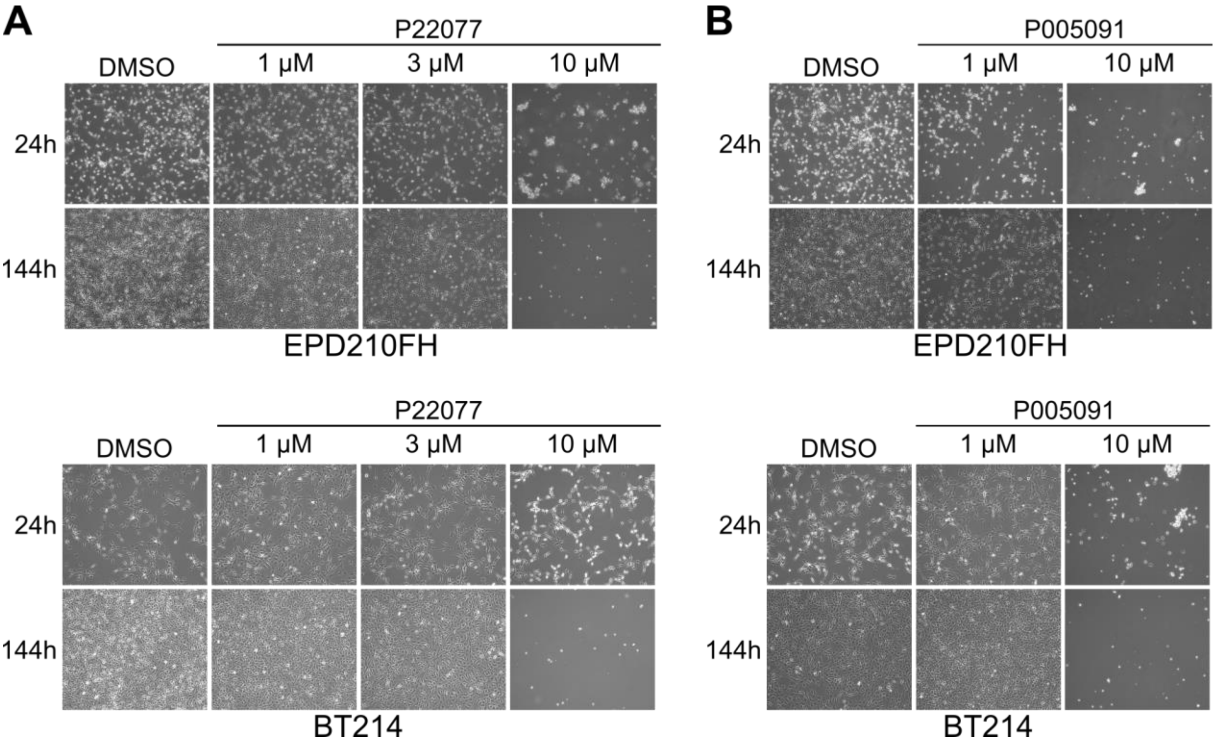

Figure 25 | The response of PFA ependymoma to USP7 inhibitors

*Brightfield images of EPD210FH (upper panel) or BT214 (lower panel) after treatment with P22077 (**A**) or P005091 (**B**) at the indicated concentrations or corresponding DMSO control for 24 h or 144h. Magnification 20x.*

Furthermore, I wanted to test the effects of the two USP7 degraders Gü3866 and Gü4095 on the viability of PFA ependymoma cells. However, the effects were smaller than expected. Gü3866 reduced the viability of EPD210FH and VBT420 cells to a minimum of about 60% at the highest concentration. The two DMG cell lines showed almost no reduction in viability, but even increased viability at the lower doses, hinting that Gü3866 is not specifically ineffective in killing PFA ependymoma cells (**Figure 26A**). The second VHL-recruiting PROTAC, Gü4095, also increased viability in the PFA ependymoma cell line BT214, but at the same time lowered it to about 50% at higher doses (**Figure 26B**). EPD210FH cells were affected by both USP7 degraders at comparable levels. However, the effect of Gü4095 showed more fluctuations resulting in high standard deviations. Even though experiments had proven the effectiveness of the degraders to reduce USP7 and EZHIP levels, the observed on the viability of PFA ependymoma cells after USP7 degrader treatment was little, especially compared to the effect of the USP7 inhibitors. One explanation could be off-target effects of the USP7 inhibitors affecting PFA ependymoma viability. Another possibility for the small effect of the dergaders might be that the reduction of USP7 left enough residual protein to keep minimal functions ongoing, which wouldn't affect the cell viability as much as the inhibition of all USP7 enzymes by the small molecules. To test this, I combined a fixed Gü3866 concentration of 50 µM (which alone did not affect cell viability much) with the concentration range of P22077 or P005091. In both the EPD210FH and VBT420 PFA ependymoma cells, combination of the degrader with the inhibitors reduced cell viability drastically. Even at the lowest small molecule concentrations that had almost no effect alone, viability of the PFA ependymoma cell was now reduced to almost 50% (**Figure 26C**). This data could be interpreted such that the residual USP7 protein left under the degrader treatment needs lower small molecule amounts to be completely inhibited, which means lower USP7 inhibitor levels can cause more harm in the cells.

Taken together, the above line of *in vitro* treatments could show that USP7 inhibitors are effective in targeting PFA ependymoma cells *in vitro*. Additionally, the discrepancy to the non-effectiveness of USP7 inhibitors in human astrocytes provides a therapeutic opportunity.

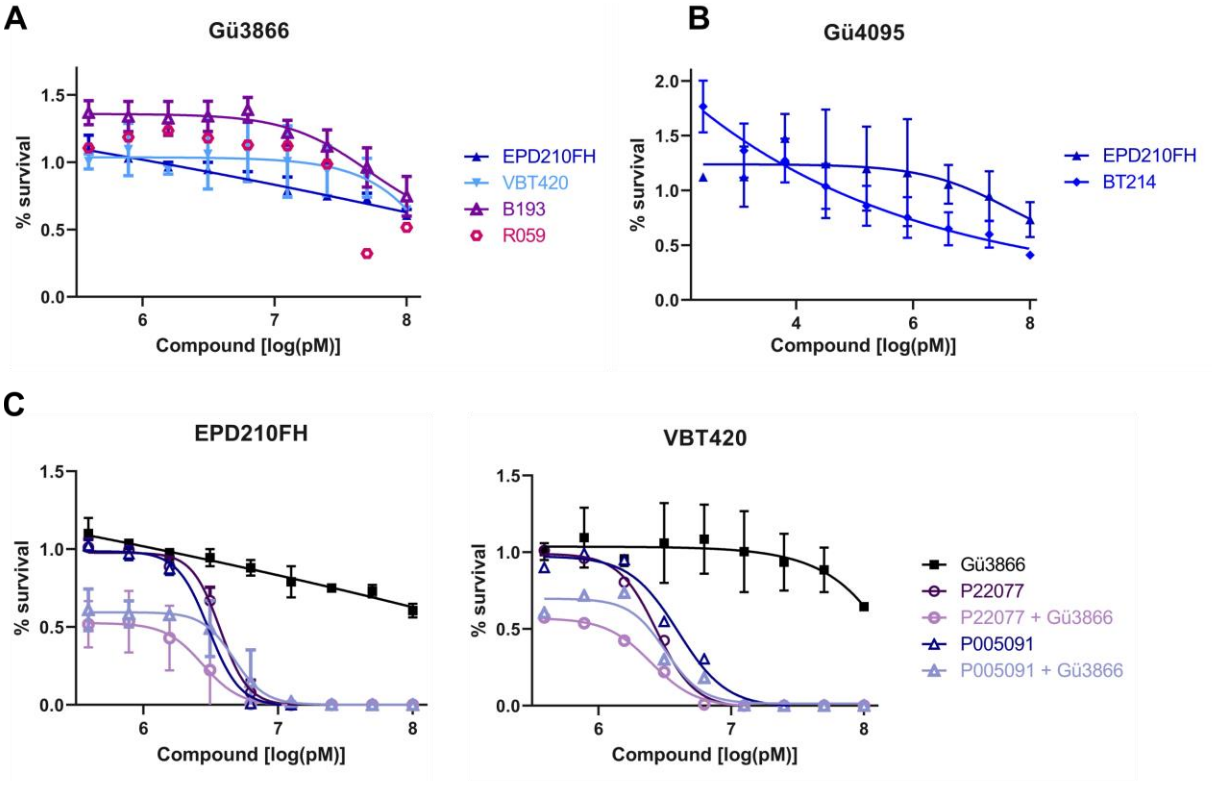

Figure 26 | The effect of USP7 degradation on PFA ependymoma

*(**A**) Dose-responses of EPD210FH, VBT420, B193 and R059 cells treated with the USP7 degrader Gü3866 at the indicated concentrations for 144 h. Survival is relative to DMSO control. Data represents mean and SEM from three independent experiments (EPD210FH; B193, VBT420) or three technical replicates (R059). (**B**) Dose-responses of EPD210FH and BT214 cells treated with the USP7 degrader Gü4095 at the indicated concentrations for 144 h. Survival is relative to DMSO control. Data represents mean and SEM from three independent experiments. (**C**) Dose-responses of EPD210FH (left panel) or VBT420 (right panel) cell treated with Gü3866, P22077 or P005091 at the indicated concentrations alone or together with 50 µM Gü3866. Data represents mean and SEM from three independent experiments (Gü3866) or three technical replicates.*

Table 14 | IC50 values of USP7 inhibitors in different cell lines

IC50 values of USP7 inhibitors of different cell lines in µM. NA refers to an IC50 out of range.

IC50 [µM]	Human Astrocytes	EPD210FH	BT214	BT232	VBT420	B193	R059	EP1NS
P22077	11.92	3.82	10.53	7.01	1.72	8.09	8.68	12.2
P005091	12.08	3.04	11.22	4.65	1.62	4.51	12.25	8.9
FT671	NA	10.03	0.2	0.27	0.2	174.25	56.1	0.22
HBX41108		5.26						3.2
USP7-IN-1		NA						NA
GNE6776		NA						NA
XL177A		23.9	25.02					

5.9.2 Targeting USP7 pharmacologically- *in vivo*

In vitro drug testing is a great tool to estimate the effectiveness of certain pharmaceuticals. However, the results cannot be translated into the clinics easily. One main reason is the lack of intra- and inter-cellular complexity in the cell culture model system. Cell lines are often clonally selected or at least highly synchronized and genetically similar, whereas tumors are characterized by multiclonal growth [44, 361-363]. Additionally, brain tumors are surrounded by a network of different cell types like neurons, the stroma, immune and blood cells. All these interactions can influence the reaction of the cancer cells to drugs [106, 364]. Another important difference when treating brain tumors is the blood brain barrier (BBB), a multi-cell organization which prevents substances from entering the brain. Many drugs can either not pass this BBB, are actively exported back to the blood stream at a high rate immediately or can only enter at low concentrations. To address these problems, drugs need to be tested in additional model systems, such as organoids or animals. Since my group has great expertise in patient-derived orthotopic xenografts (PDOX), where human tumor cells are injected into immunocompromised mice at their original location, I decided to use this animal model to test the effect of USP7 inhibitors on PFA ependymoma cells in the cerebellum.

To monitor tumor growth during treatment, tumor volume can be measured using luciferase-labeled cells, whose signal can be quantified after i.p. injection of luciferin even through the skull. To be able to use this strategy, I had to label PFA ependymoma PDOX cells first, as the group´s standard PDOX establishment protocol does not include this step (see Methods 4.2.29). I chose to label the BT232 PDOX model (BT232-Luc), because I had performed *in vitro* testing with the corresponding BT232 cell line, which had been previously passaged through mice, and which showed promising results (**Figure 24A**).

Table 15 | Blood-brain barrier penetration scores

BBB penetration scores for the USP7 inhibitors FT671, P005091 and P20077 based on different prediction models extracted via www.unite-bdpp.dkfz.de [7].

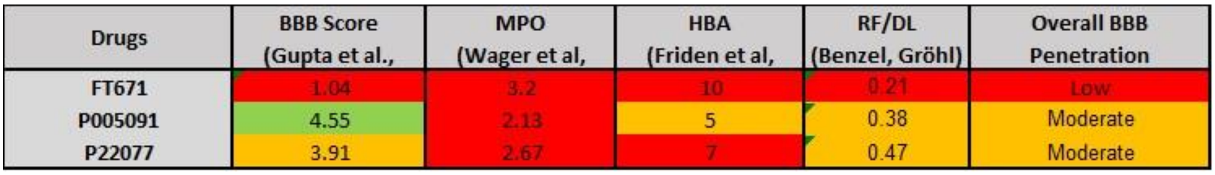

Drugs	BBB Score (Gupta et al.,	MPO (Wager et al,	HBA (Friden et al,	RF/DL (Benzel, Gröhl)	Overall BBB Penetration
FT671	1.04	3.2	10	0.21	Low
P005091	4.55	2.13	5	0.38	Moderate
P22077	3.91	2.67	7	0.47	Moderate

For the *in vivo* testing of USP7 inhibitors, I selected P22077 and P005091 for two reasons: they were the most potent inhibitors in the PFA ependymoma cells *in vitro* and there was data about previous *in vivo* experiments available. For P005091, one publication reported its successful use in an orthotopic glioblastoma model, which indicated that the drug can cross the BBB [325]. However, I wanted to assure that P22077 and P005091 are likely to cross BBB. Thus, I compared predictions for BBB penetrance from several prediction tools [7]. The overall prediction for P005091 and P22077 to penetrate the BBB was moderate, whereas FT761 only scored a low likelihood (**Table 15)**.

Since literature reported treatments with P005091 and P22077 in a range of 5 mg/kg to 25 mg/kg or 30 mg/kg respectively (see chapter 1.5.5), a toxicity test in healthy NSG mice was performed. For this, concentrations of 10 (P22077 only), 15 or 20 mg/kg, applied i.p. daily (P22077) or twice daily (P005091), in a 5-days-on followed by 2-days-off schedule were used and compared to vehicle injections. During the treatment period, the weight of the mice was monitored three times per week and a weight reduction to 80% of their starting weight was the drop-out criteria. Mice treated with 15 mg/kg or 20 mg/kg with either USP7 inhibitors showed symptoms of toxicity like bloated abdomen and weight reduction. Mice treated with 10 mg/kg P22077 did not show any symptoms of toxicity after 10 days and were maintaining their weight (**Figure 27B**). However, since the treatment study was estimated to require treatments for more than one month, I decided to use 10 mg/kg for both P22077 and P005091 (**Figure 27A)**.

Using a stereotactic frame, 40 immunocompromised NSG mice were intracranially injected with 2x10^6 BT232-Luc cells. Starting two weeks after injection, their luciferase signal was monitored weekly. At four weeks after injection, 38/40 mice had signal over 2x10^6 p/s which led to their enrollment into the three treatment arms randomly: 12 animals were assigned into the vehicle group, 13 animals into the P005091 10 mg/kg and 13 animals into the P22077 10 mg/kg group. From this point on, the weight of the mice was monitored three times per week instead of weekly. As shown in **Figure 27C**, the average weight of mice dropped slightly after the start of the treatment, which is an expectable reaction to the stress of the treatment injections. The drop was stronger in the group treated with the USP7 inhibitors, but these mice still kept over 90% of their starting weight. After 40 days of treatment, almost all mice were back at their starting weight and continued to gain weight indicating a bearable amount of general toxicity and tumor burden for them. The luminescence signal of the mice was tracked weekly and no big difference between the development of tumor signal was observed between the vehicle and the inhibitor treated mice (**Figure 27D**). For all three groups, the luciferase signal increased steadily. During the first five weeks under treatment, the increase was substantial but was below 50x of their starting signal, but eventually resulted in a logarithmic increase of signal for almost all mice. This development also reflected in the survival data of the mice (**Figure 27E**), where no meaningful difference was detected between the groups. Mean survival was 88.3 days under treatment (33-126 days) and vehicle treated mice survived the longest with 99.1 days under treatment on average, which might be attributed to light toxicity effects of the drugs in the USP7 inhibitor treatment groups. In conclusion, even though they reduced viability of BT232 cells *in vitro*, the USP7 inhibitors P22077 and P005091 were not able to reduce tumor growth in the BT232 PFA ependymoma PDOX model. The reasons for this could be manifold, but one possibility is that the effective dosage was not reached in the tumors, which could be improved by synergystically combining drugs to lower their effective doses.

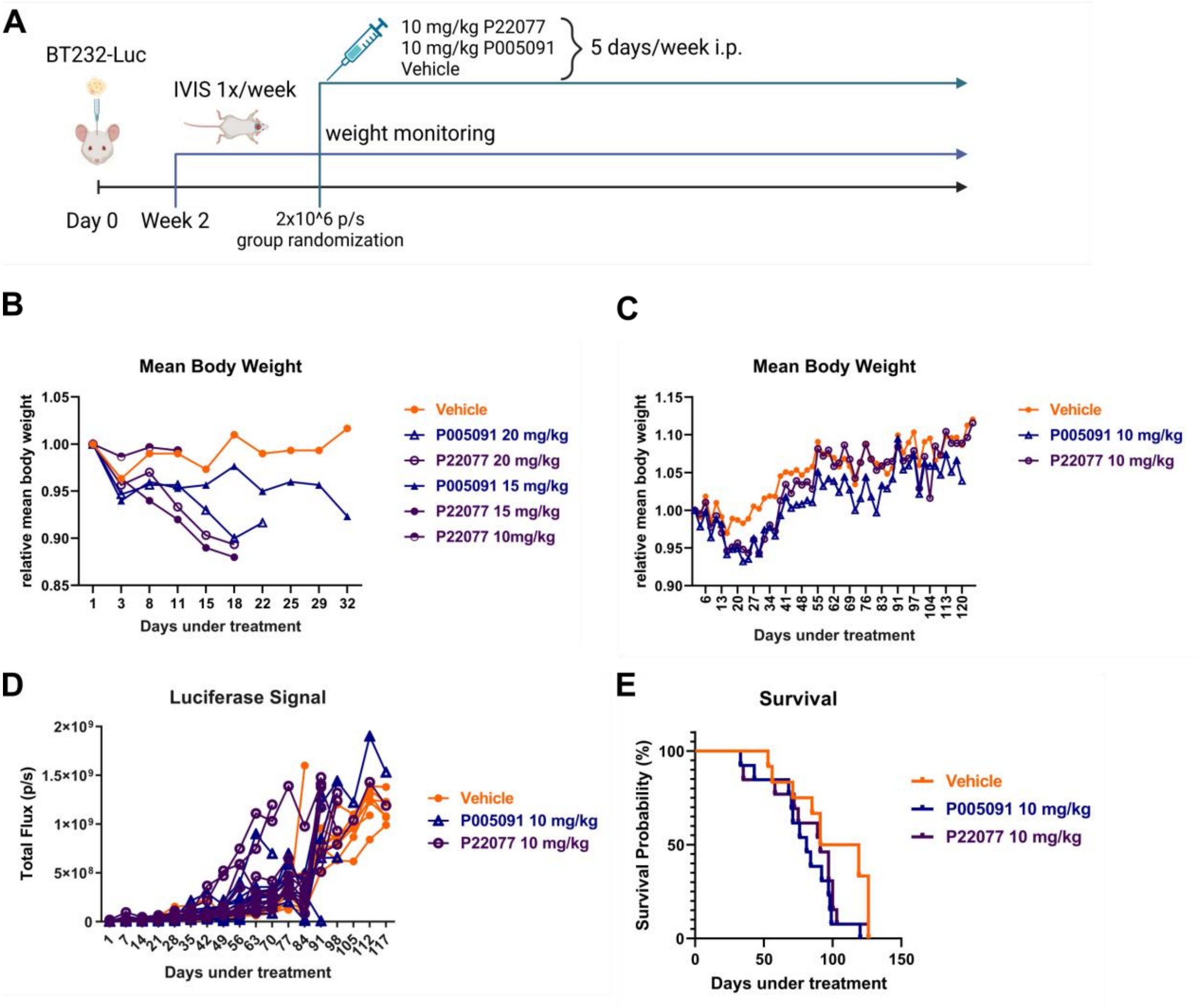

Figure 27 | In vivo treatment of BT232 PDOX with USP7 inhibitors

*(**A**) Schematic overview of the treatment plan: Luciferase labeled BT232 cells (BT232-Luc) were injected into NSG mice. From 2 week after injection, luciferase signal was measured weakly using the IVIS system. Once 38/40 tumors exceeded 2x10^6 p/s, all animals were randomized into treatment groups: 10 mg/kg P22077, 10 mg/kg P005091 or Vehicle, treated for 5 days/week i.p.. Weight was monitored three times per week after treatment start. (**B**) Relative mean bodyweight per treatment group of the toxicity assessment in healthy NSG mice. Group sizes n=3. (**C**) Relative mean bodyweight per treatment group. Group sizes n=13 (P005091 10 mg/kg, P22077 10 mg/kg) or n=12 (vehicle). (**D**) Total flux (p/s) luciferase signal of individual animals under treatment. Group sizes n=13 (P005091 10 mg/kg, P22077 10 mg/kg) or n=12 (vehicle). (**E**) Kaplan-Meier plot showing the survival probability of mice in the treatment groups. Group sizes n=13 (P005091 10 mg/kg, P22077 10 mg/kg) or n=12 (vehicle).*

5.10 BET inhibitors act synergistically with USP7 inhibitors in PFA ependymoma

Even though USP7 inhibitors achieved low micromolar IC50s in my *in vitro* studies in PFA ependymoma cells (chapter 5.9.1), these treatment doses can be difficult to achieve (pre-) clinically. I therefore aimed to identify synergistic drug combinations to allow the use of lower but still effective drug concentrations. The strategy was to perform a mid-throughput combination screen in the three PFA ependymoma cell lines EPD210FH, BT232 and BT214 in collaboration with the Clinical Cooperation Unit Pediatric Oncology at DKFZ, which is the home of the targeted drug screening unit (TDSU). The idea was to test the effect of a drug library alone or in combination with the IC25 concentration of the USP7 inhibitors P22077 or P005091. Here, it is important to use a USP7 inhibitor dose that achieves a survival inhibition of clearly less than 50%, to allow for the additional drugs to show their effect, which ideally should be more than additive. Since the screen was to be performed in a 384-well format as spheres for 72 h, I was not able to extract the IC25 from my previous treatment data. I thus performed an IC25 determination for 72 h as spheres in 96-well U-bottom plates. The difference between 384-well and 96-well drug response is negligible based on the TDSU previous experiences and is more feasible to perform by hand. In the EPD210FH cell line, the response to the USP7 inhibitors P22077 and P005091 was almost the same in this set-up as in the adherent, but longer treatment (**Figure 28**; **Table 14**). For the BT232 and BT214 cells, the spheroid conditions and shorter time under treatment resulted in lower treatment responses which were reflected in comparably high IC25 values (**Figure 28 A+B**). The IC25 values used for the screen were rounded and are shown in **Figure 28C**.

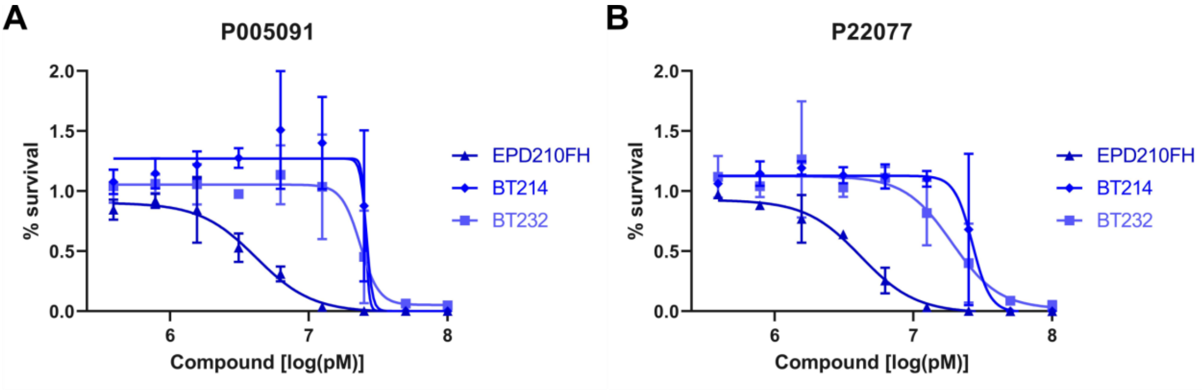

C

	EPD210FH	BT214	BT232
P005091	4.5 µM	25 µM	17.5 µM
P22077	3 µM	22 µM	15 µM

Figure 28 | IC25 determination of PFA ependymoma cells upon USP7 inhibitor treatment

*(**A+B**) Dose-response curves of EPD210FH, BT214 and BT232 upon P005091 (**A**) or P22077 (**B**) treatment in the indicated doses. Survival is relative to DMSO and data is from three independent experiments. (**C**) IC25 values determined from the dose-response curves, rounded and used for the USP7 inhibitor combination screen.*

Together with the TDSU, I used a mid-throughput 384-well sphere approach to perform the combination drug screen in the three PFA cell lines. I decided to test the effect of 102 drugs in a customized standard library which was based on their epigenetic library and contained a mix of FDA/EMA-approved and test compounds, some of which are in late clinical phases (**Supplementary Table 1**) alone or in combination with the IC25 dose of the USP7 inhibitors P22077 or P005091. All drugs were printed to the plates before addition of the cell suspension. The screen with the BT232 and BT214 cell line failed as they did not pass the QC criteria for the USP7 inhibitor single treatments and the positive control treatments with the strong apoptosis-inducer staurosporine. The reasons are not entirely resolved, but it seems that they were multifactorial including problems with the drug printer and the USP7 inhibitor handling, as the single drug treatments for the BT232 passed the QC. Therefore, I continued the analysis of the combination screen with only the EPD210FH cells (**Figure 29**). For each drug, the drug sensitivity score ($DSS_{asym)}$ was calculated in comparison to the DMSO control and staurosporine as positive control for the single treatment and in combination with each USP7 inhibitor. The difference of the single and combo DSS_{asym} equals the differential combo DSS ($dcDSS_{asym}$). A $dcDSS_{asym}$ equal or greater than three indicates an additional effect of the drug combination and a potentially beneficial combination, whereas a $dcDSS_{asym}$ equal or smaller than minus three indicates adverse effects. In combination with P22077, eight drugs showed a $dcDSS_{asym}$ smaller than three (**Figure 29A**). Among these eight, no class effect could be identified. For the combination with P005091, no drug showed a $dcDSS_{asym}$ below minus three. In general, $dcDSS_{asym}$ scores for the combination with P005091 were closer to zero and only eight drugs showed an increased performance in combination (**Figure 29B**), whereas 33 drugs showed an increased performance together with P22077 (**Figure 29A**). Five drugs showed a $dcDSS_{asym}$ greater than three in combination with P22077 and P005091: The chemotherapeutic cisplatin, the FGFR inhibitor Erdafitinib, the BET inhibitor Mivebresib and the pan-HDAC inhibitors CUDC-907 and Panobinostat (**Figure 29C**). Even though two HDAC inhibitors showed a high $dcDSS_{asym}$ in combination with both USP7 inhibitors, other HDAC inhibitors included in the screen did not or even showed a lowered $dcDSS_{asym}$, as for example Pacritinib in the combination with P22077. Additionally, based on the experience of the TDSU, the class of HDAC inhibitors are often found to be hits in such screens and should only be considered for validations upon very strong effects for all HDAC inhibitors, which was not the result of this screen. Therefore, I instead focused on the class of BET inhibitors, as Mivebresib showed an increased performance in combination with both USP7 inhibitors, and the second BET inhibitor iBET151 showed a $dcDSS_{asym}$ over 10 in combination with P22077 (**Figure 29D**).

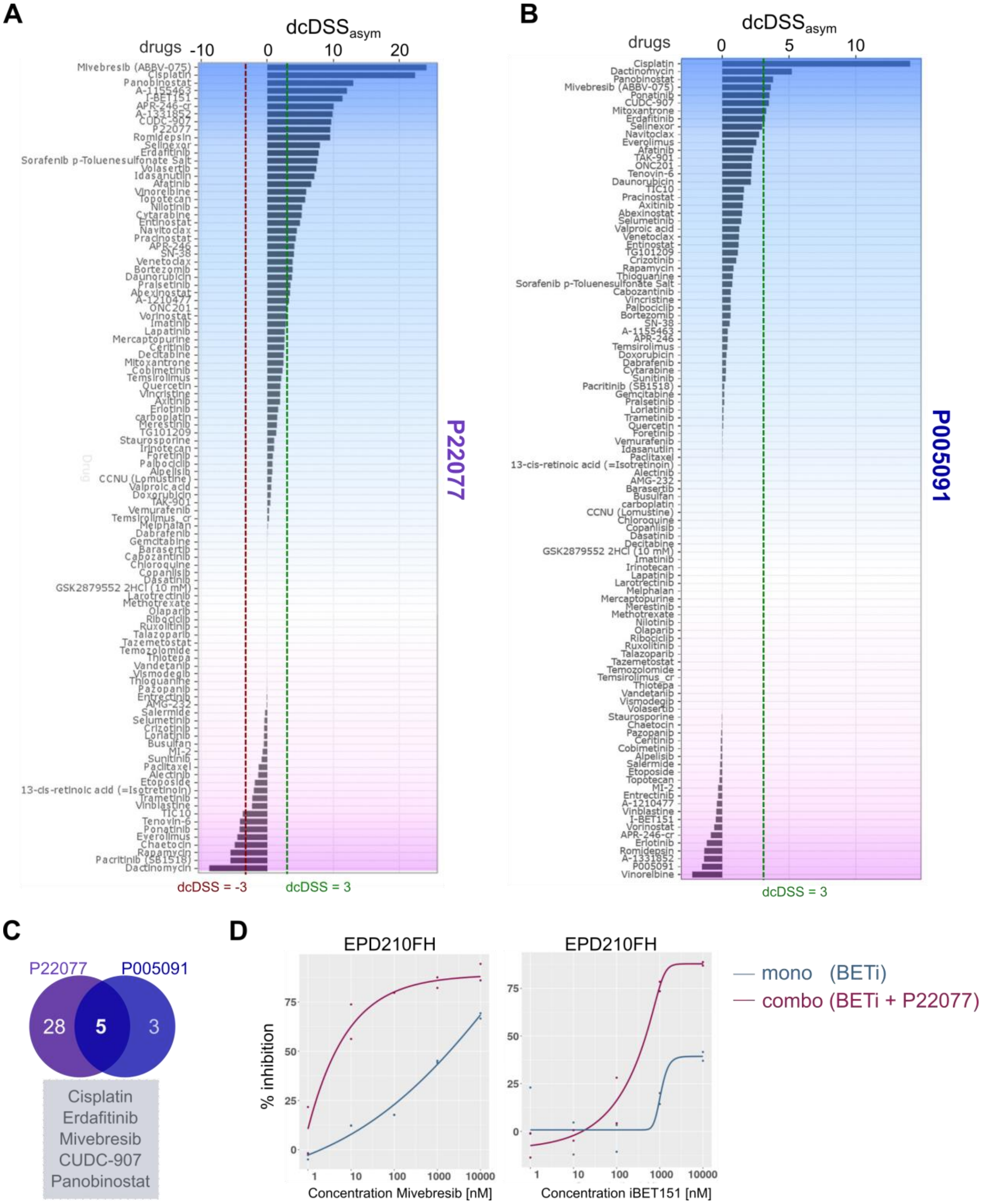

Figure 29 | USP7 inhibitor combination drug screen in PFA ependymoma

*(**A+B**) dcDSSasym scores for the 102 drugs of the mid-library screen in EPD210FH in combination with P22077 (**A**) or P005091 (**B**). Increased effectiveness upon combination is indicated as dcDSSasym greater or equal to three, whereas reduced effectiveness in indicated by a dcDSSasym smaller or equal to minus three. (**C**) Venn diagram showing that 28 drugs showed a increased effectiveness in combination with P22077, 3 in combination with P005091 and the 5 listed one showed increased effectiveness in combination with both. (**D**) Dose-response curves of EPD210FH treated with Mivebresib (left panel) or iBET151 (right panel) alone (blue) or in combination with 3 µM P22077 (purple) at the indicated concentration. Data is extracted from the screen.*

Next, I aimed to test whether the combination of USP7 inhibitors and BET inhibitors acts synergistically in PFA ependymoma. Even though the mid-throughput screen can identify a drug combination that increase the effect of a drug, it is not set up to identify synergy. The idea of drug synergy is an effect of a drug combination that is higher than the addition of the single effects of these drugs, whereas an antagonistic drug combination shows an effect smaller than the addition of the single effects. Mathematically, there are different models to define and calculate synergy. For my experiment, I decided to focus on the Loewe synergy model, which assumes that the combined drugs are acting independently [365]. Using a matrix-layout, I combined a range of concentrations of the USP7 inhibitors P22077 or P005091 with a range of the BET inhibitors Mivebresib, iBET-151 or Birabresib (OTX015) in the PFA ependymoma cell lines EPD210FH and BT214. Synergy was calculated using the SynergyFinder+ online tool (https:\\www.synergyfinder.org). As evidenced by the 2D maps of the synergy values, all tested combinations of USP7 and BET inhibitors showed synergy in the EPD210FH cells (**Figure 30A**). Interestingly, peak synergy values were always detected at 0.75 – 3 µM of the USP7 inhibitors. At 6 µM, the USP7 inhibitors alone already affected the cells much, so that the combination couldn't exceed the additive effect anymore. In line with the screening results, the BET inhibitor iBET-151 showed milder synergy than Mivebresib and in combination with P005091 also showed clear antagonistic tendencies in some combinations. In comparison to EPD210FH, the BT214 cell lines showed lower overall synergy scores and higher synergy scores were calculated for the higher USP7 inhibitors concentrations at 3-6 µM (**Figure 30B**), which is in line with the previous observation that BT214 are less sensitive to USP7 inhibition than EPD210FH (**Figure 24 & Figure 28**). This trend can be validated by looking into the concentrations that lead to the highest detected synergy values (**Figure 31A**). In EPD210FH, the highest synergy scores determined using the Loewe and the HAS model are based on the combination of 3.2 µM OTX015 and 1.5 µM P005091. For this, as well as the combination of P005091 and OTX015, also the mean synergy score of all combinations was greater than 10, which is usually considered to indicate synergy. In the BT214 cells, no combination showed a mean synergy score greater than 10, but again the combinations of P005091 with Mivebresib or OTX015 showed the highest mean synergy scores over five. Based on these results, I considered the combination of USP7 and BET inhibitors to act synergistically in PFA ependymoma. Mechanistically, I could thereafter show that the drug combination of OTX015 and P005091 induced apoptosis in the EPD210FH cell line (**Figure 31B**). Interestingly, the combinations with 3 µM P005091 induced the strongest cleavage of Caspases 3/7. The effect is barely detectable after 8 h, very clear after 24 h, and only slightly increased after 48 h, indicating a peak effect after 24 h. This confirms the observations from the mass spectrometry measurements after 6 h and 24 h of P22077 treatment (**Figure 15**). Taken together, I could show that USP7 inhibitors in combination with BET inhibitors synergistically induces apoptosis in PFA ependymoma. As OTX015 is already in clinical development [366], this combination is a promising lead towards targeted therapies in PFA ependymoma.

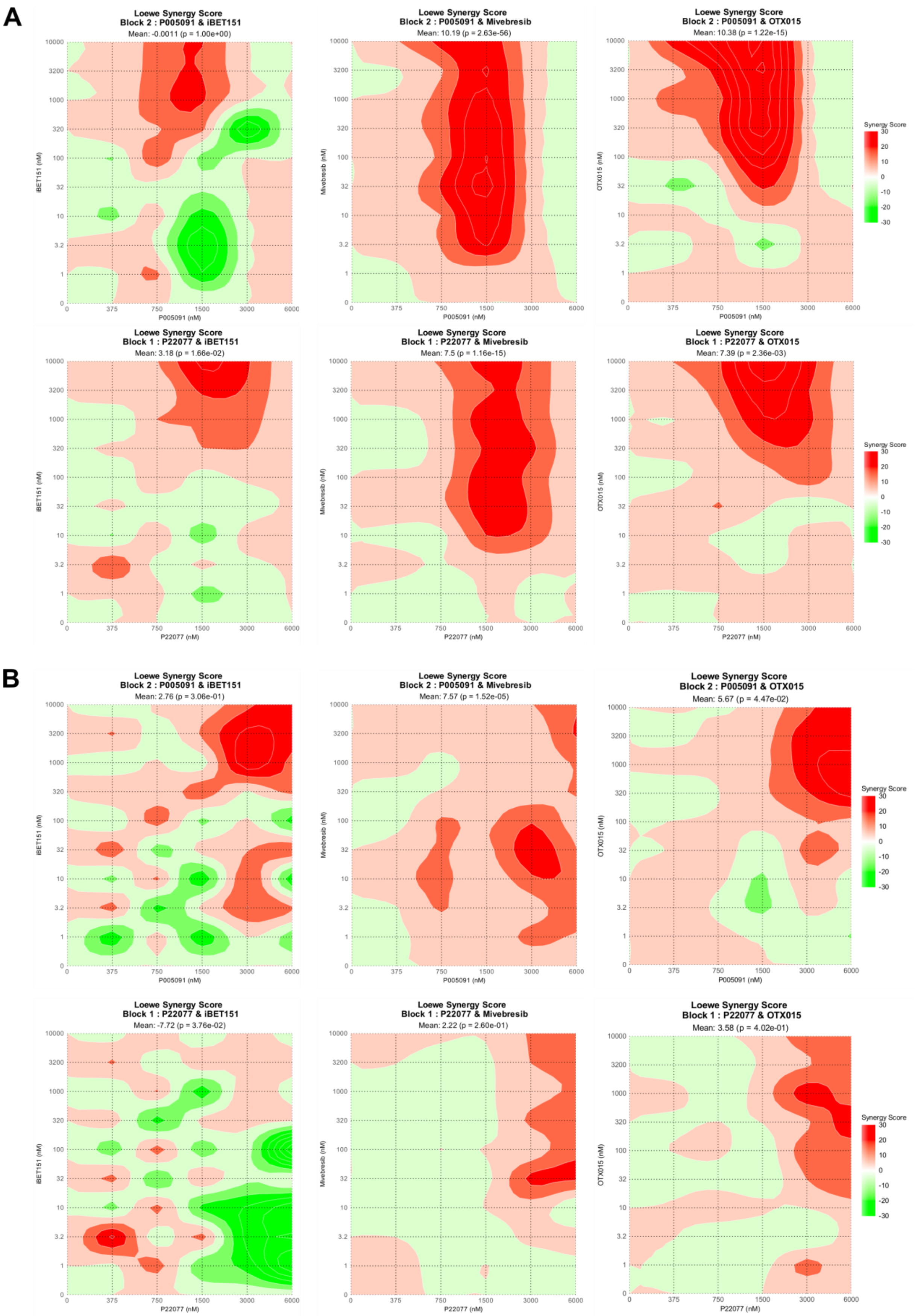

Figure 30 | Synergy determination of USP7 and BET inhibitors in PFA ependymoma

*2D maps of Loewe synergy scores of EPD210FH (**A**) and BT214 (**B**) cells- Matrix layout includes the USP7 inhibitor P005091 or P22077 in combination with one of the BET inhibitors (iBET151, Mivebresib, OTX015). Data is based on metabolic readouts after 72 h, relative to DMSO control.*

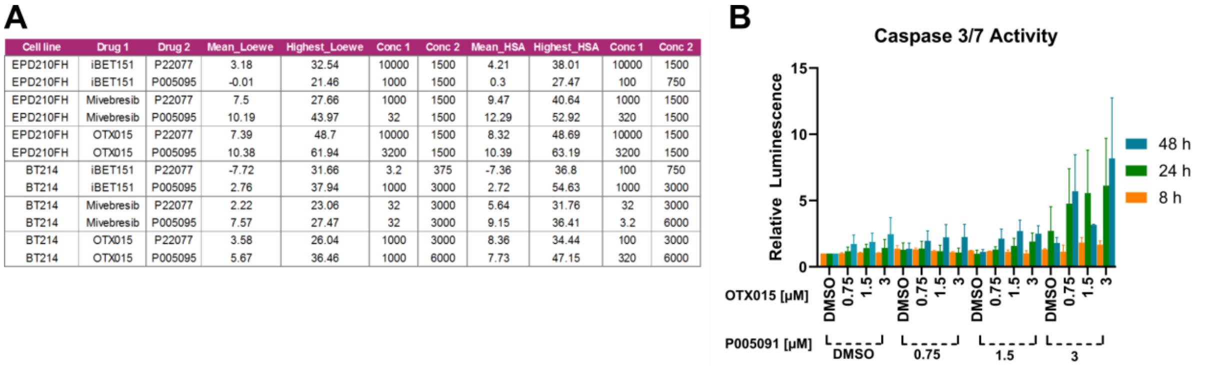

Cell line	Drug 1	Drug 2	Mean_Loewe	Highest_Loewe	Conc 1	Conc 2	Mean_HSA	Highest_HSA	Conc 1	Conc 2
EPD210FH	iBET151	P22077	3.18	32.54	10000	1500	4.21	38.01	10000	1500
EPD210FH	iBET151	P005095	-0.01	21.46	1000	1500	0.3	27.47	100	750
EPD210FH	Mivebresib	P22077	7.5	27.66	1000	1500	9.47	40.64	1000	1500
EPD210FH	Mivebresib	P005095	10.19	43.97	32	1500	12.29	52.92	320	1500
EPD210FH	OTX015	P22077	7.39	48.7	10000	1500	8.32	48.69	10000	1500
EPD210FH	OTX015	P005095	10.38	61.94	3200	1500	10.39	63.19	3200	1500
BT214	iBET151	P22077	-7.72	31.66	3.2	375	-7.36	36.8	100	750
BT214	iBET151	P005095	2.76	37.94	1000	3000	2.72	54.63	1000	3000
BT214	Mivebresib	P22077	2.22	23.06	32	3000	5.64	31.76	32	3000
BT214	Mivebresib	P005095	7.57	27.47	32	3000	9.15	36.41	3.2	6000
BT214	OTX015	P22077	3.58	26.04	1000	3000	8.36	34.44	100	3000
BT214	OTX015	P005095	5.67	36.46	1000	6000	7.73	47.15	320	6000

Figure 31 | USP7 and BET inhibitors act synergistically in PFA ependymoma

*(**A**) Overview table of mean and highest synergy scores using the Loewe synergy model or the HSA synergy model in EPD210FH and BT214 cells. Concentrations are in nM. (**B**) Apoptosis assay measuring caspase 3/7 activity in EPD210FH cells after treatment with OTX015 and/or P005091 at the indicated concentrations after 8 h, 24 h or 48 h of treatment. Luminescence is relative to the DMSO+DMSO control of the respective time point. Data is from three biological replicates and represent the mean and SEM.*

5.11 Identification of pharmacological treatments of PFA ependymoma

Since the overall aim of this work was to identify ways to target PFA ependymoma, I employed two main strategies to do so. My first approach was to again make use of the collaboration with theT DSU at the KiTZ and their semi-automated mid-throughput library drug screening platform. Secondly, I tested specific hypothesis-driven targets, thereby leveraging published mechanisms I could apply to PFA ependymoma.

5.11.1 Mid-throughput drug screening

Drug library screening can be a powerful tool to identify drugs or drug classes to target cells *in vitro*. Similar to the previous chapter where I identified treatment combinations, cells were treated with a multitude of drugs as single treatments simultaneously in a 384-well format. As PFA ependymoma are characterized by a changed epigenome, I used the epigenetic targeted library, which includes 102 commercially available drugs for epigenetic regulators or epigenetically involved pathways (**Supp Table 2**) and conducted the readouts (cell titer glo) after 72 h. To identify PFA ependymoma specific vulnerabilities, I performed the screen in the PFA ependymoma EPD210FH and the two ST-ZFTA cell lines EP1NS and BT165 for comparison. The DSS_{asym} for all drugs was calculated in comparison to the DMSO control and staurosporine as negative and positive controls, respectively, and are shown in **Figure 32** [353, 359]. I considered DSS_{asym} values greater than 10 for interpretation. The results for all three cell lines were not stricingly different. All three showed relevant drug sensitivies to over 20 drugs, among them multiple HDAC inhibitors (e.g. Romidepsin, Entinostat, Pracinostat, Belinostat) and bromodomain targeting drugs (e.g. Mivebresib, dBET1. CUDC-907, Bromosporine) (**Figure 32A**). To be able to identify cell line specifically acting drugs better, the selective drug sensitivity score $sDSS_{asym}$ was calculated, which subtracts a mean DSS_{asym} acquired from healthy control cell lines from the DSS_{asym} of the tested cell line (**Figure 33A**). $sDSS_{asym}$ values greater than five indicate an above-average drug effect. EP1NS cells showed a $sDSS_{asym}$ greater than five for 14 drugs, BT165 for 21 and EPD210FH for 10 drugs (**Figure 33B**). Interestingly, this focus on above-control performance reduced the overlap of identified drug candidates, as only four drugs showed selective drug sensitivity in all three cell lines:

Mivebresib, Mitoxantrone 2HCl, Pacritinib and JQ1 (**Table 16**). The three drugs that show specific sensitivity in EPD210FH cells were the HDAC inhibitor Curcumin, the histone methyltransferase (HMT) inhibitor Chaetocin and the EZH2 inhibitor UNC199. Although there is no clear drug class enriched in specificity for the PFA ependymoma cell lines, one could imagine a certain sensitivity towards EZH2 inhibitors as this is a histone methyltransferase. In contrast, multiple other EZH2 inhibitors were included in the screen, but showed little to no effect on EPD210FH cells. All in all, the screen showed a certain vulnerability of ependymoma cells towards epigenetic drugs, specifically HDAC and bromodomain inhibitors, but did not extract a reliable lead towards a drug class to target PFA ependymomas specifically.

Table 16 | Epigenetic drug screen top hits in ependymoma

Drugs with a sDSSasym equal or greater than five in the two ST-ZFTA cell lines (red) and the PFA ependymoma cells (orange) and the corresponding values. Bromodomain inhibitors are in blue, HDAC inhibitors in light orange.

BT165		EP1NS		EPH210FH	
Drug	**sDSS$_{asym}$**	**Drug**	**sDSS$_{asym}$**	**Drug**	**sDSS$_{asym}$**
dBET1	19.63	Mivebresib(ABBV-075)	18.94	Mitoxantrone 2HCl	11.43
Mivebresib(ABBV-075)	19.08	Pacritinib (SB1518)	12.98	Tenovin-6	11.24
Mitoxantrone 2HCl	15.67	Atuveciclib	11.16	Mivebresib(ABBV-075)	9.29
BAY 87-2243	14.85	OTX015	9.55	Chaetocin	7.6
Pacritinib (SB1518)	14.81	TIC10	9.3	Curcumin	7.26
Atuveciclib	13.41	Mitoxantrone 2HCl	9.19	Citarinostat (ACY-241)	6.48
GSK J4 HCl	10.78	Bromosporine	8.87	Pacritinib (SB1518)	5.89
TAK-901	10.1	(+)-JQ1	8.34	UNC1999	5.74
Citarinostat (ACY-241)	9.91	ABBV-744	6.19	dBET1	5.63
TIC10	9.75	Tenovin-6	5.64	(+)-JQ1	5.54
(+)-JQ1	9.01	Amodiaquine dihydrochloride dihydrate	5.48		
Bromosporine	8.16	GSK J4 HCl	5.42		
OTX015	7.69	I-BET-762	5.09		
Azacitidine	7.26	GSK1324726A (I-BET726)	5.02		
MI-2 (Menin-MLL Inhibitor)	6.38				
GSK6853	6.34				
SF2523	5.71				
I-BET-762	5.51				
Tubastatin A	5.41				
Ricolinostat	5.33				
Rucaparib	5.25				

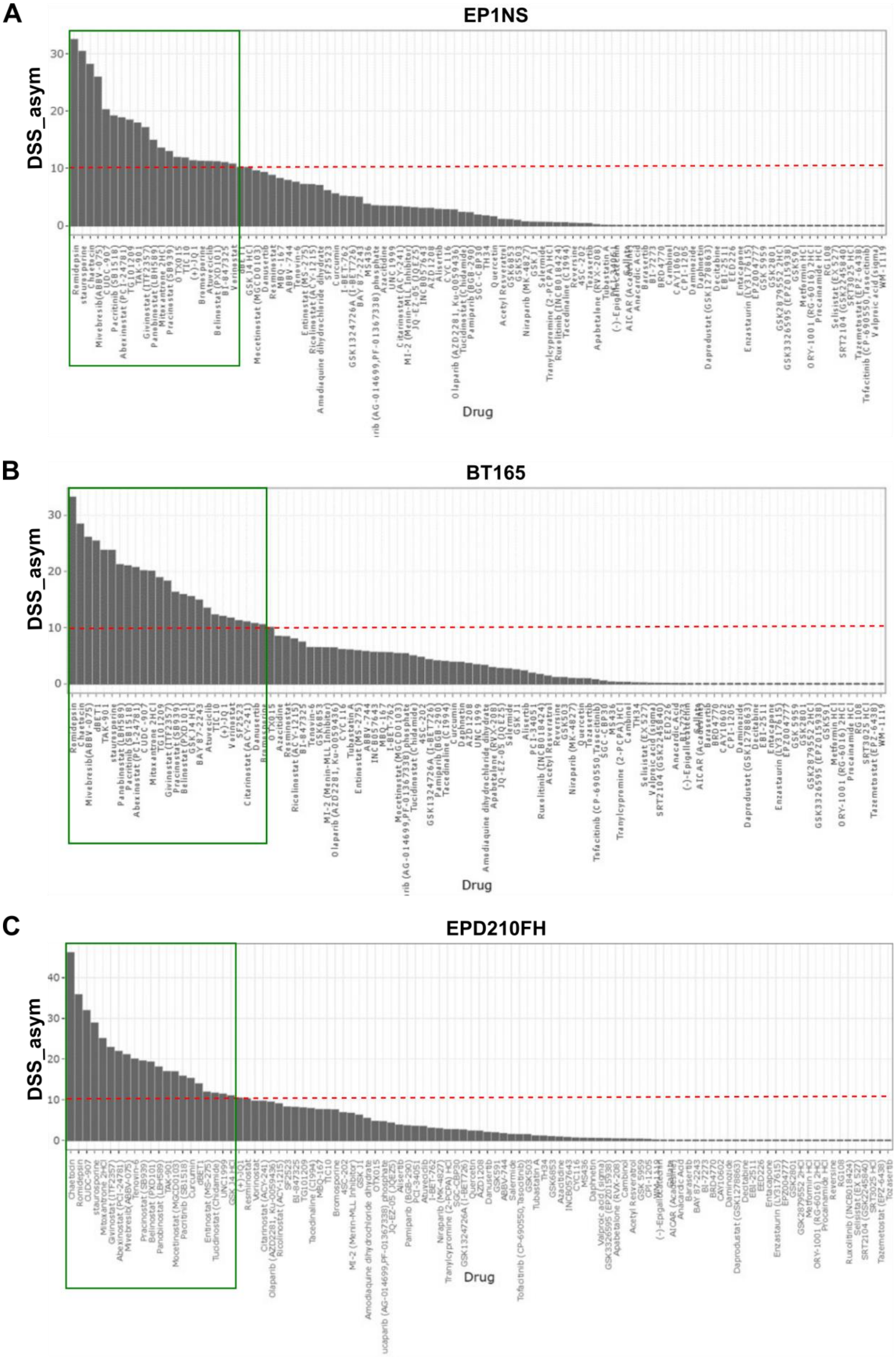

Figure 32 | Epigenetic drug screen in ST-ZFTA and PFA ependymoma

Results of the epigenetic drug screen in the two ST-ZFTA cell lines EP1NS (A) and BT165 (B) as well as the PFA ependymoma line PED210FH (C). 102 drugs are sorted by their DSSasym score. Drugs with a score above 10 (red dotted line) are included in the green square.

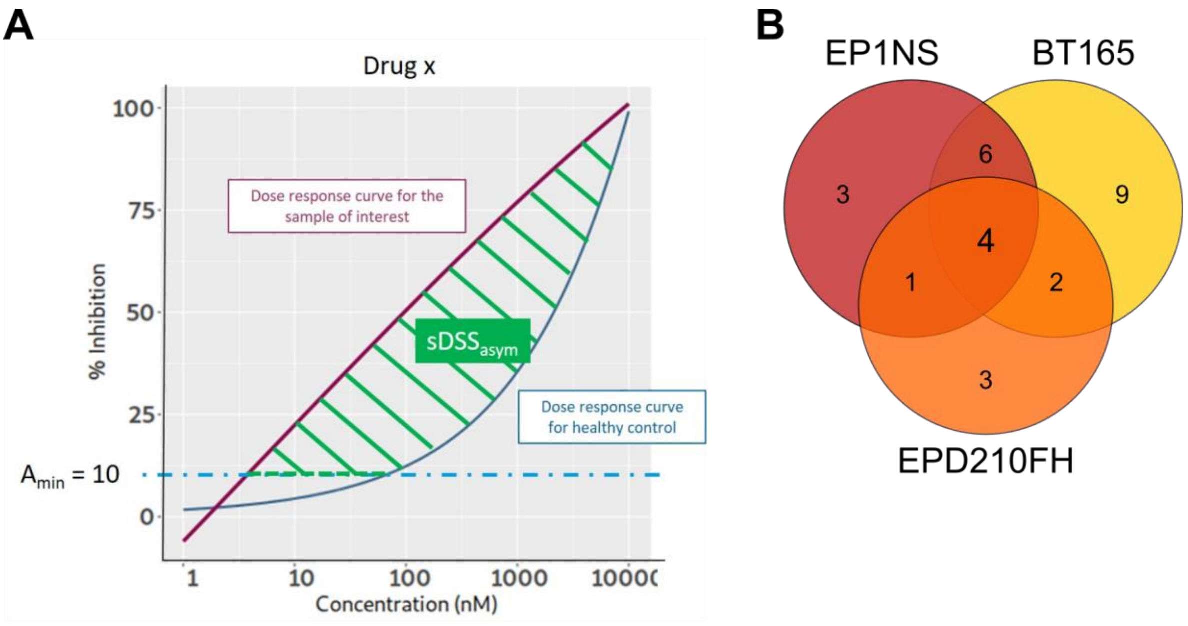

Figure 33 | Selective drug identification in ependymoma cell lines

*(**A**) Schematic showing how the selective drug sensitivity score (sDSSasym) is determined by subtraction of the DSSasym from healthy control cells from the DSSasy of the tested cell line (**B**) Venn Diagram showing the distribution of drugs with a sDSSasym greater or equal to 5. Four drugs met the criteria in all three tested ependymoma cell lines.*

5.11.2 Hypothesis-based targeted therapies

For the informed target identification, I looked into genes that were highly expressed in PFA ependymoma in our in-house pediatric brain tumor dataset. One of these genes is peroxisome proliferator-activated receptor gamma (PPARγ), whose expression is elevated in the 163 PFA ependymoma (orange) but is almost not expressed in the other pediatric brain tumors (total n=1914) including the K27M oncohistone-driven DMGs (green) and other ependymoma subtypes (**Figure 34A**). I then confirmed this PFA ependymoma specific overexpression of PPARγ in PFA ependymoma cell line samples (n=4), which express it at much higher level than the four ST-ZFTA cell line profiles (**Figure 34B**).

Additionally, I screened literature for links between PPARγ biology and PFA ependymoma. In 2020, there was only one paper linking PPARγ to PFA ependymoma, which found PPARγ RNA to be higher expressed in PF-EPN compared to ST-EPN or SP-EPN, linking this to changes in DNA methylation status[367]. Additionally, there were indirect links, such as Lee et al. who showed that USP7 de-ubiquitinates and thus stabilizes PPARγ [368] or Meel et al., that identified the MELK-PPARγ axis as potential target in DIPG[369]. By now, there are additional publications, e.g. showing that inhibition of catalytic EZH2 activity leads to reduction of H3K27me3 and activated transcription of the PPARγ locus [370]. Therefore, I decided to test the effect of PPARγ agonists GQ-16 and Rosiglitazone on PFA ependymoma cells *in vitro*. In the EPD210FH cell line, both agonists reduced the viability at higher doses (**Figure 34C**). The antidiabetic drug Rosiglitazone did not reduce survival to less than 50% at the highest dose and also the better performing PPARγ agonist GQ-16 only acted at an IC50 of 19.8 µM. As this was clearly less potent than other compounds, and since GQ-16 is a still understudied compound without clinical or pharmacokinetic data, I decided to abandon PPARγ as target for PFA ependymoma.

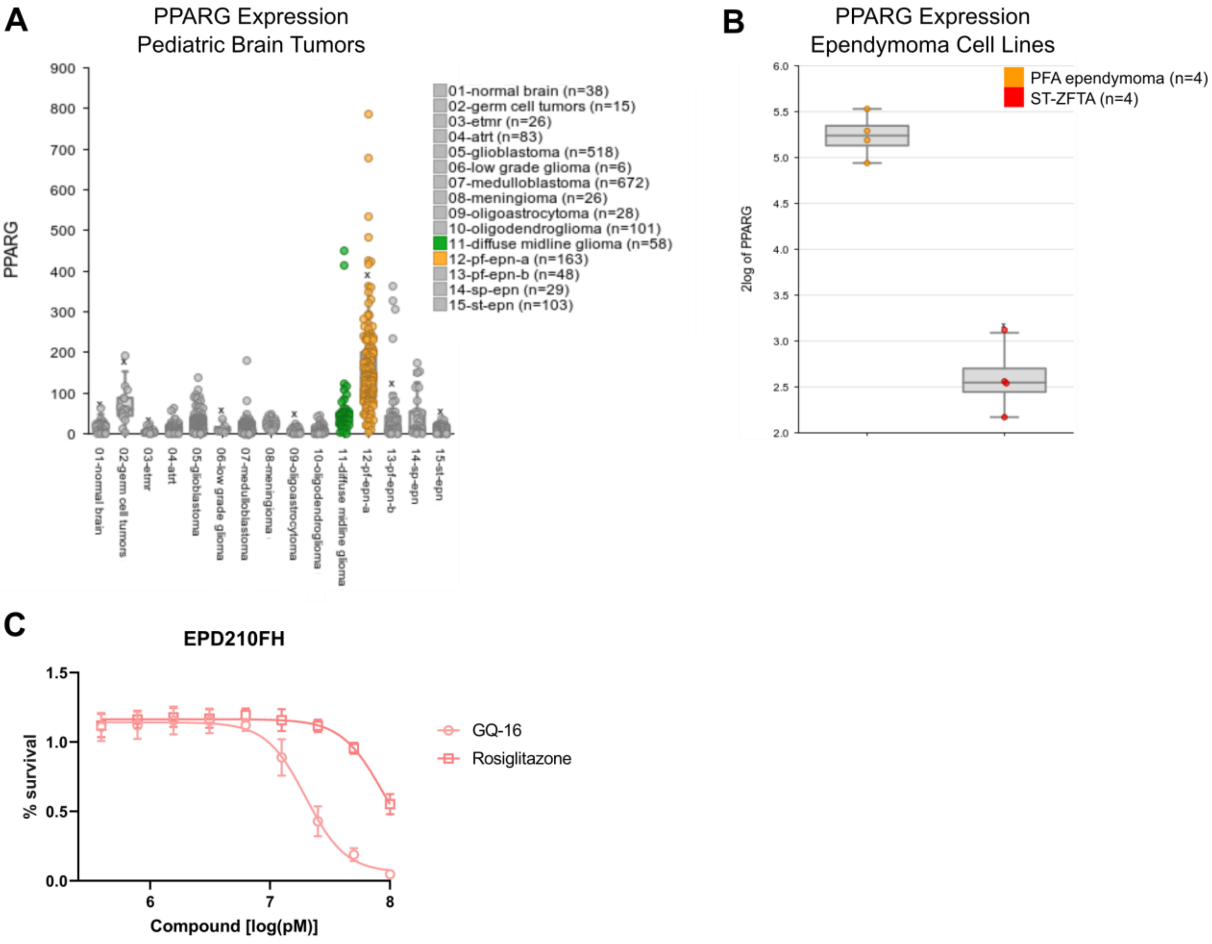

Figure 34 | PPARG as potential target in PFA ependymoma

*(**A**) Affymetrix-based box-dot plots of expression data of PPARG in a pediatric brain tumor panel (n=1914). DMG data is highlighted in green (n=58), PFA ependymoma are in orange (n=163). (**B**) Affymetrix-based box-dot plots of expression data of PPARG in PFA (orange; n=4) and ST-ZFTA (red; n=4) ependymoma cell lines. (**C**) Does-response curve of EPD210FH treated with the indicated concentrations of GQ-16 or Rosiglitazone for 144 h. Survival is relative to the DMSO control. Data shows the mean and SEM of three independent biological experiments.*

The next potential targets were based on published results on PFA ependymoma from Michealraj et al. and Han et al. [120, 170]. The first paper included a genome-wide *in vitro* CRISPR screen, which identified the PRC2 core components SUZ12, EED and EZH2 as top 10 essential genes in PFA ependymoma. As a follow-up, they showed a selectivity of EED and EZH2 inhibitors for PFA ependymoma compared to ST-EPN cells. Thus, I wanted to see whether unbalancing the PRC2 complex could also potentially target my PFA ependymoma cells, selecting four EZH2 inhibitors, one EED inhibitor, as well as the S- adenosylhomocysteine (SAM) hydrolase inhibitor DZNep, which deprives EZH2 of its cofactor SAM. As shown in **Figure 35A**, four EZH2 inhibitors and the EED inhibitor MAK683 only reduced EPD210FH cell viability at the highest concentration of 100 µM. Only the EZH2 inhibitor UNC199 showed a clear effect on EPD210FH at an IC50 of 5.8 µM, which was the inhibitor used in the publication and had also emerged as potential target in the epigenetic drug screen for EPD210FH (**Table 16**). Interestingly, DZNep showed the strongest effect in EPD210FH with an IC50 of

160 nM. DZNep was already tested in flank and orthotopic PFA ependymoma PDX models in 2014. It was able to reduce tumor growth and improve survival [154].

The second paper from Han et al. described a sensitization of tumor cells to poly(ADP-ribose) polymerase (PARP) inhibitors upon the inhibition of homologous recombination repair by EZHIP [170], and added a recent publication in 2024 about the beneficial combination of PARP inhibitors and chemotherapy in PFA ependymoma [371]. As PFA ependymoma cells are characterized by a high EZHIP expression, I hypothesized that they should be sensitive to PARP inhibition and opted to test four PARP inhibitors, selected based on potency and BBB penetrance, in our *in vitro* models for 144 h:

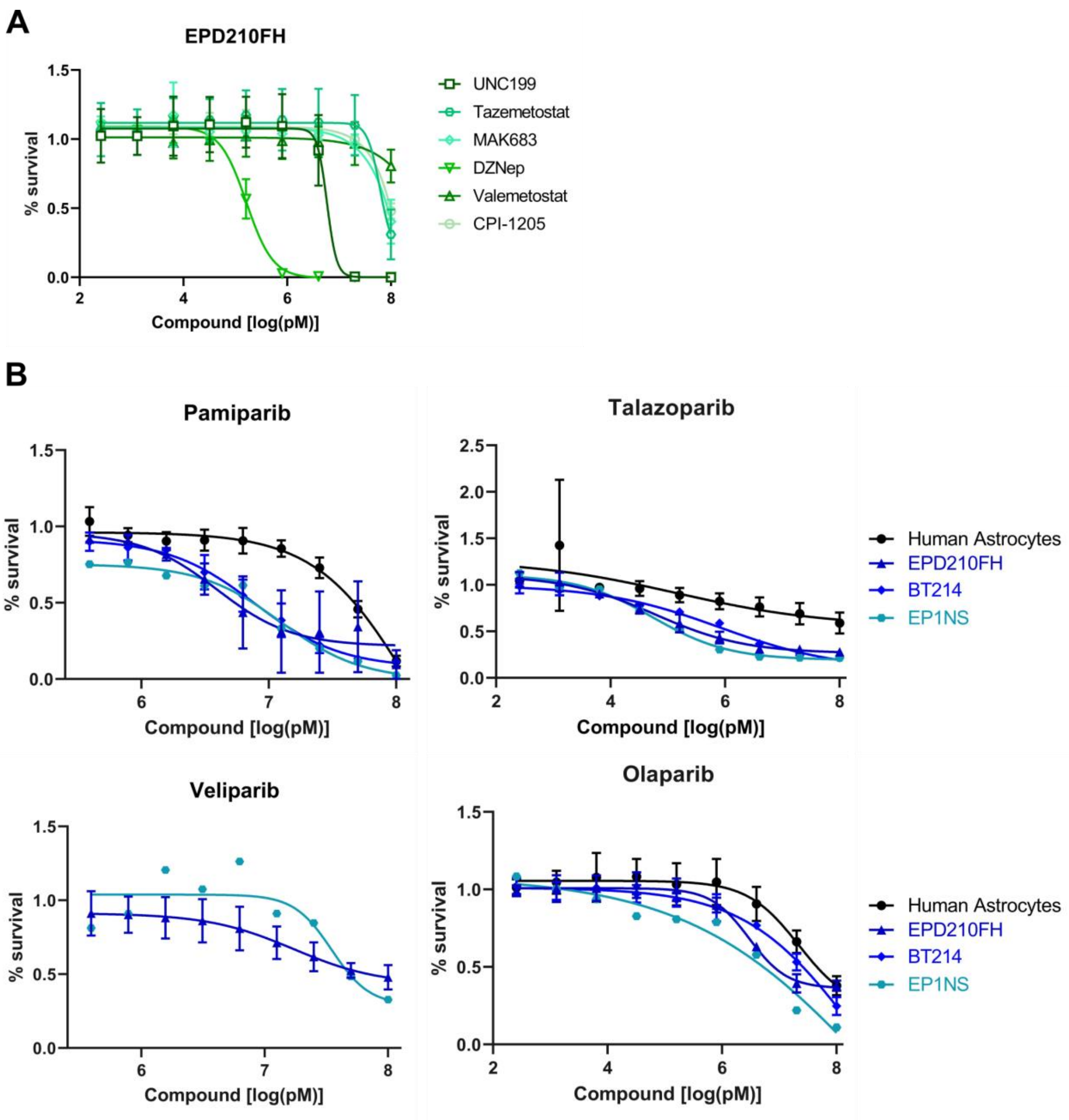

Figure 35 | EZH2 and PARP inhibitors in PFA ependymoma

*(**A**) Dose-responses of EPD210FH treated with six EZH2 inhibitors at the indicated concentrations for 144 h. Survival is relative to DMSO control. Data represents mean and SEM from three independent experiments. (**B**) Dose-responses of human astrocytes, EPD210FH, BT214, BT214 and EP1NA cells treated with the PARP inhibitors Pamiparib, Talazoparib, Veliparib or Olaparib at the indicated concentrations for 144 h. Survival is relative to DMSO control. Data represents mean and SEM from three independent experiments or technical triplicates (EP1NS).*

Pamiparib, Talazoparib, Olaparib and Veliparib (**Figure 35B**). I compared their ability to reduce cell survival in the PFA ependymoma cell line EPD210FH to the ST-ZFTA line EP1NS, and included the second PFA ependymoma cell line BT214 and human astrocytes for Pamiparib, Talazoparib and Olaparib. These three PARP inhibitors affected the viability of ependymoma cells more than the viability of human astrocytes, which served as healthy control. There was little difference in the results of the three ependymoma lines, also when treated with veliparib, which indicated that the observed effects were not driven by EZHIP expression. Together with the small difference in astrocyte to ependymoma sensitivity, this confirms the results of the epigenetic drug screen (chapter 5.10.1). The screen, which tested the cells grown as spheres for only 72 h, included four PARP inhibitors (Niraparib, Olaparib, Pamiparib, Rucaparib), none of which showed a meaningful sensitivity score for the PFA ependymoma cells, but Rucaparib showed a sDSS$_{asym}$ over five for the ST-ZFTA BT165 cells (**Table 16**). Of the four PARP inhibitors tested manually, Talazoparib showed the strongest effects with IC50 values at the high nanomolar level, whereas Veliparib failed to reduce ependymoma cell viability even at the highest concentrations (**Table 17**). This is in concurrence with the low PARP trapping ability of Veliparib and the high ability of Talazoparib [174, 372], which on the other hand is opposed to their ability to cross the BBB, rendering Talazoparib impractical to use in PFA ependymoma.

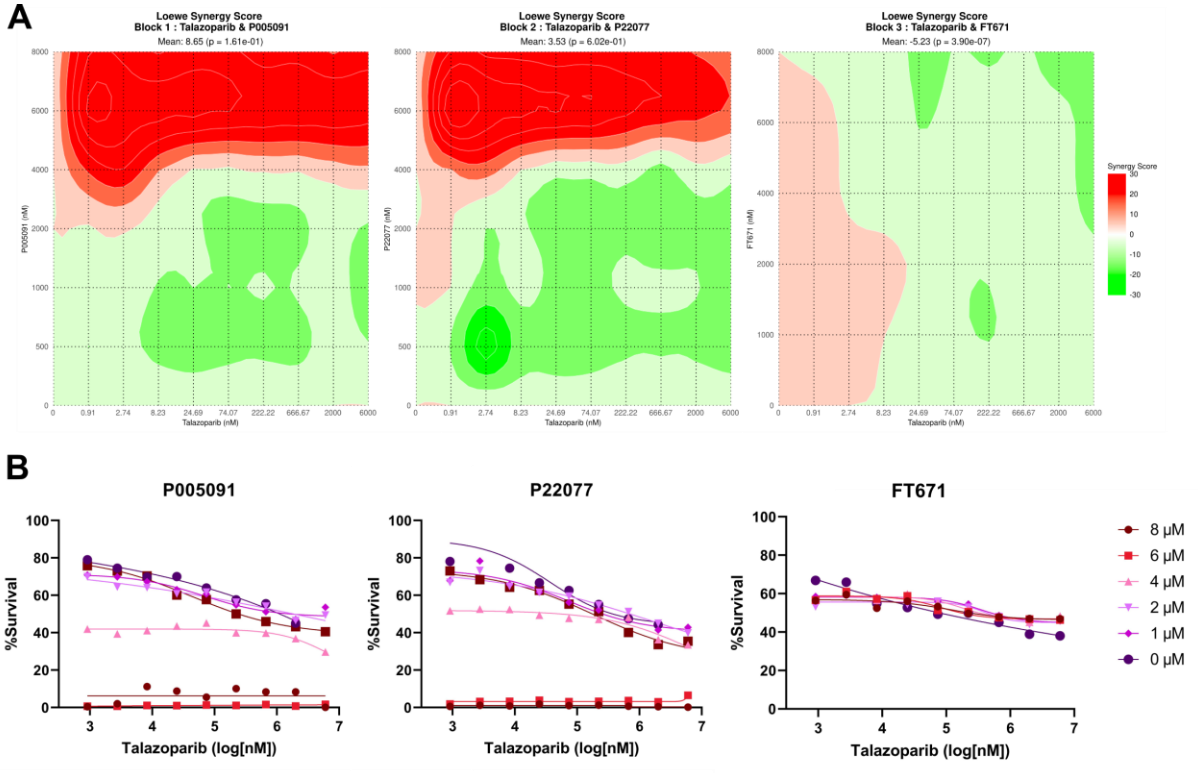

Figure 36 | USP7 and PARP inhibitors are not synergistic in PFA ependymoma

*(**A**) 2D maps of Loewe synergy scores in EPD210FH treated with a matrix-layout of Talazoparib together with the USP7 inhibitors P005091, P22077 or FT671. (**B**) Dose-response curves of EPD210FH cells treated with the indicated Talazoparib concentrations (x-axis) in combination 0 µM (DMSO) or up to 8 µM (see legend) of either P005091, P22077 or FT671 for 144 h. Data is relative to the double DMSO control and represents technical triplicates.*

The lower the minimum therapeutically effective dose of a drug, the less drug needs to be able to reach tumors. Thus, lowering the effective dose of drugs, especially of drugs with low ability to cross the BBB like Talazoparib, is crucial to enable treatments. One possibility to lower effective doses is combining two or more drugs to achieve synergistic effects between them, which means that their combined effect is higher than the expected addition of their singular effects [365]. Multiple publications have described a sensitization of cells to PARP inhibitors by USP7 inhibitors and even hinted towards a possible synergy between the two inhibitor classes [373-376]. I could already show that PFA ependymoma cells are sensitive to both inhibitor classes alone, but the two PARP inhibitors Olaparib and Talazoparib included in the USP7 inhibitor synegery screen (chapter 5.10) did not show an additive effect. To exclude a false-negative effect in the setting of the screen, I tested the combination of most the effective, but only mildly BBB penetrant, PARP inhibitor Talazoparib with the three USP7 inhibitors P005091, P22077 and FT671. I treated EPD210FH cells for 72 h applying a matrix layout with Talazoparib concentrations between 6 µM and 0.91 nM in combination with USP7 inhibitors ranging between 8 µM and 0.5 µM and loewe synergy was again determined with SynergyFinder+ (see chaper 5.10) [357]. The synergy maps for the combination of Talazoparib and P22077 or P005091 are highly comparable (**Figure 36A**). Synergy was detected at the higher USP7 inhibitor concentrations, whereas concentrations below 4 µM in combination with Talazoparib were marked with a negative Synergy Score, which indicates an antagonistic effect. For the combination of Talazoparib with FT671, the calculated Synergy Scores were overall less strong. For the lower Talazoparib concentrations (0-2.74 nM), mild synergism was detected, whereas all other concentrations were rather antagonistic. However, the combination of FT671 and Talazoparib never reduced the viability of EPD210FH below 40% but always below 80%, not even indicating additive effects upon inspection by eye, which confirms the lack of calculated synergy (**Figure 36B**). For P005091 and P22077, the dose-response curves oppose the calculated synergy levels. The cells treated with 6 µM or 8 µM of the USP7 inhibitors show viability of less than 10% upon single treatment already, so that the addition of Talazoparib often cannot further reduce the viability. Thus, there might be a mathematically detected synergy, but the data it is based on contradicts that. Therefore, I concluded that Talazoparib does not act synergistically with USP7 inhibitors in PFA ependymoma cells.

Table 17 | IC50 Values of hypothesis-based targets

IC50 values of PPARγ activators, EZH2 inhibitors, and PARP inhibitors of different cell lines in µM. NA refers to an IC50 out of range.

IC50 [µM]	Human Astrocytes	EPD210FH	BT214	BT232	VBT420	B193	R059	EP1NS
Rosiglitazone		147.74						
GQ-16		21.19						
UNC199		5.4						
Tazemetostat		70.33						
MAK683		54.8						
DZNep		0.16						
Valemetostat		61.94						
CPI-1205		61.09						
Olaparib	NA	2.97	21.45					5.68
Talazoparib	0.41	0.05	0.47					0.04
Pamiparib	64.66	5.24	7.52					12.33
Veliparib		15.77						34.72

VI Discussion

The presumed oncogenic drivers of PFA ependymoma are an aberrant overexpression of EZHIP or, in rare cases, the presence of the oncohistone mutation H3K27M, which is mutually exclusive with EZHIP. Expression of EZHIP or H3K27M causes inhibition of EZH2 and the PRC2 complex, which in turn leads to a reduction of the repressive epigenetic H3K27me3 mark and a change in gene expression that keeps progenitor cells in a proliferative state [5, 153]. However, targeting EZHIP directly is not yet easily possible, leaving treatment options for PFA ependymoma mostly to surgery and radiotherapy alone [123, 377]. More effective targeted strategies need to be developed to improve the survival of PFA ependymoma patients. Thus, this thesis aimed to identify and validate new starting points for mechanistically-sound targeting therapies. A visual summary of my results is shown in **Figure 37**.

One approach to discover new drugs with high potency in PFA ependymoma was to apply an epigenetic drug library screen, which aimed to exploit that ependymoma are an epigenetically driven disease. In the two ST-ZFTA and one PFA ependymoma cell lines I tested, BET inhibitors and HDAC inhibitors stood out (**Table 16**). Additionally, I mined literature for hints of potential mechanism-based treatment strategies and therefore tested PPARγ agonists, EZH2 and PARP inhibitors. While PPARγ agonists did not affect PFA ependymoma survival, the EZH2 inhibitor DZNep and the PARP inhibitor Talazoparib reduced PFA ependymoma cell viability at nanomolar potencies.

The main target I have been focusing on in my thesis is USP7. I identified USP7 as interaction partner of EZHIP and showed that this interaction is independent from the presence of EZH2. USP7 interacts with EZHIP via the USP7 TRAF-like domain, removes ubiquitin from EZHIP and therefore stabilizes it on the protein level. Targeting USP7 genetically, with a degrader or with small molecule inhibitors *in vitro* reduced EZHIP protein levels, induced apoptosis and affected the survival of PFA ependymoma cells. Furthermore, I identified BET inhibitors as synergistic partners of USP7 inhibitors. However, despite the promising results of targeting USP7 *in vitro*, testing the two USP7 inhibitors P22077 and P005091 in an orthotopic PFA ependymoma PDOX model did not reduce tumor growth or prolong mouse survival, probably because of insufficient brain penetrance of these drugs. To test this and to validate whether USP7 is in principle still a good target in PFA ependymoma, we are currently testing P005091 also in the same PFA ependymoma PDX model, but this time with tumors engrafted subcutaneously. Moreover, we are at the same time also testing whether the combination the BET inhibitor OTX015 with P005091 works better than the USP7 inhibitor alone.

To my knowledge, the combination of USP7 and BET inhibitors has never been described as synergistic before. A reason for the synergism of the two drug classes in PFA ependymoma could be that they both affect epigenetic signaling. Based on my results, the inhibition of USP7 may affect the transcriptional repressor mark H3K27me3 through the regulation of EZHIP. At the same time, the inhibition of bromodomain proteins prevents the reading of H3K27ac signals, which are marking regions of active chromatin. In ependymoma, H3K27ac- mediated enhancer signaling has been shown to be a subgroup-specific dependency, which informed the use of the BET inhibitor JQ1 *in vitro* [14]. Interestingly, single treatments with the BET inhibitor OTX015 were shown to be effective *in vivo* in a ST ependymoma model and in one of two PFA PDX models [366], which is in line with my observation from the epigenetic library screen which showed good scores for many bromodomain inhibitors for targeting ST-ZFTA and PFA ependymoma (**Table 16**). Additionally, the responsiveness of only one of the two *in vivo* models also highlights the heterogeneity between ependymoma models and underlines that new treatments should always be tested in multiple models. Other studies on solid pediatric tumors, including neuroblastoma, reported a mode of action for BET inhibitors connected to the expression of NMYC [378-382]. As USP7 has also been reported to regulate MYC stability in neuroblastoma, SCLC and NSCs,

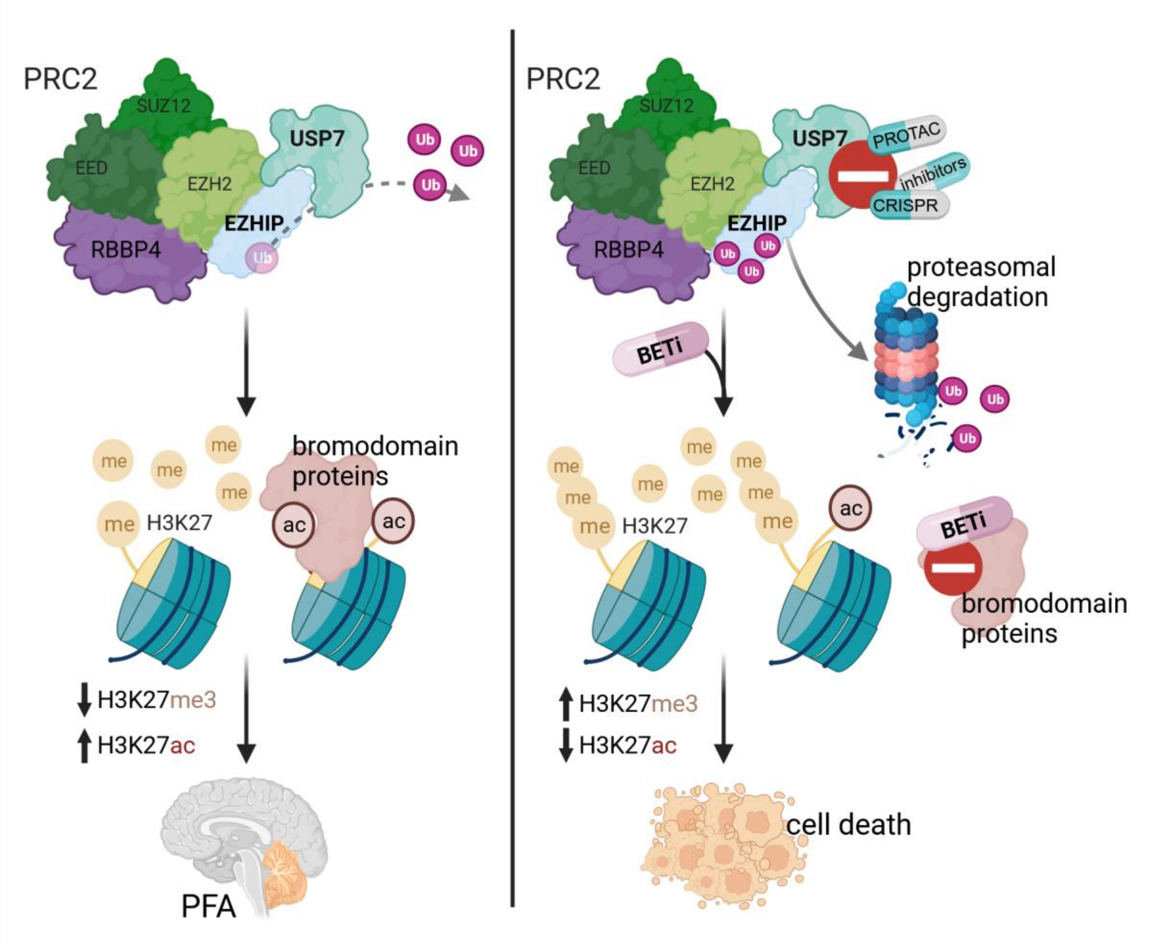

Figure 37 | Graphic Summary

Working model of the interplay of EZHIP and USP7 in PFA ependymoma. In PFA ependymoma, the deubiquitination by USP7 stabilizes EZHIP, which leads to PRC2 repression, reduced H3K27me3 and increased H3K27ac levels driving the tumors. Upon manipulation of USP7, inhibition or protein depletion, EZHIP stays ubiquitinated and gets proteasomally degraded. This results in changed H3K27 modifications and apoptosis of PFA ependymoma, which can be synergistically increased by combination with BET inhibitors. Figure was created using biorender.com.

MYC de-regulation could be a second mechanistical overlap strengthening the synergy of USP7 and BET inhibitors in PFA ependymoma [301-303, 383]. In 2017, Piunti et al. reported the effectiveness of BET inhibition as single treatment in DMGs [189], another tumor entity characterized by a loss of H3K27me3, which is mostly caused by the expression of the H3K27M oncohistone and only seldomly (~ 3.5%) by EZHIP expression [159]. H3K27M, conversely, is expressed in 4.2% of PFAs and mutually exclusive with the expression of EZHIP, most likely due to their collective role in EZH2 inhibition [153, 159]. Since I could see a clear a potency of USP7 inhibitors in the two DMG cell lines tested (**Figure 24**), one expressing K27M and one overexpressing EZHIP, a combination of USP7 and BET inhibition should be tested in DMG models as well. Interestingly, either DMG cell line showed higher potency for one USP7 inhibitor. This points towards a sensitivity of DMG cells independent of their main oncogenic driver and could indicate that PFA ependymoma cells driven by K27M may also be targetable by USP7 inhibitors, but no K27M-driven PFA ependymoma cell line was yet available to test this. In line with the thought of targeting H3K27 signaling twice, BET inhibition and EZH2 inhibition or loss have been successfully combined to target other pediatric brain tumors such as DMG [384], medulloblastoma [385], or AT/RT [386]. Therefore, it would be interesting to test whether the addition of BET inhibitors would improve the effect of EZH2 inhibitors on PFA ependymoma cells. The combination with DZNep, which showed the strongest effect of all tested EZH2 inhibitors in my *in vitro* PFA ependymoma treatments (**Figure 35**), could be promising.

Although the combination of USP7 and BET inhibitors showed synergy in our study, translating *in vitro* findings into clinical trials and patient treatments can be difficult. Extensive preclinical (animal) studies are necessary to generate sufficient confidence in the treatment before therapies can be applied to patients. The treatment of the BT232-PDOX model with the USP7 inhibitors P22077 and P005091 failed to reduce tumor growth (**Figure 27**). The reasons for this could be manifold, including the limitation that only one model was tested *in vivo*. Although the BT232 cells showed sensitivity to USP7 inhibition *in vitro* (**Figure 24**), the model might be insensitive as PDOX, which could be confirmed by extending the tested PFA ependymoma models. Another reason could be the pharmacokinetic properties of P22077 and P005091, like their absorption and bioavailability. Low absorption or bioavailability would lead to only little or no drug reaching the blood stream and the tumor, which is already lowered by the i.p. administration compared to an intravenous injection [387]. For both inhibitors, just like for all other available USP7 inhibitors, these measures are not published, even though P22077 and P005091 are the two USP7 inhibitors that have been used in *in vivo* studies the most [388]. The amount of compound reaching the tumor could also be limited by the administered drug concentrations. As seen in my toxicity study though (**Figure 27**), no higher doses could have been administered without causing high general toxicity. One reason for this might be the ubiquitous expression of USP7 and its important role in central nervous system development [261]. Furthermore, pharmacokinetic parameters such as excretion rates, plasma clearance or half-life are not available for any USP7 inhibitors. These measures describe how the drug is handled by the body: whether it is bound to other proteins or free, how fast it will be removed from the plasma (mainly by the kidneys), how stable it is and how much it will be metabolized [387]. Determining these parameters could help understand whether e.g. a different delivery method, a change of solvent or more frequent dosing could help improve the performance of the drugs. Usually, these parameters are determined using healthy rodent models. For the translation of drugs into clinical settings, the difference between mouse, rat and human, e.g. in their liver metabolism, need to be considered [389]. As can be seen in this work, the development of PROTACS for the degradation of USP7 is an upcoming alternative to small-molecule inhibitors [299, 350, 351]. After the field grew exponentially since the development of the highly effective VHL and CRBN-based degraders [348], clinical development started in 2019 with the first clinical phase I trial of the PROTAC ARV-110 (NCT03888612), which targets the androgen receptor, and showed drug-like properties and safety in patients. Currently, the estrogen receptor targeting PROTAC Vepdegestrant (ARV-471) is in a phase III trial (NCT05654623) and was approved for fast track development by the food and drug agency (FDA) in the USA. A smaller E3-ligase independent degrader of the estrogen receptor has been approved for treatment of estrogen receptor–positive, human epidermal growth factor receptor 2–negative advanced breast cancer in January 2023 as first of its kind [390, 391].

Another major obstacle for brain tumor treatment is the BBB penetrance of drugs. The BBB is a physiological semi-permeable barrier that prevents molecules and cells from entering the brain. Surrounding the blood vessels in the CNS, the neurovascular unit (NVU) is an organized and functional structure composed of extracellular matrix (ECM) and different cell types such as endothelial cells, neurons, astrocytes, microglia and pericytes. The endothelial cells line the lumen and are connected via junctional complexes formed from tight junction proteins such as claudins, occludins, cadherins or connexins, which tighten the BBB and regulate the pericellular entry. Molecules can also cross the BBB via passive diffusion, transcellular lipophilic transport, or assisted by different transporters [392]. At the same time, molecules are constantly pumped back to the lumen of the blood stream by efflux pumps like the ATP-binding cassette transporters (ABC transporters) [393]. To preempt this problem, I used *in silico* prediction tools for BBB penetrance that base their prognosis on mathematical modeling, previous publications and the physio-chemical properties of the compounds. P005091 and P22077 were chosen over the USP7 inhibitor FT671, as the overall prediction for BBB penetrance was good for P005091 and medium for P22077, indicating potential BBB penetrance (**Table 15**). One publication even reported a successful *in vivo* treatment of an orthotopic glioblastoma model with P005091 [325]. However, a reason for the successful treatment with P005091 in this study could have been a leaky and tumor-disrupted BBB. Especially for glioblastoma, many studies have shown that the BBB in these patients is altered at least partially [394]. However, little is known about the BBB or blood-tumor barrier in PFA ependymoma and so it should be assumed to be intact.

Several methods can be applied to measure BBB penetrance of a drug, but the standard is the MS-based detection of compound in blood-free brain or tumor sections [395]. Therefore, I had collected blood, tumor, and brain tissue from USP7 inhibitor treated BT232-PDX mice from 1h after their last injection and submitted them for compound concentration determination. However, the available liquid chromatography and MS/MS setup was not able to detect P22077 or P005091, as both compounds, which are highly similar in structure, did not ionize in the applied electrospray ionization. An alternative method to ionize and then quantify could have been a Matrix Assisted Laser Desorption/Ionization (MALDI), but the method was not available at his point. Instead, a proof of concept study in a subcutaneous BT232 PDX model is being performed at the moment, testing the efficacy of P005091, alone or in combination with the BET inhibitor OTX015. OTX015 is a well-studied, orally available BET inhibitor, which already has been used in pre-clinical studies on glioblastoma and was tolerated well in a phase IIa study, which is why it will be included here [396-398]. Further, the pharmacokinetic characterization of OTX015 from the human phase I study reported plasma concentrations in patients that resemble the applied *in vitro* concentrations for synergism with USP7 inhibitors [399]. Additionally, these plasma concentrations were shown to be reached with safely tolerated doses in mice [400]. Another BET inhibitor BMS-986378 (CC-90010) is currently in clinical trials for pediatric brain tumors and evaluation of brain penetrance is ongoing (NCT04047303; NCT04324840). Nevertheless, there is a need and potential market for new specific, well-tolerated and CNS penetrant bromodomain inhibitors [401].

Another strategy to overcome the BBB penetrance limitation for treatment of CNS tumors is to improve the delivery of drugs to the tumor, either by modifications to the compound itself or applying nanodrug delivery systems. The active metabolite of topoisomerase II inhibitor irinotecan, SN-38, has been modified in multiple ways to better its performance. Nanoparticles - lipid-based, protein-based, polymeric or others- as well as packaging of drug into liposomes or micelles, have been used to improve intravenous delivery, while oral delivery and functionality were mainly optimized by chemical compound modifications [402]. Adding poly(ethylene glycol) (PEG) as macromolecular carrier to four coupled SN-38 molecules enhanced the retention time of SN-38 via degradation protection, increased its BBB penetrance and the accumulation of SN-38 in solid tumor tissue [403, 404], optimizing it for the use in brain cancer therapy. In ependymoma, nanoparticle delivery of short interfering RNAs (siRNAs) have been used to radiosensitize cultured cells [405], while a 2023 *in vivo* study of medulloblastoma used nanoparticles to deliver the PARP inhibitor Talazoparib to the brain [406].

Since Talazoparib is an otherwise non-CNS penetrant PARP inhibitor, technological improvements such as nanoparticle delivery or pegylation could also help the use of PARP inhibitors in PFA ependymoma [407]. The most commonly used BBB-penetrant PARP inhibitor is Pamiparib [174, 372], as for many other inhibitors BBB penetrance is opposing their PARP trapping ability [408]. In my experiments, Pamiparib showed strong low micromolar potency for PFA ependymoma cells (**Figure 37**). Currently, other CNS penetrant PARP inhibitors are in clinical development, such as the PARP1 -specific AZD9574 [409] or the dual PARP and tankyrase inhibitor E7449 (Stenoparib) [410]. Talazoparib as strong PARP trapper showed the highest potency in PFA ependymoma cells, affecting EPD210FH cells at an IC50 of 50 nM and BT214 cells at 470 nM. Unpublished experiments from the ITCC-P4 consortium tested Talazoparib in combination with pegylated SN-38 in an ependymoma PDX model and showed strong tumor regression. The fact that Talazoparib also affected the ST-ZFTA cell line EP1NS at a slightly lower IC50 (40 nM) could indicate that the effect of Talazoparib may not be mediated by PFA ependymoma biology, even though previous publications had suggested a PARP inhibition sensitizing role for EZHIP [170, 371, 411]. However, ST-ZFAT cells may just be sensitive for other reasons, but since the human astrocytes also showed sensitivity (IC50 410 nM), an insensitive cell line as comparison is still missing to rule out unspecific toxicity. Nevertheless, Talazoparib showed the strongest effect of all drugs tested in my studies, which should be followed up on. PARP inhibitors are established in the clinics for the use in DNA repair deficient, mainly BRCA mutated, cancers like breast, prostate or ovarian cancer [412], and are also being tested for use in brain cancer, either as single treatment or in combination with radio-or chemotherapy [413]. Clinical research on PARP inhibitor treatment of ependymoma is limited. One case report recently reported stable radiological disease of patient with a SP-MPE after 10 cycles of Olaparib combined with Temozolomide [414]. Additionally, two studies on the combination of PARP inhibitors with chemotherapy (temozolomide) in pediatric cancers included patients with ependymoma. The combination with Veliparib lead to stable disease for over six months in one out of four ependymoma patients [415], while the combination of temozolomide with Talazoparib did not induce a response in two pediatric ependymoma cases [416]. One similar study testing the use of Olaparib in a multitude of relapsed or refractory patients with DNA damage repair defects is ongoing (NCT03233204). Significance of these studies should not be overrated, as patient numbers are anecdotally and no subgroups have been specified.

The second strongest response on PFA ependymoma survival I observed was elicited by DZNep (**Figure 35**). The SAM hydrolase inhibitor, which is not specific for EZH2 but inhibits all SAM-dependent histone methyltransferases, has been reported to selective target PFA ependymoma compared to ST ependymoma *in vitro* before, while reducing H3K27me3 levels through PRC2 degradation [154]. In the 2014 study, DZNep targets PFA ependymoma cells at an IC50 of 95-262 nM, which is comparable to the 160 nM reported in my work (**Table 16**). *In vivo* PFA ependymoma PDOX treatments delayed tumor growth, but failed to cure mice [154]. Checking whether DZNep also degrades PRC2 components in my cells would be a good next step to study its effects. Degradation of PRC2 components would be in line with a proposed “Goldilocks-models” for PFA ependymoma, hypothesizing that the activity of the PRC2 complex, even though already inhibited by EZHIP, is still crucial for PFA ependymoma biology and presents a targetable vulnerability [120]. Overall, the role of EZH2 in cancer is highly context dependent and it can have oncogenic as well as tumor suppressive functions [198]. Since it is found mutated or overly expressed in many entities, increasing attention has been on developing EZH2 inhibitors for the clinics. In 2020, Tazemetostat has been approved by the FDA for the treatment of follicular lymphoma and epithelioid sarcoma [417]. However, Tazemetostat barely affected the EPD210FH PFA ependymoma cells tested in this study (**Table 16**), further indicating that PRC2 degradation might be the effect to use for targeting PFA ependymoma.

Furthermore, the combination of DZNep with PARP inhibitors should be tested for treating PFA ependymoma. EZH2 inhibition has been proposed to overcome PARP resistance, as EZH2 itself regulates the expression of DNA repair mediators. As a result, dual PARP and EZH2 inhibitors have been developed recently [418, 419]. However, the results of PARP and EZH2 inhibitor combinations seem to be again context dependent [420]. In BRCA2-deficient breast cancer cells, the addition of the EZH2 inhibitor GSK126 diminished the anti-proliferative effect of the PARP inhibitor [421]. Whether and how EZHIP and its presumed DNA repair impairing function would affect the combination treatment of EZH2 and PARP inhibitors would have to be evaluated.

EZHIP is the presumed main driver of PFA ependymoma [4]. Since EZHIP itself does not possess any known enzymatic functions and executes its tumor-driving inhibition of EZH2 by steric hindrance, removing EZHIP from the tumors is another promising approach to target PFA ependymoma. Thus, creating a degrader or PROTAC for EZHIP would be a good step, but is not easily achieved even though methods are improving rapidly [422]. To design a bimodal PROTAC, the ligand binding the protein of interest (EZHIP), a ligand recruiting the E3 Ligase and a linker need to be determined. The structure of these parts themselves as well as the combination of all three determine the efficacy of the PROTAC [423, 424]. Different E3 Ligases can be recruited by PROTACs, but VHL and CRBN are the most common ones and seem to work well for many targets independent of whether they target them physiologically or not. Since I could show that EZHIP is ubiquitinated as part of its stability regulation in this thesis, knowing which E3 Ligase is ubiquitinating EZHIP could be employed for PROTAC development. So far though, I was not able to identify a clear candidate from the available IP-MS data. From literature, a few E3 Ligases are known to interact with, counteract and be regulated by USP7, such as the well-studied MDM2 [322]. Another example is the E3 Ligase TRIM27, whose stability is also regulated by USP7 [259, 289]. The other hurdle to overcome would be to find a ligand to specifically bind EZHIP. Since only the structure of the EZH2 binding part of EZHIP is resolved, knowledge-based designs won´t be reasonable, but compound libraries will probably have to be tested. Of course, one could also try to base the EZHIP binding element of the EZH2 catalytic site structure. However, this might bind to the structurally highly similar tail of H3 as well, which would nullify the desired effect of restoring H3K27me3 signals [5]. Additionally, targeting single members of multi-protein complexes can be tricky. Bringing the E3 ligase into proximity can induce the ubiquitination and degradation of other complex members, which can be beneficial if the complete removal of a complex is desired [425, 426]. In the case of EZHIP, this could lead to the degradation of the PRC2 complex, which would not restore H3K27me3 levels, but might still be affecting PFA ependymoma survival. This so-called bystander effect could also be a reason why the PROTAC-mediated degradation of USP7 has the strongest effect on EZHIP protein levels, compared to USP7 KO or inhibition.

A question that remains to be answered after this thesis work is the role of the mutations found in EZHIP. Due to their location close to predicted USP7 TRAF-like domain recognition sites, I had hypothesized that they might influence the regulation of EZHIP by USP7, which seems not to be the case (**Figure 19**). However, as some mutations (S30P, F110C, R214G) showed an increase in protein levels, they might still influence EZHIP protein stability through other mechanisms. Of course, I only tested the effect of five hand-selected mutations in this study. Increasing the number of tested mutations may help to gain further clarity on the role of these mutations. Further, combining several mutations in one overexpression construct may improve visibility of smaller effects that alone would be under the detection limit. However, in patients we never see two mutations at the same time. Interestingly, Pajtler *et al.* did not see any increased protein levels of EZHIP mutants in their overexpression experiments, but showed that the mutants they tested (T73S, I88F, Y184C) still localize to the nucleus and reduce H3K27me3 levels [153]. I also did not test any consequences of the mutations for the non-PRC2 mediated functions described for EZHIP [170] or characterized the mutants with regards to their proliferative effect or tumor-initiating potential. Even though they are not detected in all PFA ependymoma patients, the mutations may play a role in the early stages of tumor development.

However, further studies to characterize the role of the EZHIP mutations and learn more about EZHIP itself are limited by a lack of enough and easy to handle PFA ependymoma models. Modern genetic engineering methods such as base editing can enable elegant studies introducing point mutations into the germline of cell lines [427]. However, applying these methods to PFA ependymoma cell lines is very difficult, as they cannot be grown as single cells, which would be needed to grow a homogenously mutated cell line. To understand EZHIP`s role in tumor initiation, introducing (mutated) EZHIP into cerebellar progenitor cells, e.g. derived from iPSCs or cerebellar organoids, may aid identifying novel functions and lead to a better understanding of the tumor-initiating function of EZHIP. So far though, no EZHIP-driven organoid model for PFA ependymoma has been published. Earlier attempts from my group to introduce tumors in mice by EZHIP overexpression failed. Jens Hübner had co-electroporated plasmids for the expression of *EZHIP* and *insulin growth factor 2* (*IGF2*), a known tumor progression factor highly expressed in PFA ependymoma, into the fourth ventricle of E13.5 Ctrl:CD1(ICR) embryos, but mice did not develop tumors (unpublished data). However, this experiment only tested one single developmental timepoint and did not co-introduce any background mutations, as they are needed e.g. in DMG mouse models, where histone 3 mutations alone also do not induce tumors. But in contrast to DMG, where several recurrent co-mutations have been identified next to the histone 3 mutations, such co-mutations have not been identified in PFA ependymoma [4, 186]. Most likely, it is another aberrantly expressed gene that is needed to drive tumorigenesis together with EZHIP. A syngeneic GEMM of PFA ependymoma driven by EZHIP expression (alone or in combination with one or more other genes) would be an additional great model system for the investigation of the role of EZHIP and its mutations in PFA ependymoma. It would not only allow the study of EZHIP at different timepoints during PFA ependymoma development, but would also allow the observation of immune-related phenotypes. All in all, further studies will be needed to understand the role of these EZHIP mutations and their potential implications for e.g., patient stratifications or treatment options.

Targeting the immune system has emerged as growing pillar of cancer therapy [428], but the role of the immune system in PFA ependymoma is not well understood. Although ependymoma are considered “immune cold” showing little immune cell infiltration, which is common in many tumors of the brain, recent studies characterized a substantial myeloid cell compartment in ependymoma and detected over 30% immune cells, which is higher than in other pediatric brain tumors [429]. In PFA ependymoma, eight myeloid-derived subpopulations were identified that mainly localize in hypoxic and necrotic areas and create an immunosuppressive environment [430]. Clinical trials on immunotherapy in pediatric brain tumors mainly focus on H3K27M mutated DMGs and include cancer vaccines (priming the immune cells to target the cancer cells), adoptive cellular therapies like T-lymphocytes expressing chimeric antigen receptors (CAR T-cells), or immune checkpoint blockage [431]. One trial testing the anti-programmed cell death protein 1 (PD-1) antibody Pembrolizumab in pediatric solid tumors (NCT02359565) also recruits patients with recurrent ependymoma. PD-1 is a lymphocyte immune checkpoint receptor, which detects its ligand PD-L1 on target cells as “don´t eat me” signal, preventing cytotoxic actions. Tumor cells often upregulate PD-L1 expression to escape immune cell regulation [432]. Between the molecular subgroups of ependymoma, ST-ZFTA tumors show high PD-L1 expression in tumor and myeloid cells, indicating potential for checkpoint blockage treatment [433, 434]. Interestingly, USP7 has been connected to PD-L1 expression. Their mRNA expression was shown to correlate in gastric cancer and USP7 stabilizes PD-L1 protein in macrophages and cancer cells [435, 436]. Therefore, inhibition of USP7 has been proposed to sensitize tumor cells to T-cell killing in combination therapy with anti-PD-1 antibodies [436, 437]. Thus, adding immune checkpoint blockage to the single drug activity of USP7 inhibitors might be a promising strategy to target PFA ependymoma.

CAR T-cells are T lymphocytes, extracted from the patient and reintroduced, which are engineered *ex vivo* with an additional receptor directing the cells to new target molecules presented on the outside of the cancer cells [438]. One common CAR T target in pediatric solid tumors is B7-H3, a immunoregulatory transmembrane protein that is not expressed in normal tissue but high in many brain tumors including ependymoma [439]. Medulloblastoma, osteosarcoma and Ewing sarcoma have been shown to respond to B7-H3 CAR T therapy *in vivo*, and clinical trials, mainly in glioma, are ongoing [439, 440]. The disialoganglioside GD2 has been shown to be an effective CAR T target for H3K27M-driven DMGs *in vivo* [441, 442], and first clinical tests reported only local toxicities and improved clinical and radiographic presentation of the patients [443]. Since DMGs and PFA ependymoma share an oncogenic driving mechanism, anti-GD2 therapy may also be tested in PFA ependymoma, potentially as combination therapy as it was used to eradicate neuroblastomas *in vivo* [444]. A recent study in medulloblastoma used the EZH2 inhibitor Tazemetostat to increase GD2 expression and sensitize cells to GD2 CAR T-cell treatments [445], a strategy which may be applied to PFA ependymoma cells as well, potentially combining DZNep with the CAR therapy and using its additional viability reducing potency. As CAR T therapy develops, a trivalent CAR targeting EPHA2, HER2 and the interleukin 13 receptor has been tested successfully in a PFA PDX mouse model recently [446], providing a rationale to further expand the research of immunotherapies for PFA ependymoma.

Taken together, my thesis presents a starting point for targeted PFA ependymoma therapies focused on USP7 inhibition. However, USP7 inhibitor treatment alone in orthotopic PFA ependymoma models did not reduce tumor growth. Therefore, either more effective or brain penetrant USP7 inhibitors are needed. Alternatively, USP7 inhibitors may be combines with synergistic drugs such as the BET inhibitors presented in this study. Subcutaneous *in vivo* combination treatments to confirm the feasibility of USP7 and BET inhibitor treatments in PFA ependymoma are ongoing. However, more work is needed to progress PFA ependymoma therapies from bench to bedside. Advancing the understanding of PFA ependymoma biology will be the basis to fuel new hypotheses and mechanistically characterize drug targets, which cannot be done without creating more and better models. More and higher-complexity models will also improve the preclinical drug selection and testing, and allow for more meaningful *in vivo* treatments.

VII Supplementary Material

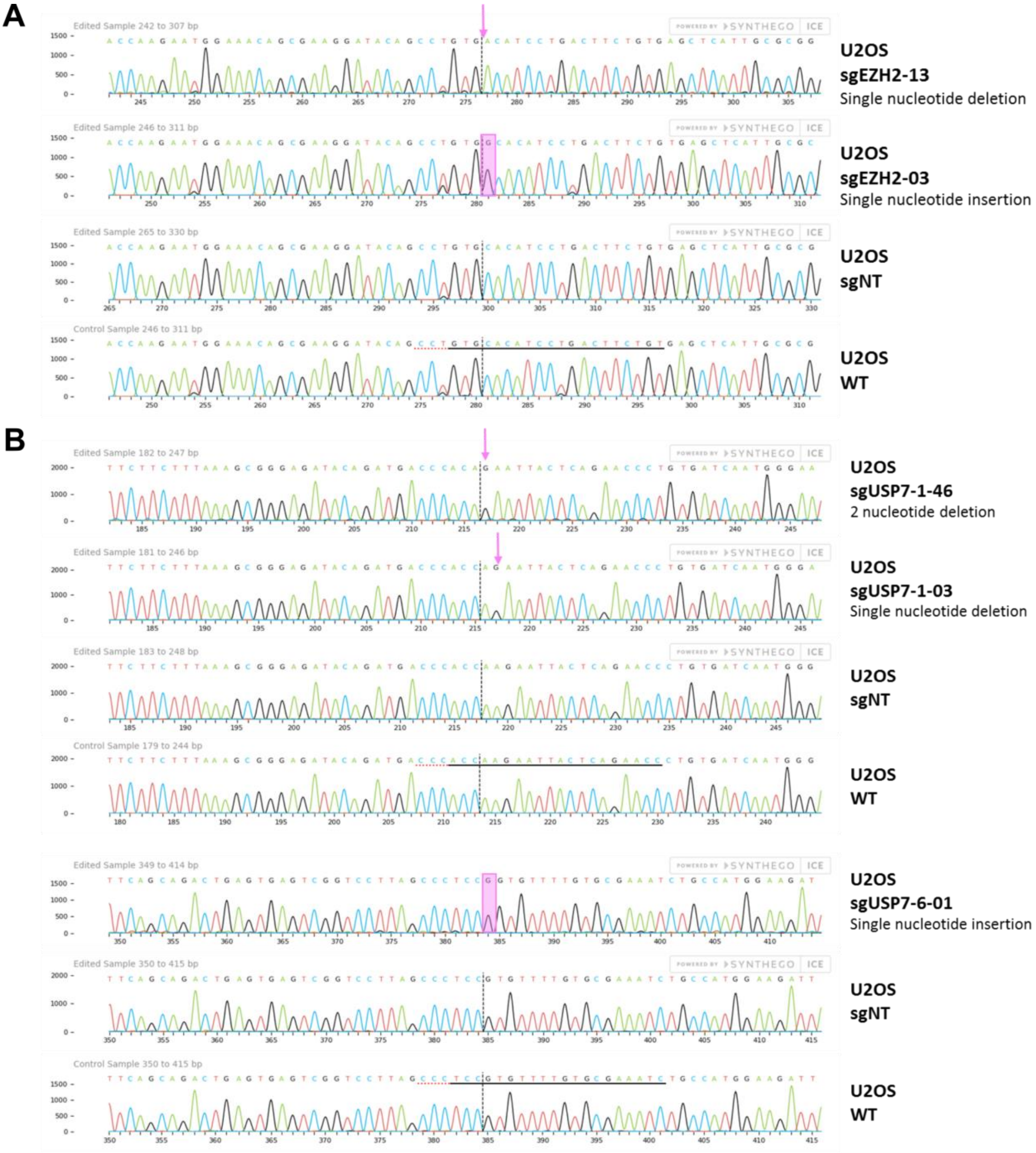

Supplementary Figure 1 | Chromatograms of U2OS EZH2 KO and USP7 KO clones

*(**A**) Chromatograms showing sanger sequencing results of genomic DNA of U2OS CRISPR clones (WT (no CRIPSR), sgNT (Control), sgEZH2 clone 03 and sgEZH2 clone 13). Pink box and arrow indicate the location of Indels. (**B**) Chromatograms showing sanger sequencing results of genomic DNA of U2OS CRISPR clones (WT (no CRIPSR), sgNT (Control), sgUSP7-6 clone 01, sgUSP7-1 clone 03 and clone 46). Pink box and arrow indicate the location of Indels.*

Supplementary Table 1 | Drug Library for the USP7i +X combination screen

Drug	Target/Mechanism
A-1155463	BCL-XL inhibitor
A-1210477	MCL-1 inhibitor
A-1331852	Bcl-XL inhibitor
Abexinostat	pan-HDAC
Afatinib	EGFR inhibitor
Alectinib	ALK (incl gatekeeper mut) inhib
Alpelisib	PI3K Inhibitor
AMG-232	MDM2 inhibitor
APR-246	P53 activator, thioredoxin reductase 1 inhibitor
APR-246_cr	P53 stabilizer
Axitinib	VEGFR, PDGFR, KIT inhibitor
Barasertib	Aurora B
Bortezomib	Proteasome inhibitor (26S subunit)
Busulfan	Alkylating agent
Cabozantinib	VEGFR2, Met, FLT3, Tie2, Kit and Ret inhibitor
Carboplatin	Platinum-based antineoplastic agent
CCNU (Lomustine)	Alkylating agent
Ceritinib	ALK inhibitor
Chaetocin	HMT
Chloroquine	Antimalaria agent; chemo/radio sensitizer
Cisplatin	Platinum-based antineoplastic agent
Cobimetinib	MEK1/2 inhibitor
Copanlisib	pan calss-I PI3K inhibitor
Crizotinib	ALK, c-Met inhibitor
CUDC-907	HDAC1/2/3/10
Cytarabine	Antimetabolite, interferes with DNA synthesis
Dabrafenib	B-Raf(V600E) inhibitor
Dactinomycin	RNA and DNA synthesis inhibitor
Dasatinib	Abl, Src, Kit, EphR... Inhibitor
Daunorubicin	Topoisomerase II inhibitor
Decitabine	Nucleoside analog DNA methyl transferase inhibitor
Doxorubicin	Topoisomerase II inhibitor
Entinostat	HDAC inhibitor
Entrectinib	TRK, ROS1, ALK inhibitor
Erdafitinib	FGFR inhibitor
Erlotinib	EGFR inhibitor
Etoposide	Topoisomerase II inhibitor
Everolismus	binds FKBP12, causes inhibition of mTORC1
Foretinib	MET, VEGFR2 inhibitor
Gemcitabine	Antimetabolite; Nucleoside analog
GSK2879552 2HCl	LSD1
I-BET151	BET family inhibitor

Idasanutlin	MDM2 inhibitor
Imatinib	Abl, Kit, PDGFRB inhibitor
Irinotecan	Topoisomerase I inhibitor
Isotretionin	retinoid and vitamin A derivative
Lapatinib	HER2, EGFR inhibitor
Larotrectinib	TRK inhibitor
Lorlatinib	ROS1, ALK, Tki
Melphalan	Alkylating agent
Mercaptopurine	Antimetabolite
Merestinib	Met inhibitor
Methothrexate	Antimetabolite; Anti-folate agent
MI-2	menin MLL-interaction
Mitoxantrone	Topoisomerase II inhibitor
Mivebresib	BET family bromodomain
Navitoclax	Bcl-2/Bcl-xL inhibitor
Nilotinib	Abl inhibitor
Olaparib	PARP inhibitor
ONC201	DRD2 antagonist
Paclitaxel	Mitotic inhibitor, taxane microtubule stabilizer
Pacritinib	JAK2, FLT3
Palbociclib	CDK4/6 inhibitor
Panobinostat	HDAC inhibitor
Pazopanib	VEGFR inhibitor
Ponatinib	Broad TK inhibitor
Pracinostat	pan-HDAC
Pralsetinib	RET inhibitor
Quercetin	SIRT1
Rapamycin	binds FKBP12, causes inhibition of mTORC1
Ribociclib	CDK4/6 inhibitor
Romidepsin	HDAC inhibitor
Ruxolitinib	JAK1&2 inhibitor
Salermide	SIRT1, SIRT2
Selinexor	CRM1 inhibitor
Selumetinib	MEK1/2 inhibitor
SN-38	Topoisomerase I inhibitor (active metabolite of irinotecan)
Sorafenib p-Toluenesulfonate Salt	B-Raf, FGFR-1, VEGFR-2 & -3, PDGFR-beta, KIT, and FLT3 inhib
Staurosporin	positive control
Sunitinib	Broad TK inhibitor
TAK-901	Aurora A/B
Talazoparib	PARP1/2 inhibitor
Tazemetostat	EZH2 inhibitor
Temozolomide	Alkylating agent
Temsirolimus	binds FKBP12, causes inhibition of mTORC1
Tenovin-6	Tenovin-6 is a small molecule activator of P53 transcriptional activity
TG101209	JAK2

Thioguanine	Antimetabolite; Purine analog
Thiotepa	Alkylating agent
TIC-10 (ONC201)	inactivates Akt and ERK to induce TNF-related apoptosis-inducing ligand (TRAIL) through Foxo3a
Topotecan	Topoisomerase I inhibitor. Camptothecin analog
Trametinib	MEK1/2 inhibitor
Valproic acid	HDAC inhibitor
Vandetanib	VEGFR,EGFR, RET inhibitor
Vemurafenib	B-Raf(V600E) inhibitor
Venetoclax	Bcl-2-selective inhibitor
Vinblastine	Mitotic inhibitor. Vinca alkaloid microtubule depolymerizer
Vincristine	Mitotic inhibitor. Vinca alkaloid microtubule depolymerizer
Vinorelbine	Mitotic inhibitor. Vinca alkaloid microtubule depolymerizer
Vismodegib	Smothened (Hh) inhibitor
Volasertib	PLK1 inhibitor
Vorinostat	HDAC inhibitor

Supplementary Table 2 | Targeted epigenetic drug library

Drug name	**Mechanism/targets**
(-)-Epigallocatechin Gallate	telomerase and DMT
(+)-JQ1	BET bromodomain
4SC-202	class I HDAC
ABBV-744	BET bromodomain - BRD2, 3, 4
Abexinostat (PCI-24781)	pan-HDAC
Acetyl Resveratrol	antioxidant
AICAR (Acadesine)	AMPK activator
Alisertib (MLN8237)	Aurora A
Amodiaquine dihydrochloride dihydrate	histamine N-methyl transferase
Anacardic Acid	p300 and p300/CBP-associated factor histone acetyltranferases
Apabetalone (RVX-208)	BET bromodomain
Atuveciclib (BAY-1143572)	PTEFb/CDK9
Azacitidine	DNA methyltransferase
AZD1208	Pim1, Pim2, and Pim3 (serine/threonine kinase inhibitor)
Barasertib (AZD1152-HQPA)	Aurora B
BAY 87-2243	HIF-1
Belinostat (PXD101)	HDAC1 and HDAC3
BI-7273	BRD9
BI-847325	dual MEK/Aurora kinase
Birabresib (OTX015)	BET bromodomain
BRD4770	BRD4770

Bromosporine	broad spectrum inhibitor for bromodomains - BRD2, 4, 9 and CECR2
Cambinol	SIRT1 and SIRT2
CAY10602	SIRT1
Chaetocin	HMT
Citarinostat (ACY-241)	HDAC6
CPI-1205	KMT
CUDC-907	HDAC1/2/3/10
Curcumin	HDAC
CYC116	Aurora A/B
Daminozide	KDM2/7 JmjC
Danusertib (PHA-739358)	Aurora kinase
Daphnetin	protein kinase C
Daprodustat (GSK1278863)	hypoxia-inducible factor-prolyl hydroxylase
dBET1	CRBN-based BET degrader
Decitabine	DNA methyltransferase
EBI-2511	EZH2
EED226	PRC2
Entacapone	catechol-O-methyltransferase(COMT)
Entinostat (MS-275)	HDAC1 and HDAC3
Enzastaurin (LY317615)	protein kinase C
EPZ004777	DOT1L
Givinostat (ITF2357)	HDAC
GSK 5959	BRPF1 bromodomain
GSK J1	JMJD3/UTX
GSK J4 HCl	JMJD3/UTX
GSK1324726A (I-BET726)	BET family proteins
GSK2801	BAZ2A/B
GSK2879552 2HCl	LSD1
GSK3326595 (EPZ015938)	arginine methyltransferase 5
GSK503	EZH2
GSK591	arginine methyltransferase
GSK6853	BRPF1
I-BET-762	BET family proteins
INCB057643	BET
JQ-EZ-05 (JQEZ5)	EZH1/2
MBQ-167	dual Rac and Cdc42
Metformin HCl	glucose production suppressor
MI-2 (Menin-MLL Inhibitor)	menin-MLL interaction
Mitoxantrone 2HCl	type II topoisomerase
Mivebresib(ABBV-075)	BET family bromodomain
Mocetinostat (MGCD0103)	HDAC1
MS436	BET bromodomain
Niraparib (MK-4827)	PARP1/2

Olaparib (AZD2281, Ku-0059436)	PARP1/2
ORY-1001 (RG-6016) 2HCl	LSD1/KDM1A
Pacritinib (SB1518)	JAK2 and FLT3
Pamiparib (BGB-290)	PARP1 and PARP2
Panobinostat (LBH589)	broad spectrum-HDAC
PCI-34051	HDAC8
Pracinostat (SB939)	pan-HDAC
Procainamide HCl	sodium channel blocker, and also a DNA methyltransferase inhibitor
Quercetin	SIRT1
Resminostat	HDAC1, 3, 6
Reversine	pan-aurora
RG108	DMT
Ricolinostat (ACY-1215)	HDAC6
Romidepsin (FK228, Depsipeptide)	HDAC1 and HDAC2
Rucaparib (AG-014699,PF-01367338) phosphate	PARP1 and PARP2
Ruxolitinib (INCB018424)	JAK1/2
Salermide	SIRT1 and SIRT2
Selisistat (EX 527)	SIRT1
SF2523	PI3Kα, PI3Kγ, DNA-PK, BRD4 and mTOR
SGC-CBP30	CREBBP/EP300
SRT2104 (GSK2245840)	SIRT1
SRT3025 HCl	SIRT1
Tacedinaline (CI994)	class I HDAC
TAK-901	Aurora A/B
Tazemetostat (EPZ-6438)	EZH2
Tenovin-6	Tenovin-6 is a small molecule activator of P53 transcriptional activity
TG101209	JAK2
TH34	HDACs 6, 8 and 10
TIC10 (ONC201)	Inactivates Akt and ERK to induce TNF-related apoptosis-inducing ligand (TRAIL) through Foxo3a
Tofacitinib (CP-690550, Tasocitinib)	JAK3
Tozasertib (VX-680, MK-0457)	pan-Aurora
Tranylcypromine (2-PCPA) HCl	CYP2A6
Tubastatin A	HDAC6
Tucidinostat (Chidamide)	HDAC1, 2, 3 and 10
UNC1999	EZH1/2
Valproic acid	HDAC
Vorinostat (SAHA, MK0683)	HDAC
WM-1119	KAT

VIII Publications

Ongoing work

Jenseit, A. ,Camgöz, A., Mauermann, M., Mack, N., Schwalm, B., Mohr, J., Wittenburg, S., Steinebach, C. Gütschow, M., Peterziel, H., Friedenauer, A., Jaunecker, C., Lötsch-Gojo, D., Oehme, I., Pfister, S.M., Kool, M. **USP7 de-ubiquitinates and stabilizes EZHIP making it a therapeutic target in PFA ependymoma.** Manuscript in preparation

Publications in peer-reviewed journals

Mazzaferro, E., Mujica, E., Zhang, H., Emmanouilidou, A., **Jenseit, A**., Evcimen, B., Dethlefsen, O., Loos, R.F.J., Vienberg, S.G., Larsson, A., Allalou, A., den Hoed, M. (2024) **Functionally characterizing obesity-susceptibility genes using CRISPR/Cas9, in vivo imaging and deep learning**. Submitted

Okonechnikov, K., Camgoz, A., Chapman, O., Wani, S., Park, D. E., Hubner, J. M., Chakraborty, A., Pagadala, M., Bump, R., Chandran, S., Kraft, K., Acuna-Hidalgo, R., Reid, D., Sikkink, K., Mauermann, M., Juarez, E. F., **Jenseit, A**., Robinson, J. T., Pajtler, K. W., Milde, T., Jager, N., Fiesel, P., Morgan, L., Sridhar, S., Coufal, N. G., Levy, M., Malicki, D., Hobbs, C., Kingsmore, S., Nahas, S., Snuderl, M., Crawford, J., Wechsler-Reya, R. J., Davidson, T. B., Cotter, J., Michaiel, G., Fleischhack, G., Mundlos, S., Schmitt, A., Carter, H., Michealraj, K. A., Kumar, S. A., Taylor, M. D., Rich, J., Buchholz, F., Mesirov, J. P., Pfister, S. M., Ay, F., Dixon, J. R., Kool, M., Chavez, L. (2023). **3D genome mapping identifies subgroup-specific chromosome conformations and tumor-dependency genes in ependymoma**. Nat Commun 14, 2300. 10.1038/s41467-023-38044-0.

Jenseit, A., Camgoz, A., Pfister, S.M., and Kool, M. (2022). **EZHIP: a new piece of the puzzle towards understanding pediatric posterior fossa ependymoma**. Acta Neuropathol 143, 1-13. 10.1007/s00401-021-02382-4.

Kosti, A., de Araujo, P. R., Li, W. Q., Guardia, G. D. A., Chiou, J., Yi, C., Ray, D., Meliso, F., Li, Y. M., Delambre, T., Qiao, M., Burns, S. S., Lorbeer, F. K., Georgi, F., Flosbach, M., Klinnert, S., **Jenseit, A**., Lei, X., Sandoval, C. R., Ha, K., Zheng, H., Pandey, R., Gruslova, A., Gupta, Y. K. ,Brenner, A., Kokovay, E., Hughes, T. R., Morris, Q. D., Galante, P. A. F., Tiziani, S., Penalva, L. O. F. (2020). **The RNA-binding protein SERBP1 functions as a novel oncogenic factor in glioblastoma by bridging cancer metabolism and epigenetic regulation**. Genome Biol 21, 195. 10.1186/s13059-020-02115-y.

IX References

1. Pajtler, K.W., et al., *Molecular Classification of Ependymal Tumors across All CNS Compartments, Histopathological Grades, and Age Groups.* Cancer Cell, 2015. **27**(5): p. 728-43.
2. Ostrom, Q.T., et al., *CBTRUS Statistical Report: Primary Brain and Other Central Nervous System Tumors Diagnosed in the United States in 2015-2019.* Neuro Oncol, 2022. **24**(Suppl 5): p. v1-v95.
3. Pohl, L.C., et al., *Molecular characteristics and improved survival prediction in a cohort of 2023 ependymomas.* Acta Neuropathol, 2024. **147**(1): p. 24.
4. Jenseit, A., et al., *EZHIP: a new piece of the puzzle towards understanding pediatric posterior fossa ependymoma.* Acta Neuropathol, 2022. **143**(1): p. 1-13.
5. Hubner, J.M., et al., *EZHIP/CXorf67 mimics K27M mutated oncohistones and functions as an intrinsic inhibitor of PRC2 function in aggressive posterior fossa ependymoma.* Neuro Oncol, 2019. **21**(7): p. 878-889.
6. Claudia Spix, F.E., Desiree Grabow, Cécile Ronckers, *Krebs im Kindes- und Jugendalter in Deutschland – ein Überblick.* Journal of Health Monitoring, 2023. **8**(2): p. 82-97.
7. Gupta, M., et al., *The Blood-Brain Barrier (BBB) Score.* J Med Chem, 2019. **62**(21): p. 9824-9836.
8. Pozhidaeva, A. and I. Bezsonova, *USP7: Structure, substrate specificity, and inhibition.* DNA Repair (Amst), 2019. **76**: p. 30-39.
9. Lange, S.M., L.A. Armstrong, and Y. Kulathu, *Deubiquitinases: From mechanisms to their inhibition by small molecules.* Mol Cell, 2022. **82**(1): p. 15-29.
10. Erdmann F, K.P., Grabow D, Spix C., *German Childhood Cancer Registry - Annual Report 2019 (1980-2018).* Institute of Medical Biostatistics, Epidemiology and Informatics (IMBEI) at the University Medical Center of the Johannes Gutenberg University Mainz, 2020.
11. Goldstick, J.E., R.M. Cunningham, and P.M. Carter, *Current Causes of Death in Children and Adolescents in the United States.* N Engl J Med, 2022. **386**(20): p. 1955-1956.
12. Siegel, R.L., et al., *Cancer statistics, 2022.* CA Cancer J Clin, 2022. **72**(1): p. 7-33.
13. Behjati, S., R.J. Gilbertson, and S.M. Pfister, *Maturation Block in Childhood Cancer.* Cancer Discov, 2021. **11**(3): p. 542-544.
14. Mack, S.C., et al., *Therapeutic targeting of ependymoma as informed by oncogenic enhancer profiling.* Nature, 2018. **553**(7686): p. 101-105.
15. Capper, D., et al., *DNA methylation-based classification of central nervous system tumours.* Nature, 2018. **555**(7697): p. 469-474.
16. Durbin, A.D., et al., *Selective gene dependencies in MYCN-amplified neuroblastoma include the core transcriptional regulatory circuitry.* Nat Genet, 2018. **50**(9): p. 1240-1246.
17. Kratz, C.P., et al., *Predisposition to cancer in children and adolescents.* Lancet Child Adolesc Health, 2021. **5**(2): p. 142-154.
18. Grobner, S.N., et al., *The landscape of genomic alterations across childhood cancers.* Nature, 2018. **555**(7696): p. 321-327.
19. Averill, L.W., et al., *Update on pediatric leukemia and lymphoma imaging.* Semin Ultrasound CT MR, 2013. **34**(6): p. 578-99.
20. Bhakta, N., et al., *Childhood cancer burden: a review of global estimates.* Lancet Oncol, 2019. **20**(1): p. e42-e53.
21. Bailey, P. and H. Cushing, *Microchemical Color Reactions as an Aid to the Identification and Classification of Brain Tumors.* Proc Natl Acad Sci U S A, 1925. **11**(1): p. 82-4.
22. Scheithauer, B.W., *Development of the WHO Classification of Tumors of the Central Nervous System: A Historical Perspective.* Brain Pathology, 2009. **19**(4): p. 551-564.
23. Zulch, K.J., *Principles of the new World Health Organization (WHO) classification of brain tumors.* Neuroradiology, 1980. **19**(2): p. 59-66.
24. Board, W.C.o.T.E., *Central Nervous System Tumorus*. 5th ed. WHO Classification of Tumours. Vol. 6. 2021.
25. Louis, D.N., et al., *The 2007 WHO classification of tumours of the central nervous system.* Acta Neuropathol, 2007. **114**(2): p. 97-109.
26. Louis, D.N., et al., *The 2016 World Health Organization Classification of Tumors of the Central Nervous System: a summary.* Acta Neuropathol, 2016. **131**(6): p. 803-20.
27. Sturm, D., et al., *New Brain Tumor Entities Emerge from Molecular Classification of CNS-PNETs.* Cell, 2016. **164**(5): p. 1060-1072.

28. Giannini, C., et al., *Oligodendrogliomas: reproducibility and prognostic value of histologic diagnosis and grading.* J Neuropathol Exp Neurol, 2001. **60**(3): p. 248-62.
29. Godfraind, C., *Classification and controversies in pathology of ependymomas.* Childs Nerv Syst, 2009. **25**(10): p. 1185-93.
30. Ellison, D.W., et al., *Histopathological grading of pediatric ependymoma: reproducibility and clinical relevance in European trial cohorts.* J Negat Results Biomed, 2011. **10**: p. 7.
31. Bird, A., *DNA methylation patterns and epigenetic memory.* Genes Dev, 2002. **16**(1): p. 6-21.
32. Titus, A.J., et al., *Cell-type deconvolution from DNA methylation: a review of recent applications.* Hum Mol Genet, 2017. **26**(R2): p. R216-R224.
33. Loyfer, N., et al., *A DNA methylation atlas of normal human cell types.* Nature, 2023. **613**(7943): p. 355-364.
34. Nishiyama, A. and M. Nakanishi, *Navigating the DNA methylation landscape of cancer.* Trends Genet, 2021. **37**(11): p. 1012-1027.
35. Mawrin, C., et al., *A new amplicon-based gene panel for next generation sequencing characterization of meningiomas.* Brain Pathol, 2022. **32**(2): p. e13046.
36. Nikiforova, M.N., et al., *Targeted next-generation sequencing panel (GlioSeq) provides comprehensive genetic profiling of central nervous system tumors.* Neuro Oncol, 2016. **18**(3): p. 379-87.
37. Sturm, D., et al., *Multiomic neuropathology improves diagnostic accuracy in pediatric neuro-oncology.* Nat Med, 2023. **29**(4): p. 917-926.
38. Comitani, F., et al., *Diagnostic classification of childhood cancer using multiscale transcriptomics.* Nat Med, 2023. **29**(3): p. 656-666.
39. Vermeulen, C., et al., *Ultra-fast deep-learned CNS tumour classification during surgery.* Nature, 2023. **622**(7984): p. 842-849.
40. Djirackor, L., et al., *Intraoperative DNA methylation classification of brain tumors impacts neurosurgical strategy.* Neurooncol Adv, 2021. **3**(1): p. vdab149.
41. Vladoiu, M.C., et al., *Childhood cerebellar tumours mirror conserved fetal transcriptional programs.* Nature, 2019. **572**(7767): p. 67-73.
42. Filbin, M.G., et al., *Developmental and oncogenic programs in H3K27M gliomas dissected by single-cell RNA-seq.* Science, 2018. **360**(6386): p. 331-335.
43. Hovestadt, V., et al., *Resolving medulloblastoma cellular architecture by single-cell genomics.* Nature, 2019. **572**(7767): p. 74-79.
44. Gojo, J., et al., *Single-Cell RNA-Seq Reveals Cellular Hierarchies and Impaired Developmental Trajectories in Pediatric Ependymoma.* Cancer Cell, 2020. **38**(1): p. 44-59 e9.
45. Okonechnikov, K., et al., *Mapping pediatric brain tumors to their origins in the developing cerebellum.* Neuro Oncol, 2023.
46. Price, M., et al., *Childhood, adolescent, and adult primary brain and central nervous system tumor statistics for practicing healthcare providers in neuro-oncology, CBTRUS 2015-2019.* Neurooncol Pract, 2024. **11**(1): p. 5-25.
47. Ostrom, Q.T., et al., *CBTRUS Statistical Report: Pediatric Brain Tumor Foundation Childhood and Adolescent Primary Brain and Other Central Nervous System Tumors Diagnosed in the United States in 2014-2018.* Neuro Oncol, 2022. **24**(Suppl 3): p. iii1-iii38.
48. Sturm, D., S.M. Pfister, and D.T.W. Jones, *Pediatric Gliomas: Current Concepts on Diagnosis, Biology, and Clinical Management.* J Clin Oncol, 2017. **35**(21): p. 2370-2377.
49. Louis, D.N., et al., *The 2021 WHO Classification of Tumors of the Central Nervous System: a summary.* Neuro Oncol, 2021. **23**(8): p. 1231-1251.
50. Hovestadt, V., et al., *Medulloblastomics revisited: biological and clinical insights from thousands of patients.* Nat Rev Cancer, 2020. **20**(1): p. 42-56.
51. Ostrom, Q.T., et al., *Alex's Lemonade Stand Foundation Infant and Childhood Primary Brain and Central Nervous System Tumors Diagnosed in the United States in 2007-2011.* Neuro Oncol, 2015. **16 Suppl 10**(Suppl 10): p. x1-x36.
52. Curtin SC, M.A., Anderson RN., *Declines in cancer death rates among children and adolescents in the United States, 1999–2014.* NCHS data brief, 2016.
53. Hoffman, L.M., et al., *Clinical, Radiologic, Pathologic, and Molecular Characteristics of Long-Term Survivors of Diffuse Intrinsic Pontine Glioma (DIPG): A Collaborative Report From the International and European Society for Pediatric Oncology DIPG Registries.* J Clin Oncol, 2018. **36**(19): p. 1963-1972.
54. Thomas, B.C., et al., *CAR T cell therapies for diffuse midline glioma.* Trends Cancer, 2023. **9**(10): p. 791-804.
55. C, C., C. A, and J. T, *New Molecular Targets and Treatments for Pediatric Brain Tumors*, in *Evolution of the Molecular Biology of Brain Tumors and the Therapeutic Implications*. 2013.

56. Kandoth, C., et al., *Mutational landscape and significance across 12 major cancer types.* Nature, 2013. **502**(7471): p. 333-339.
57. Campbell, B.B., et al., *Comprehensive Analysis of Hypermutation in Human Cancer.* Cell, 2017. **171**(5): p. 1042-1056 e10.
58. Waszak, S.M., et al., *Spectrum and prevalence of genetic predisposition in medulloblastoma: a retrospective genetic study and prospective validation in a clinical trial cohort.* Lancet Oncol, 2018. **19**(6): p. 785-798.
59. Waszak, S.M., et al., *Germline Elongator mutations in Sonic Hedgehog medulloblastoma.* Nature, 2020. **580**(7803): p. 396-401.
60. Miranda Alcalde, B., et al., *The importance of Li-Fraumeni syndrome, a hereditary cancer predisposition disorder.* Arch Argent Pediatr, 2021. **119**(1): p. e11-e17.
61. Guerrini-Rousseau, L., et al., *Pediatric high-grade glioma MYCN is frequently associated with Li-Fraumeni syndrome.* Acta Neuropathol Commun, 2023. **11**(1): p. 3.
62. Huether, R., et al., *The landscape of somatic mutations in epigenetic regulators across 1,000 paediatric cancer genomes.* Nat Commun, 2014. **5**: p. 3630.
63. Jones, D.T.W., et al., *Molecular characteristics and therapeutic vulnerabilities across paediatric solid tumours.* Nat Rev Cancer, 2019. **19**(8): p. 420-438.
64. Roosen, M., et al., *The oncogenic fusion landscape in pediatric CNS neoplasms.* Acta Neuropathol, 2022. **143**(4): p. 427-451.
65. Jones, D.T., et al., *Oncogenic RAF1 rearrangement and a novel BRAF mutation as alternatives to KIAA1549:BRAF fusion in activating the MAPK pathway in pilocytic astrocytoma.* Oncogene, 2009. **28**(20): p. 2119-23.
66. Zheng, T., et al., *Cross-Species Genomics Reveals Oncogenic Dependencies in ZFTA/C11orf95 Fusion-Positive Supratentorial Ependymomas.* Cancer Discov, 2021. **11**(9): p. 2230-2247.
67. Parker, M., et al., *C11orf95-RELA fusions drive oncogenic NF-kappaB signalling in ependymoma.* Nature, 2014. **506**(7489): p. 451-5.
68. Schwartzentruber, J., et al., *Driver mutations in histone H3.3 and chromatin remodelling genes in paediatric glioblastoma.* Nature, 2012. **482**(7384): p. 226-31.
69. Sturm, D., et al., *Hotspot mutations in H3F3A and IDH1 define distinct epigenetic and biological subgroups of glioblastoma.* Cancer Cell, 2012. **22**(4): p. 425-37.
70. Sweet-Cordero, E.A. and J.A. Biegel, *The genomic landscape of pediatric cancers: Implications for diagnosis and treatment.* Science, 2019. **363**(6432): p. 1170-1175.
71. Ghasemi, D.R., et al., *MYCN amplification drives an aggressive form of spinal ependymoma.* Acta Neuropathol, 2019. **138**(6): p. 1075-1089.
72. Hutter, S., et al., *Modeling and Targeting MYC Genes in Childhood Brain Tumors.* Genes (Basel), 2017. **8**(4).
73. Keck, M.K., et al., *Amplification of the PLAG-family genes-PLAGL1 and PLAGL2-is a key feature of the novel tumor type CNS embryonal tumor with PLAGL amplification.* Acta Neuropathol, 2023. **145**(1): p. 49-69.
74. Wu, J., T.S. Armstrong, and M.R. Gilbert, *Biology and management of ependymomas.* Neuro Oncol, 2016. **18**(7): p. 902-13.
75. Bouffet, E., et al., *Ependymoma: lessons from the past, prospects for the future.* Childs Nerv Syst, 2009. **25**(11): p. 1383-4; author reply 1385.
76. Kilday, J.P., et al., *Pediatric ependymoma: biological perspectives.* Mol Cancer Res, 2009. **7**(6): p. 765-86.
77. Witt, H., et al., *DNA methylation-based classification of ependymomas in adulthood: implications for diagnosis and treatment.* Neuro Oncol, 2018. **20**(12): p. 1616-1624.
78. Pajtler, K.W., et al., *YAP1 subgroup supratentorial ependymoma requires TEAD and nuclear factor I-mediated transcriptional programmes for tumorigenesis.* Nat Commun, 2019. **10**(1): p. 3914.
79. Szulzewsky, F., et al., *Comparison of tumor-associated YAP1 fusions identifies a recurrent set of functions critical for oncogenesis.* Genes & Development, 2020. **34**(15-16): p. 1051-1064.
80. Pollack, I.F., S. Agnihotri, and A. Broniscer, *Childhood brain tumors: current management, biological insights, and future directions.* J Neurosurg Pediatr, 2019. **23**(3): p. 261-273.
81. Malgulwar, P.B., et al., *C11orf95-RELA fusions and upregulated NF-KB signalling characterise a subset of aggressive supratentorial ependymomas that express L1CAM and nestin.* J Neurooncol, 2018. **138**(1): p. 29-39.
82. Zhu, J.J., et al., *C11orf95-RELA reprograms 3D epigenome in supratentorial ependymoma.* Acta Neuropathol, 2020. **140**(6): p. 951-960.
83. Kupp, R., et al., *ZFTA Translocations Constitute Ependymoma Chromatin Remodeling and Transcription Factors.* Cancer Discov, 2021. **11**(9): p. 2216-2229.

84. Coy, S., et al., *An update on the CNS manifestations of neurofibromatosis type 2.* Acta Neuropathologica, 2019. **139**(4): p. 643-665.
85. Asthagiri, A.R., et al., *Neurofibromatosis type 2.* The Lancet, 2009. **373**(9679): p. 1974-1986.
86. Plotkin, S.R., et al., *Spinal ependymomas in neurofibromatosis Type 2: a retrospective analysis of 55 patients.* J Neurosurg Spine, 2011. **14**(4): p. 543-7.
87. Neyazi, S., et al., *Transcriptomic and epigenetic dissection of spinal ependymoma (SP-EPN) identifies clinically relevant subtypes enriched for tumors with and without NF2 mutation.* Acta Neuropathol, 2024. **147**(1): p. 22.
88. Cavalli, F.M.G., et al., *Heterogeneity within the PF-EPN-B ependymoma subgroup.* Acta Neuropathol, 2018. **136**(2): p. 227-237.
89. Araki, A., et al., *Chromosome 1q gain and tenascin-C expression are candidate markers to define different risk groups in pediatric posterior fossa ependymoma.* Acta Neuropathologica Communications, 2016. **4**(1).
90. Rajeshwari, M., et al., *Evaluation of chromosome 1q gain in intracranial ependymomas.* Journal of Neuro-Oncology, 2016. **127**(2): p. 271-278.
91. Donson, A.M., et al., *Significant increase of high-risk chromosome 1q gain and 6q loss at recurrence in posterior fossa group A ependymoma: a multicenter study.* Neuro Oncol, 2023.
92. Olsen, T.K., et al., *Genomic characterization of ependymomas reveals 6q loss as the most common aberration.* Oncol Rep, 2014. **32**(2): p. 483-90.
93. Baroni, L.V., et al., *Ultra high-risk PFA ependymoma is characterized by loss of chromosome 6q.* Neuro Oncol, 2021. **23**(8): p. 1360-1370.
94. Korshunov, A., et al., *Molecular staging of intracranial ependymoma in children and adults.* J Clin Oncol, 2010. **28**(19): p. 3182-90.
95. Godicke, S., et al., *Clinically relevant molecular hallmarks of PFA ependymomas display intratumoral heterogeneity and correlate with tumor morphology.* Acta Neuropathol, 2024. **147**(1): p. 23.
96. Saleh, A.H., et al., *The biology of ependymomas and emerging novel therapies.* Nat Rev Cancer, 2022. **22**(4): p. 208-222.
97. Cage, T.A., et al., *A systematic review of treatment outcomes in pediatric patients with intracranial ependymomas.* J Neurosurg Pediatr, 2013. **11**(6): p. 673-81.
98. Adolph, J.E., et al., *Local and systemic therapy of recurrent ependymoma in children and adolescents: short- and long-term results of the E-HIT-REZ 2005 study.* Neuro Oncol, 2021. **23**(6): p. 1012-1023.
99. Ruda, R., et al., *EANO guidelines for the diagnosis and treatment of ependymal tumors.* Neuro Oncol, 2018. **20**(4): p. 445-456.
100. Merchant, T.E., et al., *Conformal radiotherapy after surgery for paediatric ependymoma: a prospective study.* Lancet Oncol, 2009. **10**(3): p. 258-66.
101. Yecies, D., et al., *Long-Term Supratentorial Radiologic Effects of Surgery and Local Radiation in Children with Infratentorial Ependymoma.* World Neurosurg, 2019. **122**: p. e1300-e1304.
102. DeWire, M., et al., *An open-label, two-stage, phase II study of bevacizumab and lapatinib in children with recurrent or refractory ependymoma: a collaborative ependymoma research network study (CERN).* J Neurooncol, 2015. **123**(1): p. 85-91.
103. Grill, J., et al., *Postoperative chemotherapy without irradiation for ependymoma in children under 5 years of age: a multicenter trial of the French Society of Pediatric Oncology.* J Clin Oncol, 2001. **19**(5): p. 1288-96.
104. Pajtler, K.W., et al., *Intraventricular etoposide safety and toxicity profile in children and young adults with refractory or recurrent malignant brain tumors.* J Neurooncol, 2016. **128**(3): p. 463-71.
105. Umbach, G., et al., *Extraneural metastatic anaplastic ependymoma: a systematic review and a report of metastases to bilateral parotid glands.* Neurooncol Pract, 2020. **7**(2): p. 218-227.
106. Simeonova, I. and E. Huillard, *In vivo models of brain tumors: roles of genetically engineered mouse models in understanding tumor biology and use in preclinical studies.* Cell Mol Life Sci, 2014. **71**(20): p. 4007-26.
107. Katt, M.E., et al., *In Vitro Tumor Models: Advantages, Disadvantages, Variables, and Selecting the Right Platform.* Frontiers in Bioengineering and Biotechnology, 2016. **4**.
108. Hanahan, D. and R.A. Weinberg, *Hallmarks of cancer: the next generation.* Cell, 2011. **144**(5): p. 646-74.
109. Lilienblum, W., et al., *Alternative methods to safety studies in experimental animals: role in the risk assessment of chemicals under the new European Chemicals Legislation (REACH).* Arch Toxicol, 2008. **82**(4): p. 211-36.
110. Hausser, H.J. and R.E. Brenner, *Phenotypic instability of Saos-2 cells in long-term culture.* Biochem Biophys Res Commun, 2005. **333**(1): p. 216-22.

111. Ghallab, A., *In Vitro Test Systems and Their Limitations.* Excli Journal, 2013. **12**: p. 1024-1026.
112. Gillet, J.P., et al., *Redefining the relevance of established cancer cell lines to the study of mechanisms of clinical anti-cancer drug resistance.* Proc Natl Acad Sci U S A, 2011. **108**(46): p. 18708-13.
113. Johnson, J.I., et al., *Relationships between drug activity in NCI preclinical in vitro and in vivo models and early clinical trials.* Br J Cancer, 2001. **84**(10): p. 1424-31.
114. Tang-Schomer, M.D., et al., *Human Patient-Derived Brain Tumor Models to Recapitulate Ependymoma Tumor Vasculature.* Bioengineering (Basel), 2023. **10**(7).
115. Capes-Davis, A., et al., *Check your cultures! A list of cross-contaminated or misidentified cell lines.* Int J Cancer, 2010. **127**(1): p. 1-8.
116. Pisapia, D.J., et al., *Next-Generation Rapid Autopsies Enable Tumor Evolution Tracking and Generation of Preclinical Models.* JCO Precis Oncol, 2017. **2017**.
117. Lago, C., et al., *Patient- and xenograft-derived organoids recapitulate pediatric brain tumor features and patient treatments.* EMBO Mol Med, 2023. **15**(12): p. e18199.
118. Lee, J., et al., *Tumor stem cells derived from glioblastomas cultured in bFGF and EGF more closely mirror the phenotype and genotype of primary tumors than do serum-cultured cell lines.* Cancer Cell, 2006. **9**(5): p. 391-403.
119. Xu, J., et al., *Pediatric brain tumor cell lines.* J Cell Biochem, 2015. **116**(2): p. 218-24.
120. Michealraj, K.A., et al., *Metabolic Regulation of the Epigenome Drives Lethal Infantile Ependymoma.* Cell, 2020. **181**(6): p. 1329-1345 e24.
121. Sanden, E., et al., *A standardized and reproducible protocol for serum-free monolayer culturing of primary paediatric brain tumours to be utilized for therapeutic assays.* Sci Rep, 2015. **5**: p. 12218.
122. Milde, T., et al., *A novel human high-risk ependymoma stem cell model reveals the differentiation-inducing potential of the histone deacetylase inhibitor Vorinostat.* Acta Neuropathol, 2011. **122**(5): p. 637-50.
123. Hwang, E.I., et al., *Why haven't we solved intracranial pediatric ependymoma? Current questions and barriers to treatment advances.* Neoplasia, 2023. **39**: p. 100895.
124. Di Lullo, E. and A.R. Kriegstein, *The use of brain organoids to investigate neural development and disease.* Nat Rev Neurosci, 2017. **18**(10): p. 573-584.
125. Bian, S., et al., *Genetically engineered cerebral organoids model brain tumor formation.* Nat Methods, 2018. **15**(8): p. 631-639.
126. Wimmer, R.A., et al., *Generation of blood vessel organoids from human pluripotent stem cells.* Nat Protoc, 2019. **14**(11): p. 3082-3100.
127. Sun, X.Y., et al., *Generation of vascularized brain organoids to study neurovascular interactions.* Elife, 2022. **11**.
128. Roosen, M., et al., *Biol-11. Preclinical Modelling of Pediatric Brain Tumors Using Organoid Technology.* Neuro-Oncology, 2023. **25**(Supplement_1): p. i8-i8.
129. Monaco, G., et al., *A comparison of human and mouse gene co-expression networks reveals conservation and divergence at the tissue, pathway and disease levels.* BMC Evol Biol, 2015. **15**: p. 259.
130. Mouse Genome Sequencing, C., et al., *Initial sequencing and comparative analysis of the mouse genome.* Nature, 2002. **420**(6915): p. 520-62.
131. Polli, J.E., *In vitro studies are sometimes better than conventional human pharmacokinetic in vivo studies in assessing bioequivalence of immediate-release solid oral dosage forms.* AAPS J, 2008. **10**(2): p. 289-99.
132. Smith, C.L., et al., *Mouse Genome Database (MGD)-2018: knowledgebase for the laboratory mouse.* Nucleic Acids Res, 2018. **46**(D1): p. D836-D842.
133. Sharpless, N.E. and R.A. Depinho, *The mighty mouse: genetically engineered mouse models in cancer drug development.* Nat Rev Drug Discov, 2006. **5**(9): p. 741-54.
134. Tabata, H. and K. Nakajima, *Efficient in utero gene transfer system to the developing mouse brain using electroporation: visualization of neuronal migration in the developing cortex.* Neuroscience, 2001. **103**(4): p. 865-72.
135. Saito, T. and N. Nakatsuji, *Efficient gene transfer into the embryonic mouse brain using in vivo electroporation.* Dev Biol, 2001. **240**(1): p. 237-46.
136. Ozawa, T., et al., *A De Novo Mouse Model of C11orf95-RELA Fusion-Driven Ependymoma Identifies Driver Functions in Addition to NF-kappaB.* Cell Rep, 2018. **23**(13): p. 3787-3797.
137. Arabzade, A., et al., *ZFTA-RELA Dictates Oncogenic Transcriptional Programs to Drive Aggressive Supratentorial Ependymoma.* Cancer Discov, 2021. **11**(9): p. 2200-2215.
138. Eden, C.J., et al., *Orthotopic models of pediatric brain tumors in zebrafish.* Oncogene, 2015. **34**(13): p. 1736-42.

139. Papapetrou, E.P., *Patient-derived induced pluripotent stem cells in cancer research and precision oncology.* Nat Med, 2016. **22**(12): p. 1392-1401.
140. Huszthy, P.C., et al., *In vivo models of primary brain tumors: pitfalls and perspectives.* Neuro Oncol, 2012. **14**(8): p. 979-93.
141. Brabetz, S., et al., *A biobank of patient-derived pediatric brain tumor models.* Nat Med, 2018. **24**(11): p. 1752-1761.
142. Hidalgo, M., et al., *Patient-derived xenograft models: an emerging platform for translational cancer research.* Cancer Discov, 2014. **4**(9): p. 998-1013.
143. Houghton, J.A., P.J. Houghton, and A.A. Green, *Chemotherapy of Childhood Rhabdomyosarcomas Growing as Xenografts in Immune-Deprived Mice.* Cancer Research, 1982. **42**(2): p. 535-539.
144. Fiebig, H.H., et al., *Comparison of tumor response in nude mice and in the patients.* Behring Inst Mitt, 1984(74): p. 343-52.
145. Dobson, T.H.W. and V. Gopalakrishnan, *Preclinical Models of Pediatric Brain Tumors-Forging Ahead.* Bioengineering (Basel), 2018. **5**(4).
146. Tanaka, K., et al., *The first Japanese biobank of patient-derived pediatric acute lymphoblastic leukemia xenograft models.* Cancer Sci, 2022. **113**(11): p. 3814-3825.
147. Townsend, E.C., et al., *The Public Repository of Xenografts Enables Discovery and Randomized Phase II-like Trials in Mice.* Cancer Cell, 2016. **29**(4): p. 574-586.
148. Federico, A., et al., *Abstract 3571: The ITCC-P4 sustainable platform of fully characterized PDXs supports the preclinical proof-of-concept drug testing of high-risk pediatric tumor models.* Cancer Research, 2023. **83**(7_Supplement): p. 3571-3571.
149. Marques Da Costa, M.E., et al., *A biobank of pediatric patient-derived-xenograft models in cancer precision medicine trial MAPPYACTS for relapsed and refractory tumors.* Commun Biol, 2023. **6**(1): p. 949.
150. Gopisetty, A., *ITCC-P4: Molecular characterization and multi-omics analysis of pediatric patient tumor and Patient-Derived Xenograft (PDX) models for preclinical model selection*. 2023, Ruprecht-Karls-University Heidelberg.
151. Liang, M.L., et al., *Application of Drug Testing Platforms in Circulating Tumor Cells and Validation of a Patient-Derived Xenograft Mouse Model in Patient with Primary Intracranial Ependymomas with Extraneural Metastases.* Diagnostics (Basel), 2023. **13**(7).
152. Pierce, A.M., et al., *Establishment of patient-derived orthotopic xenograft model of 1q+ posterior fossa group A ependymoma.* Neuro Oncol, 2019. **21**(12): p. 1540-1551.
153. Pajtler, K.W., et al., *Molecular heterogeneity and CXorf67 alterations in posterior fossa group A (PFA) ependymomas.* Acta Neuropathol, 2018. **136**(2): p. 211-226.
154. Mack, S.C., et al., *Epigenomic alterations define lethal CIMP-positive ependymomas of infancy.* Nature, 2014. **506**(7489): p. 445-50.
155. Bayliss, J., et al., *Lowered H3K27me3 and DNA hypomethylation define poorly prognostic pediatric posterior fossa ependymomas.* Sci Transl Med, 2016. **8**(366): p. 366ra161.
156. Nambirajan, A., et al., *EZH2 inhibitory protein (EZHIP/Cxorf67) expression correlates strongly with H3K27me3 loss in posterior fossa ependymomas and is mutually exclusive with H3K27M mutations.* Brain Tumor Pathol, 2021. **38**(1): p. 30-40.
157. Ryall, S., et al., *H3 K27M mutations are extremely rare in posterior fossa group A ependymoma.* Childs Nerv Syst, 2017. **33**(7): p. 1047-1051.
158. Jain, S.U., et al., *PFA ependymoma-associated protein EZHIP inhibits PRC2 activity through a H3 K27M-like mechanism.* Nat Commun, 2019. **10**(1): p. 2146.
159. Castel, D., et al., *Histone H3 wild-type DIPG/DMG overexpressing EZHIP extend the spectrum diffuse midline gliomas with PRC2 inhibition beyond H3-K27M mutation.* Acta Neuropathol, 2020. **139**(6): p. 1109-1113.
160. Pratt, D., et al., *Diffuse intrinsic pontine glioma-like tumor with EZHIP expression and molecular features of PFA ependymoma.* Acta Neuropathol Commun, 2020. **8**(1): p. 37.
161. Antin, C., et al., *EZHIP is a specific diagnostic biomarker for posterior fossa ependymomas, group PFA and diffuse midline gliomas H3-WT with EZHIP overexpression.* Acta Neuropathol Commun, 2020. **8**(1): p. 183.
162. Dewaele, B., et al., *Identification of a novel, recurrent MBTD1-CXorf67 fusion in low-grade endometrial stromal sarcoma.* Int J Cancer, 2014. **134**(5): p. 1112-22.
163. Djureinovic, D., et al., *Profiling cancer testis antigens in non-small-cell lung cancer.* JCI Insight, 2016. **1**(10): p. e86837.
164. Piunti, A., et al., *CATACOMB: An endogenous inducible gene that antagonizes H3K27 methylation activity of Polycomb repressive complex 2 via an H3K27M-like mechanism.* Sci Adv, 2019. **5**(7): p. eaax2887.

165. Uhlen, M., et al., *Proteomics. Tissue-based map of the human proteome.* Science, 2015. **347**(6220): p. 1260419.
166. Ragazzini, R., et al., *EZHIP constrains Polycomb Repressive Complex 2 activity in germ cells.* Nat Commun, 2019. **10**(1): p. 3858.
167. Lewis, P.W., et al., *Inhibition of PRC2 activity by a gain-of-function H3 mutation found in pediatric glioblastoma.* Science, 2013. **340**(6134): p. 857-61.
168. Ardehali, M.B., et al., *Polycomb Repressive Complex 2 Methylates Elongin A to Regulate Transcription.* Mol Cell, 2017. **68**(5): p. 872-884 e6.
169. Karremann, M., et al., *Diffuse high-grade gliomas with H3 K27M mutations carry a dismal prognosis independent of tumor location.* Neuro Oncol, 2018. **20**(1): p. 123-131.
170. Han, J., et al., *Elevated CXorf67 Expression in PFA Ependymomas Suppresses DNA Repair and Sensitizes to PARP Inhibitors.* Cancer Cell, 2020. **38**(6): p. 844-856 e7.
171. Sonnenblick, A., et al., *An update on PARP inhibitors--moving to the adjuvant setting.* Nat Rev Clin Oncol, 2015. **12**(1): p. 27-41.
172. Sun, K., et al., *A comparative pharmacokinetic study of PARP inhibitors demonstrates favorable properties for niraparib efficacy in preclinical tumor models.* Oncotarget, 2018. **9**(98): p. 37080-37096.
173. Wu, W., et al., *Glioblastoma multiforme (GBM): An overview of current therapies and mechanisms of resistance.* Pharmacol Res, 2021. **171**: p. 105780.
174. Xiong, Y., et al., *Pamiparib is a potent and selective PARP inhibitor with unique potential for the treatment of brain tumor.* Neoplasia, 2020. **22**(9): p. 431-440.
175. Ning, J. and H. Wakimoto, *Therapeutic Application of PARP Inhibitors in Neuro-Oncology.* Trends Cancer, 2020. **6**(2): p. 147-159.
176. Hanna, C., et al., *Pharmacokinetics, safety, and tolerability of olaparib and temozolomide for recurrent glioblastoma: results of the phase I OPARATIC trial.* Neuro Oncol, 2020. **22**(12): p. 1840-1850.
177. Jain, S.U., et al., *H3 K27M and EZHIP Impede H3K27-Methylation Spreading by Inhibiting Allosterically Stimulated PRC2.* Mol Cell, 2020. **80**(4): p. 726-735 e7.
178. Justin, N., et al., *Structural basis of oncogenic histone H3K27M inhibition of human polycomb repressive complex 2.* Nat Commun, 2016. **7**: p. 11316.
179. Mackay, A., et al., *Integrated Molecular Meta-Analysis of 1,000 Pediatric High-Grade and Diffuse Intrinsic Pontine Glioma.* Cancer Cell, 2017. **32**(4): p. 520-537 e5.
180. Kasper, L.H. and S.J. Baker, *Invited Review: Emerging functions of histone H3 mutations in paediatric diffuse high-grade gliomas.* Neuropathol Appl Neurobiol, 2020. **46**(1): p. 73-85.
181. Paugh, B.S., et al., *Genome-Wide Analyses Identify Recurrent Amplifications of Receptor Tyrosine Kinases and Cell-Cycle Regulatory Genes in Diffuse Intrinsic Pontine Glioma.* Journal of Clinical Oncology, 2011. **29**(30): p. 3999-4006.
182. Paugh, B.S., et al., *Novel Oncogenic PDGFRA Mutations in Pediatric High-Grade Gliomas.* Cancer Research, 2013. **73**(20): p. 6219-6229.
183. Wu, G., *The genomic landscape of diffuse intrinsic pontine glioma and pediatric non-brainstem high-grade glioma.* Nature Genetics, 2014. **46**(5): p. 444-450.
184. Taylor, K.R., et al., *Recurrent activating ACVR1 mutations in diffuse intrinsic pontine glioma.* Nature Genetics, 2014. **46**(5): p. 457-461.
185. Khuong-Quang, D.-A., et al., *K27M mutation in histone H3.3 defines clinically and biologically distinct subgroups of pediatric diffuse intrinsic pontine gliomas.* Acta Neuropathologica, 2012. **124**(3): p. 439-447.
186. Funato, K., et al., *Use of human embryonic stem cells to model pediatric gliomas with H3.3K27M histone mutation.* Science, 2014. **346**(6216): p. 1529-1533.
187. Haag, D., et al., *H3.3-K27M drives neural stem cell-specific gliomagenesis in a human iPSC-derived model.* Cancer Cell, 2021. **39**(3): p. 407-422 e13.
188. Mohammad, F., et al., *EZH2 is a potential therapeutic target for H3K27M-mutant pediatric gliomas.* Nature Medicine, 2017. **23**(4): p. 483-492.
189. Piunti, A., et al., *Therapeutic targeting of polycomb and BET bromodomain proteins in diffuse intrinsic pontine gliomas.* Nat Med, 2017. **23**(4): p. 493-500.
190. Mikkelsen, T.S., et al., *Genome-wide maps of chromatin state in pluripotent and lineage-committed cells.* Nature, 2007. **448**(7153): p. 553-60.
191. Venneti, S., et al., *Evaluation of histone 3 lysine 27 trimethylation (H3K27me3) and enhancer of Zest 2 (EZH2) in pediatric glial and glioneuronal tumors shows decreased H3K27me3 in H3F3A K27M mutant glioblastomas.* Brain Pathol, 2013. **23**(5): p. 558-64.
192. Harutyunyan, A.S., et al., *H3K27M induces defective chromatin spread of PRC2-mediated repressive H3K27me2/me3 and is essential for glioma tumorigenesis.* Nature Communications, 2019. **10**(1).

193. Wu, G., et al., *Somatic histone H3 alterations in pediatric diffuse intrinsic pontine gliomas and non-brainstem glioblastomas.* Nature Genetics, 2012. **44**(3): p. 251-253.
194. Bender, S., et al., *Reduced H3K27me3 and DNA Hypomethylation Are Major Drivers of Gene Expression in K27M Mutant Pediatric High-Grade Gliomas.* Cancer Cell, 2013. **24**(5): p. 660-672.
195. Chan, K.M., et al., *The histone H3.3K27M mutation in pediatric glioma reprograms H3K27 methylation and gene expression.* Genes Dev, 2013. **27**(9): p. 985-90.
196. Bernstein, B.E., et al., *A bivalent chromatin structure marks key developmental genes in embryonic stem cells.* Cell, 2006. **125**(2): p. 315-26.
197. Silveira, A.B., et al., *H3.3 K27M depletion increases differentiation and extends latency of diffuse intrinsic pontine glioma growth in vivo.* Acta Neuropathol, 2019. **137**(4): p. 637-655.
198. Duan, R., W. Du, and W. Guo, *EZH2: a novel target for cancer treatment.* J Hematol Oncol, 2020. **13**(1): p. 104.
199. Ntziachristos, P., et al., *Genetic inactivation of the polycomb repressive complex 2 in T cell acute lymphoblastic leukemia.* Nat Med, 2012. **18**(2): p. 298-301.
200. Wang, Y., et al., *Ezh2 Acts as a Tumor Suppressor in Kras-driven Lung Adenocarcinoma.* Int J Biol Sci, 2017. **13**(5): p. 652-659.
201. Gan, L., et al., *The polycomb group protein EZH2 induces epithelial-mesenchymal transition and pluripotent phenotype of gastric cancer cells by binding to PTEN promoter.* J Hematol Oncol, 2018. **11**(1): p. 9.
202. Bachmann, I.M., et al., *EZH2 expression is associated with high proliferation rate and aggressive tumor subgroups in cutaneous melanoma and cancers of the endometrium, prostate, and breast.* J Clin Oncol, 2006. **24**(2): p. 268-73.
203. Varambally, S., et al., *The polycomb group protein EZH2 is involved in progression of prostate cancer.* Nature, 2002. **419**(6907): p. 624-9.
204. Wierzbicki, K., et al., *Targeting and Therapeutic Monitoring of H3K27M-Mutant Glioma.* Curr Oncol Rep, 2020. **22**(2): p. 19.
205. Nomura, M., et al., *DNA demethylation is associated with malignant progression of lower-grade gliomas.* Sci Rep, 2019. **9**(1): p. 1903.
206. Yamashita, A.S., et al., *Demethylation and epigenetic modification with 5-azacytidine reduces IDH1 mutant glioma growth in combination with temozolomide.* Neuro Oncol, 2019. **21**(2): p. 189-200.
207. Venne, A.S., L. Kollipara, and R.P. Zahedi, *The next level of complexity: crosstalk of posttranslational modifications.* Proteomics, 2014. **14**(4-5): p. 513-24.
208. Wang, H., et al., *Protein post-translational modifications in the regulation of cancer hallmarks.* Cancer Gene Ther, 2023. **30**(4): p. 529-547.
209. Goldstein, G., et al., *Isolation of a polypeptide that has lymphocyte-differentiating properties and is probably represented universally in living cells.* Proc Natl Acad Sci U S A, 1975. **72**(1): p. 11-5.
210. Komander, D. and M. Rape, *The ubiquitin code.* Annu Rev Biochem, 2012. **81**: p. 203-29.
211. Pickart, C.M. and M.J. Eddins, *Ubiquitin: structures, functions, mechanisms.* Biochim Biophys Acta, 2004. **1695**(1-3): p. 55-72.
212. Hershko, A., et al., *Components of ubiquitin-protein ligase system. Resolution, affinity purification, and role in protein breakdown.* Journal of Biological Chemistry, 1983. **258**(13): p. 8206-8214.
213. Liu, L., et al., *UbiHub: a data hub for the explorers of ubiquitination pathways.* Bioinformatics, 2019. **35**(16): p. 2882-2884.
214. Clague, M.J., C. Heride, and S. Urbe, *The demographics of the ubiquitin system.* Trends Cell Biol, 2015. **25**(7): p. 417-26.
215. Schulman, B.A. and J.W. Harper, *Ubiquitin-like protein activation by E1 enzymes: the apex for downstream signalling pathways.* Nat Rev Mol Cell Biol, 2009. **10**(5): p. 319-31.
216. Hershko, A., A. Ciechanover, and I.A. Rose, *Resolution of the ATP-dependent proteolytic system from reticulocytes: a component that interacts with ATP.* Proc Natl Acad Sci U S A, 1979. **76**(7): p. 3107-10.
217. Hough, R., G. Pratt, and M. Rechsteiner, *Ubiquitin-lysozyme conjugates. Identification and characterization of an ATP-dependent protease from rabbit reticulocyte lysates.* Journal of Biological Chemistry, 1986. **261**(5): p. 2400-2408.
218. Senft, D., J. Qi, and Z.A. Ronai, *Ubiquitin ligases in oncogenic transformation and cancer therapy.* Nat Rev Cancer, 2018. **18**(2): p. 69-88.
219. Bravo, M., et al., *Polycomb RING1A- and RING1B-dependent histone H2A monoubiquitylation at pericentromeric regions promotes S-phase progression.* J Cell Sci, 2015. **128**(19): p. 3660-71.

220. Shukla, A. and S.R. Bhaumik, *H2B-K123 ubiquitination stimulates RNAPII elongation independent of H3-K4 methylation.* Biochem Biophys Res Commun, 2007. **359**(2): p. 214-20.
221. Zhou, S., et al., *Role of H2B mono-ubiquitination in the initiation and progression of cancer.* Bull Cancer, 2021. **108**(4): p. 385-398.
222. Chen, Y., et al., *Monoubiquitination in Homeostasis and Cancer.* Int J Mol Sci, 2022. **23**(11).
223. Braten, O., et al., *Numerous proteins with unique characteristics are degraded by the 26S proteasome following monoubiquitination.* Proc Natl Acad Sci U S A, 2016. **113**(32): p. E4639-47.
224. Livneh, I., et al., *Monoubiquitination joins polyubiquitination as an esteemed proteasomal targeting signal.* Bioessays, 2017. **39**(6).
225. Ronai, Z.A., *Monoubiquitination in proteasomal degradation.* Proc Natl Acad Sci U S A, 2016. **113**(32): p. 8894-6.
226. Meyer, H.J. and M. Rape, *Enhanced protein degradation by branched ubiquitin chains.* Cell, 2014. **157**(4): p. 910-21.
227. Song, L. and Z.Q. Luo, *Post-translational regulation of ubiquitin signaling.* J Cell Biol, 2019. **218**(6): p. 1776-1786.
228. Sadowski, M., et al., *Protein monoubiquitination and polyubiquitination generate structural diversity to control distinct biological processes.* IUBMB Life, 2012. **64**(2): p. 136-42.
229. Ikeda, F., et al., *SHARPIN forms a linear ubiquitin ligase complex regulating NF-kappaB activity and apoptosis.* Nature, 2011. **471**(7340): p. 637-41.
230. Tokunaga, F., et al., *SHARPIN is a component of the NF-kappaB-activating linear ubiquitin chain assembly complex.* Nature, 2011. **471**(7340): p. 633-6.
231. Tokunaga, F., et al., *Involvement of linear polyubiquitylation of NEMO in NF-kappaB activation.* Nat Cell Biol, 2009. **11**(2): p. 123-32.
232. Swatek, K.N. and D. Komander, *Ubiquitin modifications.* Cell Res, 2016. **26**(4): p. 399-422.
233. Bard, J.A.M., et al., *Structure and Function of the 26S Proteasome.* Annu Rev Biochem, 2018. **87**: p. 697-724.
234. Kraut, D.A. and A. Matouschek, *Proteasomal degradation from internal sites favors partial proteolysis via remote domain stabilization.* ACS Chem Biol, 2011. **6**(10): p. 1087-95.
235. Prakash, S., et al., *Substrate selection by the proteasome during degradation of protein complexes.* Nat Chem Biol, 2009. **5**(1): p. 29-36.
236. Nandi, D., et al., *The ubiquitin-proteasome system.* J Biosci, 2006. **31**(1): p. 137-55.
237. Amerik, A.Y. and M. Hochstrasser, *Mechanism and function of deubiquitinating enzymes.* Biochim Biophys Acta, 2004. **1695**(1-3): p. 189-207.
238. Clague, M.J., S. Urbe, and D. Komander, *Breaking the chains: deubiquitylating enzyme specificity begets function.* Nat Rev Mol Cell Biol, 2019. **20**(6): p. 338-352.
239. Dewson, G., P.J.A. Eichhorn, and D. Komander, *Deubiquitinases in cancer.* Nat Rev Cancer, 2023. **23**(12): p. 842-862.
240. Komander, D., M.J. Clague, and S. Urbe, *Breaking the chains: structure and function of the deubiquitinases.* Nat Rev Mol Cell Biol, 2009. **10**(8): p. 550-63.
241. Storer, A.C. and R. Menard, *Catalytic mechanism in papain family of cysteine peptidases.* Methods Enzymol, 1994. **244**: p. 486-500.
242. Everett, R.D., et al., *A novel ubiquitin-specific protease is dynamically associated with the PML nuclear domain and binds to a herpesvirus regulatory protein.* EMBO J, 1997. **16**(3): p. 566-77.
243. Meredith, M., et al., *Separation of sequence requirements for HSV-1 Vmw110 multimerisation and interaction with a 135-kDa cellular protein.* Virology, 1995. **209**(1): p. 174-87.
244. Meredith, M., A. Orr, and R. Everett, *Herpes simplex virus type 1 immediate-early protein Vmw110 binds strongly and specifically to a 135-kDa cellular protein.* Virology, 1994. **200**(2): p. 457-69.
245. Fernandez-Montalvan, A., et al., *Biochemical characterization of USP7 reveals post-translational modification sites and structural requirements for substrate processing and subcellular localization.* FEBS J, 2007. **274**(16): p. 4256-70.
246. Marchenko, N.D., et al., *Monoubiquitylation promotes mitochondrial p53 translocation.* EMBO J, 2007. **26**(4): p. 923-34.
247. Faesen, A.C., et al., *The differential modulation of USP activity by internal regulatory domains, interactors and eight ubiquitin chain types.* Chem Biol, 2011. **18**(12): p. 1550-61.
248. Kategaya, L., et al., *USP7 small-molecule inhibitors interfere with ubiquitin binding.* Nature, 2017. **550**(7677): p. 534-538.
249. Nininahazwe, L., et al., *The emerging nature of Ubiquitin-specific protease 7 (USP7): a new target in cancer therapy.* Drug Discov Today, 2021. **26**(2): p. 490-502.

250. Saridakis, V., et al., *Structure of the p53 binding domain of HAUSP/USP7 bound to Epstein-Barr nuclear antigen 1 implications for EBV-mediated immortalization.* Mol Cell, 2005. **18**(1): p. 25-36.
251. Hu, M., et al., *Crystal structure of a UBP-family deubiquitinating enzyme in isolation and in complex with ubiquitin aldehyde.* Cell, 2002. **111**(7): p. 1041-54.
252. Sheng, Y., et al., *Molecular recognition of p53 and MDM2 by USP7/HAUSP.* Nat Struct Mol Biol, 2006. **13**(3): p. 285-91.
253. Holowaty, M.N., et al., *Protein interaction domains of the ubiquitin-specific protease, USP7/HAUSP.* J Biol Chem, 2003. **278**(48): p. 47753-61.
254. Hu, M., et al., *Structural basis of competitive recognition of p53 and MDM2 by HAUSP/USP7: implications for the regulation of the p53-MDM2 pathway.* PLoS Biol, 2006. **4**(2): p. e27.
255. Molland, K., Q. Zhou, and A.D. Mesecar, *A 2.2 A resolution structure of the USP7 catalytic domain in a new space group elaborates upon structural rearrangements resulting from ubiquitin binding.* Acta Crystallogr F Struct Biol Commun, 2014. **70**(Pt 3): p. 283-7.
256. Pfoh, R., et al., *Crystal Structure of USP7 Ubiquitin-like Domains with an ICP0 Peptide Reveals a Novel Mechanism Used by Viral and Cellular Proteins to Target USP7.* PLoS Pathog, 2015. **11**(6): p. e1004950.
257. Rouge, L., et al., *Molecular Understanding of USP7 Substrate Recognition and C-Terminal Activation.* Structure, 2016. **24**(8): p. 1335-1345.
258. Khoronenkova, S.V. and G.L. Dianov, *Regulation of USP7/HAUSP in response to DNA damage: yet another role for ATM.* Cell Cycle, 2012. **11**(13): p. 2409-10.
259. Zaman, M.M., et al., *Ubiquitination-deubiquitination by the TRIM27-USP7 complex regulates tumor necrosis factor alpha-induced apoptosis.* Mol Cell Biol, 2013. **33**(24): p. 4971-84.
260. Morotti, A., et al., *BCR-ABL disrupts PTEN nuclear-cytoplasmic shuttling through phosphorylation-dependent activation of HAUSP.* Leukemia, 2014. **28**(6): p. 1326-33.
261. Kon, N., et al., *Roles of HAUSP-mediated p53 regulation in central nervous system development.* Cell Death Differ, 2011. **18**(8): p. 1366-75.
262. Zhang, X., et al., *USP7 reduction leads to developmental failure of mouse early embryos.* Exp Cell Res, 2023. **427**(2): p. 113605.
263. Liu, C., et al., *USP7 represses lineage differentiation genes in mouse embryonic stem cells by both catalytic and noncatalytic activities.* Sci Adv, 2023. **9**(20): p. eade3888.
264. Zheng, H., et al., *Expansion of the mutation spectrum and phenotype of USP7-related neurodevelopmental disorder.* Front Mol Neurosci, 2022. **15**: p. 970649.
265. Fountain, M.D., et al., *Pathogenic variants in USP7 cause a neurodevelopmental disorder with speech delays, altered behavior, and neurologic anomalies.* Genet Med, 2019. **21**(8): p. 1797-1807.
266. Hao, Y.H., et al., *USP7 Acts as a Molecular Rheostat to Promote WASH-Dependent Endosomal Protein Recycling and Is Mutated in a Human Neurodevelopmental Disorder.* Mol Cell, 2015. **59**(6): p. 956-69.
267. Huang, Z., et al., *Deubiquitylase HAUSP stabilizes REST and promotes maintenance of neural progenitor cells.* Nat Cell Biol, 2011. **13**(2): p. 142-52.
268. Callegari, K., et al., *Pharmacological inhibition of LSD1 activity blocks REST-dependent medulloblastoma cell migration.* Cell Commun Signal, 2018. **16**(1): p. 60.
269. Steger, M., et al., *Time-resolved in vivo ubiquitinome profiling by DIA-MS reveals USP7 targets on a proteome-wide scale.* Nat Commun, 2021. **12**(1): p. 5399.
270. Doherty, L.M., et al., *Integrating multi-omics data reveals function and therapeutic potential of deubiquitinating enzymes.* Elife, 2022. **11**.
271. Bhattacharya, S. and M.K. Ghosh, *HAUSP, a novel deubiquitinase for Rb - MDM2 the critical regulator.* FEBS J, 2014. **281**(13): p. 3061-78.
272. Li, M., et al., *A dynamic role of HAUSP in the p53-Mdm2 pathway.* Mol Cell, 2004. **13**(6): p. 879-86.
273. Chen, H., et al., *The Hao-Fountain syndrome protein USP7 regulates neuronal connectivity in the brain via a novel p53-independent ubiquitin signaling pathway.* bioRxiv, 2023.
274. Zheng, N., et al., *USP7 stabilizes EZH2 and enhances cancer malignant progression.* Am J Cancer Res, 2020. **10**(1): p. 299-313.
275. Li, N., et al., *USP7 inhibits TIMP2 by up-regulating the expression of EZH2 to activate the NF-kappaB/PD-L1 axis to promote the development of cervical cancer.* Cell Signal, 2022. **96**: p. 110351.
276. Lee, J.E., C.M. Park, and J.H. Kim, *USP7 deubiquitinates and stabilizes EZH2 in prostate cancer cells.* Genet Mol Biol, 2020. **43**(2): p. e20190338.
277. Lei, A., et al., *EZH2 Regulates Protein Stability via Recruiting USP7 to Mediate Neuronal Gene Expression in Cancer Cells.* Front Genet, 2019. **10**: p. 422.

278. Liefke, R., V. Karwacki-Neisius, and Y. Shi, *EPOP Interacts with Elongin BC and USP7 to Modulate the Chromatin Landscape.* Mol Cell, 2016. **64**(4): p. 659-672.
279. Maertens, G.N., et al., *Ubiquitin-specific proteases 7 and 11 modulate Polycomb regulation of the INK4a tumour suppressor.* EMBO J, 2010. **29**(15): p. 2553-65.
280. de Bie, P., D. Zaaroor-Regev, and A. Ciechanover, *Regulation of the Polycomb protein RING1B ubiquitination by USP7.* Biochem Biophys Res Commun, 2010. **400**(3): p. 389-95.
281. Lecona, E., V. Narendra, and D. Reinberg, *USP7 cooperates with SCML2 to regulate the activity of PRC1.* Mol Cell Biol, 2015. **35**(7): p. 1157-68.
282. Luo, M., et al., *Polycomb protein SCML2 associates with USP7 and counteracts histone H2A ubiquitination in the XY chromatin during male meiosis.* PLoS Genet, 2015. **11**(1): p. e1004954.
283. van der Knaap, J.A., et al., *GMP synthetase stimulates histone H2B deubiquitylation by the epigenetic silencer USP7.* Mol Cell, 2005. **17**(5): p. 695-707.
284. Sarkari, F., et al., *EBNA1-mediated recruitment of a histone H2B deubiquitylating complex to the Epstein-Barr virus latent origin of DNA replication.* PLoS Pathog, 2009. **5**(10): p. e1000624.
285. Maat, H., et al., *The USP7-TRIM27 axis mediates non-canonical PRC1.1 function and is a druggable target in leukemia.* iScience, 2021. **24**(5): p. 102435.
286. Liu, C., et al., *MAGED4B Promotes Glioma Progression via Inactivation of the TNF-alpha-induced Apoptotic Pathway by Down-regulating TRIM27 Expression.* Neurosci Bull, 2023. **39**(2): p. 273-291.
287. Tacer, K.F. and P.R. Potts, *Cellular and disease functions of the Prader-Willi Syndrome gene MAGEL2.* Biochem J, 2017. **474**(13): p. 2177-2190.
288. Sakamoto, T., et al., *TRIM27-USP7 complex promotes tumour progression via STAT3 activation in human hepatocellular carcinoma.* Liver Int, 2023. **43**(1): p. 194-207.
289. Cai, J., et al., *USP7-TRIM27 axis negatively modulates antiviral type I IFN signaling.* FASEB J, 2018. **32**(10): p. 5238-5249.
290. Galarreta, A., et al., *Coordinating DNA Replication and Mitosis through Ubiquitin/SUMO and CDK1.* Int J Mol Sci, 2021. **22**(16).
291. Galarreta, A., et al., *USP7 limits CDK1 activity throughout the cell cycle.* EMBO J, 2021. **40**(11): p. e99692.
292. Faustrup, H., et al., *USP7 counteracts SCFbetaTrCP- but not APCCdh1-mediated proteolysis of Claspin.* J Cell Biol, 2009. **184**(1): p. 13-9.
293. Nicholson, B. and K.G. Suresh Kumar, *The multifaceted roles of USP7: new therapeutic opportunities.* Cell Biochem Biophys, 2011. **60**(1-2): p. 61-8.
294. Oh, Y.M., et al., *Chfr is linked to tumour metastasis through the downregulation of HDAC1.* Nat Cell Biol, 2009. **11**(3): p. 295-302.
295. Oh, Y.M., S.J. Yoo, and J.H. Seol, *Deubiquitination of Chfr, a checkpoint protein, by USP7/HAUSP regulates its stability and activity.* Biochem Biophys Res Commun, 2007. **357**(3): p. 615-9.
296. Valles, G.J., et al., *USP7 Is a Master Regulator of Genome Stability.* Front Cell Dev Biol, 2020. **8**: p. 717.
297. Giovinazzi, S., et al., *Usp7 protects genomic stability by regulating Bub3.* Oncotarget, 2014. **5**(11): p. 3728-42.
298. Su, D., et al., *Ubiquitin-specific protease 7 sustains DNA damage response and promotes cervical carcinogenesis.* J Clin Invest, 2018. **128**(10): p. 4280-4296.
299. Yi, J., et al., *Inhibition of USP7 induces p53-independent tumor growth suppression in triple-negative breast cancers by destabilizing FOXM1.* Cell Death Differ, 2023. **30**(7): p. 1799-1810.
300. Zhu, Q., et al., *USP7 deubiquitinase promotes ubiquitin-dependent DNA damage signaling by stabilizing RNF168.* Cell Cycle, 2015. **14**(9): p. 1413-25.
301. Grunblatt, E., et al., *MYCN drives chemoresistance in small cell lung cancer while USP7 inhibition can restore chemosensitivity.* Genes Dev, 2020. **34**(17-18): p. 1210-1226.
302. Tavana, O., et al., *HAUSP deubiquitinates and stabilizes N-Myc in neuroblastoma.* Nat Med, 2016. **22**(10): p. 1180-1186.
303. Nicklas, S., et al., *A complex of the ubiquitin ligase TRIM32 and the deubiquitinase USP7 balances the level of c-Myc ubiquitination and thereby determines neural stem cell fate specification.* Cell Death Differ, 2019. **26**(4): p. 728-740.
304. Wu, H.T., et al., *K63-polyubiquitinated HAUSP deubiquitinates HIF-1alpha and dictates H3K56 acetylation promoting hypoxia-induced tumour progression.* Nat Commun, 2016. **7**: p. 13644.
305. Novellasdemunt, L., et al., *USP7 Is a Tumor-Specific WNT Activator for APC-Mutated Colorectal Cancer by Mediating beta-Catenin Deubiquitination.* Cell Rep, 2017. **21**(3): p. 612-627.
306. Shan, H., et al., *USP7 deubiquitinates and stabilizes NOTCH1 in T-cell acute lymphoblastic leukemia.* Signal Transduct Target Ther, 2018. **3**: p. 29.

307. Sun, X., et al., *Usp7 regulates Hippo pathway through deubiquitinating the transcriptional coactivator Yorkie.* Nat Commun, 2019. **10**(1): p. 411.
308. Song, M.S., et al., *The deubiquitinylation and localization of PTEN are regulated by a HAUSP-PML network.* Nature, 2008. **455**(7214): p. 813-7.
309. Schauer, N.J., et al., *Advances in Discovering Deubiquitinating Enzyme (DUB) Inhibitors.* J Med Chem, 2020. **63**(6): p. 2731-2750.
310. Oliveira, R.I., R.A. Guedes, and J.A.R. Salvador, *Highlights in USP7 inhibitors for cancer treatment.* Front Chem, 2022. **10**: p. 1005727.
311. Lamberto, I., et al., *Structure-Guided Development of a Potent and Selective Non-covalent Active-Site Inhibitor of USP7.* Cell Chem Biol, 2017. **24**(12): p. 1490-1500 e11.
312. Turnbull, A.P., et al., *Molecular basis of USP7 inhibition by selective small-molecule inhibitors.* Nature, 2017. **550**(7677): p. 481-486.
313. Gavory, G., et al., *Discovery and characterization of highly potent and selective allosteric USP7 inhibitors.* Nat Chem Biol, 2018. **14**(2): p. 118-125.
314. Zhang, W., et al., *Generation and Validation of Intracellular Ubiquitin Variant Inhibitors for USP7 and USP10.* J Mol Biol, 2017. **429**(22): p. 3546-3560.
315. Colland, F., et al., *Small-molecule inhibitor of USP7/HAUSP ubiquitin protease stabilizes and activates p53 in cells.* Mol Cancer Ther, 2009. **8**(8): p. 2286-95.
316. Reverdy, C., et al., *Discovery of specific inhibitors of human USP7/HAUSP deubiquitinating enzyme.* Chem Biol, 2012. **19**(4): p. 467-77.
317. Altun, M., et al., *Activity-based chemical proteomics accelerates inhibitor development for deubiquitylating enzymes.* Chem Biol, 2011. **18**(11): p. 1401-12.
318. Chauhan, D., et al., *A small molecule inhibitor of ubiquitin-specific protease-7 induces apoptosis in multiple myeloma cells and overcomes bortezomib resistance.* Cancer Cell, 2012. **22**(3): p. 345-58.
319. Weinstock, J., et al., *Selective Dual Inhibitors of the Cancer-Related Deubiquitylating Proteases USP7 and USP47.* ACS Med Chem Lett, 2012. **3**(10): p. 789-92.
320. Chen, C., et al., *Synthesis and biological evaluation of thiazole derivatives as novel USP7 inhibitors.* Bioorg Med Chem Lett, 2017. **27**(4): p. 845-849.
321. Ritorto, M.S., et al., *Screening of DUB activity and specificity by MALDI-TOF mass spectrometry.* Nat Commun, 2014. **5**: p. 4763.
322. Qi, S.M., et al., *Targeting USP7-Mediated Deubiquitination of MDM2/MDMX-p53 Pathway for Cancer Therapy: Are We There Yet?* Front Cell Dev Biol, 2020. **8**: p. 233.
323. An, T., et al., *USP7 inhibitor P5091 inhibits Wnt signaling and colorectal tumor growth.* Biochem Pharmacol, 2017. **131**: p. 29-39.
324. Hu, T., et al., *Targeting the overexpressed USP7 inhibits esophageal squamous cell carcinoma cell growth by inducing NOXA-mediated apoptosis.* Mol Carcinog, 2019. **58**(1): p. 42-54.
325. Pan, T., et al., *USP7 inhibition induces apoptosis in glioblastoma by enhancing ubiquitination of ARF4.* Cancer Cell Int, 2021. **21**(1): p. 508.
326. Fan, Y.H., et al., *USP7 inhibitor P22077 inhibits neuroblastoma growth via inducing p53-mediated apoptosis.* Cell Death Dis, 2013. **4**(10): p. e867.
327. Xiang, M., et al., *Pharmacological inhibition of USP7 suppresses growth and metastasis of melanoma cells in vitro and in vivo.* J Cell Mol Med, 2021. **25**(19): p. 9228-9240.
328. Chen, H., et al., *Ubiquitin-specific protease 7 is a druggable target that is essential for pancreatic cancer growth and chemoresistance.* Invest New Drugs, 2020. **38**(6): p. 1707-1716.
329. Zhao, S., et al., *A ubiquitin switch controls autocatalytic inactivation of the DNA-protein crosslink repair protease SPRTN.* Nucleic Acids Res, 2021. **49**(2): p. 902-915.
330. Lei, H., et al., *Targeting USP47 overcomes tyrosine kinase inhibitor resistance and eradicates leukemia stem/progenitor cells in chronic myelogenous leukemia.* Nat Commun, 2021. **12**(1): p. 51.
331. Di Lello, P., et al., *Discovery of Small-Molecule Inhibitors of Ubiquitin Specific Protease 7 (USP7) Using Integrated NMR and in Silico Techniques.* J Med Chem, 2017. **60**(24): p. 10056-10070.
332. Bashore, C., et al., *Cyanopyrrolidine Inhibitors of Ubiquitin Specific Protease 7 Mediate Desulfhydration of the Active-Site Cysteine.* ACS Chem Biol, 2020. **15**(6): p. 1392-1400.
333. Schauer, N.J., et al., *Selective USP7 inhibition elicits cancer cell killing through a p53-dependent mechanism.* Sci Rep, 2020. **10**(1): p. 5324.
334. O'Dowd, C.R., et al., *Identification and Structure-Guided Development of Pyrimidinone Based USP7 Inhibitors.* ACS Med Chem Lett, 2018. **9**(3): p. 238-243.
335. Leger, P.R., et al., *Discovery of Potent, Selective, and Orally Bioavailable Inhibitors of USP7 with In Vivo Antitumor Activity.* J Med Chem, 2020. **63**(10): p. 5398-5420.

336. Ohol, Y.M., et al., *Novel, Selective Inhibitors of USP7 Uncover Multiple Mechanisms of Antitumor Activity In Vitro and In Vivo.* Mol Cancer Ther, 2020. **19**(10): p. 1970-1980.
337. Li, P. and H.M. Liu, *Recent advances in the development of ubiquitin-specific-processing protease 7 (USP7) inhibitors.* Eur J Med Chem, 2020. **191**: p. 112107.
338. Li, P., et al., *Design, synthesis, biological evaluation and structure-activity relationship study of quinazolin-4(3H)-one derivatives as novel USP7 inhibitors.* European Journal of Medicinal Chemistry, 2021. **216**.
339. Li, M., et al., *N-benzylpiperidinol derivatives as novel USP7 inhibitors: Structure-activity relationships and X-ray crystallographic studies.* Eur J Med Chem, 2020. **199**: p. 112279.
340. Li, X., et al., *Parthenolide inhibits ubiquitin-specific peptidase 7 (USP7), Wnt signaling, and colorectal cancer cell growth.* J Biol Chem, 2020. **295**(11): p. 3576-3589.
341. Guo, N.J., et al., *USP7 as an emerging therapeutic target: A key regulator of protein homeostasis.* Int J Biol Macromol, 2024. **263**(Pt 1): p. 130309.
342. Zhang, X.W., et al., *Neuroinflammation inhibition by small-molecule targeting USP7 noncatalytic domain for neurodegenerative disease therapy.* Sci Adv, 2022. **8**(32): p. eabo0789.
343. Jing, B., et al., *Characterization of naturally occurring pentacyclic triterpenes as novel inhibitors of deubiquitinating protease USP7 with anticancer activity in vitro.* Acta Pharmacol Sin, 2018. **39**(3): p. 492-498.
344. Zafar, S., et al., *Ursolic acid: a natural modulator of signaling networks in different cancers.* Cancer Cell Int, 2022. **22**(1): p. 399.
345. Wang, Q.Q., et al., *Polyprenylated acylphloroglucinols as deubiquitinating protease USP7 inhibitors from Hypericum hookerianum.* Fitoterapia, 2020. **146**: p. 104678.
346. Yamaguchi, M., et al., *Spongiacidin C, a pyrrole alkaloid from the marine sponge Stylissa massa, functions as a USP7 inhibitor.* Bioorg Med Chem Lett, 2013. **23**(13): p. 3884-6.
347. Guedeney, N., et al., *PROTAC technology: A new drug design for chemical biology with many challenges in drug discovery.* Drug Discov Today, 2023. **28**(1): p. 103395.
348. Bekes, M., D.R. Langley, and C.M. Crews, *PROTAC targeted protein degraders: the past is prologue.* Nat Rev Drug Discov, 2022. **21**(3): p. 181-200.
349. Liu, X. and A. Ciulli, *Proximity-Based Modalities for Biology and Medicine.* ACS Cent Sci, 2023. **9**(7): p. 1269-1284.
350. Pei, Y., et al., *Discovery of a Potent and Selective Degrader for USP7.* Angew Chem Int Ed Engl, 2022. **61**(33): p. e202204395.
351. Murgai, A., et al., *Targeting the deubiquitinase USP7 for degradation with PROTACs.* Chem Commun (Camb), 2022. **58**(63): p. 8858-8861.
352. Ji, L., et al., *USP7 inhibits Wnt/beta-catenin signaling through promoting stabilization of Axin.* Nat Commun, 2019. **10**(1): p. 4184.
353. ElHarouni, D., et al., *iTReX: Interactive exploration of mono- and combination therapy dose response profiling data.* Pharmacol Res, 2022. **175**: p. 105996.
354. Gonzalez-Sanchez, J.C., et al., *Mechnetor: a web server for exploring protein mechanism and the functional context of genetic variants.* Nucleic Acids Res, 2021. **49**(W1): p. W366-W374.
355. Tyanova, S., et al., *The Perseus computational platform for comprehensive analysis of (prote)omics data.* Nat Methods, 2016. **13**(9): p. 731-40.
356. Ge, S.X., D. Jung, and R. Yao, *ShinyGO: a graphical gene-set enrichment tool for animals and plants.* Bioinformatics, 2020. **36**(8): p. 2628-2629.
357. Zheng, S., et al., *SynergyFinder Plus: Toward Better Interpretation and Annotation of Drug Combination Screening Datasets.* Genomics Proteomics Bioinformatics, 2022. **20**(3): p. 587-596.
358. Berker, Y., et al., *Magnetic Resonance Spectroscopy-based Metabolomic Biomarkers for Typing, Staging, and Survival Estimation of Early-Stage Human Lung Cancer.* Sci Rep, 2019. **9**(1): p. 10319.
359. Peterziel, H., et al., *Drug sensitivity profiling of 3D tumor tissue cultures in the pediatric precision oncology program INFORM.* NPJ Precis Oncol, 2022. **6**(1): p. 94.
360. Curran, T. and B.R. Franza, Jr., *Fos and Jun: the AP-1 connection.* Cell, 1988. **55**(3): p. 395-7.
361. Gillen, A.E., et al., *Single-Cell RNA Sequencing of Childhood Ependymoma Reveals Neoplastic Cell Subpopulations That Impact Molecular Classification and Etiology.* Cell Rep, 2020. **32**(6): p. 108023.
362. Borsi, G., et al., *Single-cell RNA sequencing reveals homogeneous transcriptome patterns and low variance in a suspension CHO-K1 and an adherent HEK293FT cell line in culture conditions.* J Biotechnol, 2023. **364**: p. 13-22.
363. Zhu, Q., et al., *Single cell multi-omics reveal intra-cell-line heterogeneity across human cancer cell lines.* Nat Commun, 2023. **14**(1): p. 8170.

364. Loewa, A., J.J. Feng, and S. Hedtrich, *Human disease models in drug development.* Nat Rev Bioeng, 2023: p. 1-15.
365. Roell, K.R., D.M. Reif, and A.A. Motsinger-Reif, *An Introduction to Terminology and Methodology of Chemical Synergy-Perspectives from Across Disciplines.* Front Pharmacol, 2017. **8**: p. 158.
366. Servidei, T., et al., *The BET Inhibitor OTX015 Exhibits In Vitro and In Vivo Antitumor Activity in Pediatric Ependymoma Stem Cell Models.* Int J Mol Sci, 2021. **22**(4).
367. Rogers, H.A., et al., *Supratentorial and spinal pediatric ependymomas display a hypermethylated phenotype which includes the loss of tumor suppressor genes involved in the control of cell growth and death.* Acta Neuropathol, 2012. **123**(5): p. 711-25.
368. Lee, K.W., et al., *Herpesvirus-associated ubiquitin-specific protease (HAUSP) modulates peroxisome proliferator-activated receptor gamma (PPARgamma) stability through its deubiquitinating activity.* J Biol Chem, 2013. **288**(46): p. 32886-96.
369. Meel, M.H., et al., *MELK Inhibition in Diffuse Intrinsic Pontine Glioma.* Clin Cancer Res, 2018. **24**(22): p. 5645-5657.
370. Lan, T., et al., *Paeoniflorin promotes PPARgamma expression to suppress HSCs activation by inhibiting EZH2-mediated histone H3K27 trimethylation.* Phytomedicine, 2024. **128**: p. 155477.
371. Han, J., et al., *Synergistic effect of poly (ADP-ribose) polymerase (PARP) inhibitor with chemotherapy on CXorf67-elevated posterior fossa group A ependymoma.* Chin Med J (Engl), 2024.
372. Wang, H., et al., *Discovery of Pamiparib (BGB-290), a Potent and Selective Poly (ADP-ribose) Polymerase (PARP) Inhibitor in Clinical Development.* J Med Chem, 2020. **63**(24): p. 15541-15563.
373. Cheng, X., et al., *Deubiquitination of FBP1 by USP7 blocks FBP1-DNMT1 interaction and decreases the sensitivity of pancreatic cancer cells to PARP inhibitors.* Mol Oncol, 2022. **16**(7): p. 1591-1607.
374. Molkentine, D.P., et al., *p16 Represses DNA Damage Repair via a Novel Ubiquitin-Dependent Signaling Cascade.* Cancer Res, 2022. **82**(5): p. 916-928.
375. Malapelle, U., et al., *USP7 inhibitors, downregulating CCDC6, sensitize lung neuroendocrine cancer cells to PARP-inhibitor drugs.* Lung Cancer, 2017. **107**: p. 41-49.
376. Morra, F., et al., *The combined effect of USP7 inhibitors and PARP inhibitors in hormone-sensitive and castration-resistant prostate cancer cells.* Oncotarget, 2017. **8**(19): p. 31815-31829.
377. Vitanza, N.A. and S. Partap, *Pediatric Ependymoma.* J Child Neurol, 2016. **31**(12): p. 1354-66.
378. Gryder, B.E., et al., *PAX3-FOXO1 Establishes Myogenic Super Enhancers and Confers BET Bromodomain Vulnerability.* Cancer Discov, 2017. **7**(8): p. 884-899.
379. Marchesi, I., et al., *Bromodomain Inhibitor JQ1 Provides Novel Insights and Perspectives in Rhabdomyosarcoma Treatment.* Int J Mol Sci, 2022. **23**(7).
380. Henssen, A., et al., *Targeting MYCN-Driven Transcription By BET-Bromodomain Inhibition.* Clin Cancer Res, 2016. **22**(10): p. 2470-81.
381. Puissant, A., et al., *Targeting MYCN in neuroblastoma by BET bromodomain inhibition.* Cancer Discov, 2013. **3**(3): p. 308-23.
382. Groves, A., J. Clymer, and M.G. Filbin, *Bromodomain and Extra-Terminal Protein Inhibitors: Biologic Insights and Therapeutic Potential in Pediatric Brain Tumors.* Pharmaceuticals (Basel), 2022. **15**(6).
383. Le Clorennec, C., et al., *USP7 Inhibition Suppresses Neuroblastoma Growth via Induction of p53-Mediated Apoptosis and EZH2 and N-Myc Downregulation.* Int J Mol Sci, 2023. **24**(18).
384. Zhang, Y., et al., *Combination of EZH2 inhibitor and BET inhibitor for treatment of diffuse intrinsic pontine glioma.* Cell Biosci, 2017. **7**: p. 56.
385. Gabriel, N., et al., *Loss of H3K27 Trimethylation Promotes Radiotherapy Resistance in Medulloblastoma and Induces an Actionable Vulnerability to BET Inhibition.* Cancer Res, 2022. **82**(10): p. 2019-2030.
386. Ishi, Y., et al., *Therapeutic Targeting of EZH2 and BET BRD4 in Pediatric Rhabdoid Tumors.* Mol Cancer Ther, 2022. **21**(5): p. 715-726.
387. Grogan S, P.C., *Pharmacokinetics. [Updated 2023 Jul 30]*. 2024, StatPearls [Internet]: Treasure Island (FL): StatPearls Publishing.
388. Carreira, L.D., et al., *Ubiquitin-specific protease 7 (USP7): an emerging drug target for cancer treatment.* Expert Opin Ther Targets, 2023. **27**(11): p. 1043-1058.
389. Koolen, S.L., et al., *From mouse to man: predictions of human pharmacokinetics of orally administered docetaxel from preclinical studies.* J Clin Pharmacol, 2012. **52**(3): p. 370-80.
390. Bidard, F.C., et al., *Elacestrant (oral selective estrogen receptor degrader) Versus Standard Endocrine Therapy for Estrogen Receptor-Positive, Human Epidermal Growth Factor Receptor*

2-Negative Advanced Breast Cancer: Results From the Randomized Phase III EMERALD Trial. J Clin Oncol, 2022. **40**(28): p. 3246-3256.

391. Fang, Y., et al., *Targeted protein degrader development for cancer: advances, challenges, and opportunities.* Trends Pharmacol Sci, 2023. **44**(5): p. 303-317.
392. Arvanitis, C.D., G.B. Ferraro, and R.K. Jain, *The blood-brain barrier and blood-tumour barrier in brain tumours and metastases.* Nat Rev Cancer, 2020. **20**(1): p. 26-41.
393. Gawdi R, S.K., Emmady PD, *Physiology, Blood Brain Barrier*. 2024, StatPearls [Internet]. Treasure Island (FL): StatPearls
394. Sarkaria, J.N., et al., *Is the blood-brain barrier really disrupted in all glioblastomas? A critical assessment of existing clinical data.* Neuro Oncol, 2018. **20**(2): p. 184-191.
395. Fresnais, M., et al., *Rapid and Sensitive Drug Quantification in Tissue Sections Using Matrix Assisted Laser Desorption Ionization-Ion Mobility-Mass Spectrometry Profiling.* J Am Soc Mass Spectrom, 2020. **31**(3): p. 742-751.
396. Berenguer-Daize, C., et al., *OTX015 (MK-8628), a novel BET inhibitor, displays in vitro and in vivo antitumor effects alone and in combination with conventional therapies in glioblastoma models.* Int J Cancer, 2016. **139**(9): p. 2047-55.
397. Ishida, C.T., et al., *BH3-mimetics and BET-inhibitors elicit enhanced lethality in malignant glioma.* Oncotarget, 2017. **8**(18): p. 29558-29573.
398. Hottinger, A.F., et al., *Dose optimization of MK-8628 (OTX015), a small molecule inhibitor of bromodomain and extra-terminal (BET) proteins, in patients (pts) with recurrent glioblastoma (GB).* Journal of Clinical Oncology, 2016. **34**(15_suppl): p. e14123-e14123.
399. Odore, E., et al., *Phase I Population Pharmacokinetic Assessment of the Oral Bromodomain Inhibitor OTX015 in Patients with Haematologic Malignancies.* Clin Pharmacokinet, 2016. **55**(3): p. 397-405.
400. Gaudio, E., et al., *Bromodomain inhibitor OTX015 (MK-8628) combined with targeted agents shows strong in vivo antitumor activity in lymphoma.* Oncotarget, 2016. **7**(36): p. 58142-58147.
401. Liu, Y., et al., *Brain co-delivery of first-line chemotherapy drug and epigenetic bromodomain inhibitor for multidimensional enhanced synergistic glioblastoma therapy.* Exploration (Beijing), 2022. **2**(4): p. 20210274.
402. Yang, J., et al., *Recent advances in SN-38 drug delivery system.* Int J Pharm, 2023. **637**: p. 122886.
403. Santi, D.V., E.L. Schneider, and G.W. Ashley, *Macromolecular Prodrug That Provides the Irinotecan (CPT-11) Active-Metabolite SN-38 with Ultralong Half-Life, Low Cmax , and Low Glucuronide Formation.* Journal of Medicinal Chemistry, 2014. **57**(6): p. 2303-2314.
404. Fontaine, S.D., et al., *PLX038: a PEGylated prodrug of SN-38 independent of UGT1A1 activity.* Cancer Chemotherapy and Pharmacology, 2019. **85**(1): p. 225-229.
405. Kievit, F.M., et al., *Nanoparticle mediated silencing of DNA repair sensitizes pediatric brain tumor cells to γ-irradiation.* Molecular Oncology, 2015. **9**(6): p. 1071-1080.
406. Khang, M., et al., *Intrathecal delivery of nanoparticle PARP inhibitor to the cerebrospinal fluid for the treatment of metastatic medulloblastoma.* Sci Transl Med, 2023. **15**(720): p. eadi1617.
407. Fontaine, S.D., et al., *A Very Long-Acting PARP Inhibitor Suppresses Cancer Cell Growth in DNA Repair-Deficient Tumor Models.* Cancer Res, 2021. **81**(4): p. 1076-1086.
408. Lord, C.J. and A. Ashworth, *PARP inhibitors: Synthetic lethality in the clinic.* Science, 2017. **355**(6330): p. 1152-1158.
409. Staniszewska, A.D., et al., *Preclinical Characterization of AZD9574, a Blood-Brain Barrier Penetrant Inhibitor of PARP1.* Clin Cancer Res, 2023.
410. Plummer, R., et al., *First-in-human study of the PARP/tankyrase inhibitor E7449 in patients with advanced solid tumours and evaluation of a novel drug-response predictor.* Br J Cancer, 2020. **123**(4): p. 525-533.
411. Smith, M.A., et al., *Initial testing (stage 1) of the PARP inhibitor BMN 673 by the pediatric preclinical testing program: PALB2 mutation predicts exceptional in vivo response to BMN 673.* Pediatr Blood Cancer, 2015. **62**(1): p. 91-8.
412. Mateo, J., et al., *A decade of clinical development of PARP inhibitors in perspective.* Ann Oncol, 2019. **30**(9): p. 1437-1447.
413. Sim, H.W., E. Galanis, and M. Khasraw, *PARP Inhibitors in Glioma: A Review of Therapeutic Opportunities.* Cancers (Basel), 2022. **14**(4).
414. Mahalingam, P., et al., *PARP inhibition utilized in combination therapy with Olaparib-Temozolomide to achieve disease stabilization in a rare case of BRCA1-mutant, metastatic myxopapillary ependymoma.* Rare Tumors, 2023. **15**: p. 20363613231152333.
415. Su, J.M., et al., *A phase I trial of veliparib (ABT-888) and temozolomide in children with recurrent CNS tumors: a pediatric brain tumor consortium report.* Neuro Oncol, 2014. **16**(12): p. 1661-8.

416. Schafer, E.S., et al., *Phase 1/2 trial of talazoparib in combination with temozolomide in children and adolescents with refractory/recurrent solid tumors including Ewing sarcoma: A Children's Oncology Group Phase 1 Consortium study (ADVL1411).* Pediatr Blood Cancer, 2020. **67**(2): p. e28073.
417. Hoy, S.M., *Tazemetostat: First Approval.* Drugs, 2020. **80**(5): p. 513-521.
418. Li, X., et al., *Dual target PARP1/EZH2 inhibitors inducing excessive autophagy and producing synthetic lethality for triple-negative breast cancer therapy.* Eur J Med Chem, 2024. **265**: p. 116054.
419. Wang, C., et al., *Discovery of First-in-Class Dual PARP and EZH2 Inhibitors for Triple-Negative Breast Cancer with Wild-Type BRCA.* J Med Chem, 2021. **64**(17): p. 12630-12650.
420. Zhang, X., et al., *Combined inhibition of PARP and EZH2 for cancer treatment: Current status, opportunities, and challenges.* Front Pharmacol, 2022. **13**: p. 965244.
421. Rondinelli, B., et al., *EZH2 promotes degradation of stalled replication forks by recruiting MUS81 through histone H3 trimethylation.* Nat Cell Biol, 2017. **19**(11): p. 1371-1378.
422. Zheng, S., et al., *Accelerated rational PROTAC design via deep learning and molecular simulations.* Nature Machine Intelligence, 2022. **4**(9): p. 739-748.
423. Paiva, S.L. and C.M. Crews, *Targeted protein degradation: elements of PROTAC design.* Curr Opin Chem Biol, 2019. **50**: p. 111-119.
424. Troup, R.I., C. Fallan, and M.G.J. Baud, *Current strategies for the design of PROTAC linkers: a critical review.* Explor Target Antitumor Ther, 2020. **1**(5): p. 273-312.
425. Webb, T., C. Craigon, and A. Ciulli, *Targeting epigenetic modulators using PROTAC degraders: Current status and future perspective.* Bioorg Med Chem Lett, 2022. **63**: p. 128653.
426. Bondeson, D.P., et al., *Lessons in PROTAC Design from Selective Degradation with a Promiscuous Warhead.* Cell Chem Biol, 2018. **25**(1): p. 78-87 e5.
427. Wang, J.Y. and J.A. Doudna, *CRISPR technology: A decade of genome editing is only the beginning.* Science, 2023. **379**(6629): p. eadd8643.
428. Dobosz, P. and T. Dzieciatkowski, *The Intriguing History of Cancer Immunotherapy.* Front Immunol, 2019. **10**: p. 2965.
429. Cao, L., et al., *The unique immune ecosystems in pediatric brain tumors: integrating single-cell and bulk RNA-sequencing.* Front Immunol, 2023. **14**: p. 1238684.
430. Griesinger, A.M., et al., *Multi-omic approach identifies hypoxic tumor-associated myeloid cells that drive immunobiology of high-risk pediatric ependymoma.* iScience, 2023. **26**(9): p. 107585.
431. Plant-Fox, A.S., K. O'Halloran, and S. Goldman, *Pediatric brain tumors: the era of molecular diagnostics, targeted and immune-based therapeutics, and a focus on long term neurologic sequelae.* Curr Probl Cancer, 2021. **45**(4): p. 100777.
432. Yi, M., et al., *Combination strategies with PD-1/PD-L1 blockade: current advances and future directions.* Mol Cancer, 2022. **21**(1): p. 28.
433. Nam, S.J., et al., *Tumor-infiltrating immune cell subpopulations and programmed death ligand 1 (PD-L1) expression associated with clinicopathological and prognostic parameters in ependymoma.* Cancer Immunol Immunother, 2019. **68**(2): p. 305-318.
434. Witt, D.A., et al., *Specific expression of PD-L1 in RELA-fusion supratentorial ependymoma: Implications for PD-1-targeted therapy.* Pediatr Blood Cancer, 2018. **65**(5): p. e26960.
435. Dai, X., et al., *USP7 targeting modulates anti-tumor immune response by reprogramming Tumor-associated Macrophages in Lung Cancer.* Theranostics, 2020. **10**(20): p. 9332-9347.
436. Wang, Z., et al., *Abrogation of USP7 is an alternative strategy to downregulate PD-L1 and sensitize gastric cancer cells to T cells killing.* Acta Pharm Sin B, 2021. **11**(3): p. 694-707.
437. Korenev, G., et al., *USP7 Inhibitors in Cancer Immunotherapy: Current Status and Perspective.* Cancers (Basel), 2022. **14**(22).
438. June, C.H., et al., *CAR T cell immunotherapy for human cancer.* Science, 2018. **359**(6382): p. 1361-1365.
439. Guo, X., et al., *B7-H3 in Brain Malignancies: Immunology and Immunotherapy.* Int J Biol Sci, 2023. **19**(12): p. 3762-3780.
440. Majzner, R.G., et al., *CAR T Cells Targeting B7-H3, a Pan-Cancer Antigen, Demonstrate Potent Preclinical Activity Against Pediatric Solid Tumors and Brain Tumors.* Clin Cancer Res, 2019. **25**(8): p. 2560-2574.
441. El Malki, K., et al., *Glucosylceramide Synthase Inhibitors Induce Ceramide Accumulation and Sensitize H3K27 Mutant Diffuse Midline Glioma to Irradiation.* Int J Mol Sci, 2023. **24**(12).
442. Mount, C.W., et al., *Potent antitumor efficacy of anti-GD2 CAR T cells in H3-K27M(+) diffuse midline gliomas.* Nat Med, 2018. **24**(5): p. 572-579.
443. Majzner, R.G., et al., *GD2-CAR T cell therapy for H3K27M-mutated diffuse midline gliomas.* Nature, 2022. **603**(7903): p. 934-941.

444. Theruvath, J., et al., *Anti-GD2 synergizes with CD47 blockade to mediate tumor eradication.* Nat Med, 2022. **28**(2): p. 333-344.
445. Ciccone, R., et al., *GD2-targeting CAR T-cell therapy for patients with GD2+ medulloblastoma.* Clin Cancer Res, 2024.
446. Donovan, L.K., et al., *Locoregional delivery of CAR T cells to the cerebrospinal fluid for treatment of metastatic medulloblastoma and ependymoma.* Nat Med, 2020. **26**(5): p. 720-731.

X Acknowledgements

This work would not have been possible without the support, encouragement and supervision of many people, all of whom I want to thank sincerely. Thank you for enabling me to perform this work. Thank you for making it a good time!

Thank you, **Marcel**, for bringing me to your lab and allowing me to perform my work as part of your group. With your supervision and support, you helped me improve myself as a scientist, showing me how to be inspired by science and stay focused on my experiments at the same time. You questioned me (and my results) where needed, but at the same time always gave me a feeling of safety and positivity. It was easy to follow someone that obviously still enjoys his job and makes work a fun place, be it through group outings, the annual summer barbecue or the trips to Utrecht. Most importantly, thank you for always seeing me as a person and guiding me through difficult times with compassion.

I would also like to thank **Stefan** for all the support und supervision over the years. You always took the time to listen and offered comments and guidance when needed. Thank you also for making "Pediatric Neurooncology" such a great division and place to work and for personally ensuring a great atmosphere among us colleagues- at the KiTZ parties, the retreat or simply by sponsoring pizza on a Friday afternoon.

Additionally, I would like to extend my gratitude to my **TAC members**, Darjus Tschaharganeh and Rob Russell, who also acts as referee for this thesis. Thank you for taking the time to follow my progress and offer valuable feedback, criticism and new perspectives, which improved my work as well as my scientific thinking. Further, I want to thank Gert Fricker and Moritz Mall for their participation in my PhD defense committee.

I firmly believe that PhD students are only as good as their colleagues. In my case, I could not have been blessed with better people than the members of the **Kool group**. Thank you for all the support, the love, coffee and good times!

Monika, you are amazing! I could always rely on you, you supported me wherever you could and taught me so much. But most importantly: I thoroughly enjoyed working with you. Your love for what you do shows, be it in cell culture, baking cakes or dancing it all out in Utrecht. You inspired me and motivated me to always perform best.

Without you, Norman and Benni, no *in vivo* experiments would have been possible. Thank you for taking care of all the mice, injections or treatments. It is impressive to see how much experience one can acquire at such young age. You kept it real and protected me from too high expectations.

From the moment we met at the selection, Aylin, your energy and love for science was contagious! Thank you so much for not only being my personal postdoc, but my friend. I learned from you, in science and in live, and will always look back at this time thinking about our numerous discussions, deep talks, cell culture crises and of course our marvelous AACR trip. We make a good A-Team.

Even though you left me behind, I am grateful to have shared some of my PhD time with you, Sonja and Felix. I benefitted from your experience and your ability to maneuver a PhD and live like not many others.

From holidays to triathlons, you led by example how to make the most out of a doctorate. Thank you, Sonja, for reading this thesis voluntarily!
A big thank you needs to be extended to Aniello, Enrique, Shanzheng, and Neal. Thank you not only for answering every possible data analysis question I could have, but also for sharing the office (well, not you Enrique) and all the fun moments. I hope I will be able to keep the educational post-lunch sessions a habit.
To all the other current or previous members of the Kool group, Islam, Dennis, Johannes, Annette, Joudi, Pascal, Jacky: Thank you for making it a special time.

Dank je wel, **Utrecht group**! Thank you for many fun memories, at the Christmas market in Heidelberg or at the bars in Utrecht, and for lively discussions and exchange during our Wednesday meetings.

An experience I won´t forget soon – the **Career Day R&D 2021**. Without you as team, Sabine, Sam, Martha, Jonas, Shiv, Ekaterina, and Julia, it would have never been this amazing journey you allowed me to be a part of.

To **everyone I collaborated with**, and who made this thesis possible: Thank you! Special mentioning goes to Christian, Sophie and Michael. Without your degraders my work would be missing much. Your attitude towards open science and collaborative efforts is unparalleled. Further, Aileen, Heike, Ina and the whole KiTZ TDSU made so many experiments possible that otherwise would not have been possible. To the Vienna crew, thank you for all the exchange, of ideas and cell lines. A big thank you also to all the DKFZ core facility members for FACS, Light Microscopy and Mass Spectrometry for supporting me and this project.

My entire doctorate experience would not have been the same without all you members of **B06x, the KiTZ and B062 especially**. I can count myself lucky to have met all of you. All the discussions and problem solving sessions were just as invaluable as the great atmosphere, the fun and collegiality. I am excited to see how all these bonds will tighten in the new building. Special thanks go to Andrea, for her support in the lab. To Jasmin, for answering my million questions about everything non-lab and for the fun chats. To the members of all S2 cell cultures, 1st floor and 4th floor. Hours of pipetting are simply more fun in good company. Thank you, Emma, for reading this thesis beforehand!

What is a PhD without other PhDs to complain about your PhD? Thank you, **Anna and Pavle**, for taking these roles after your great performance as master students.

Moreover, having a place outside of work to turn to was vital – thank you to all my **friends, roommates and teammates in Heidelberg**. Thank you, Heidelbeeren, for being understanding if my mood was bad during lines, if you had to listen to another stupid lab story, and always ensuring me that there is so much more than work. Special thanks to Lisa, Amelie, and Kati for keeping me sane during all the lockdowns and running through every part of the Neuenheimer fields with me. Isa, thanks to you I will always pack a change of clothes in my carry-on. I will gladly remember our great USA trip, the sunburn, laughter and Aperölchen! Your input for this thesis was more than the proof-reading. To Torben, Nike and Nils – your company in the WG during all the years kept me grounded and opened my horizons.

Thank you to everyone in **Pfungstadt** for getting me out of the Heidelberg bubble every now and then. I owe countless hours of fun, Pfungstädter, sunbathing in Amorbach (on crutches if necessary), Siedler, dancing, and midnight-discussions to you! Thank you for accepting me as non-local and supporting me and my dreams.

Hannah and Bine, you are two of my oldest friends. Thank you for still being in my life! I value your opinions, sharing moments and spending time with you.

A big thank you goes out to my **family**, kindred or in-law. All the birthday parties, Raclette sessions, soccer matches, and gardening experiences brighten my life. Thank you for being in it.

A great portion of my success I ow to my boyfriend, **Manuel**. Manu, without you this entire experience would have been so much harder. You create a safe place for me to feel myself, let go and recharge. You plant tomatoes for me, provide a shoulder to lean on and have mastered to art of making me laugh when I didn’t know I needed to. Ich liebe dich.

Der vielleicht größte Dank geht an meine **Mutter**. Du hast immer an mich geglaubt und bist mein größter Fan. Du schaffst es, mich anzuspornen, mir Selbstbewusstsein zu vermitteln und mich geliebt zu fühlen. Deine Unterstützung bedeutet mir alles.

Ein letzter Dank geht an Papa, Oma, und Opa. Es schmerzt mich, dass ihr diese Zeilen nicht mehr lesen könnt. Ich weiß ihr wärt stolz.